

**DOTTORATO DI RICERCA IN IL FUTURO DELLA
TERRA, CAMBIAMENTI CLIMATICI E SFIDE
SOCIALI
Ciclo XXXVI**

Settore concorsuale: 02/CI - Astronomia, Astrofisica, Fisica della Terra e dei Pianeti

Settore scientifico disciplinare: FIS/06 - Fisica per il Sistema Terra e il Mezzo Circumterrestre

**FAST RADIATIVE TRANSFER ALGORITHMS FOR
ATMOSPHERIC RADIANCE COMPUTATION IN THE
PRESENCE OF SCATTERING**

Presentata da: Michele Martinazzo

**Coordinatore Dottorato:
Prof.ssa Silvana Di Sabatino**

**Supervisore:
Prof. Tiziano Maestri**

Esame finale anno 2024

Abstract

This thesis explores the implementation of fast scaling methodologies for the computation of mid and far-infrared spectrally resolved radiances in the presence of scattering. These methods aim to reduce the computational cost of solving the radiative transfer equation by avoiding the direct computation of multiple scattering effects. The study focuses on their application in operational satellite radiance data assimilation and remote sensing retrievals. In the first part of the work, two important scaling methodologies, Chou's scaling [13] and the similarity principle [23], initially developed for fluxes calculation, are considered. The assessment of their accuracy in reproducing spectrally resolved radiances in the mid and far-infrared is performed using a reference code in a nadir-looking geometry representative of the FORUM instrument (100-1600 cm^{-1}). The results indicate good performance of the Chou method in reproducing radiances in the mid-infrared for water and ice clouds. However, limitations arise for ice clouds in the far-infrared, leading to overestimation of upwelling radiances.

To address computational errors in the basic scaling method, a correction term is introduced based on the solution proposed by Tang et al. (2018) [106]. This correction term, originally derived for fluxes computation, is extended to spectrally resolved radiances through coefficient optimization. The application of this routine produces reduction in radiance residuals for various cloudy cases, especially for thin cirrus clouds targeted by the FORUM mission. However, challenges persist for medium-large optical depths and small effective radii.

The radiative parameters needed for the Chou and Tang schemes are parametrized using polynomial functions of the effective dimension of the cloud particle size distribution. These parameters are then integrated into the σ -IASI/F2N code, a forward model for fast radiance and derivative calculations with respect to atmospheric and spectroscopic parameters.

Finally, this thesis presents an improved approach called MAMA for solving the radiative transfer equation efficiently. This solution can be interpreted as an asymmetric adjusted scaling, and it excels in simulating spectrally resolved upwelling radiances in the presence of atmospheric diffusive layers, particularly for optically thin scattering layers like cirrus clouds. The algorithm simplifies the radiative transfer equation, introducing the angular back-scattering coefficient derived from the particle size distribution's phase function. Moreover, its flexibility allows for straightforward updates of optical properties based on any single scattering properties database.

Contents

1 Aim of the Work	1
1.1 Introduction	2
1.2 The Far Infrared Region of Earth's emission spectrum	4
1.2.1 Climate feedbacks and the far infrared region	6
1.3 The FORUM mission	9
2 The radiative transfer equation and its solution	13
2.1 Definitions of radiative quantities	13
2.2 Derivation of the radiative transfer equation	16
2.2.1 Exchange of photons	17
2.2.2 Absorption of photons	18
2.2.3 Scattering of photons	19
2.2.4 Emission of photons	19
2.2.5 The radiative transfer equation	20
2.2.6 The direct-diffuse splitting	20
2.3 Solution for the diffuse radiative transfer equation	21
2.3.1 Discrete ordinate method	23
2.3.2 Scaling methods	26
3 Application of scaling methods to spectral radiance computation	31
3.1 Introduction	31
3.2 Atmosphere, clouds, and aerosols characterization	33
3.2.1 Liquid water clouds	34
3.2.2 Ice clouds	35
3.2.3 Aerosols	36
3.3 Computational methodologies	37
3.3.1 Full scattering	38
3.3.2 CA method	39
3.3.3 Similarity principle	40
3.4 Results	41
3.4.1 Accurate computation and parameterization of b	41
3.4.2 Scattering correction term for CA and SP	43

3.4.3	Spectral radiance analysis	44
3.4.4	Liquid water clouds	45
3.4.5	Ice clouds	48
3.4.6	Aerosols	53
3.5	Final considerations	56
4 	Tang's adjustment scheme and its application	59
4.1	Errors in the scaling methods	59
4.2	Adjustment scheme for flux computations	60
4.3	Extension of adjustment schemes for upwelling radiances computation	65
4.3.1	Calculation of $k(\mu)$	66
5 	σ-IASI/F2N radiative transfer code	73
5.1	Introduction to σ -IASI	73
5.2	The basic radiative transfer in σ -IASI/F2N	75
5.2.1	Transmittance calculations and the optical depth lookup table	79
5.2.2	Cloud optical depth parameterization, the C-mode	80
5.2.3	The C-T mode	84
5.3	Methods	85
5.4	Evaluation of the C-mode with IASI data	86
5.5	Final considerations	94
6 	Asymmetric adjusted scaling for upward radiances computation	95
6.1	Introduction	95
6.2	The radiative transfer equation and its approximation	96
6.2.1	The mean upward ambient radiation $\langle I_u(\tau, \mu) \rangle$	99
6.2.2	The mean downward ambient radiation $\langle I_d(\tau, \mu) \rangle$	100
6.2.3	Solution of the radiative transfer equation	101
6.3	Methods and Results	103
6.3.1	Assumptions on Liquid Water and Ice Clouds	104
6.3.2	Comparison with the reference Model	106
6.4	Final considerations	115
7 	Summary and final discussions	117
A 	Similarity principle analysis	121
B 	Derivation of \vec{I}	125
C 	Optical Properties of Water and Ice Clouds	127
D 	Solution for off-nadir observation angles	131
E 	Tang's adjustment and MAMA solution	133

List of Figures

1.1	Simulated up-welling radiance at the top of the atmosphere for a tropical standard atmosphere (blue solid line). Dashed red lines show the equivalent blackbody emission at the given temperature. The red and orange shaded areas highlight the Far- and Mid-Infrared Regions, FIR and MIR respectively.	5
1.2	Annual mean all-sky OLR in 2019, derived from AIRS and CERES observation. Measurements from 2019. Figure adapted from L'Ecuyer et al. (2021) [58].	6
1.3	Estimated fraction of OLR in FIR wavelength. Figure adapted from L'Ecuyer et al. (2021) [58].	6
1.4	Ice cloud occurrence frequency over the globe. Figure adapted from Hong and Liu (2015) [44].	8
1.5	Simulated up-welling radiance at the top of the atmosphere for a tropical standard atmosphere (blue solid line). The red and blue bands represent the measure spectral range of FORUM and IASI-NG respectively. The purple dots are representative of the observation channels of the PREFIRE spectrometers.	10
2.1	Definition of the local spherical-coordinate system. Adapted from Zdunkowski et al., (2007) [123].	14
2.2	Elements in radiance definition. Adapted from Zdunkowski et al., (2007) [123].	16
2.3	Eulerian representation of the continuity equation. Adapted from Zdunkowski et al., (2007) [123].	18
3.1	Vertical profiles of temperature (black solid line) and water vapor mixing ratio (red dashed line) for the considered scenarios. Light blue and purple shaded layers show the height position and thickness of the analyzed ice clouds and liquid water clouds, respectively.	34
3.2	Imaginary part of the refractive indices used for the computation of the cloud and aerosol particle size distributions.	37
3.3	Flow diagram of the code chain used for the radiative transfer simulations. Databases are in red boxes, codes are in blue and outputs are in yellow. The three methodologies are highlighted in green. The final spectrum is a synthetic FORUM-like observation. See text for more details.	39

3.4	Left panel: Comparison of the backscattering function b versus the asymmetry parameter g of liquid water PSDs for three computation approaches: exact integral using Monte Carlo (blue dots, Equation 3.16), polynomial by Chou et al. (black line, Equation 3.9), and polynomial fit with updated coefficients, UniboWAT (red line, Table 3.3). Right panel: same as left panel, but for ice aggregates PSDs. The updated polynomial fit (red line, Table 3.3) is called UniboICE.	42
3.5	Optical depth re-scaling terms (see legend and text) in case of CA (blue line) and SP (orange) approaches, as a function of wavenumber. Upper panel: liquid water PSD with $r_{eff} = 10 \text{ cm}^{-1}$. Bottom panel: ice aggregates PSD with $r_{eff} = 30 \text{ cm}^{-1}$	44
3.6	Top panel: top of the atmosphere FORUM spectral radiances computed with the FS approach for a 50°N atmosphere in the presence of a liquid water cloud layer, whose top is placed at 1.5 km and with $\text{OD} = 15$. Bottom panel: radiance differences between CA and FS approaches for the same clouds as in the top panel. FGN is highlighted by a grey-shaded area.	46
3.7	Radiance (ΔI , contour) and brightness temperature (ΔBT , color) differences between CA and FS approaches at 1203 cm^{-1} (MIR), for liquid water clouds. The white color indicates differences below the FORUM noise level, marked by the red contour line. Y-axes are in log scale.	47
3.8	Radiance (ΔI , contour) and brightness temperature (ΔBT , color) differences between CA and FS approaches at 531 cm^{-1} (FIR), for liquid water clouds. The white color indicates differences below the FORUM noise level, marked by the red contour line. Y-axes are in log scale.	48
3.9	Top panel: top of the atmosphere FORUM spectral radiances computed with the FS approach for a 50°N atmosphere in the presence of an ice cloud layer, whose top is placed at 8 km height and with $\text{OD} = 1$. Bottom panel: radiance differences between CA and FS approaches for the same clouds as in the top panel. FGN is highlighted by a grey-shaded area.	50
3.10	Radiance (ΔI , contour) and brightness temperature (ΔBT , color) differences between CA and FS approaches at 1203 cm^{-1} (MIR), for ice clouds. The white color indicates differences below the FORUM noise level (red contour line). Y-axes are in log scale.	51
3.11	Radiance (ΔI , contour) and brightness temperature (ΔBT , color) differences between CA and FS approaches at 410 cm^{-1} (FIR), for ice clouds. The white color indicates differences below the FORUM noise level (red contour line). Y-axes are in log scale.	52

3.12	Radiance (ΔL , contour) and brightness temperature (ΔBT , color) differences between CA and FS approaches, at MIR (top panels, 1203 cm^{-1}) and FIR (bottom panels, 410 cm^{-1}) wavenumbers. All the panels refer to the same low latitude scenario (34°N), and to an ice cloud with top placed at 15 km . The cloud geometrical thickness is indicated on the top of the upper panels and ranges from 500 m to 4500 m . The white color indicates differences below the FORUM noise level, marked by the red contour line. Y-axes are in log scale.	53
3.13	Top panel: spectral differences between FORUM-like observations in clear sky or in the presence of an aerosol-loaded atmosphere with dust-like particles. Bottom panel: differences between radiances computed using the CA and the FS approaches for the same aerosol cases presented in the upper panel. The simulations are obtained considering a 34°N atmosphere, and $r_{eff} = 2.0\ \mu\text{m}$. FGN is highlighted by a grey shaded area.	54
3.14	Top panel: spectral differences between FORUM-like observations in clear sky or in presence of an aerosol-loaded atmosphere with volcanic dust particles. Bottom panel: differences between radiances computed using the CA and the FS approaches for the same aerosol cases presented in the upper panel. The simulations are obtained considering a 50°N atmosphere, and $r_{eff} = 2.0\ \mu\text{m}$. FGN is highlighted by a grey shaded area.	55
4.1	Errors in the TOA and surface fluxes for high, middle, and low clouds. Solid and dashed lines represent the case where scattering is neglected and the case where the scaling method proposed by Chou is implemented respectively. The calculations are obtained for a mid-latitude summer atmosphere. Figure adapted from Chou et al., (1999) [13] Figure 5.	59
4.2	Single layer representation assuming plane-parallel approximation. The quantity τ_j represents the optical depth from the top of the atmosphere to the level j	62
4.3	Example of adjustment scheme algorithm flowcharts	64
4.4	Error of TOA upward and surface downward irradiances vs reference TOA upward irradiance scatterplot of three schemes: neglect scattering (black), Chou scaling (cyan), and Chou-Tang adjustment (red). The results are presented for 1 integration point (A) and for 3 integration points (B). Adapted from Tang et al., (2018) [106].	64
4.5	Flow diagram of the code chain used for the radiative transfer simulations. Databases are in red boxes, codes are in blue and outputs are in yellow. The two final solutions are highlighted in green and are convolved to a FORUM-like resolution. See text for more details.	67
4.6	Coefficients for water spheres (A) and column aggregates (B) as a function of the effective radius (μm). The black solid line represents the parameterization as a function of the effective radius of the PSD.	68

4.7	Radiance differences between Chou's solution (blu line) and Tang adjusted solution (orange line) with respect to the reference solution (DISORT) for a water cloud scenario. Tang correction routine is applied considering a suitable k coefficients as described above. The water cloud is described by an $OD = 5.0$, $r_{eff} = 10 \mu m$ and its top altitude is 3 km.	69
4.8	Radiance differences between Chou's solution (blu line) and Tang adjusted solution (orange line) with respect to the reference solution (DISORT) for an ice cloud scenario. Tang correction routine is applied considering a suitable k coefficients as described above. The ice cloud is described by an $OD = 1.0$, $r_{eff} = 30 \mu m$ and its top altitude is 8 km.	70
4.9	Vertical profiles of temperature (black solid line) and water vapor mixing ratio (red solid line) for the considered scenarios. Light blue shaded layers show the height position and thickness of the analyzed ice clouds.	70
4.10	Radiance differences ΔI , $mW/(m^2srcm^{-1})$, between Chou solution (upper panels) or Tang solution (lower panels) and the DISORT code as a function of multiple combinations of PSD effective radius and cloud optical depths. The $410 cm^{-1}$ (FIR) spectral channel is considered. The three panels of each row are for ice clouds at 6 km, 8 km, and 12 km of altitude, respectively. The white color indicates differences below the FORUM noise level, marked by the red contour line. Y-axes are in log scale. The green line indicates the $OD-r_{eff}$ combination obtained from the Sun (2001) [105] parameterization.	71
5.1	Schematic representation of σ -IASI.	74
5.2	The definition of the atmospheric pressure levels used in σ -IASI/F2N.	76
5.3	σ -IASI/F2N layering. The level L represents the last layer of the model ($L = 60$). The optical depth values τ_j are calculated from the level j to the TOA.	76
5.4	Radiances derivatives with respect to q_w (A) and r_{eff} (B) for a water cloud on a tropical atmosphere. On the right part of the panels, the vertical profile of the cloud property is presented.	83
5.5	Radiances derivatives with respect to q_i (A) and D_{eff} (B) for an ice cloud on a tropical atmosphere. On the right part of the panels, the vertical profile of the cloud property is presented.	83
5.6	Flowchart describing the implementation of the C-T mode within σ -IASI/F2N. The incorporation of the new routine exploits the linearity of the correction term, allowing for a complete independent subroutine. If the C-T mode is activated, the correction term is linearly added to the Chou solution.	84
5.7	IASI-B and C footprints in the database. The data are over the sea, and are collected in the period that goes from 8 September 2021 23:45 to 10 September 2021 00:15, coinciding with the ECMWF analysis runs. The color indicates the IASI observation measurement time.	86

5.8	Example of σ -IASI/F2N spectrum showing the spectral channels selected to check the consistency between observations and simulations.	87
5.9	Comparison of the spatial maps of the observed (IASI) and calculated (σ -IASI/F2N) radiances in the first three of six selected channels (660 cm^{-1} , 791.75 cm^{-1} , and 867.75 cm^{-1}).	88
5.10	As in Figure 5.9 but in the last three selected channels (1052 cm^{-1} , 1499.25 cm^{-1} , and 1576 cm^{-1}).	88
5.11	Histograms of Obs-Calc for the six channels listed in Figure 5.8. The difference in the figure corresponds to cloudy soundings (in the number 32364) in the maps of Figure 5.7.	90
5.12	Histograms of Obs-Calc for the six channels listed in Figure 5.8. The difference in the figure corresponds to clear soundings (in the number 2269) in the maps of Figure 5.7.	91
5.13	Observations and Calculations averaged over the whole set of night-time clear sky soundings.	92
5.14	Observations and Calculations averaged over the whole set of night-time cloudy sky soundings.	92
5.15	Observations and Calculations averaged over the whole set of day-time clear sky soundings.	93
5.16	Observations and Calculations averaged over the whole set of day-time cloudy sky soundings.	93
6.1	The angular coefficients $1 - c(\mu)$ (red) and $c(\mu)$ (green). The semicircle indicates the hemispheric radiation scattered in the μ direction by the layer. In the figure $\mu = 1$	98
6.2	Temperature (black solid line) and water vapor mixing ratio (red dashed line) vertical profiles for three different scenarios. Light blue and purple shaded bands indicate the height position and thickness of the ice and liquid water clouds, respectively, used in the computations.	104
6.3	Top panel: radiance differences between approximate solutions (Chou's scaling method in blue and MAMA solution in orange) and the reference approach for a mid-latitude water cloud with $OD = 10$, $r_{eff} = 4\ \mu\text{m}$ and cloud top at 3 km . Bottom panel: the same as upper panel, but for an effective radius of $15\ \mu\text{m}$. The range of values of the FORUM NESR are highlighted by a grey shaded area.	107
6.4	Radiance differences (ΔI) between the MAMA and the reference solution at 1203 cm^{-1} (MIR), for multiple liquid water clouds (varying ODs and r_{eff}) and atmospheric conditions (Low, Mid and High latitude). If present, the red and blue contour lines highlight the regions where the differences values are above the goal FORUM NESR.	108
6.5	Same as Figure 6.4 but for radiance differences (ΔI) at 531 cm^{-1} (FIR).	109

- 6.6 Top panel: radiance differences between the approximate solutions (Chou's scaling method in blue and MAMA in orange) and the reference algorithm in the presence of a mid latitude ice cloud with $OD = 1$, $r_{eff} = 20 \mu m$ and top altitude at $8 km$. Bottom panel: the same as above, but for an effective radius of $30 \mu m$. The range of values of the FORUM NESR are highlighted by a grey shaded area 111
- 6.7 Radiance differences (ΔI , contour) between the MAMA and the full-physics solution at $1203 cm^{-1}$ (MIR), for multiple ice clouds (varying ODs and r_{eff}) and atmospheric conditions (Low, Mid and High latitude). If present, the red and blue contour lines highlight the regions where the differences values are above the goal FORUM NESR. 112
- 6.8 Radiance differences (ΔI , contour) as in Figure 6.7 but for values at $410 cm^{-1}$ (FIR). 113
- 6.9 Top panels: Radiance differences (ΔI , contour) between the MAMA and the full-physics solution at $1203 cm^{-1}$ (MIR), for ice clouds characterized by plates crystals (left panel) and solid columns (right panel) and varying ODs and r_{eff} . The cloud is placed at $12 km$ of altitude and in tropical conditions (Low latitude). Red and blue contour lines indicate the regions where the differences values are above the goal FORUM NESR. Bottom panels: same as above but at $410 cm^{-1}$ (FIR). 114
- A.1 Radiance (ΔL , contour plot) and brightness temperature (ΔBT , color scale) differences between SP and FS for liquid water clouds at $1203 cm^{-1}$ (MIR). The white color indicates differences below the FORUM noise level, marked by the red contour line. Y-axes are in log scale. 121
- A.2 Radiance (ΔL , contour plot) and brightness temperature (ΔBT , color scale) differences between SP and FS for liquid water clouds at $531 cm^{-1}$ (FIR). The white color indicates differences below the FORUM noise level, marked by the red contour line. Y-axes are in log scale. 122
- A.3 ΔL , contour plot) and brightness temperature (ΔBT , color scale) differences between SP and FS for column aggregates ice clouds at $1203 cm^{-1}$ (FIR). The white color indicates differences below the FORUM noise level, marked by the red contour line. Y-axes are in log scale. 123
- A.4 ΔL , contour plot) and brightness temperature (ΔBT , color scale) differences between SP and FS for column aggregates ice clouds at $410 cm^{-1}$ (FIR). The white color indicates differences below the FORUM noise level, marked by the red contour line. Y-axes are in log scale. 124
- B.1 Schematic representation of the processes assumed to model the horizontal radiance \vec{I} within a cloud layer. 125

C.1	Upper panel: angular back-scattering $c(\mu = 1)$ and back-scattering b coefficients for water clouds as a function of the wavenumber. Two effective radii are considered as reported in the legend. Lower panel: the same as upper panel but for ice clouds.	128
C.2	Upper panel: Values of the asymmetry parameter g (solid line) and the gamma coefficient $\gamma(\mu = 1)$ (dotted line) of a water cloud as a function of the wavenumber. The values are reported for two different effective radii of the distribution. Lower panel: the same of above but for an ice cloud.	129
C.3	Angular back-scattering coefficient, $c(\mu)$, as a function of the viewing angle (in degrees). A water cloud with an effective radius of $10 \mu m$ is considered. The blue and pink lines refer to wavenumbers at 531 (FIR) and 1203 (MIR) cm^{-1} , respectively.	130
C.4	Angular back-scattering coefficient, $c(\mu)$, as a function of the viewing angle (in degrees). An ice cloud with an effective radius of $20 \mu m$ is considered. The blue and pink lines refer to wavenumbers at 410 (FIR) and 1203 (MIR) cm^{-1} , respectively.	130
E.1	Radiance differences ΔI , $mW / (m^2 s r cm^{-1})$, between Chou solution (first column), Tang solution (second column) or MAMA solution (third column) and the DISORT. The results are presented as a function of multiple combinations of PSD effective radius and cloud optical depths. The $410 cm^{-1}$ (FIR) spectral channel is considered. The three panels of each row are for ice clouds at $6 km$, $8 km$, and $12 km$ of altitude, respectively. The white color indicates differences below the FORUM noise level, marked by the red contour line. Y-axes are in log scale.	134

List of Tables

3.1	Main features of the selected scenarios. Data from the ERA 5 database.	33
3.2	Values and ranges of the cloud and aerosol parameters used in the selected case studies.	35
3.3	Coefficients for the polynomial fitting of b versus g . The fits are in the form $b = 1 - \sum_i a_i g^{i-1}$	43
3.4	Precipitable water vapor in the atmospheric column above the case studies cloud top.	49
4.1	Values and ranges of the cloud parameters used in the selected case studies.	67
4.2	Values of the coefficients P_i used in the expression 4.13.	69

5.1	Quantities contained in the σ -IASI/F2N state vector.	75
6.1	The main cloud parameters (and their range) used for the simulation comparisons.	106

Abbreviations

BT	Brightness Temperature
CA	Chou Approximation
DISORT	Discrete Ordinate Radiative Transfer
ESA	European Space Agency
FIR	Far InfraRed
FORUM	Far-infrared Outgoing Radiation Understanding and Monitoring
FS	Full Scattering
FGN	FORUM Goal NESR
LBLDIS	LBLRTM + DISORT
LBLRTM	Line-by-Line Radiative Transfer Model
MIR	Mid InfraRed
NASA	National Aeronautics and Space Administration
NESR	Noise Equivalent Spectral Radiance
OD	Optical Depth
PCRTM	Principal Component-based Radiative Transfer Model
PSD	Particle Size Distribution
PREFIRE	Polar Radiant Energy in the Far-InfraRed Experiment
PWV	Precipitable Water Vapor
RTM	Radiative Transfer Model
RU	Radiance Units
SP	Similarity Principle
SST	Sea Surface Temperature

I | Aim of the Work

This chapter serves as an introduction to the primary framework that underpins the foundation of this thesis work.

The main goal of this thesis is to present an overview over the application of a special class of methods, called scaling method, to the simulation of upwelling spectrally-resolved radiances, for the far-infrared radiative transfer problem in the presence of scattering. Specifically, these routines will be applied to the simulation of FORUM-like measurements in retrieval algorithms, with the goal of obtaining level 2 products (e.i. the state of the observed scene). The application of these methodologies allows to speed up the computation of the radiation field. However, this acceleration comes at the inevitable cost of introducing errors into the simulation. Given a particular physical problem and given a set of models describing this problem, the trade-off between accuracy, computational efficiency, and ease of implementation is a key factor in the model's decision-making process. In this thesis, these three factors stand as the focal points for evaluating the efficacy of this class of methods, for the simulation of nadir-looking geometry radiances.

The thesis is structured as follows:

- **Chapter 1:** The main framework is presented. The European Space Agency FORUM mission is introduced.
- **Chapter 2:** The theoretical background is presented, and all the fundamental quantities used in this thesis are derived.
- **Chapter 3:** The applicability of the scaling methodologies to the simulation of spectrally resolved radiances is evaluated.
- **Chapter 4:** The adjustment scheme for the scaling solutions presented by Tang et al., (2018) [106] is introduced and applied to spectral radiance computations.
- **Chapter 5:** The fast radiative transfer code σ -IASI is described.
- **Chapter 6:** An original scheme for the computation of the upwelling radiances in presence of clouds is described.
- **Chapter 7:** Conclusions and final considerations.



1.1 | Introduction

With the era of satellite missions for environmental and meteorological applications, radiative transfer in the Earth's atmosphere has become a topic that is at the forefront of all physically-based remote sensing applications. Initially, radiative transfer calculations were primarily confined to clear skies and simplistic one-layer opaque cloud scenarios (emissivity equal to 1), e.g. [28, 79]. However, recognizing the importance and significance of clouds' impact on weather and climate, researchers have dedicated efforts to formulate appropriate schemes for solving the fundamental equations in cloudy atmospheres. One result soon achieved with satellite observations is that the Earth globe is, on average, covered by clouds by more than 65% [55]. After years of observations, it is now well recognized (e.g. [50]) that cloud identification and properties retrieval are fundamental for the definition of the radiative balance at the surface and at the top of the atmosphere, and that assessing the impact of clouds on the global circulation represents a significant task in improving climate models.

In the last two decades, the scientific community has increased its involvement in the study of the Earth emission at Far Infrared (FIR) wavenumbers (approximately $10\text{-}667\text{ cm}^{-1}$). The growing interest in this part of the spectrum is justified by the important role played by FIR radiation in shaping the Earth's energy balance and by its sensitivity to essential climate variables such as temperature, water vapor, surface emissivity, and clouds. At terrestrial temperature, roughly half of the Earth's total energy emission occurs at FIR wavelengths. In this spectral region, the water vapor exhibits important absorption features, making the FIR highly valuable for improving the characterization of the atmospheric water vapor content and profile [81]. In conditions of low humidity, such as those encountered at high latitudes or at elevated locations, the water vapor absorption at FIR is reduced thus allowing surface emitted radiation to escape. This opens the possibility of deriving the FIR surface emissivity from satellite observations [5, 100] and possibly reduce uncertainties in climate models related to wrong assumptions on ice and snow emission properties (i.e [29]). Radiation fields at FIR wavelengths are also strongly influenced by the presence of clouds. In particular, recent studies have demonstrated the larger sensitivity of FIR radiances to the scattering by ice particles with respect to the mid-infrared part of the spectrum [66, 96, 122]. Despite its significance, mostly due to technical difficulties, the FIR remains currently unobserved from space. To address this observational gap, both the European Space Agency (ESA) and the National Aeronautics and Space Administration (NASA) are running innovative satellite projects, which aim at measuring the FIR component at different spectral resolutions. Specifically, ESA, in 2019, selected the Far-infrared Outgoing Radiation Understanding and Monitoring (FORUM) mission as its ninth Earth Explorer, scheduled to launch in 2027 [88]. FORUM will collect measurements of the outgoing longwave radiation in the spectral range that goes from $100\text{ to }1600\text{ cm}^{-1}$, with 0.5 cm^{-1} (un-apodized) spectral resolution. On its side, NASA will launch, in 2024, two CubeSats loading the Polar Radiant Energy in the Far-InfraRed Experiment (PREFIRE) [58] which will measure the $0\text{-}54\text{ }\mu\text{m}$ region at $0.84\text{ }\mu\text{m}$ spectral resolution.

In this context, the scientific community involved in the FORUM and PREFIRE missions is currently assessing the ability of fast radiative transfer codes to simulate radiance fields at

FIR wavelengths in order to set up the appropriate algorithms for the definition of the level 2 products and the analysis of the future measurements that will be performed by the sensors of the two aforementioned missions. The approach used to solve the radiative transfer equation has a significant impact on the accuracy and speed of the simulation. In a clear sky scenario, as long as the thermal infrared region is considered (say 4 to 100 μm), radiative transfer in the atmosphere is dominated by absorption and emission processes. In this case, the solution is straightforward and once the gaseous optical depths are known the simulation run can be very fast. On the other hand, when clouds or aerosols are considered, the radiative transfer solution complicates due to multiple scattering processes.

In the last half century, a large number of *numerical* methods (e.g. doubling-adding [27, 104], discrete ordinate methods [61], Monte Carlo method [11] or the successive-orders-of-scattering approach [83]) have been developed to solve the radiative transfer equation in the presence of scattering layers such as clouds and aerosols. These "reference" methodologies have been used to extensively validate the single scattering properties database against measurements in the FIR and MIR part of the spectrum (i.e [4, 9, 19, 68]).

Nevertheless, radiative transfer algorithms laying on numerical schemes which rigorously solve the multiple scattering equation require significant computational time, thus they are unsuitable in numerical weather prediction data assimilation routines [80], or to be used for the analysis of large datasets or for fast operational retrievals of geophysical parameters and atmospheric composition (e.g. [1, 21]). Hyper-fast methodologies exist, capable of computing high-resolution radiances over the full infrared spectrum in less than 0.05 seconds on a standard personal computer. An example is PCRTM [63], which exploits the principal component analysis to reconstruct the entire spectra given few computations on assigned monochromatic channels. Usually, this class of models relies on pre-computed lookup tables, neural networks, or statistical routines, making difficult to ingest new releases of optical properties without remarkable computational efforts. In addition, an explicit treatment of the micro-physics is generally missing.

In this framework, fast, analytical, and approximate methods are desirable. The two- and four-stream approximations are important examples of these methodologies, widely applied to perform fast irradiance and radiance computations [22, 62, 107] in a time of the order of few seconds on a normal personal computer. To further reduce the computational time, one can utilize a scaling approach, which allows to simplify the radiative transfer equation by avoiding the direct computation of the multiple scattering scheme. A notable example is the Chou approximation [13]. In this class of schemes, the multiple scattering effects are accounted for by scaling the optical depth of the layer, reducing the radiative transfer equation to a Schwarzschild-like equation. These approximations yield an extremely simple solution, which can be implemented in models originally running in clear sky conditions only, without affecting the modeling structure of the code. Nevertheless, assumptions made to apply scaling methods introduce errors in the simulation, which results in a general overestimation of the computed fluxes and radiances as assessed in the works by [57, 74, 106]. In the last years, efforts have been made to enhance the accuracy of these scaling methodologies. An example is the adjustment scheme proposed by Tang et al. (2018) [106] for the computation of the long-wave upwelling irradiances, recently adapted to the computation of radiances by

[71].

In this thesis work, an overview on the application of scaling methods to the computation of spectrally resolved radiances is presented.

1.2 | The Far Infrared Region of Earth's emission spectrum

The Earth system is a cool object in the space [37]. If we would measure its brightness temperature (i.e. the temperature of an equivalent blackbody), we would obtain a value of about 255 K. From the Planck radiation law, we know that this temperature implies a peak in the emitted radiation at about 500 cm^{-1} , with almost 35% of the energy emitted at lower wavenumbers.

Even if there is not a precise definition of where the boundaries of the far-infrared region occur, a general choice is to consider FIR all the spectral region that goes from 10 to 667 cm^{-1} . With this definition, and given what is stated above, we can say that the FIR accounts for almost 45% of the total energy leaving our planet [37]. This fraction can exceed 60% if we move toward the polar regions during the winter season [58].

In this segment of the electromagnetic spectrum, the atmospheric emission and absorption is driven by the rotational absorption band of the water vapour molecules. This region is characterized by the presence of strong absorption lines interspersed with narrow regions, called dirty micro-windows, where the absorption intensity is reduced. These features are represented in Figure 1.1, which shows the simulated up-welling radiance at the top of the atmosphere for a tropical standard atmosphere, and some of its spectral features.

The FIR (red area in Figure 1.1) ends with the strong CO_2 absorption band, centered at 667 cm^{-1} . In the mid infrared region (wavenumbers greater than 667 cm^{-1}), it is possible to note the band at 1045 cm^{-1} , due to O_3 , and the extended absorption above 1250 cm^{-1} , mainly due to H_2O and other gases, such as CH_4 . Along with water vapour, also other species present spectral features in the FIR, like O_3 , N_2O , HNO_3 , and NH_3 . The contribution of these molecules is generally insignificant compared with water vapour [37], however, to obtain a correct modeling of Earth's emission spectrum, also these gases must be included in the atmospheric composition.

Around the center, the spectral lines of water vapour in the FIR are well described by a Voigt line shape [60]. On the other hand, due to both collisional and Doppler broadening, these lines exhibit absorption properties even far from the line center. The behavior of these *far wings* is still not well understood. Specifically, it is found that the absorption in these far regions is stronger than is predicted by any of the current theories of collisional or pressure broadening [37]. The two prevailing theories to account for these discrepancies are: (i) changes in the line shapes due to molecule-molecule interactions and (ii) the creation of new molecules (dimers or polymers) as a result of collisions. A common choice is to define

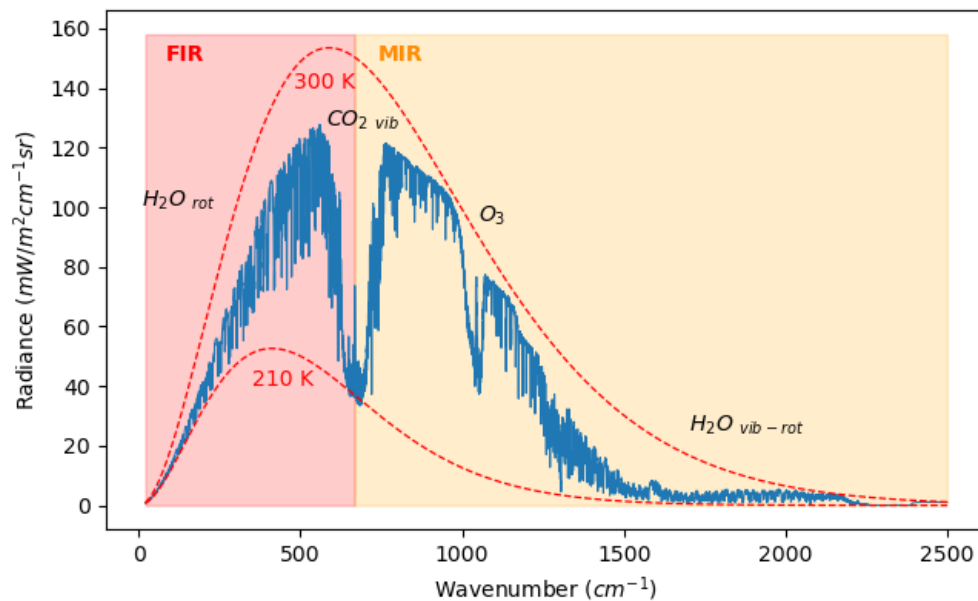


FIGURE 1.1: Simulated up-welling radiance at the top of the atmosphere for a tropical standard atmosphere (blue solid line). Dashed red lines show the equivalent blackbody emission at the given temperature. The red and orange shaded areas highlight the Far- and Mid-Infrared Regions, FIR and MIR respectively.

the *water vapour continuum* as all the absorptions due to water vapour not attributable to collisional broadening, and it is usually modeled through observations [84]. The continuum absorption due to water vapour plays a crucial role in the FIR as its strength is higher in this spectral region [81].

Spectrally resolved observation of the outgoing Earth's radiation at these longer wavelengths is particularly valuable for different reasons. Studies conducted by Merrelli and Turner (2012) [81] and Sinha and Harries (1995) [101] have shown that the good sensitivity of the FIR to small changes in water vapour concentration in the Upper Troposphere/Lower Stratosphere (UTLS) can be exploited to improve our knowledge on water vapour processes. Moreover, following what found by Solomon et al. (2010) [102], even slight variations in water vapour concentration in the lower stratosphere can act as important source of the decadal variability in the average surface temperature. In these terms, the far infrared region becomes important not only for the ERB, but also for the atmospheric dynamics.

FIR exhibits distinct sensitivities also to the presence of water clouds, thin ice clouds, and, when visible, also to surface conditions [58]. At this regard, in this part of the spectrum, long-wave radiation scattering induced by ice particles becomes more and more important, increasing the sensitivity of the outgoing long-wave radiation to ice crystal habit and size [66]. For these reasons, a comprehensive investigation of the Earth's radiation budget (ERB) ne-

ecessitates the consideration of precise, global, all-sky measurements of outgoing radiance, including the far-infrared part of the spectrum.

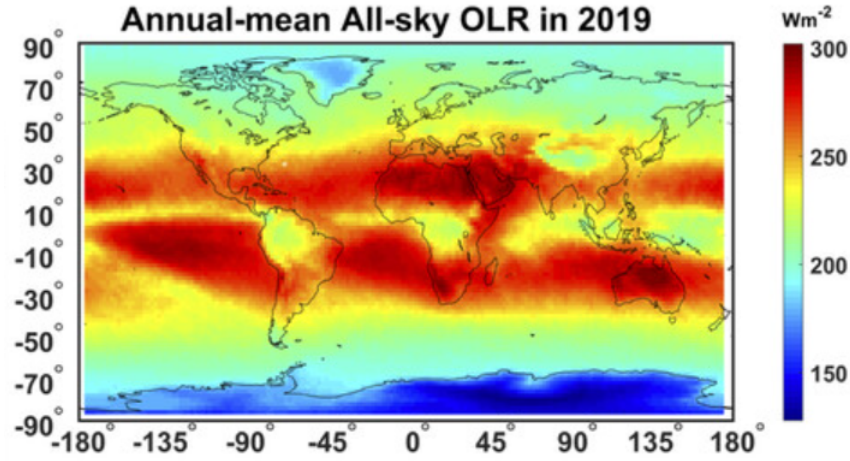


FIGURE 1.2: Annual mean all-sky OLR in 2019, derived from AIRS and CERES observation. Measurements from 2019. Figure adapted from L'Ecuyer et al. (2021) [58].

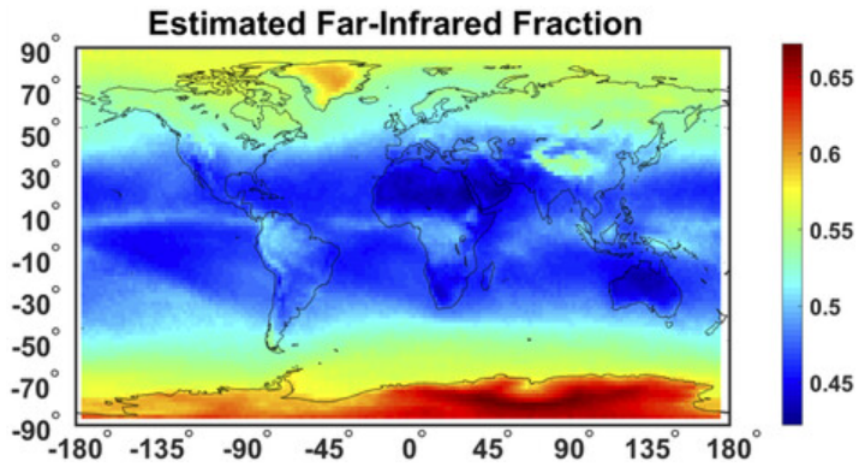


FIGURE 1.3: Estimated fraction of OLR in FIR wavelength. Figure adapted from L'Ecuyer et al. (2021) [58].

1.2.1 | Climate feedbacks and the far infrared region

The Earth's climate is governed by the balance between energy absorption from the Sun and energy loss to space, which occurs through the reflection of solar radiation and the emis-

sion of infrared radiation. The combination of these phenomena is called the *Earth Radiation Budget* (ERB). The ERB is of fundamental importance for understanding the climate since it is directly linked to the Earth's average temperature, which in turn is determined by the ERB. Another important quantity is the spectral energy emitted by the Earth as Outgoing Long-wave Radiation (OLR). Over 99% of this thermal radiation falls within the spectral range between 4 and 100 μm , with almost 50% of it irradiated in the FIR (above 15 μm). Figures 1.2 and 1.3 show the annual mean all-sky OLR in 2019 and the FIR fraction derived from satellite observations [58].

As previously mentioned, both water vapour distribution and clouds have important FIR effects on Earth's radiation budget. In this region, the energy that Earth emits to space as part of the cooling processes is strongly modulated by the presence of H_2O , which acts as an important greenhouse gas. Defining the Earth's greenhouse effect as the difference between the surface emission and the OLR, simulations demonstrate that a substantial fraction, ranging from 1/4 to 1/3 of the total clear sky greenhouse effect, occurs within the FIR [10]. This result highlights the critical role of this spectral region in regulating Earth's clear-sky cooling to space.

Any warming induced by changes in the levels of greenhouse gases can result in more water vapour entering the atmosphere, causing, in turn, an amplification of the warming effect. The phenomenon described above is an example of *climate feedback*. In the context of climate study, climate feedbacks are defined as physical processes that respond to the surface-temperature change induced by a radiative forcing, such as an anthropogenic increase in CO_2 concentration, amplifying or reducing the original perturbation [26]. It is widely accepted, within the scientific community, that uncertainties associated with the magnitude and, in some cases, even the sign of these feedbacks, significantly influence our ability to predict future climates. At this regard, the utilization of spectrally-resolved, top-of-atmosphere Earth's radiation measurements plays a crucial role in advancing our understanding on climate feedbacks and climate evolution over time. A significant work on this topic is the one done by Huang et al. (2010) [47]. In this study, the authors quantify the signature of temperature, water vapor, and clouds at different atmospheric levels on the overall OLR change (feedback effects), in response to an initial doubling of CO_2 (initial perturbation). The results show how the original forcing has a quite distinct spectral signal with respect to the feedback signals. Moreover, the study revealed that a substantial portion of all feedback mechanisms, including the CO_2 forcing, predominantly occurs within the FIR segment of the spectrum. To conclude, spectrally resolved measurements of the top-of-the-atmosphere OLR allow us to appreciate the spectral signature of the processes that come into play in the climate system, and link the changes in Earth's energy balance to the underlying physical mechanisms.

Clouds are another essential element of the Earth's system. These objects constitute one of the most important ERB regulators, affecting it through competing greenhouse and albedo effects. It is commonly accepted that, if the clouds are lying in an atmospheric level where the temperature is nearly uniform, we can assume that the cloud surface absorbs and emits like a gray-body. However, both albedo and opacity of the clouds tend to increase with the liquid water content causing a competition between these two opposite effects that is gener-

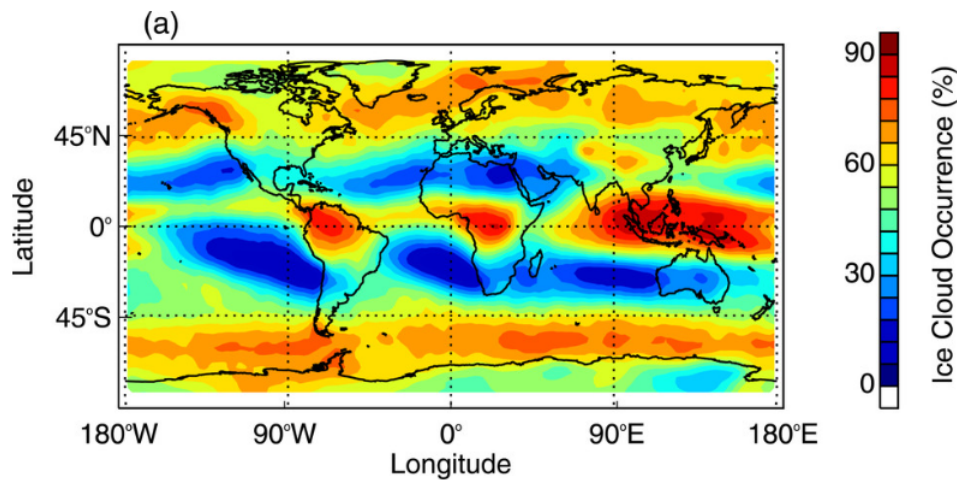


FIGURE 1.4: Ice cloud occurrence frequency over the globe. Figure adapted from Hong and Liu (2015) [44].

ally difficult to characterize in a model. Understanding the balance between these two effects is of critical importance for the study of the climate system as the incomplete knowledge on the impact of clouds and their contributions to the radiation budget is one of the main reasons of uncertainty in current climate models [50].

Typically, the clouds coverage in the sky is greater than 60% on a global scale [55], and the evolution of the climate system is strongly regulated by them. Their horizontal extent, vertical positioning, thermodynamic phase, and water content are fundamental parameters that govern the interplay between the two primary competing factors: the greenhouse effect and the albedo effect. Hence, it is evident that gathering statistics on not only the occurrence of clouds but also their microphysical properties is of great importance. Thin high ice clouds, such as cirrus, generally present a stronger greenhouse effect, resulting in a net warming radiative effect. On the other hand, lower clouds over the ocean produce an increasing of the albedo without affecting very much the TOA-outgoing radiation, resulting in an opposite forcing.

The total impact of clouds on the radiation balance is complex, and in general it is not possible to fully characterize it and its influence on the climate system.

Of particular interest are the ice clouds. The presence of these types of clouds causes lower emitting temperatures with respect to the surface. This produces the shifting in the emission spectrum towards longer wavelengths, i.e. in the FIR, and, consequently, a reduction in the thermal radiation emitted to space. Figure 1.4 shows the ice cloud occurrence frequency over the globe, derived from four years of CloudSat and CALIPSO observations.

Cirrus clouds play a critical role in our comprehension of the climate system. IPCC (2013) [50] reported that *"The role of thin cirrus clouds for cloud feedback is not known and re-*

mains a source of possible systematic bias". This type of clouds cover more than 20% of the Earth and contributes up to 40% of the total clouds. The impact of cirrus clouds on the radiation balance is complex. More than this, unlike the spherical droplets found in liquid water clouds, the highly complex shapes of ice crystals observed in cirrus clouds (the crystal habits) make modeling their effects on radiation particularly challenging.

The significance of understanding these cloud properties to accurately characterize their radiative forcing effects is underscored by numerous authors, which have also recognized the importance of the FIR to improve the retrieval of the cirrus microphysical and radiative properties [18]. Nowadays, there are few data available on the impact of cirrus in this spectral region. Spectrally resolved FIR measurement can provide an important contribution for our comprehension of this class of clouds, and reduce the uncertainties associated with cirrus impact in the radiative and climate models.

1.3 | The FORUM mission

Recognizing the value of FIR observation, in September 2019 the Far-infrared Outgoing Radiation Understanding and Monitoring (FORUM) mission was selected as ESA's ninth Earth Explorer [88]. In the same period, the National Aeronautics and Space Administration (NASA) selected the Polar Radiant Energy in the Far Infrared Experiment (PREFIRE) [58] as a complementary satellite mission, dedicated to mapping Earth's far-infrared emission globally.

PREFIRE will employ two CubeSat to provide global coverage of the far-infrared signature of the Earth system, with a particular focus on the polar regions. The CubeSat is equipped with a Thermal Infrared Spectrometer (TIRS), capable of collecting 64-channel spectra, mapping the thermal emission between 5 and 54 μm , with the goal of quantifying the variations in spectral surface emissivity, variations in atmospheric water vapour, and the identification of clouds at both poles.

FORUM, on the other hand, is an ESA Earth Explorer mission. These missions are devoted to demonstrating the potential of new innovative Earth Observation techniques, addressing questions that have a direct bearing on scientific and societal issues, such as the availability of water, energy and resources problems, climate change or public health [26]. The scientific objectives of the FORUM mission are related to the improvement of our understanding of the infrared component of the terrestrial radiation budget, and the characterization of the role of the far-infrared in shaping the climate system. Specifically, FORUM aims at reducing our uncertainty in predictions of future climate by:

- building a global reference data-set for the far-infrared radiation, useful for the validation of Earth system models.
- providing measurements with a wide spectral bandwidth, useful to identify climate process signatures with high accuracy.

- characterizing the clouds impact on radiation budget, with a particular focus on high and thin ice clouds.
- providing information on the FIR, to improve our comprehension of critical feedback mechanisms active in that spectral region.

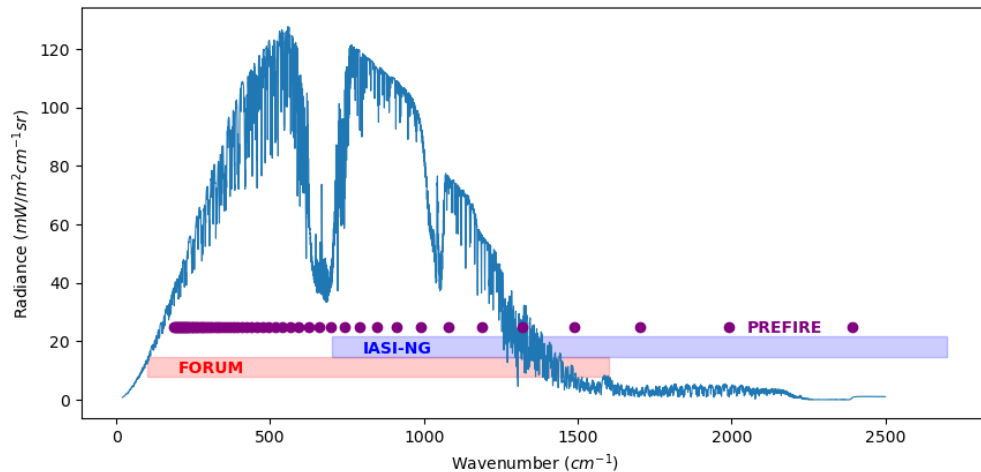


FIGURE 1.5: Simulated up-welling radiance at the top of the atmosphere for a tropical standard atmosphere (blue solid line). The red and blue bands represent the measure spectral range of FORUM and IASI-NG respectively. The purple dots are representative of the observation channels of the PREFIRE spectrometers.

FORUM aims at measuring the Earth’s top-of-atmosphere emission spectrum in the spectral interval that goes from 100 to 1600 cm^{-1} , providing, for the first time, a spectrally resolved measure of the FIR from the space in its entirety. The mission’s main instrument is a Fourier Transform Spectrometer (FTS), measuring with nadir geometry the electromagnetic spectrum a nominal resolution of at least 0.5 cm^{-1} (defined as full width at half maximum of the instrumental spectral response function). FORUM will fly in loose formation with another instrument: the Infrared Atmospheric Sounder Interferometer New Generation (IASI-NG), carried by the MetOp-SG-1A satellite [93]. IASI-NG will collect measurements of the entire MIR (from 645 up to 2760 cm^{-1}), allows to retrieve operational meteorology data such as temperature and humidity atmospheric profiles and also monitor other gases like ozone, methane or carbon monoxide on a global scale. The synergy between FORUM and IASI-NG measurements allows for a complete mapping of the Earth’s emission spectrum.

Figure 1.5 shows the measure spectral range of FORUM, comparing it with the measure spectral range of PREFIRE and IASI-NG [7].

The primary output of the FORUM mission will consist of the *Level 1* products, specifically

the calibrated spectral radiances. However, the collected data will undergo additional processing to derive information on the atmospheric and surface state, resulting in *Level 2* products [93]. Between these products, will be included the water vapour profile, cloud parameters and spectral fluxes. These quantities will synergically complement the IASI-NG data, providing crucial information for climate studies.



2 | The radiative transfer equation and its solution

This chapter will introduce the main physical quantities and concepts that come into play when we are dealing with the radiative transfer problem. The derivation of these quantities is presented in accordance with the description given by [33], [60] and [123].

2.1 | Definitions of radiative quantities

In the atmospheric science framework, with the term *radiative transfer problem*, we generally refer to the problem of describing the behavior of the radiation field in the atmosphere, and its interaction with the elements that compound the Earth system.

To introduce this problem it is necessary to give a complete description of the quantities and the terminologies that play a role in this field.

It is a common use in the study of radiative transfer, to assume a semi-classical approach, in which one part of a system is described quantum mechanically, whereas the other is treated classically. In this framework, we can consider a photon as an idealized small particle with zero rest mass, carrying an energy:

$$\epsilon(\nu) = h\nu \quad (2.1)$$

where h is the Planck's constant ($h = 6.626196 \cdot 10^{-34} J \cdot s$), and ν (Hz^{-1}) is the frequency of the electromagnetic radiation. Now it is well known that photons, along with energy, are carrying also a momentum:

$$\mathbf{p}(\nu) = \frac{\epsilon(\nu)}{c} \mathbf{\Omega} \quad (2.2)$$

where the photon is assumed to propagate in the vacuum with a direction defined by the unit vector $\mathbf{\Omega}$ and speed c ($c = 299792458 m/s$). As soon as the photon interferes with matter, different types of interactions between the atoms of the material and the photon may occur (e.g. absorption or scattering). In the treatment of radiative transfer here proposed, we consider only scattering processes where the photon suffers no change in frequency (elastic

scattering). Although, it is important to note that there exist examples of inelastic scattering also for atmospheric applications, such as Raman scattering.

To obtain an unambiguous and effective description of a photon at time t , six coordinates are required. Three coordinates are used for the position vector \mathbf{r} , one for the magnitude of momentum and finally two angles for the unitary vector $\mathbf{\Omega}$. It is important to note that there is another degree of freedom that we should consider: the polarization of the radiation (or, if we want, the spin of the photon). However, in this discussion we will assume that the radiation is unpolarized. A representation of this coordinate system is proposed in Figure 2.1.

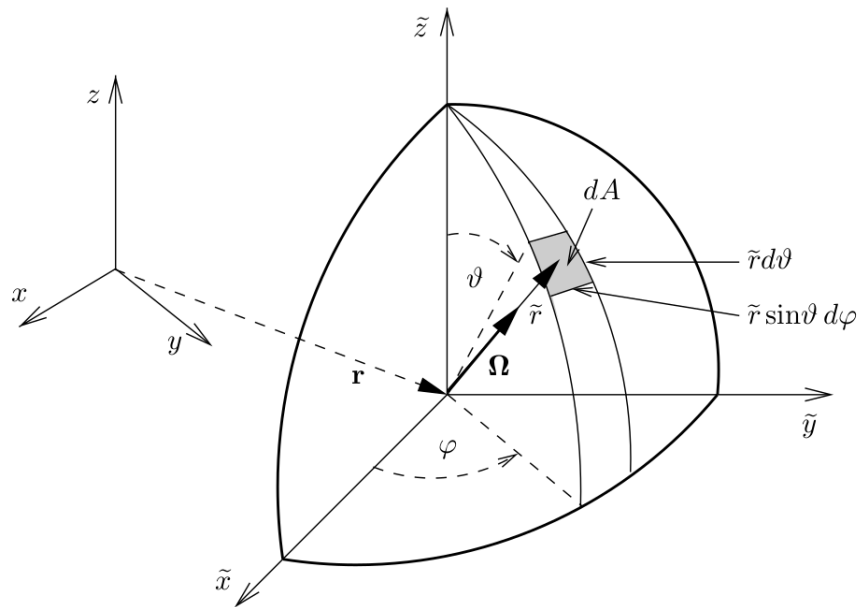


FIGURE 2.1: Definition of the local spherical-coordinate system. Adapted from Zdunkowski et al., (2007) [123].

We can define a differential area element on a sphere with radius \tilde{r} as $dA = \tilde{r}^2 \sin(\theta) d\theta d\phi$. From which, the definition for the differential *solid angle element* is straightforward:

$$d\Omega = \frac{dA}{\tilde{r}^2} = \sin(\theta) d\theta d\phi \quad (2.3)$$

with the normalization:

$$\int_{4\pi} d\Omega = 4\pi \quad (2.4)$$

Using this frame of reference, we can uniquely describe the position of a single photon in any point of space. However, since we are interested in the radiation field, it is necessary

to use a distribution function to account for the number N of photons that at time t are contained within the volume element dV , centered at \mathbf{r} , with flight direction $\mathbf{\Omega}$ and frequency ν . Let's call this photon distribution function $f_\nu(\mathbf{r}, \mathbf{\Omega}, t)$, such as:

$$N_\nu(\mathbf{r}, \mathbf{\Omega}, t) = f_\nu(\mathbf{r}, \mathbf{\Omega}, t)dVd\mathbf{\Omega}d\nu \quad (2.5)$$

Even if the photon distribution function is a very clear object from a physical point of view, it is more common to use another quantity, called *spectral radiance* $I_\nu(\mathbf{r}, \mathbf{\Omega}, t)$, which is defined as:

$$I_\nu(\mathbf{r}, \mathbf{\Omega}, t) = ch\nu f_\nu(\mathbf{r}, \mathbf{\Omega}, t) \quad (2.6)$$

The spectral radiance is expressed in units of $[W m^{-2} sr^{-1} Hz^{-1}]$. An interpretation of the spectral radiance quantity can be obtained as follows. If we consider an infinitesimal volume $dV = d\sigma \cdot \mathbf{\Omega}cdt$, with $d\sigma$ an infinitesimal oriented area, the fraction of monochromatic energy $[J]$ flowing within the solid angle element $d\mathbf{\Omega}$ during dt , is given by:

$$du_\nu(\mathbf{r}, \mathbf{\Omega}, t) = h\nu N_\nu(\mathbf{r}, \mathbf{\Omega}, t) = h\nu f_\nu(\mathbf{r}, \mathbf{\Omega}, t)\cos\theta d\sigma cdt d\mathbf{\Omega}d\nu \quad (2.7)$$

where θ is the angle between the normal to the surface $d\sigma$ and the direction $\mathbf{\Omega}$. From equation 2.6:

$$du_\nu(\mathbf{r}, \mathbf{\Omega}, t) = I_\nu(\mathbf{r}, \mathbf{\Omega}, t)\cos\theta d\sigma d\mathbf{\Omega}d\nu dt \quad (2.8)$$

This term can be interpreted as the radiative energy contained within the frequency interval $(\nu, \nu + d\nu)$ streaming during the time interval $(t, t + dt)$ at \mathbf{r} , through the surface element $d\sigma$ with direction $\mathbf{\Omega}$ (Figure 2.2).

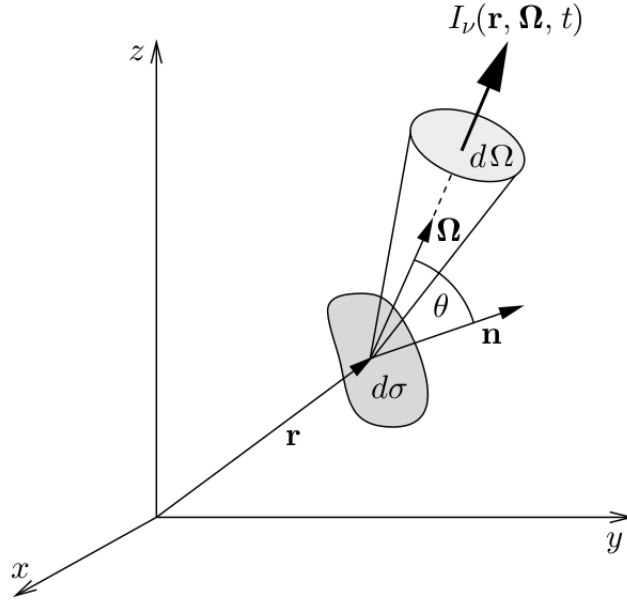


FIGURE 2.2: Elements in radiance definition. Adapted from Zdunkowski et al., (2007) [123].

Another fundamental quantity is the *radiative flux density*. According to 2.7 the spectral differential radiative energy crossing $d\sigma$ during dt is:

$$d\epsilon_\nu(\mathbf{r}, \boldsymbol{\Omega}, t) = \frac{du_\nu(\mathbf{r}, \boldsymbol{\Omega}, t)}{d\sigma dt} = I_\nu(\mathbf{r}, \boldsymbol{\Omega}, t) \cos\theta d\Omega d\nu \quad (2.9)$$

The total flux can be obtained by integrating this relation over the solid angle and over all the spectral frequencies, and it is expressed in units of $[W m^{-2}]$. In this way, the net radiative flux density (in the direction of the oriented plane) is given by:

$$E(\mathbf{r}, t) = \int_0^\infty \int_{4\pi} \Omega I_\nu(\mathbf{r}, \boldsymbol{\Omega}, t) d\Omega d\nu \quad (2.10)$$

2.2 | Derivation of the radiative transfer equation

An elegant way to find a description for the radiative transfer problem is to create a budget equation for photons in a medium where scattering, absorption and emission processes can take place. Using this Eulerian approach we will obtain, as final results, the so-called *radiative transfer equation* (RTE) which is a linear integro-differential equation for the radiance.

We can start by defining a 6- D volume element in $(x, y, z, \theta, \phi, \nu)$ -space, constant over time. According to what described in previous paragraphs, the total number of photons is given by:

$$N_\nu(\mathbf{r}, \boldsymbol{\Omega}, t) = f_\nu(\mathbf{r}, \boldsymbol{\Omega}, t) \Delta V \Delta \Omega \Delta \nu \quad (2.11)$$

To derive the photon budget equation we need to know the time derivative of the quantity that come into play.

$$\frac{\partial N_\nu}{\partial t} = \frac{\partial f_\nu}{\partial t} \Delta V \Delta \Omega \Delta \nu \quad (2.12)$$

Where we drop the explicit dependence of the terms on the coordinate system. The volume element is placed in a medium that has a certain probability of interacting with the radiation. The variation over time of the number of photons can be induced by:

- Exchange of photons of the considered (x, y, z) -volume element with the exterior surrounding (without interaction).
- Absorption by the medium of photons with frequency ν and direction $\boldsymbol{\Omega}$.
- Scattering of photons with frequency ν and direction $\boldsymbol{\Omega}$ towards other directions $\boldsymbol{\Omega}'$ (outscattering).
- Scattering of photons with frequency ν and direction $\boldsymbol{\Omega}'$ towards $\boldsymbol{\Omega}$ (inscattering).
- Emission by the medium of photons with frequency ν and direction $\boldsymbol{\Omega}$.

At this point, it is sufficient to find a mathematical representation for each of these terms.

2.2.1 | Exchange of photons

The first term we consider is the exchange of photons. This process can be treated in analogy to the continuity equation for the conservation of a physical quantity (figure 2.3). If it is possible to define a density of our physical quantity ρ , and its velocity \mathbf{v} , it is possible to obtain the well-known continuity equation:

$$\frac{\partial \rho}{\partial t} = -\nabla \cdot (\rho \mathbf{v}) \quad (2.13)$$

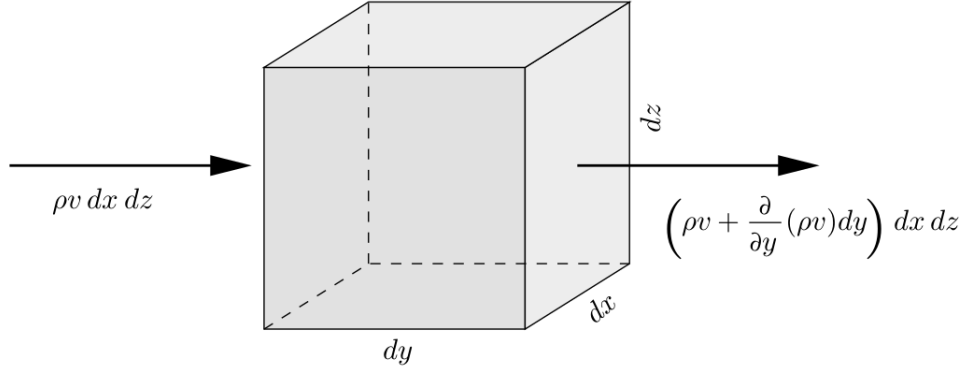


FIGURE 2.3: Eulerian representation of the continuity equation. Adapted from Zdunkowski et al., (2007) [123].

Now, given the Cartesian unit vectors \mathbf{i} , \mathbf{j} and \mathbf{k} , we can define the velocity of a photon as:

$$\mathbf{v} = c\boldsymbol{\Omega} = c(\Omega_x\mathbf{i} + \Omega_y\mathbf{j} + \Omega_z\mathbf{k}) \quad (2.14)$$

And recalling the photon distribution function f_ν , we can define a density in the $(x, y, z-)$ space:

$$\rho = f_\nu \Delta\Omega\Delta\nu \quad (2.15)$$

so that we can obtain the time rate of change for the number of photons due to the exchange with the surroundings as:

$$\frac{\partial N_\nu}{\partial t} \Big|_{exch} = -\nabla \cdot (\boldsymbol{\Omega} f_\nu) c \Delta V \Delta\Omega\Delta\nu \quad (2.16)$$

It's clear that this derivation is obtained under the assumption of homogeneity in the space considered (real part of the index of refraction is constant in space and time), otherwise, the photon path would be subject to refraction, and their trajectories would be curved in space.

2.2.2 | Absorption of photons

We can define an absorption rate of photons within the 6- D volume element simply as the product of the photon number and the probability that a photon is absorbed during the time interval $(t, t+dt)$. If we define the probability of a photon being absorbed along the path ds as $d\tau_{abs} = k_{abs,\nu}(\mathbf{r}, t) ds$, where $k_{abs,\nu}$ is the absorption coefficient and τ_{abs} is the absorption optical depth, we can write:

$$\frac{d\tau_{abs}}{dt} = k_{abs,\nu} \frac{ds}{dt} = k_{abs,\nu} c \quad (2.17)$$

from which the total absorption rate is given by:

$$\frac{\partial N_\nu}{\partial t}|_{abs} = -f_\nu k_{abs,\nu} c \Delta V \Delta \Omega \Delta \nu \quad (2.18)$$

where the negative sign is due to the absorption nature. The absorption coefficient, k_{abs} , introduced above, can be decomposed as the product of two contributions $k_{abs,\nu} = \beta_{abs,\nu} \cdot N_0^{pa}$. The quantity $\beta_{abs,\nu}$ is called *absorption cross-section* and N_0^{pa} is the number of absorbing particles per unit of volume.

2.2.3 | Scattering of photons

There are two main scattering processes that we have to consider: the outscattering and the inscattering. Analogously to what already done with the absorption, we can define the probability that a photon, coming from the direction Ω , is scattered toward the direction Ω' along the path ds as $d\tau_{sca} = k_{sca,\nu}(\Omega \rightarrow \Omega') ds = k_{sca,\nu} \frac{1}{4\pi} P_\nu(\Omega \rightarrow \Omega') ds$, where $k_{sca,\nu}$ is called scattering coefficient and $P_\nu(\Omega \rightarrow \Omega')$ is called phase function. It is possible to define the number of photons that are scattered from $\Omega \rightarrow \Omega'$ as:

$$N_\nu \frac{d}{dt} [\tau_{sca}(\Omega \rightarrow \Omega')] = f_\nu \Delta V \Delta \Omega \Delta \nu k_{sca}(\Omega \rightarrow \Omega') d\Omega' c \quad (2.19)$$

from which, the total loss of photons due to outscattering is obtained by integrating over all the possible outgoing directions.

$$\frac{\partial N_\nu}{\partial t}|_{outsc} = -f_\nu \Delta V \Delta \Omega \Delta \nu \frac{c}{4\pi} \int_{4\pi} k_{sca} P_\nu(\Omega \rightarrow \Omega') d\Omega' \quad (2.20)$$

However, since we have that $\frac{1}{4\pi} \int_{4\pi} P_\nu(\Omega \rightarrow \Omega') d\Omega' = 1$, we can write:

$$\frac{\partial N_\nu}{\partial t}|_{outsc} = -f_\nu k_{sca} c \Delta V \Delta \Omega \Delta \nu \quad (2.21)$$

In a similar manner we may find the gain of photons for the direction Ω due to inscattering from all the other directions, obtaining:

$$\frac{\partial N_\nu}{\partial t}|_{insec} = k_{sca} \Delta V \Delta \Omega \Delta \nu \frac{c}{4\pi} \int_{4\pi} f_\nu(\Omega') P_\nu(\Omega' \rightarrow \Omega) d\Omega' \quad (2.22)$$

which describes the multiple-scattering effects that may take place within the medium. As already done for the absorption coefficient, we can express the scattering coefficient as $k_{sca,\nu} = \beta_{sca,\nu} \cdot N_0^{ps}$, with $\beta_{sca,\nu}$ the scattering cross-section and N_0^{ps} the number of scattering particles per unit of volume.

2.2.4 | Emission of photons

The last term we have to characterize is the emission term, which is simply given by:

$$\frac{\partial N_\nu}{\partial t} \Big|_{em} = j_\nu \Delta V \Delta \Omega \Delta \nu \quad (2.23)$$

where j_ν is a general isotropic photon source density function. In case of local thermodynamic equilibrium (LTE), these emission processes are deeply related to the Planckian function.

2.2.5 | The radiative transfer equation

The final budget equation for the photon distribution function f_ν is obtained by adding each individual contribution derived in the previous sections.

$$\frac{\partial f_\nu}{\partial t} = -\nabla \cdot (\mathbf{\Omega} f_\nu) c - f_\nu k_{abs, \nu} c - f_\nu k_{sca, \nu} c + k_{sca} \frac{c}{4\pi} \int_{4\pi} f_\nu(\mathbf{\Omega}') P_\nu(\mathbf{\Omega}' \rightarrow \mathbf{\Omega}) d\mathbf{\Omega}' + j_\nu \quad (2.24)$$

where the common factors have been simplified. Introducing the definition of the extinction coefficient, $k_{ext} = k_{sca} + k_{abs}$, and noting that the unit vector $\mathbf{\Omega}$ is divergence-free ($\nabla \cdot \mathbf{\Omega} = 0$), we can rewrite the above equation as follow:

$$\frac{\partial f_\nu}{\partial t} = -\mathbf{\Omega} \cdot \nabla f_\nu c - f_\nu k_{ext, \nu} c + k_{sca} \frac{c}{4\pi} \int_{4\pi} f_\nu(\mathbf{\Omega}') P_\nu(\mathbf{\Omega}' \rightarrow \mathbf{\Omega}) d\mathbf{\Omega}' + j_\nu \quad (2.25)$$

At this point using the definition of radiance ($I_\nu = ch_\nu f_\nu$)

$$\frac{1}{c} \frac{\partial I_\nu}{\partial t} + \mathbf{\Omega} \cdot \nabla I_\nu = -I_\nu k_{ext, \nu} + \frac{k_{sca}}{4\pi} \int_{4\pi} I_\nu(\mathbf{\Omega}') P_\nu(\mathbf{\Omega}' \rightarrow \mathbf{\Omega}) d\mathbf{\Omega}' + J_\nu^e \quad (2.26)$$

where we have introduced the *source function for true emission* $J_\nu^e = hv j_\nu$, which is related to the isotropic sources of radiation.

It's worth highlighting that also the extinction coefficient can be viewed as the product $k_{ext} = \beta_{ext} \cdot N_0^p$, where β_{ext} is the extinction cross-section and N_0^p is the number of particles for unit of volume. Moreover, it is useful to introduce another quantity: the *extinction efficiency*, $Q_{ext} = \beta_{ext}/A$, where A is the particle cross-sectional area.

To conclude, it is important to note that for most atmospheric applications the term $\frac{1}{c} \frac{\partial I_\nu}{\partial t}$ can be neglected in comparison to the remaining terms. Finally, the term describing the exchange of photons can be expressed as follows:

$$\mathbf{\Omega} \cdot \nabla I_\nu = \frac{d}{ds} I_\nu \quad (2.27)$$

2.2.6 | The direct–diffuse splitting

The total radiation field is given by the sum of the *direct solar beam* and the *diffuse radiation*. A common way to account for these two components is to split the radiance as follows:

$$I_\nu = I_{\nu, d} + S_\nu \delta(\mathbf{\Omega} - \mathbf{\Omega}_0) \quad (2.28)$$

where δ is the Dirac δ -function, and $\mathbf{\Omega}_0$ the solar beam direction. By using equation 2.28 in 2.26, the radiative transfer equation becomes:

$$\begin{aligned} \mathbf{\Omega} \cdot \nabla (I_{\nu,d} + S_{\nu} \delta(\mathbf{\Omega} - \mathbf{\Omega}_0)) &= -I_{\nu,d} k_{ext,\nu} - S_{\nu} \delta(\mathbf{\Omega} - \mathbf{\Omega}_0) k_{ext,\nu} + \\ &+ \frac{k_{sca}}{4\pi} \int_{4\pi} I_{\nu,d}(\mathbf{\Omega}') P_{\nu}(\mathbf{\Omega}' \rightarrow \mathbf{\Omega}) d\mathbf{\Omega}' \\ &+ \frac{k_{sca}}{4\pi} P_{\nu}(\mathbf{\Omega}_0 \rightarrow \mathbf{\Omega}) S_{\nu} + J_{\nu}^e \end{aligned} \quad (2.29)$$

Where we can identify two main regimes. When we have $\mathbf{\Omega} = \mathbf{\Omega}_0$, we obtain:

$$\mathbf{\Omega} \cdot \nabla S_{\nu} = \frac{dS_{\nu}}{ds} = -S_{\nu} k_{ext,\nu} \quad (2.30)$$

Which is called Beer's law. On the other hand, when $\mathbf{\Omega} \neq \mathbf{\Omega}_0$, we obtain the diffuse radiative transfer equation:

$$\begin{aligned} \mathbf{\Omega} \cdot \nabla I_{\nu,d} = \frac{dI_{\nu,d}}{ds} &= -I_{\nu,d} k_{ext,\nu} + \frac{k_{sca}}{4\pi} \int_{4\pi} I_{\nu,d}(\mathbf{\Omega}') P_{\nu}(\mathbf{\Omega}' \rightarrow \mathbf{\Omega}) d\mathbf{\Omega}' \\ &+ \frac{k_{sca}}{4\pi} P_{\nu}(\mathbf{\Omega}_0 \rightarrow \mathbf{\Omega}) S_{\nu} + J_{\nu}^e \end{aligned} \quad (2.31)$$

In this thesis work, when we talk about the radiative transfer equation, we refer to this equation (equation 2.31). It is crucial to recall that, in this treatment, we are considering unpolarized and incoherent radiation. This is not generally true, but, for the applications we are interested in (satellite infrared remote sensing), it is not necessary to add this additional layer of complexity.

2.3 | Solution for the diffuse radiative transfer equation

The multiple-scattering term in 2.31 makes the radiative transfer equation (RT) an integrodifferential equation. The presence of this term introduces additional complexity to the problem for two primary reasons: (1) it is not a function of the local condition alone, but it depends on the state of the atmosphere at any other point in space, (2) the phase function can be an extremely complex function.

The strategy used to handle the multiple-scattering term plays a key role in shaping both the accuracy and the computational cost of the approach used to solve the RT problem.

Over the last century, a wide number of methods have been developed and employed to solve the diffuse radiative transfer equation. While various approaches exist for tackling this problem, three main points have to be kept in mind when developing our RT solver (i.e. the suite of methods and codes responsible for the solution of the RT equation) [56]:

- The solver needs to accurately model the physical processes that come into play in the radiative transfer.
- The solver needs to be numerically stable.
- The computation of the solution needs to be sufficiently fast (where the meaning of sufficiently depends on the application).

In this dissertation, we focus on two main methodologies widely exploited to solve the radiative transfer problem, with different levels of approximation: the discrete ordinate method and the scaling methods.

Before moving into these approaches, it is convenient to introduce some important additional approximations for the equation 2.31. First, we can assume that the scatterers within the medium have random orientations; it follows that the scattering phase function depends only on the angle between the input and the output direction $P_\nu(\mathbf{\Omega}' \rightarrow \mathbf{\Omega}) = P_\nu(\mathbf{\Omega}' \cdot \mathbf{\Omega})$. Finally, we can consider a problem with horizontal symmetry (plane-parallel approximation) where, for each vertical level, we can assume local thermodynamic equilibrium conditions (so that $J_\nu^e = k_{abs,\nu} B_\nu(T)$).

Calling the cosine of the zenith angle $\mu = \mathbf{\Omega} \cdot \mathbf{k}$, where \mathbf{k} is the Cartesian unit vector associated with the vertical coordinate z , we can write:

$$\begin{aligned} \mu \frac{dI_{\nu,d}}{dz} = & -I_{\nu,d} k_{ext,\nu} + \frac{k_{sca,\nu}}{4\pi} \int_{4\pi} I_{\nu,d}(\mathbf{\Omega}') P_\nu(\mathbf{\Omega}' \cdot \mathbf{\Omega}) d\mathbf{\Omega}' + \\ & + \frac{k_{sca}}{4\pi} P_\nu(\mathbf{\Omega}_0 \cdot \mathbf{\Omega}) S_\nu + k_{abs,\nu} B_\nu(T) \end{aligned} \quad (2.32)$$

Then, noting that the extinction optical depth in the vertical direction is defined as $d\tau_{ext} = -k_{ext} dz = d\tau$, we can write the final form for the diffuse radiative transfer equation assuming plane-parallel approximation as:

$$\begin{aligned} \mu \frac{dI_\nu(\tau, \mathbf{\Omega})}{d\tau} = & I_\nu(\tau, \mathbf{\Omega}) - \frac{\tilde{\omega}_\nu(\tau)}{4\pi} \int_{4\pi} I_\nu(\tau, \mathbf{\Omega}') P_\nu(\tau, \mathbf{\Omega}' \cdot \mathbf{\Omega}) d\mathbf{\Omega}' + \\ & + \frac{\tilde{\omega}_\nu(\tau)}{4\pi} P_\nu(\tau, \mathbf{\Omega}_0 \cdot \mathbf{\Omega}) S_\nu + (1 - \tilde{\omega}_\nu(\tau)) B_\nu(T(\tau)) \end{aligned} \quad (2.33)$$

where we made explicit the dependency on the vertical coordinate τ and direction $\mathbf{\Omega}$, and we defined the single scattering albedo as $\tilde{\omega}_\nu = k_{sca,\nu}/k_{ext,\nu}$.

If we assume that multiple scattering effects can be neglected the integral term in equation 2.33 disappear. This is a common choice when we are considering the longwave spectral regime, where the longwave absorption dominates over the longwave scattering. If we include all the primary sources of radiation in a single term:

$$\frac{\tilde{\omega}_v(\tau)}{4\pi} P_v(\tau, \mathbf{\Omega}_0 \cdot \mathbf{\Omega}) S_v + (1 - \tilde{\omega}_v(\tau)) B_v(T(\tau)) = \Sigma_v(\tau, \mathbf{\Omega}) \quad (2.34)$$

the RT equation can be written as follows:

$$\mu \frac{dI_v(\tau, \mathbf{\Omega})}{d\tau} = I_v(\tau, \mathbf{\Omega}) - \Sigma_v(\tau, \mathbf{\Omega}) \quad (2.35)$$

Equation 2.35 is a first order linear differential equation, and it admits solutions of the type:

$$I_v(\tau, \mathbf{\Omega}) = I_v(0, \mathbf{\Omega}) e^{-\tau_{tot}/\mu} + \int_0^{\tau_{tot}} \Sigma_v(\tau', \mathbf{\Omega}) e^{-(\tau_{tot}-\tau')/\mu} \frac{d\tau'}{\mu} \quad (2.36)$$

Where $I_v(0, \mathbf{\Omega})$ is a boundary condition and τ_{tot} is the total optical path. This solution is particularly important in the study of longwave radiative transfer, and it is called *Schwarzschild equation*. Although this solution is extremely simple to implement and computationally efficient, its application should be limited to clear-sky scenarios only. It has been proved, from previous study, that the application of this class of solutions in global circulation models can leads to important overestimation in the simulation of the OLR, as scattering effects induced by clouds and aerosols are still visible in the longwave spectral range [57].

2.3.1 | Discrete ordinate method

The discrete ordinate method (DOM) [12] is a wide used approach for solving the RT equation in a plane-parallel atmosphere. It also belongs to the most accurate techniques and it is generally used for calculating benchmark solutions to certain problems. The starting point for generating this solution is equation 2.33. Following Chandrasekhar (1960), we expand the phase function, $P_v = P$, into a series of Legendre polynomials P_l , with $N + 1$ terms.

$$\tilde{\omega}(\tau) P(\tau, \mathbf{\Omega}' \cdot \mathbf{\Omega}) = \sum_{l=0}^N \alpha_l(\tau) P_l(\mathbf{\Omega}' \cdot \mathbf{\Omega}) \quad (2.37)$$

Where the coefficients α_l are given by:

$$\alpha_l(\tau) = \frac{(2l+1)}{2} \int_{-1}^{+1} P_l(\mathbf{\Omega}' \cdot \mathbf{\Omega}) \tilde{\omega}(\tau) P(\tau, \mathbf{\Omega}' \cdot \mathbf{\Omega}) d(\mathbf{\Omega}' \cdot \mathbf{\Omega}) \quad (2.38)$$

From the cosine law of spherical trigonometry, we can decompose the cosine of the scattering angle as $\mathbf{\Omega}' \cdot \mathbf{\Omega} = \mu \mu' + (1 - \mu)^{1/2} (1 - \mu')^{1/2} \cos(\phi - \phi')$, where $\mu = \mathbf{\Omega} \cdot \mathbf{k}$ and ϕ is the azimuth angle. Using this relation, it is possible to prove the Legendre addition theorem:

$$P_l(\mathbf{\Omega}' \cdot \mathbf{\Omega}) = P_l(\mu)P_l(\mu') + 2 \sum_{m=1}^l \frac{(l-m)!}{(l+m)!} P_l^m(\mu)P_l^m(\mu') \cos(m(\phi - \phi')) \quad (2.39)$$

where P_l^m are the associated Legendre polynomials and where $P_l^0 = P_l$. Using this relation, we can uncouple the μ -dependence from the ϕ -dependence. Substituting 2.39 in 2.37, we have:

$$\tilde{\omega}(\tau)P(\tau, \mathbf{\Omega}' \cdot \mathbf{\Omega}) = \sum_{m=0}^N \rho^m(\tau, \mu, \mu') \cos(m(\phi - \phi')) \quad (2.40)$$

where:

$$\rho^m(\tau, \mu, \mu') = \sum_{l=m}^N (2 - \delta_{0m}) \alpha_l(\tau) \frac{(l-m)!}{(l+m)!} P_l^m(\mu)P_l^m(\mu') \quad (2.41)$$

with δ_{nm} the Kronecker δ -function. The ρ^m coefficients have some important symmetry properties, which derive from the fact that $P_l^m(-\mu) = (-1)^{m+l} P_l^m(\mu)$. These properties are:

$$\begin{aligned} \rho^m(\tau, \mu, -\mu') &= \rho^m(\tau, -\mu, \mu') \\ \rho^m(\tau, -\mu, -\mu') &= \rho^m(\tau, \mu, \mu') \end{aligned} \quad (2.42)$$

In view of uncoupling the two angular dependencies, we include all the primary sources of radiation in a single term $\Sigma(\tau, \mu, \phi)$. Then we can expand the latter and the radiance terms in 2.33 as Fourier series in the azimuthal variable:

$$I(\tau, \mu, \phi) = \sum_{m=0}^N I^m(\tau, \mu) \cos(m(\phi - \phi_0)) \quad (2.43)$$

$$\Sigma(\tau, \mu, \phi) = \sum_{m=0}^N \Sigma^m(\tau, \mu) \cos(m(\phi - \phi_0)) \quad (2.44)$$

with ϕ_0 a reference angle. Substituting 2.43, 2.44 and 2.40 in 2.33 and exploiting the orthogonality of Fourier series, it is possible to split up the RT equation into $N+1$ independent equations.

$$\begin{aligned} \mu \frac{dI^m(\tau, \mu)}{d\tau} &= I^m(\tau, \mu) - \frac{1}{4} (1 + \delta_{0m}) \int_{-1}^1 \rho^m(\tau, \mu, \mu') I^m(\tau, \mu') d\mu' + \\ &\quad - \Sigma^m(\tau, \mu) \quad m = (0, 1, \dots, N) \end{aligned} \quad (2.45)$$

The final solution is obtained from 2.43 given each individual solution of 2.45. When $m = 0$, the solution to this equation yields the azimuthally averaged radiation field (when

averaging over the azimuth angle ϕ , all the terms that depend linearly to $\cos(m(\phi - \phi'))$ disappear if $m \neq 0$). This is the only component needed to compute important quantities such as radiative flux densities. In the following part, we will discuss the DOM for the azimuthally averaged radiation field, and the index m will be dropped.

Given equation 2.45, it is a natural step to discretize the integral term as a sum of $2n$ radiation streams. The usual choice is to approximate the angular variable μ by $2n$ values, equal to the $2n$ roots of the Legendre polynomial $P_{2n}(\mu)$. This allows to replace the integral term with the Gaussian quadrature formula, and obtain:

$$\begin{aligned} \mu_{\pm i} \frac{dI(\tau, \mu_{\pm i})}{d\tau} &= I(\tau, \mu_{\pm i}) - \frac{1}{2} \sum_{j=1}^n a_j \rho(\tau, \mu_{\pm i}, \mu_j) I(\tau, \mu_j) + \\ &\quad - \frac{1}{2} \sum_{j=1}^n a_j \rho(\tau, \mu_{\pm i}, \mu_{-j}) I(\tau, \mu_{-j}) + \\ &\quad - \Sigma(\tau, \mu_{\pm i}) \end{aligned} \quad (2.46)$$

where a_j represents the Gaussian weights used in the quadrature. The RT equation is now transformed in a system of $2n$ first-order non-homogeneous differential equations. A more compact notation is obtained by defining two vectors:

$$\mathbf{I}^{\pm}(\tau) = [I(\tau, \pm\mu_1), I(\tau, \pm\mu_2), \dots, I(\tau, \pm\mu_n)] \quad (2.47)$$

$$\boldsymbol{\sigma}^{\pm}(\tau) = \left[\frac{\Sigma(\tau, \pm\mu_1)}{\pm\mu_1}, \frac{\Sigma(\tau, \pm\mu_2)}{\pm\mu_2}, \dots, \frac{\Sigma(\tau, \pm\mu_n)}{\pm\mu_n} \right] \quad (2.48)$$

Using this vector notation, equation 2.46 becomes:

$$\frac{d}{d\tau} \mathbf{I}^{\pm}(\tau) = \pm \mathbf{M}^{\pm}(\tau) \mathbf{I}^{\pm}(\tau) \pm \mathbf{M}^{\mp}(\tau) \mathbf{I}^{\mp}(\tau) - \boldsymbol{\sigma}^{\pm}(\tau) \quad (2.49)$$

where the matrix elements $\mathbf{M}_{n \times n}$ are defined as:

$$\mathbf{M}_{ij}^+(\tau) = \frac{1}{\mu_i} \left[\delta_{ij} - \frac{1}{2} a_j \rho(\tau, \mu_i, \mu_j) \right] \quad (2.50)$$

$$\mathbf{M}_{ij}^-(\tau) = -\frac{1}{2\mu_i} a_j \rho(\tau, \mu_i, -\mu_j) \quad (2.51)$$

To give a physical interpretation to these quantities, it is sufficient to consider that the vector terms \mathbf{I}^{\pm} are the upward (+) downward (-) radiance beams respectively. To streamline the problem, we can make the assumption that the atmosphere exhibits vertical homogeneity. This assumption is reasonable, as a typical atmospheric profile can be regarded as a continuous sequence of homogeneous layers. In this case, \mathbf{M} and $\boldsymbol{\sigma}$ lose their explicit dependence on τ .

A general solution for 2.49 is derived by combining the solution for the corresponding homogeneous part with a particular solution. Let us first consider the homogeneous part of the equation:

$$\frac{d}{d\tau} I^\pm(\tau) = \pm M^\pm I^\pm(\tau) \pm M^\mp I^\mp(\tau) \quad (2.52)$$

If we assume that the solution for 2.52 is of the form $I^\pm(\tau) \propto \mathbf{g}^\pm e^{k\tau}$, we can write:

$$k \begin{vmatrix} \mathbf{g}^+ \\ \mathbf{g}^- \end{vmatrix} = \begin{vmatrix} M^+ & M^- \\ -M^- & -M^+ \end{vmatrix} \begin{vmatrix} \mathbf{g}^+ \\ \mathbf{g}^- \end{vmatrix} \quad (2.53)$$

After some algebra, it is possible to obtain the following expression:

$$k^2(\mathbf{g}^+ + \mathbf{g}^-) = (M^+ - M^-)(M^+ + M^-)(\mathbf{g}^+ + \mathbf{g}^-) \quad (2.54)$$

This constitutes an eigenvalue problem of order n . After solving the problem for $(\mathbf{g}^+ + \mathbf{g}^-)$, we can subsequently derive the eigenvectors of the original system \mathbf{g}^\pm . The homogeneous solution can be obtained as a linear combination:

$$I(\tau, \mu_i) = \sum_{j=-n}^n L_j g_j(\mu_i) e^{-k_j \tau} \quad (2.55)$$

where k_j and $g_j(\mu)$ are the eigenvalues and eigenfunctions of 2.53. The constant values L_j are determined by $2n$ boundary conditions imposed on I^\pm at the upper and lower boundaries. The general solution is finally obtained by adding a particular solution $I_p(\tau, \mu)$ to the homogeneous solution:

$$I(\tau, \mu_i) = \sum_{j=-n}^n L_j g_j(\mu_i) e^{-k_j \tau} + I_p(\tau, \mu_i) \quad (2.56)$$

The form of the particular solution depends on the non-homogeneous terms that are contained into $\Sigma(\tau, \mu_i)$.

The formulation of the DOM, as described above, closely adheres to the derivation outlined in Stamnes et al. (1988) [103]. The authors also provided a robust software package, called DISORT, which has gained widespread acceptance in the scientific community as a reference model for the computation of high-resolution spectral radiances in the presence of multiple scattering. It's worth noting that DISORT has been coupled with another important reference code, LBLRTM (Line-by-Line Radiative Transfer Model, Clough et al. [16]), to yield the code chian LBLDIS [110].

2.3.2 | Scaling methods

The presence of the multiple scattering term in the radiative transfer equation substantially increases the computational burden of the solution. This is mainly due to the increased

dimensionality of the problem in solvers such as the discrete ordinate method (i.e. the dimension of the matrix \mathbf{M}^\pm defined in 2.50 and 2.51). Even if the computational cost of these accurate solutions can be acceptable in some research contexts, applying the same methodologies to operational applications, analysis of huge datasets, data assimilation algorithms or global circulation models is not feasible.

A possible solution for mitigating the computational burden is to avoid the direct calculation of the multiple scattering term by scaling the absorption optical depth of the cloud. In this way, the effects induced by the multiple scattering are viewed in terms of absorption and emission processes. Examples of these methodologies are the similarity principle for radiative transfer [23] or the Chou et al. (1999) scheme [13]. These schemes, originally developed for irradiance simulations, are widely applied even nowadays in the longwave radiative transfer routines, both for fluxes and radiances computations [57, 77, 98].

This section proposes the derivation of Chou's scaling method following the approach suggested by Tang et al., (2018) [106].

Starting from 2.45, we can write the radiative transfer equation in local thermodynamic equilibrium assuming plane parallel approximation with azimuthal symmetry as ($m = 0$):

$$\mu \frac{dI(\tau, \mu)}{d\tau} = I(\tau, \mu) - \frac{\tilde{\omega}(\tau)}{2} \int_{-1}^1 P(\mu, \mu') I(\tau, \mu') d\mu' - [1 - \tilde{\omega}(\tau)] B(\tau) \quad (2.57)$$

where μ is the cosine of the zenith angle, τ is the integrated optical depth from the top of the atmosphere to the level of interest, $\tilde{\omega}$ is the single scattering albedo of the layer at level τ , B is the Planck function at level τ , and $P(\mu, \mu')$ is the azimuthally averaged scattering phase function describing the scattering events for radiation entering the layer at μ' and exiting in the μ direction.

We can now split the integral term in equation 2.57 in two terms, which can be interpreted as a back-scattering and a forward-scattering contribution.

$$\begin{aligned} \mu \frac{dI(\tau, \mu)}{d\tau} = I(\tau, \mu) - \frac{\tilde{\omega}(\tau)}{2} \int_{-1}^0 P(\mu, \mu') I(\tau, \mu') d\mu' + \\ - \frac{\tilde{\omega}(\tau)}{2} \int_0^1 P(\mu, \mu') I(\tau, \mu') d\mu' - [1 - \tilde{\omega}(\tau)] B(\tau) \end{aligned} \quad (2.58)$$

If we approximate the downward and upward radiance in the integral terms with two respective constants in μ , equation 2.58 reduces to a first-order ordinary differential equation. In his radiative scheme, Chou assumed an ambient radiation $I(\tau, \mu')$ of the form:

$$I(\tau, \mu') = \begin{cases} B(\tau) & \text{if } \mu \cdot \mu' < 0 \\ I(\tau, \mu) & \text{if } \mu \cdot \mu' > 0 \end{cases} \quad (2.59)$$

The ambient radiation is considered isotropic in each hemisphere. The integral terms in equation 2.58 become:

$$\begin{cases} I(\tau, \mu) \int_{-1}^0 P(\mu, \mu') d\mu' + B(\tau) \int_0^1 P(\mu, \mu') d\mu' & \text{if } \mu < 0 \\ B(\tau) \int_{-1}^0 P(\mu, \mu') d\mu' + I(\tau, \mu) \int_0^1 P(\mu, \mu') d\mu' & \text{if } \mu > 0 \end{cases} \quad (2.60)$$

The integral terms are now solely dependent on the optical properties of the scatterer. Specifically, it is possible to compute an average quantity b , called backscattering parameter, representing the mean fraction of radiation scattered in the upward/downward direction for isotropic radiation incident from above/below¹.

$$b = \frac{1}{2} \int_0^1 \int_{-1}^0 P(\mu, \mu') d\mu' d\mu = \frac{1}{2} \int_{-1}^0 \int_0^1 P(\mu, \mu') d\mu' d\mu \quad (2.61)$$

Noting that the phase function is normalized ($\frac{1}{2} \int_{-1}^1 P(\mu, \mu') d\mu' = 1$), we can write the integral terms in 2.60 as follows:

$$\begin{cases} I(\tau, \mu) \cdot (2 - 2b) + B(\tau) \cdot 2b & \text{if } \mu < 0 \\ B(\tau) \cdot 2b + I(\tau, \mu) \cdot (2 - 2b) & \text{if } \mu > 0 \end{cases} \quad (2.62)$$

Using this expression to substitute the integral term in 2.57, the radiative transfer equation in the presence of multiple scattering can be written as:

$$\mu \frac{dI(\tau, \mu)}{d\tau} = [1 - \tilde{\omega}(\tau)(1 - b(\tau))]I(\tau, \mu) - [1 - \tilde{\omega}(\tau)(1 - b(\tau))]B(\tau) \quad (2.63)$$

We can note that the factor $1 - \tilde{\omega}(\tau)(1 - b(\tau))$ multiplies both the radiance and the non-homogeneous term. It is therefore possible to factor out this term and define an apparent optical depth $\tilde{\tau}$ as:

$$\tilde{\tau} = [1 - \tilde{\omega}(\tau)(1 - b(\tau))] \tau \quad (2.64)$$

Using this scaling, 2.63 can be written as a Schwarzschild-like equation, which admits solutions of the form 2.36.

$$\mu \frac{dI(\tilde{\tau}, \mu)}{d\tilde{\tau}} = I(\tilde{\tau}, \mu) - B(\tilde{\tau}) \quad (2.65)$$

Under these assumptions, we can interpret the multiple scattering effects induced by clouds or aerosols as apparent emissions from the layers and, consequently, significantly reduce the computational cost of the radiative transfer solution.

Since the value of the phase function depends only on the scattering angle $\mathbf{\Omega}' \cdot \mathbf{\Omega} = \tilde{\mu}$, we can introduce the Henyey-Greenstein (HG) approximation for the phase function [123]:

$$P_{HG}(\tilde{\mu}) = \frac{1}{4\pi} \frac{1 - g^2}{[1 + g^2 - 2g\tilde{\mu}]^{3/2}} = \sum_{l=0}^{\infty} (2l + 1) g^l P_l(\tilde{\mu}) \quad (2.66)$$

¹The integration is performed on the observation hemisphere.

where the last form is the commonly-used expansion in terms of the Legendre polynomials, P_l . The parameter g is called *asymmetry parameter* and it is defined as:

$$g = \frac{1}{2} \int_{-1}^1 P(\tilde{\mu}) \tilde{\mu} d\tilde{\mu} \quad (2.67)$$

Using this form, we can express the value of the backscattering parameter b as a polynomial function of the asymmetry parameter. In their 1999 work, Chou et al. proposed a third-order polynomial approximation for b :

$$b = 1 - \sum_{i=1}^4 a_i g^{i-1} \quad (2.68)$$

The four coefficients are calculated based on the optical properties of water and ice clouds, which are obtained using the Mie scattering algorithm and the method of Fu et al. (1998) [31], respectively: $a_1 = 0.5$, $a_2 = 0.3738$, $a_3 = 0.0076$, and $a_4 = 0.1186$.

Similar results can also be obtained for the similarity principle, where the scaling of optical depth is defined as follows:

$$\tilde{\tau} = \left[1 - \tilde{\omega}(\tau) \frac{1 + g(\tau)}{2} \right] \tau \quad (2.69)$$

It is important to note that both the methods reduce to the pure absorbing/emitting atmosphere solution in the limit case where $g = 1$ or $\tilde{\omega} = 0$ (b must be 0 if $g = 1$).



3 | Application of scaling methods to spectral radiance computation

The following chapter is derived and adapted from the work done by Martinazzo et al., (2021) [74].

3.1 | Introduction

The work here presented focuses on the accuracy of simple, analytical, *scaling* approximations, used to solve the radiative transfer equation in the infrared region and in the presence of clouds and aerosols, when the simplifying hypothesis of no scattering atmosphere is no more valid. As already introduced in section 2.3.2, analytical approximations, such as the one described by Chou [19], allow us to extend clear-sky fast or hyper-fast infrared radiative transfer models to scattering conditions. The gain in terms of computational time is impressive since these approximate radiative transfer algorithms can provide high spectral radiance field simulations over the full infrared spectrum in less than a second, compared to times of the order of tens or hundreds of minutes (depending on cloud properties) employed by full-scattering radiative transfer codes. Moreover, the present study is motivated by the need to check the accuracy of these existing fast schemes for the simulation of the FORUM-like measurements, i.e. capable of producing spectrally resolved TOA radiances in the 100-1600 cm^{-1} band and in all-sky conditions (e.g. see [88]).

As far as the infrared spectral range is concerned, suitable *numerical* methods (e.g. doubling-adding and discrete ordinate methods) for the radiative transfer equation do exist and have been primarily used to retrieve optical properties of aerosols and clouds (e.g. [72, 121] and references therein). In this respect, we note that one of the most popular numerical schemes for multiple scattering, that is DISORT (Discrete Ordinate Radiative Transfer [103]), has been coupled to LBLRTM (Line-by-Line Radiative Transfer Model [16]) to yield LBLDIS [110]. We have also to note here the development of schemes specialized for few channels aiming at retrieving properties of cirrus clouds (e.g. [38]).

However, radiative transfer calculations with numerical, multiple scattering schemes have a huge computational burden, and are not amenable to be included in the fast forward model developed for operative data assimilation [80], or for the purpose of fast operational retrievals for geophysical parameters and atmospheric composition (e.g. [1, 21]). In the framework of

fast and hyper-fast models, analytical, approximate methods are desirable, because accurate numerical solutions are too computationally expensive.

The Chou approximation [13], described in the previous Chapter (hereinafter – the Chou scaling approximation or "CA") allows to account for the scattering effects by clouds and aerosols by scaling the optical depth of the layer containing the particles. The multiple scattering parameterization is based on the hypothesis that the longwave radiation field is isotropic, and assumes an apparent optical thickness which includes hemispheric backscattering in the emission of a layer and in the transmission between levels.

CA was introduced and intended for flux computations [13]. However, it has been proved that CA is also useful for radiance calculations (e.g., [78]). CA scaling approximation has the advantage that the used form of the radiative transfer equation in cloudy skies is identical to the general form used for a clear atmosphere, therefore, the computational efficiency of a given radiative transfer model (RTM) is not degraded. Since CA handles scattering as a scaling of the absorption OD, the vertical profile concentration of aerosol, liquid water, and ice particles can be treated as gases in the mid and far infrared.

CA was first implemented for spectral radiance calculations in [78], and soon after used in 1-D variational data assimilation of high spectral resolution infrared radiance from satellite [39]. Today, it is routinely adopted for radiance computation in fast RTMs (e.g. [21, 64, 65, 98]). An in-depth inter-comparison of diverse, fast forward models for cloudy atmosphere, not only using CA, has been recently performed by [3]. The results show that the main differences among the codes arise from the way they deal with geometrical and geophysical parameters such as the cloud fraction and the database used for optical properties of ice and liquid water, rather than on radiative transfer methodology and approximations. It is nonetheless important to quantify the impact of these scaling methodologies (such as CA), considering their widespread adoption in fast models.

Until now, the accuracy of CA has been assessed mainly for fluxes and in the thermal infrared (≈ 645 to 3000 cm^{-1}), which is the range of modern hyper-spectral infrared sensors, whereas an assessment of the accuracy of fast analytical approximations for the far infrared (FIR, ≈ 50 to 700 cm^{-1}) spectral region is still incomplete. Yet, the FIR (which is the focus of the FORUM and PREFIRE missions) plays an essential role in processes governing the natural greenhouse effect of the Earth (e.g., [37]), and in the detection and classification of cirrus clouds [67, 68]. Until now, the analysis concerning this spectral region has been mostly limited to clear-sky for observations of the water vapour rotational band, and studies concerning the assessment of the H_2O continuum absorption (e.g. [8, 84, 85, 99, 111]). However, the promotion and planning of satellite missions dedicated to the FIR spectral region (e.g., [94, 118]) has renewed the research interest in the field of all-sky RTMs.

Thus, understanding the impact on FIR top-of-the-atmosphere radiances of multiple scattering analytical approximations, such as that provided by [13], is an important issue, which we address in this chapter.

To begin with, an updated version of the CA approximation is proposed and compared with a scaling form based on the similarity principle [106]. Radiance calculations based on these two simple scaling approaches are compared against efficient numerical computations accomplished out with the LBLDIS model chain. Results are provided for an extensive data set of

state vectors, encompassing liquid water, ice, and aerosols. The analysis covers the whole FORUM range (100-1600 cm^{-1}), so that it will be interesting also for users working in the mid-infrared.

3.2 | Atmosphere, clouds, and aerosols characterization

To simulate different atmospheric scenarios, vertical profiles of pressure, temperature, water vapor and ozone volume mixing ratios are derived from the ERA5 reanalysis data [41] at four latitudes, representative of equatorial, low-, mid-, and high- latitude scenarios (Table 3.1). Since the ERA5 data are limited to a maximum level altitude of about 60 km , the vertical profiles are extended up to 80 km using the climatological database IG2 v5.4 [92]. To smoothly combine the two in a single profile, a linear combination is assumed in the region between 55 and 60 km . The IG2 is also used for the specification of the volume mixing ratio profiles of ten minor gases (CO_2 , N_2O , CO , CH_4 , O_2 , NO , SO_2 , NO_2 , NH_3 , and HNO_3). The vertical profile of CO_2 mixing ratio, estimated by IG2 in 2013, is linearly corrected to the selected years concentration level by means of a scaling factor. The vertical profiles of temperature and water vapor mixing ratio, from the ground up to 20 km altitude, are shown in Figure 3.1 for the four selected latitudes. The geolocations correspond to grid points over the sea. The surface emissivity is derived from the database by [46], and the corresponding sea surface temperature (SST) is taken from the ERA5 dataset. The SST and the total precipitable water vapor (PWV) reported in Table 3.1 span over a large range of values accounting from a very cold and dry scenario at high latitude to a warm and wet equatorial condition.

TABLE 3.1: Main features of the selected scenarios. Data from the ERA 5 database.

Scene	Latitude (°)	Longitude (°)	Date (YYYY-MM-DD)	Time (UTC)	SST (K)	PWV (mm)
Equator	+5	+3	2018-01-15	12:00	301.3	48.2
Low latitude	+34	+19	2017-07-15	12:00	300.2	17.8
Mid latitude	+50	-20	2019-03-13	12:00	283.8	9.1
High latitude	+74	-5	2019-03-13	12:00	272.6*	2.9

*No sea ice is observed despite the SST is below 0°C (https://nsidc.org/data/seaice_index)

For each of the four scenarios reported in Table 3.1 and Figure 3.1, simulations assuming, alternatively, the presence of liquid water or ice clouds or aerosol components are performed. The geometrical, optical and micro-physical properties of the scattering layers are not derived from the ERA5 dataset but systematically varied over a wide range of values in order to account for a large variety of observational conditions. The cloud and aerosol features used in the radiative transfer computations are briefly described in the following sections.

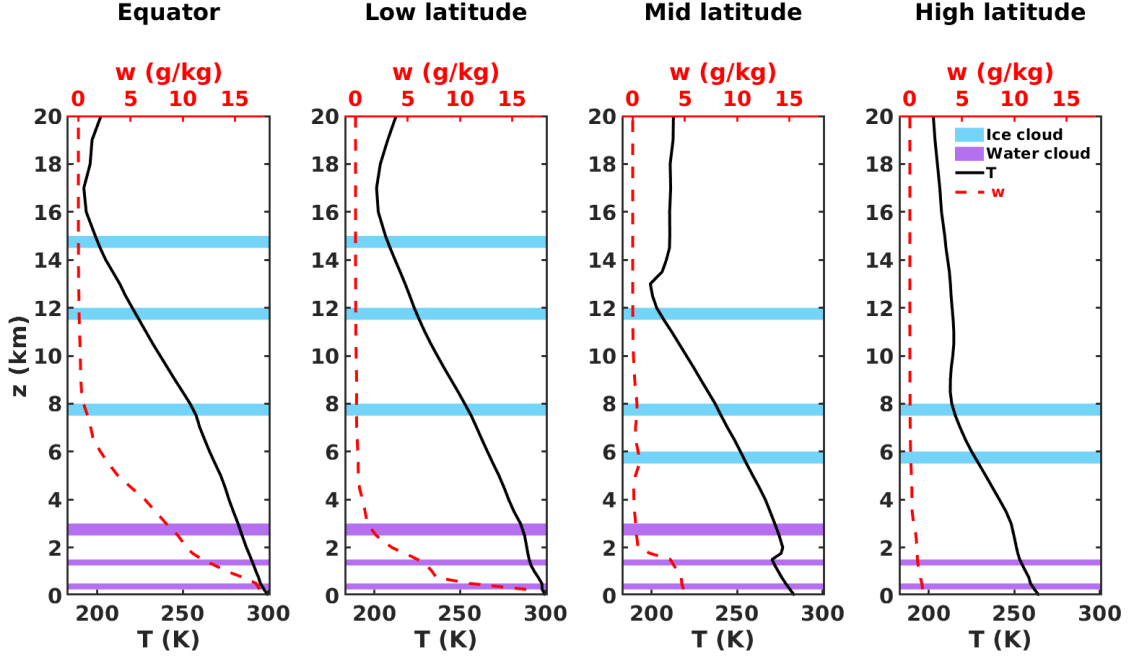


FIGURE 3.1: Vertical profiles of temperature (black solid line) and water vapor mixing ratio (red dashed line) for the considered scenarios. Light blue and purple shaded layers show the height position and thickness of the analyzed ice clouds and liquid water clouds, respectively.

3.2.1 | Liquid water clouds

Liquid water clouds are assumed as composed of a particle size distribution (PSD) of water spheres, whose single scattering single particle radiative properties are generated by using a Mie solution-based algorithm, the Scattlay code [89]. Scattlay performs calculations of scattering coefficients and efficiency factors as well as scattering phase functions for single, isolated, spherical particles. Water refractive indices by [24] are ingested for the computations. The single particle properties are then combined to generate single scattering radiative properties for the PSDs over the spectral interval of interest. PSDs of low-level stratiform clouds, as those modelled in this study, are commonly described by a lognormal distribution [82], whose number of particles per unit volume is:

$$n(r) = \frac{n_0}{r\sqrt{2\pi}\sigma} e^{-\frac{(\ln(r/r_m))^2}{2\sigma^2}} \quad (3.1)$$

where r is the particle radius, r_m is the mode radius of the distribution, σ is the scale parameter, and n_0 is a normalization factor that depends on the total number of particles per volume used in the radiative transfer computations. In this work, the scale parameter is set to $\sigma = 0.38$, according to the average value derived by [82] from in-situ measurements of low-level stratiform clouds. Assuming σ as a constant, the different PSDs are unequivocally

related to their effective radius r_{eff} , defined as the fraction of the third to the second moment of the PSD:

$$r_{eff} = \frac{\int_0^{\infty} r^3 n(r) dr}{\int_0^{\infty} r^2 n(r) dr} \quad (3.2)$$

For a lognormal PSD, the relation between effective and mode radius is derived from Equations 3.1 and 3.2 and results to be:

$$r_{eff} = r_m e^{\frac{5}{2}\sigma^2} \quad (3.3)$$

Multiple simulations are performed for different r_{eff} , total optical depth (OD, at 900 cm^{-1}), and cloud top. The ranges of the input parameters, common to every latitudinal scenario, are reported in Table 3.2. Both for liquid water and ice clouds, six different r_{eff} values are used spanning over the reported ranges. Similarly, ten different OD values are assumed in the simulations. The equation defining the total OD for vertically homogeneous clouds of thickness Δz is

$$OD = N_{tot} \beta_{ext}(r_{eff}, 900) \Delta z \quad (3.4)$$

where $\beta_{ext}(r_{eff}, 900)$ is the extinction coefficient at 900 cm^{-1} of the PSD corresponding to a specific r_{eff} , normalized to a single particle per volume (as defined in Chapter 2). N_{tot} is the total number of particles in the volume, which is computed internally by the code once the input parameters (OD, r_{eff} , and Δz) are provided. It is assumed that once r_{eff} is selected the corresponding optical properties are unequivocally defined. Liquid cloud layers are shown as purple bands in Figure 3.1. Ice clouds are in cyan in the same Figure.

TABLE 3.2: Values and ranges of the cloud and aerosol parameters used in the selected case studies.

Particle type	PSD type	r_{eff} (μm)	Top Height (km)	Thickness (km)	OD (900 cm^{-1})
Liquid water	lognormal ($\sigma=0.38$)	2–18	0.5–3	0.25–0.50	5–70
Ice Aggregates	gamma ($\mu=7$)	6–50	6–15	0.50	0.03–30
Dust-like	lognormal ($\sigma=0.788$)	2	1.5	0.25	0.05–0.25
Volcanic dust	lognormal ($\sigma=0.615$)	2	4	0.50	0.05–0.30

3.2.2 | Ice clouds

Ice clouds are commonly assumed as PSDs of non-spherical ice crystals. In nature, multiple crystal shapes are observed within ice cloud layers depending on the cloud formation conditions, its evolution, and its thermodynamic state. Crystal aggregates of eight hexagonal

ice columns are considered in this work, whose single scattering single particle radiative properties are described by [122]. A commonly used PSD for ice clouds is the three parameters gamma type distribution, here below written as a function of the maximum dimension of the ice particle D :

$$n(D) = n_0 D^\mu e^{-\lambda D} \quad (3.5)$$

where n_0 is the intercept, or normalization factor, μ is the shape parameter, and λ is the slope parameter. An average value of $\mu=7$ is assumed in this work. A positive value of μ means that the shape of the gamma distribution is of under-exponential type and the maximum of the distribution lies in between the minimum and maximum dimension of the crystals. Since μ is assumed constant and n_0 is a scaling parameter, the different PSDs can be related to the effective dimension only. For non-spherical particles, an effective dimension D_{eff} of the distribution is defined, according to [30], as

$$D_{eff} = \frac{3 \int_0^\infty V(D)n(D)dD}{2 \int_0^\infty A(D)n(D)dD} \quad (3.6)$$

where A and V are the cross-sectional area and the volume of the particle with maximum dimension D . For comparison with liquid water particles, the effective radius of the PSD is defined as $r_{eff} = 0.5D_{eff}$.

Simulations are performed at different r_{eff} values and for ODs ranging from 0.03 to 30, thus spanning from the upper limit of sub-visible cirrus clouds [97] to thick ice layers. The cloud layer top is placed at different heights, whose maximum varies according to the altitude of the Tropopause (light blue bands in Figure 3.1). All the key parameters concerning ice clouds are reported in Table 3.2.

3.2.3 | Aerosols

Globally, aerosols comprise a large variety of radiative properties due to variations in chemical composition, particle size distributions (often multimodal), and vertical concentration. Even if the most important impact on atmospheric radiances is at short wavelengths ($0.3\text{--}4 \text{ cm}^{-1}$) for some types of aerosols their effects at long wavelengths ($4\text{--}100 \text{ cm}^{-1}$) is not negligible and must be accounted for in radiative transfer computations. Two types of aerosols are considered for this study: desert dust (dust-like) and volcanic dust. For these cases, the aerosol load in the atmospheric column can reach very high values and significantly influence the local energy balance. Their optical properties are driven by the refractive indices, that are taken from the HITRAN [34] database to cover the $250\text{--}1600 \text{ cm}^{-1}$ band of the FORUM spectral range. In Figure 3.2, the imaginary part of the refractive index of volcanic dust [114] and desert dust [115] are compared to those of ice [116] and water [24]. The plot shows that both aerosols are characterized by specific absorption properties along the spectrum with local maxima between 300 and 400 cm^{-1} and at around 1000 cm^{-1} . Their single scattering single particle radiative properties are generated by using the Scattlay code

under the assumption that their shape is spherical. The aerosol PSDs are considered to follow a lognormal distribution (Equation 3.1), with a fixed scale parameter for each aerosol type based on average values found in the literature. It is assumed that $\sigma_{\text{dust-like}} = 0.788$ [42], and $\sigma_{\text{volcanic dust}} = 0.615$ [53].

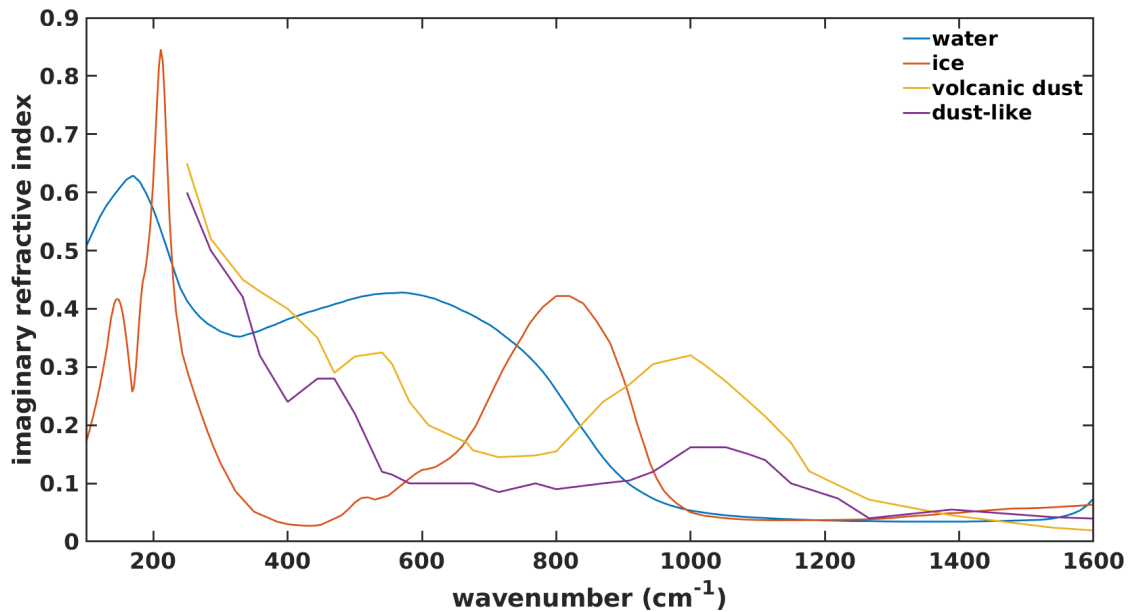


FIGURE 3.2: Imaginary part of the refractive indices used for the computation of the cloud and aerosol particle size distributions.

The aerosol contribution is analyzed in the low-latitude scenario for the dust-like particles, and in the mid-latitude scenario in case of volcanic dust. A uniform aerosol layer is considered, whose height is selected according to the work by [54] on typical Saharan aerosol plumes and by [53] on Eyjafjallajökull 2010 eruption. The range of ODs used in the desert dust simulations is based on the values stored in the CAMS database [6, 86] for the month of June 2019 off the Atlantic coast of North Africa, referred to an event of dust transportation assumed as a representative case study. The work about the Eyjafjallajökull 2010 eruption by [87] is used to determine the range of ODs for the volcanic dust simulations. The main aerosol parameters used in the radiative transfer computations are summarized in Table 3.2.

3.3 | Computational methodologies

The accurate solution for the upwelling spectral radiance at far and mid-infrared wavelengths in multiple scattering conditions is compared to fast solutions based on scaling meth-

ods. The same simulation chain of radiative transfer models (Figure 3.3) is used for each one of the considered configurations:

- the Full Scattering (FS) that exploits the full functionalities of a numerical algorithm solving the radiative transfer equation in the presence of multiple scattering events;
- the Chou Approximation (CA) that scales the absorption properties of the scattering layers by using a hemispheric backscattering function and solves the radiative transfer equation in a pure absorption/emission configuration;
- the Similarity Principle (SP) that is used, as in the CA case, to define scaled absorption properties of the scattering medium emulating the scattering process in a pure absorption/emission approximation.

For the three configurations, the only difference in the whole process concerns the set-up of the radiative transfer solution in the scattering layer, that is, any case, obtained by using the DISORT model [103]. Thus, the same radiative transfer code carries out both full scattering computations, by using all the relevant scattering parameters (FS solution), and approximated scattering computations, by using the clear sky radiative transfer equation based on the apparent optical depths computed in accordance with the Chou approximation or the similarity principle. The use of the same code chain and the same set-up in different configurations, rather than the usage of different codes, avoids the introduction of possible code-dependent systematic errors and thus allows a better assessment of the accuracy of the scaling methodology in comparison to the full scattering solution for different conditions. Figure 3.3 provides a flowchart of the code chain and highlights how the same algorithm is used in different configurations. A more detailed description of the three configurations is provided in the following sections.

3.3.1 | Full scattering

The current analysis is based on synthetic spectral radiances generated by the line-by-line radiative transfer model LBLDIS [110], a combination of the AER's LBLRTM [15] and the DISORT [103] routines.

LBLRTM is an accurate, flexible, and efficient line-by-line radiative transfer model and includes a recently updated water vapour continuum parameterization (MT_CKD v3.2, [84]) and the spectroscopic database AER v3.6, built from HITRAN 2012 [95]. The LBLRTM v12.7 is used to compute the atmospheric optical depth for each layer of the model (52, from 0 to 80 km), characterized by the vertical profiles provided in Section 3.2.

DISORT is a plane parallel discrete ordinate algorithm for monochromatic unpolarized radiative transfer in non-isothermal, vertically inhomogeneous media. LBLDIS uses the DISORT v2.0, which was compiled using double precision to solve some numerical issues. The LBLRTM outputs and the single scattering PSD properties of clouds and aerosols, described in Section 3.2, are used as input for LBLDIS to compute high spectral resolution radiances. The high-resolution spectra ($\Delta\tilde{\nu} = 0.01 \text{ cm}^{-1}$) are successively convolved with a *sinc* function

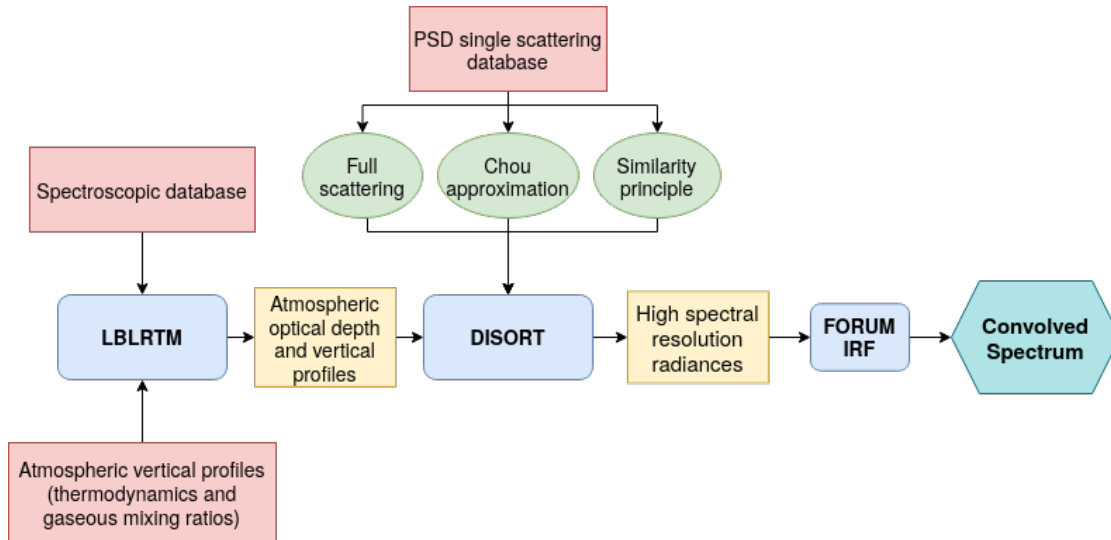


FIGURE 3.3: Flow diagram of the code chain used for the radiative transfer simulations. Databases are in red boxes, codes are in blue and outputs are in yellow. The three methodologies are highlighted in green. The final spectrum is a synthetic FORUM-like observation. See text for more details.

emulating an ideal FORUM instrumental response function. The final spectral resolution, that is the full width at half maximum of the unapodised instrument spectral sampling function, is set at 0.36 cm^{-1} [26].

The FS solution is obtained using the code chain described in Figure 3.3 in its full potentialities, meaning that the DISORT routine is run to solve the multiple scattering radiative transfer in the presence of cloud or aerosol layers. In this configuration, the required input properties for each scattering layer involve the extinction, absorption and scattering coefficients and the angular description of the phase function of the specific PSD accounted for.

3.3.2 | CA method

As shown in Section 2.3.2 and according to the work done by Chou [13], the scattering contribution can be accounted for by replacing the optical depth (τ) of each atmospheric layer with an *apparent* optical depth for extinction:

$$\tilde{\tau} = (1 - \bar{\omega})\tau + b\bar{\omega}\tau \quad (3.7)$$

where $\bar{\omega}$ is the single scattering albedo and b is the mean fraction of radiation that is scattered by the cloud/aerosol particles in the backward hemisphere. The first term on the right-hand side of Equation 3.7 represents the actual absorption of the layer, and the second term is an additional absorption related to the radiation removed from the beam because of the backscattering processes. The backscattering function b quantifies the hemispheric backscat-

tered radiation and it is formally computed through an integration of the phase function P of the considered PSD. It is defined by [13] (Eq. 10) as

$$b = \frac{1}{2} \int_0^1 \int_{-1}^0 P(\mu, \mu') d\mu' d\mu \quad (3.8)$$

where μ is the cosine of the zenith angle and the integration limits indicate that the radiation is scattered toward the incoming hemispheric direction. Chou et al. [13] (Eq.11) provides a polynomial fitting of b through the asymmetry parameter g as

$$b = 1 - \sum_{i=1}^4 a_i g^{i-1} \quad (3.9)$$

where the coefficients a_i , reported in Table 3.3, are jointly retrieved for liquid water and ice PSDs. In particular, the PSD parameters used to derive the latter relation are computed by [13] for a modified gamma distribution of liquid water droplets and for randomly oriented hexagonal ice crystals computed using the outdated method by [31].

The CA scaling method is obtained by using the code chain shown in Figure 3.3. In this case, the DISORT routine is run without accounting for scattering processes. The procedure requires to modify the input PSD radiative properties in accordance with Equation 3.7 to account for the *apparent* optical depth for extinction.

3.3.3 | Similarity principle

An approach similar to CA for fast radiative transfer computations is described by [106], based on the application of the similarity relation on ice cloud radiance calculations by [23]. As in CA, the full scattering computation is avoided by considering a pure absorbing/emitting atmosphere with scaled *apparent* optical depth for extinction:

$$\tilde{\tau} = (1 - \tilde{\omega})\tau + \left(\frac{1-g}{2}\right)\tilde{\omega}\tau \quad (3.10)$$

Similarly to Equation 3.7, the first term on the right-hand side represents the actual absorption of the layer and the second term is an additional absorption related to the radiation removed from the beam because of the scattering processes. The advantage of the SP with respect to CA consists in depending on the asymmetry parameter in a very simple way, and thus not demanding time consuming computations such as those required for the definition of the backscattering function b .

As in the CA case, the DISORT routine is run without accounting for scattering processes, and by modifying the input PSD radiative properties according to the *apparent* optical depth described in Equation 3.10.



3.4 | Results

3.4.1 | Accurate computation and parameterization of b

According to [13], the backscattering function b can be computed through the polynomial approximations (Equation 3.9), whose coefficients account for both liquid water and ice clouds. Moreover, as already noticed, the ice particle scattering properties are taken by [31] and thus do not benefit of all the scientific and computational improvements achieved in the last years as those used in this study [122].

An improvement of the CA is presented by accurately computing the b parameter using Equation 3.8 for the integration of the phase functions of the PSDs, provided with the reference database of optical properties described in Section 3.2. The integration of Equation 3.8 requires to explicit the dependence of the phase function on the incoming and exiting azimuth angles ϕ' and ϕ :

$$b = \frac{1}{2} \int_0^{2\pi} \frac{1}{2\pi} d\phi \int_0^{2\pi} \frac{1}{2\pi} d\phi' \int_0^1 d\mu \int_{-1}^0 P(\mu, \phi, \mu', \phi') d\mu' \quad (3.11)$$

A Monte Carlo technique is used, which is a common method for the evaluation of high dimensional integration problems. Given an integration problem:

$$E = \int_{\mathbb{D}} f(x) dx \quad (3.12)$$

where $\mathbb{D} \subset \mathbb{R}^n$ is the domain of integration, it is possible to prove [32] that a good estimator for E is given by

$$E \simeq \frac{1}{N} \sum_{i=1}^N \frac{f(x_i)}{g(x_i)} \quad (3.13)$$

where $g(x)$ is any probability density function which is normalized on the given domain \mathbb{D} , and the N points x_i are randomly sampled from the distribution $g(x)$. For $g(x)$ being a uniform distribution in \mathbb{D} , then E can be expressed as:

$$E \simeq \frac{V}{N} \sum_{i=1}^N f(x_i) \quad (3.14)$$

where $V = \int_{\mathbb{D}} dx$ and the approximation error is $\propto 1/\sqrt{N}$. Thus, from Equations 3.11 and 3.14, b can be computed as:

$$b \simeq \frac{1}{2N} \sum_{i=1}^N P(\mu_i, \phi_i, \mu'_i, \phi'_i) \quad (3.15)$$

being $\mathbb{D} = \{\mu \in [0, 1], \phi \in [0, 2\pi], \mu' \in [-1, 0], \phi' \in [0, 2\pi]\}$, and $V = 4\pi^2$. For a sample of randomly oriented particles, the phase function only depends on the cosine of the scattering angle $\cos \theta$. Therefore, Equation 3.15 can be expressed as:

$$b \simeq \frac{1}{2N} \sum_{i=1}^N P(\cos \theta_i) \quad (3.16)$$

where $\cos \theta_i$ is computed from spherical geometry for N quartets of incoming and outgoing directions in the domain \mathbb{D} :

$$\cos(\theta_i) = \mu_i \mu'_i + (1 - \mu_i^2)^{\frac{1}{2}} (1 - \mu_i'^2)^{\frac{1}{2}} \cos(\phi'_i - \phi_i) \quad (3.17)$$

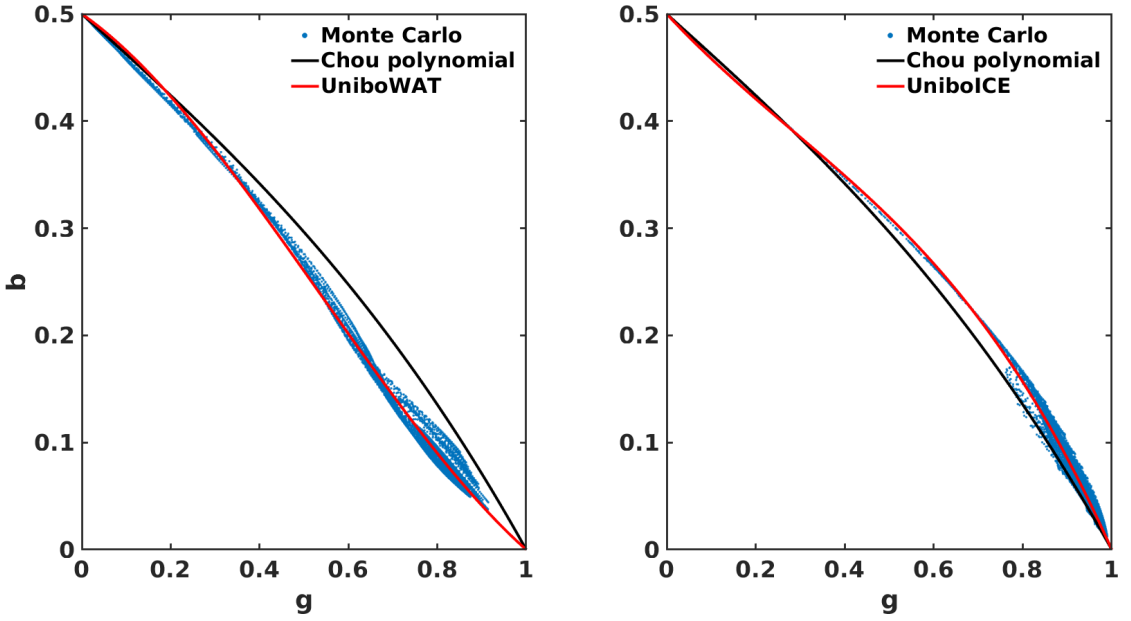


FIGURE 3.4: Left panel: Comparison of the backscattering function b versus the asymmetry parameter g of liquid water PSDs for three computation approaches: exact integral using Monte Carlo (blue dots, Equation 3.16), polynomial by Chou et al. (black line, Equation 3.9), and polynomial fit with updated coefficients, UniboWAT (red line, Table 3.3). Right panel: same as left panel, but for ice aggregates PSDs. The updated polynomial fit (red line, Table 3.3) is called UniboICE.

The results of the Monte Carlo computations of b for liquid water and ice aggregates PSDs are shown, respectively, in the left and right panel of Figure 3.4 (blue dots) for wavenumbers from 100 to 1600 cm^{-1} . They should be considered as the correct values of b for the liquid water droplets and column aggregate crystals PSDs accounted for in the present study, since they are derived from the explicit computation of the integral reported in Equation 3.11. In Figure 3.4, the backscattering functions are plotted as a function of the corresponding asymmetry parameters and compared with the values obtained by using the polynomial parameterization of Equation 3.9 (black solid line) for the same asymmetry parameter range. As particle size increases, b decreases mostly because of the increasing of the phase function

forward lobe (consequently, g increases), which makes the quantity of the energy scattered in the forward hemisphere prevail on the backscattered one.

Note that the coefficients used for Equation 3.9 are derived by [13] to simulate the b function of both liquid water and ice PSDs, thus, they are representative of average cloudy conditions. Differences among the Monte Carlo b values and the Chou parameterization are significant. In particular, Equation 3.9 provides an overestimation of b for liquid water PSDs and an underestimation of b for ice PSDs composed of column aggregates crystals. The percentage differences between the explicit computation of the backscattering function and the Chou polynomial description can be as high as 80% and 50% for liquid water and ice PSDs, respectively. Such differences in the backscattering function propagate into spectral radiance differences that reach values between 2% and 8% for liquid water and ice clouds, respectively, for the cases considered in this work (see Section 3.4.3). The use of the updated b functions is thus strongly suggested and it constitutes the adopted solution in this work.

To maintain an expression of b as a polynomial function of the asymmetry parameter, so that it would be easier to update existing codes based on the Chou approximation, a fitting procedure is applied to the Monte Carlo values of b for water and ice clouds separately (Table 3.3). The proposed polynomial expressions are formally identical to that suggested by [13] but improve the accuracy of the computation. They are named UniboWAT when specifically refer to liquid water clouds and UniboICE in the case of ice clouds. The UniboWAT and UniboICE are reported in Figure 3.4 as red curves. The coefficient of determination R^2 is 0.995 for UniboWAT and 0.989 for UniboICE.

In the present work, the re-scaling methodology is applied by using the exact values of b as computed by means of the Monte Carlo integration described above. The new parameterizations UniboWAT and UniboICE could also be used since the differences on the radiances with respect to using the exact b are negligible.

TABLE 3.3: Coefficients for the polynomial fitting of b versus g . The fits are in the form $b = 1 - \sum_i a_i g^{i-1}$.

Name	Application	a_1	a_2	a_3	a_4
Chou	Liquid water and ice clouds	0.5	0.3738	0.0076	0.1186
UniboWAT	Liquid water clouds	0.5	0.2884	0.5545	-0.3429
UniboICE	Ice aggregates clouds	0.5	0.4452	-0.3189	0.3737

3.4.2 | Scattering correction term for CA and SP

A preliminary analysis is performed to evaluate the magnitude of the additional term that, summed to the actual absorption $(1 - \tilde{\omega})\tau$, accounts for scattering in the apparent optical depth for extinction, introduced by the approximate methodologies as shown in Equations 3.7 and 3.10. Figure 3.5 compares the re-scaling terms that, once multiplied by τ , are used in the CA ($\tilde{\omega}b$) and in the SP ($\tilde{\omega}(1 - g)/2$) when in presence of a typical liquid water

cloud ($r_{eff} = 10 \text{ cm}^{-1}$, top panel) and of a typical ice cloud ($r_{eff} = 30 \text{ cm}^{-1}$, bottom panel). Note that $\tilde{\omega}b$ is computed using the accurate method described in Section 3.4.1. Results show that in the case of liquid water cloud (upper panel of the Figure) the scaling terms are very similar, especially in the FIR and up to 1000 cm^{-1} . It is thus expected that top-of-the-atmosphere radiance fields generated using the CA or SP method result in similar solutions. In case of ice clouds (lower panel of the Figure), the SP approach provides a lower contribution to the optical depth with respect to the CA along the entire spectrum. Similar behavior is observed over the whole range of the considered PSDs of ice crystals. Due to a smaller absorption, it is expected that the top of the atmosphere radiance generated using the SP solution is higher than that obtained when the CA configuration is adopted in the presence of ice clouds.

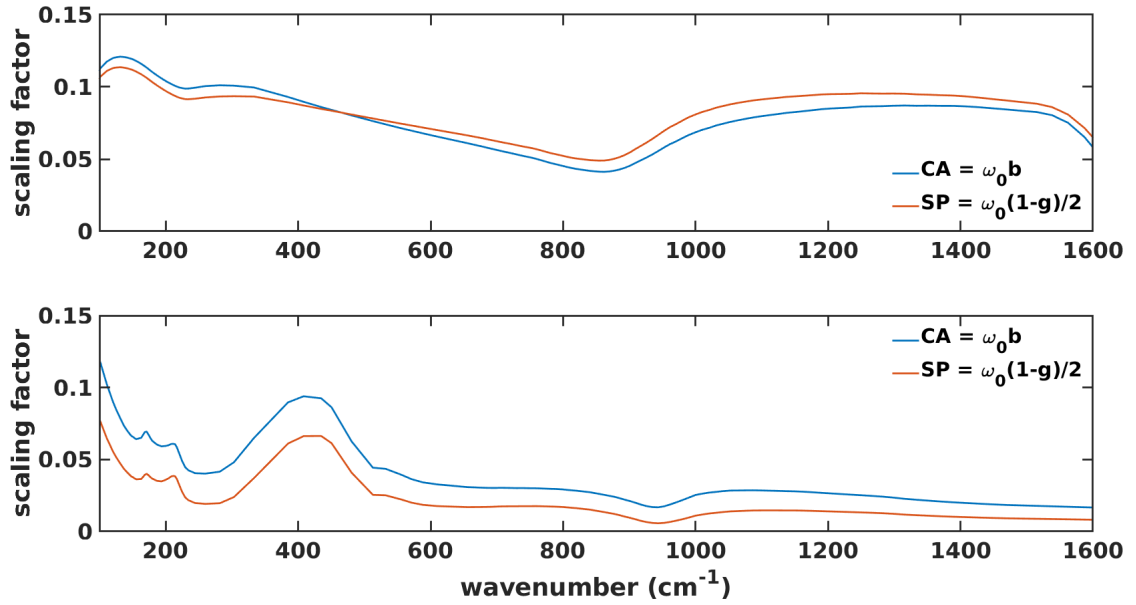


FIGURE 3.5: Optical depth re-scaling terms (see legend and text) in case of CA (blue line) and SP (orange) approaches, as a function of wavenumber. Upper panel: liquid water PSD with $r_{eff} = 10 \text{ cm}^{-1}$. Bottom panel: ice aggregates PSD with $r_{eff} = 30 \text{ cm}^{-1}$.

3.4.3 | Spectral radiance analysis

Cloud and aerosol properties described in Section 3.2 are used in a wide number of simulations to evaluate the impact of re-scaling methodologies, CA and SP, with respect to the full scattering solution for multiple scenarios.

The level of approximation when using a simplified approach instead of the FS solution is evaluated in terms of spectral radiance differences as:

$$\Delta I = I_X - I_{FS} \quad (3.18)$$

where X is either CA or SP. Radiances are reported in $mW/cm^{-1}m^2sr$ (hereinafter, radiance units – RU). The radiance differences are compared to the noise equivalent spectral radiance (NESR) specified for the FORUM mission, to evaluate the impact of the different simulation methods with a typical observational uncertainty. The FORUM goal NESR (FGN) is $0.4 mW/cm^{-1}m^2sr$ within the spectral region $200\text{--}800 cm^{-1}$, and $1.0 mW/cm^{-1}m^2sr$ outside [26]. Similarly, the differences in terms of spectral brightness temperature (BT) are also evaluated as

$$\Delta BT = BT_X - BT_{FS} \quad (3.19)$$

and expressed in Kelvin.

3.4.4 | Liquid water clouds

Low-level liquid water cloud spectra are computed for the four geolocations and for multiple values of cloud top height, r_{eff} , and OD as reported in Section 3.2.1. Figure 3.6 shows an example for a mid-latitude cloud layer with OD= 15, placed at $1.5 km$ height. The upper panel shows the FS spectral radiance for five effective radii, whereas the bottom panel shows the difference ΔI between the radiances computed using the CA and the FS solution for the same conditions. The FORUM noise is highlighted by the grey shaded area for comparison. At small and large wavenumbers, that is below about $350 cm^{-1}$ and above $1400 cm^{-1}$, ΔI is almost null. The main reasons are related to the large atmospheric opacity mostly due to the water vapor absorption, and the least amount of energy emitted in that portion of the spectrum. Thus, the assumptions on the adopted radiative transfer solution is irrelevant in these spectral regions. Similarly, the strong absorption due to the CO_2 band around $667 cm^{-1}$ masks the cloud effects on the top of the atmosphere radiance. It is noted that CA always overestimates the computed FS radiance with the only exception of a slight underestimation in the atmospheric window ($\sim 900 cm^{-1}$) for large effective radii. In the MIR region, only very small cloud particles ($r_{eff} \simeq 2 cm^{-1}$) do not allow a satisfactory approximation of the FS solution and the error is about twice the FGN. Significant discrepancies are observed at FIR wavenumbers, with a peak $\Delta I \simeq 3 \times FGN$ occurring at about $531 cm^{-1}$. For the case reported in the Figure, only for $r_{eff} \geq 10 \mu m$ the scaled approximation is within the FGN limit with respect to the FS.

A more complete picture of the level of accuracy of the CA method with respect to the FS solution is provided by Figures 3.7 and 3.8. In the Figures, ΔI and ΔBT at $1203 cm^{-1}$ and $531 cm^{-1}$ are shown for many atmospheric and water cloud conditions as a function of the cloud OD and r_{eff} . The selected wavenumbers are those where the largest MIR and FIR differences occur between the approximate method and the full scattering solution, in accordance with what is shown in Figure 3.6. The contour lines show ΔI values in RU, while the color scale highlights the ΔBT values only for ΔI larger than the FGN, that is $1.0 RU$ at $1203 cm^{-1}$ and $0.4 RU$ at $531 cm^{-1}$, delimited by the red contour line. Regions where ΔBT is smaller than the FORUM noise are in white.

Figure 3.7 demonstrates that using CA for computing top-of-the-atmosphere radiances in the presence of water clouds in the MIR is a valid approximation for most of the atmospheric

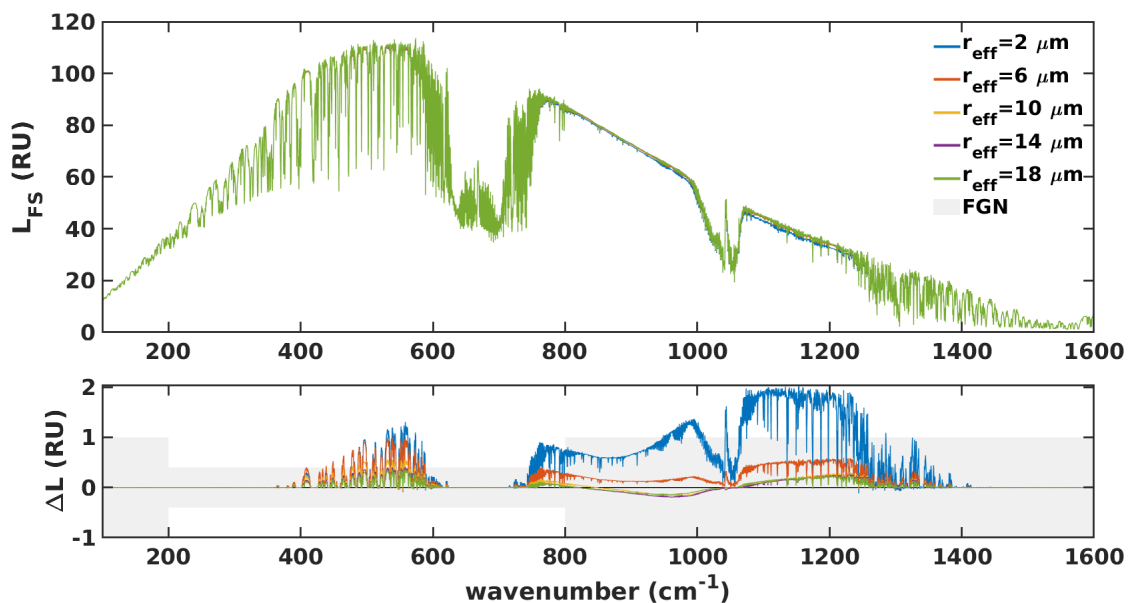


FIGURE 3.6: Top panel: top of the atmosphere FORUM spectral radiances computed with the FS approach for a 50°N atmosphere in the presence of a liquid water cloud layer, whose top is placed at 1.5 km and with $\text{OD}=15$. Bottom panel: radiance differences between CA and FS approaches for the same clouds as in the top panel. FGN is highlighted by a grey-shaded area.

and cloud conditions. Only in the presence of very small PSDs ($r_{\text{eff}} \lesssim 5\ \mu\text{m}$) differences larger than the FGN are observed. The differences are weakly dependent on cloud optical depths and mostly related to water droplet dimensions. Such small effective radii are anyway quite rare. Average liquid water cloud effective radii derived from MODIS AQUA L3 monthly products [90] for the selected geolocations and dates span over the range $11\text{--}20\ \mu\text{m}$.

In terms of radiance differences, the FIR spectral region (Figure 3.8) is comparable to what is found in the MIR. In fact, the level of approximation mostly depends on the considered PSD effective radius. Small effective radii cause a radiance overestimation that is larger than that obtained for the larger radii for each considered scenario. As noted for the MIR, the extent of CA with respect to the FS solution is weakly dependent on cloud OD, and ΔI remains almost constant over the considered OD range. Some variations are noticed for very small ODs and the cause is probably related to environmental conditions that are closer to a single scattering configuration, which is far from the assumption of isotropy that is made in the Chou approximation. Nevertheless, OD value close to unity is a very uncommon situation in case of water clouds. In fact, monthly mean optical depths at 900 cm^{-1} , derived from MODIS AQUA L3 products [48] for the same locations and time of the year considered in this study, mostly span over the range $4\text{--}18$.

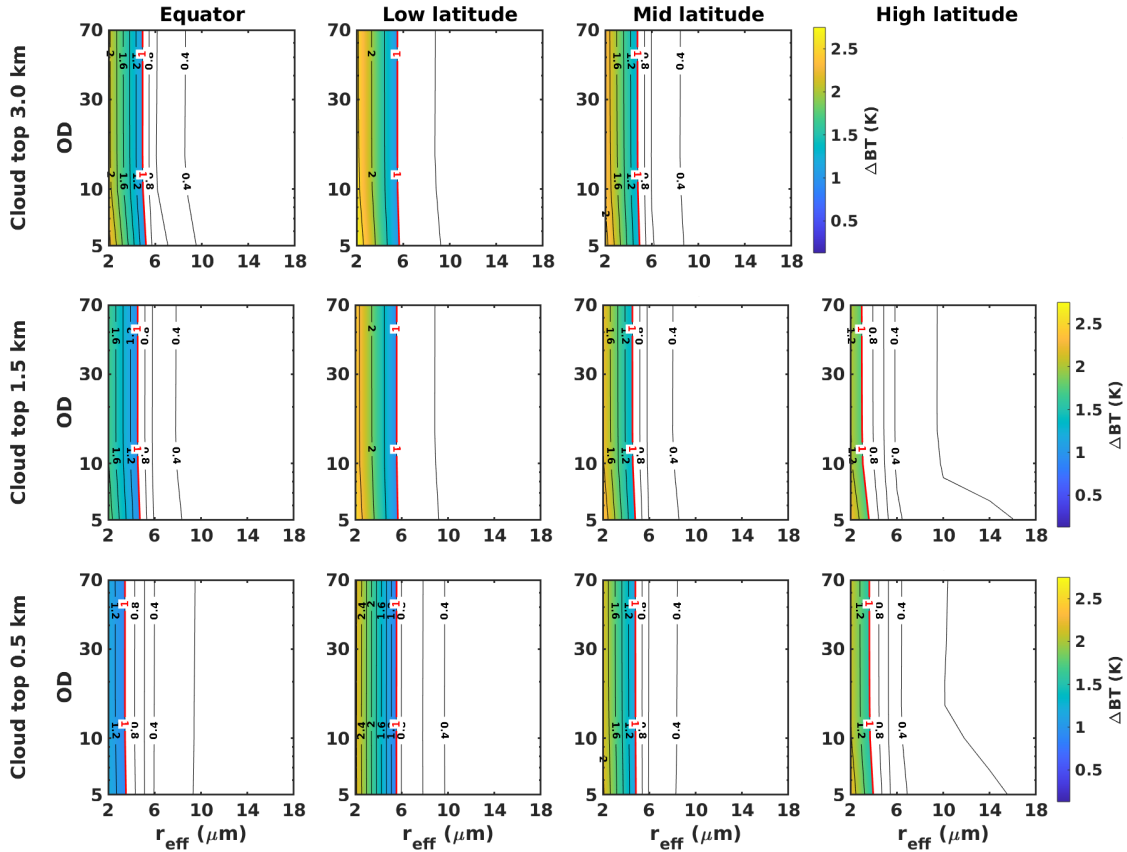


FIGURE 3.7: Radiance (ΔI , contour) and brightness temperature (ΔBT , color) differences between CA and FS approaches at 1203 cm^{-1} (MIR), for liquid water clouds. The white color indicates differences below the FORUM noise level, marked by the red contour line. Y-axes are in log scale.

At FIR, the simulated radiance differences between re-scaled and exact method are significant for almost all the cases which account for very dry atmospheric conditions. The precipitable water vapor amount above the cloud layers (Table 3.4) has an attenuating effect on cloud radiances since it is related to the upper atmospheric layer transmissivity. Moreover, it makes the atmosphere above the cloud layer more opaque, thereby reinforcing the credibility of the assumptions made by Chou concerning downward ambient radiation, as presented in 2.59. Thus, the higher the PWV above the cloud top level, the lower the radiance difference ΔI . The masking effect becomes very effective for PWV larger than about 4 mm . Thus, radiance differences increase with increasing the cloud top for a fixed latitude, as well as with increasing latitude for the same cloud top height. The CA solution is then accurate when low-level clouds and humid conditions are accounted for, and progressively degrades for drier conditions. In these latter cases, CA can provide overestimation, in terms of brightness temperature, of about 1 K at FIR wavenumbers for the worst configurations,

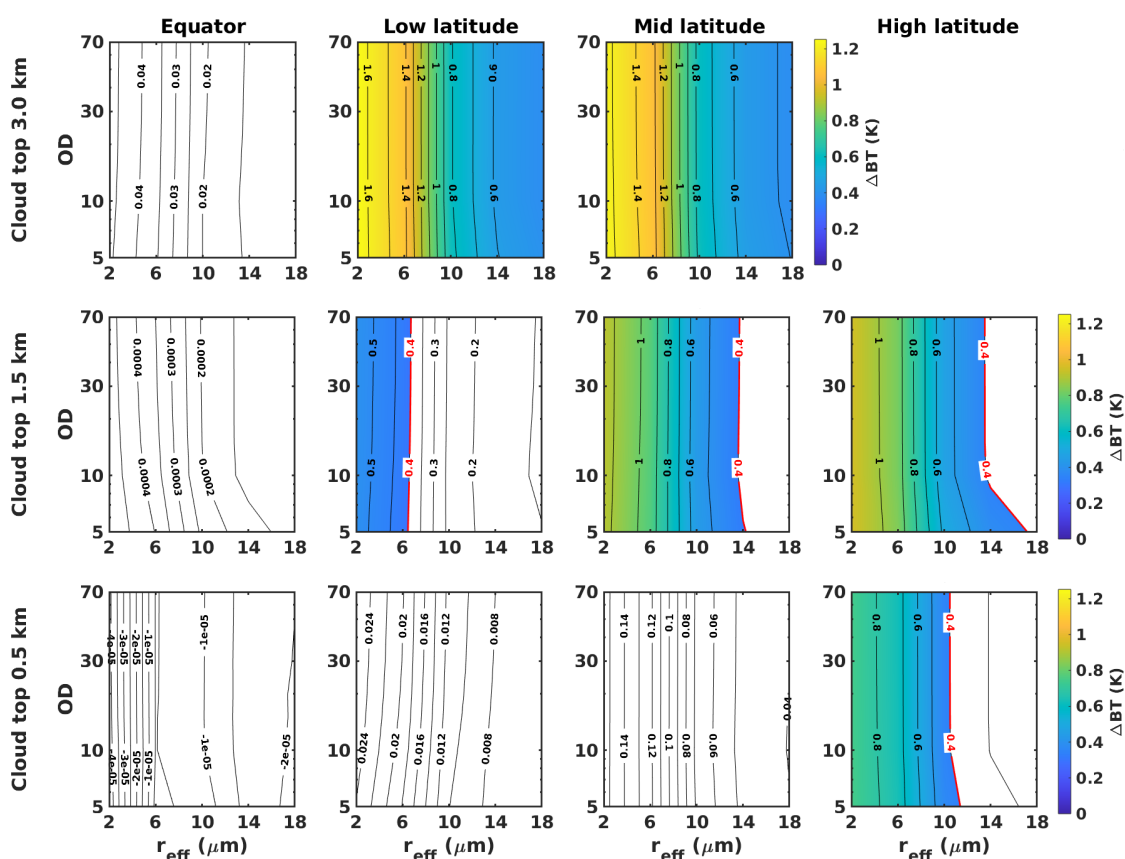


FIGURE 3.8: Radiance (ΔI , contour) and brightness temperature (ΔBT , color) differences between CA and FS approaches at 531 cm^{-1} (FIR), for liquid water clouds. The white color indicates differences below the FORUM noise level, marked by the red contour line. Y-axes are in log scale.

that is reached when considering very small water droplets.

As noted in Section 3.4.2, in the case of liquid water clouds the SP approach models very similar optical depths to those obtained using the CA solution. Since their analysis carries to the same conclusions obtained in the CA–FS case, the results of the comparison between the SP and FS radiances are here presented in the appendix A (Figures A.1 and A.2) without further comments.

3.4.5 | Ice clouds

As in the case of liquid water clouds, the spectral radiance differences between the CA method and the FS solution are computed also in the presence of ice clouds. One example is provided in Figure 3.9. In the upper panel of the Figure the top of the atmosphere radiance in the presence of a mid-latitude cirrus cloud (cloud top placed at 8 km and $OD=1$) is

TABLE 3.4: Precipitable water vapor in the atmospheric column above the case studies cloud top.

	Equator	Low latitude	Mid latitude	High latitude
Cloud top (km)	PWV (mm)	PWV (mm)	PWV (mm)	PWV (mm)
15.0	0.0033	0.0034	–	–
12.0	0.019	0.0089	0.0065	–
8.0	0.28	0.10	0.15	0.016
6.0	–	–	0.54	0.051
3.0	10.4	1.1	1.2	–
1.5	25.1	4.5	2.0	1.3
0.5	38.9	11.4	6.2	2.2

simulated using the full scattering solution for multiple assumptions on the PSD (r_{eff}). In the lower panel of the same Figure, the spectral radiance differences between the CA and FS solutions are shown for the same cloud cases reported in the upper panel. Results show that the largest residuals are found in two window regions: one in the MIR placed at 1100–1250 cm^{-1} and the other one in the FIR between 350 and 600 cm^{-1} . This last part of the spectrum becomes partially transparent for low concentrations of water vapor. Small PWV values are found in the atmospheric column above high-level clouds and at high latitudes, as reported in Table 3.4. In the same spectral region, specifically at about 410 cm^{-1} , a local minimum in the imaginary part of the refractive index of ice is found (see back at Figure 3.2), meaning that a minimum in the cloud absorption is present and scattering processes become important. Note that the radiance differences in the 350–600 cm^{-1} range are relevant, with respect to the FGN, also for the largest effective radii of the PSDs accounted for.

From the FIR and MIR window bands, two wavenumbers are selected in order to provide an assessment of the level of accuracy of the CA method for multiple atmospheric and ice cloud conditions. With reference to the lower panel of Figure 3.9, the largest ΔI occurs at 1203 cm^{-1} at MIR and at 410 cm^{-1} at FIR and thus the two wavenumbers are selected as illustrative. Figures 3.10 and 3.11 show the ΔI and ΔBT at 1203 cm^{-1} and 410 cm^{-1} for the four considered scenarios, at varying cloud altitudes and as a function of the cloud OD and r_{eff} . The OD axis (spanning from 0.03 to 30) is plotted in logarithmic scale so that the radiance and BT differences in the case of thin cirrus clouds (OD < 3) are highlighted. In Figure 3.10, the radiance and brightness temperature differences at 1203 cm^{-1} are shown. With the exception of cases considering very high clouds (cloud top higher than 12 km) with very small effective radii ($r_{eff} \lesssim 10$) and with OD at around 1, the computed ΔI and ΔBT values are very small. This is proven by the dominating white color in almost all the panels of the Figure, meaning that the CA–FS difference is less than the FORUM noise at that specific wavenumber. The result demonstrates that CA is an accurate approximation in the MIR both in the presence of thick ice clouds and in cirrus cloud conditions. Note that for

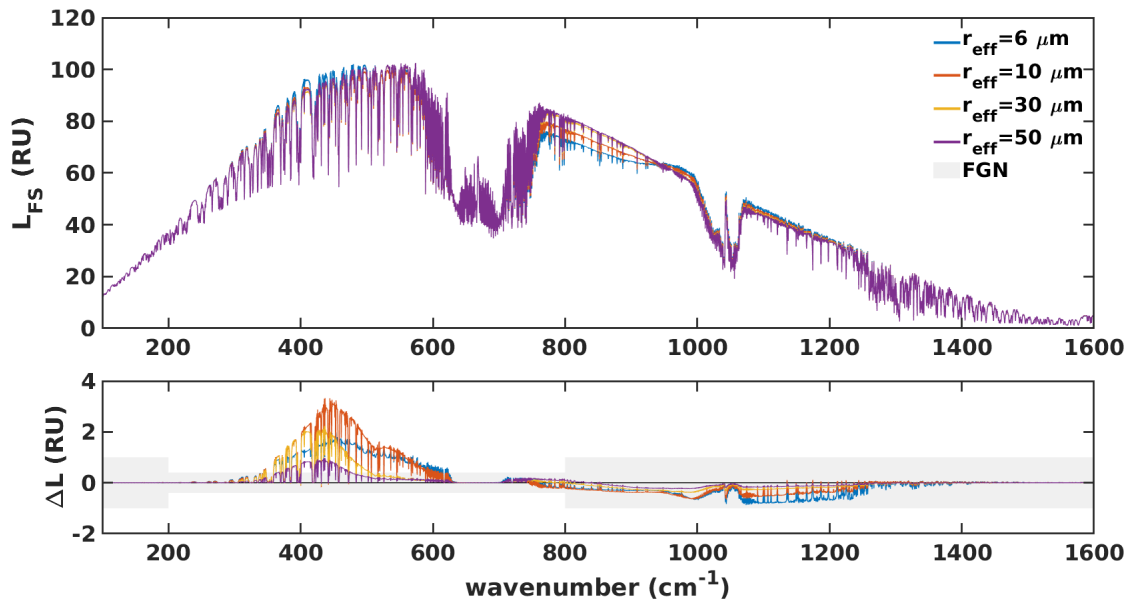


FIGURE 3.9: Top panel: top of the atmosphere FORUM spectral radiances computed with the FS approach for a 50°N atmosphere in the presence of an ice cloud layer, whose top is placed at 8 km height and with $\text{OD}=1$. Bottom panel: radiance differences between CA and FS approaches for the same clouds as in the top panel. FGN is highlighted by a grey-shaded area.

the same location and time of the year, the monthly mean r_{eff} derived from MODIS AQUA L3 products [48] is around $30\ \mu\text{m}$ when in the presence of ice clouds (including cirri). When simulations are performed at 410 cm^{-1} , the CA methodology brings relevant errors for OD larger than unity, as shown in Figure 3.11. In the Figure, ΔI and ΔBT values lower than FORUM noise (white areas) are observed for optically thin cirrus clouds almost independently of the assumed r_{eff} . As the cloud OD increases, the accuracy of the CA simulations degrades and the synthetic radiances are overestimated. The overestimation can be of the order of $8\text{--}10\text{ K}$ when OD are between 10 and 30, and for small effective radii ($r_{\text{eff}} \lesssim 10$). The ones reported in Figure 3.11 are the largest errors, in terms of radiance or BT, over the whole FORUM spectrum and show that the CA methodology is mostly inadequate to simulate FIR radiances in the presence of ice clouds with medium-large optical depths. What is shown in Figure 3.10 and 3.11 is obtained for ice clouds with a vertical extent of 0.5 km , corresponding to a single layer in the model. To evaluate if the computational differences between the full scattering solution and the scaling method may depend on cloud vertical extent, the simulations are repeated for multiple geometric thicknesses of the ice clouds: 1.5 , 3.0 , and 4.5 km , corresponding to 3, 6, and 9 layers in the model, respectively. The same scenarios and optical properties are considered, with the only difference in the cloud OD, which is distributed over a larger vertical extent. An example of the results is reported in Figure 3.12, corresponding to the scenario at 34°N and to an ice cloud with top altitude placed at 15

km. The simulations account for varying cloud thickness as reported on the top of the plots in the upper row. The Figure shows the radiance differences between simulations performed using the CA and the FS methodologies. The upper and lower rows refer to differences in the MIR (at 1203 cm^{-1}) and in the FIR (at 410 cm^{-1}) respectively.

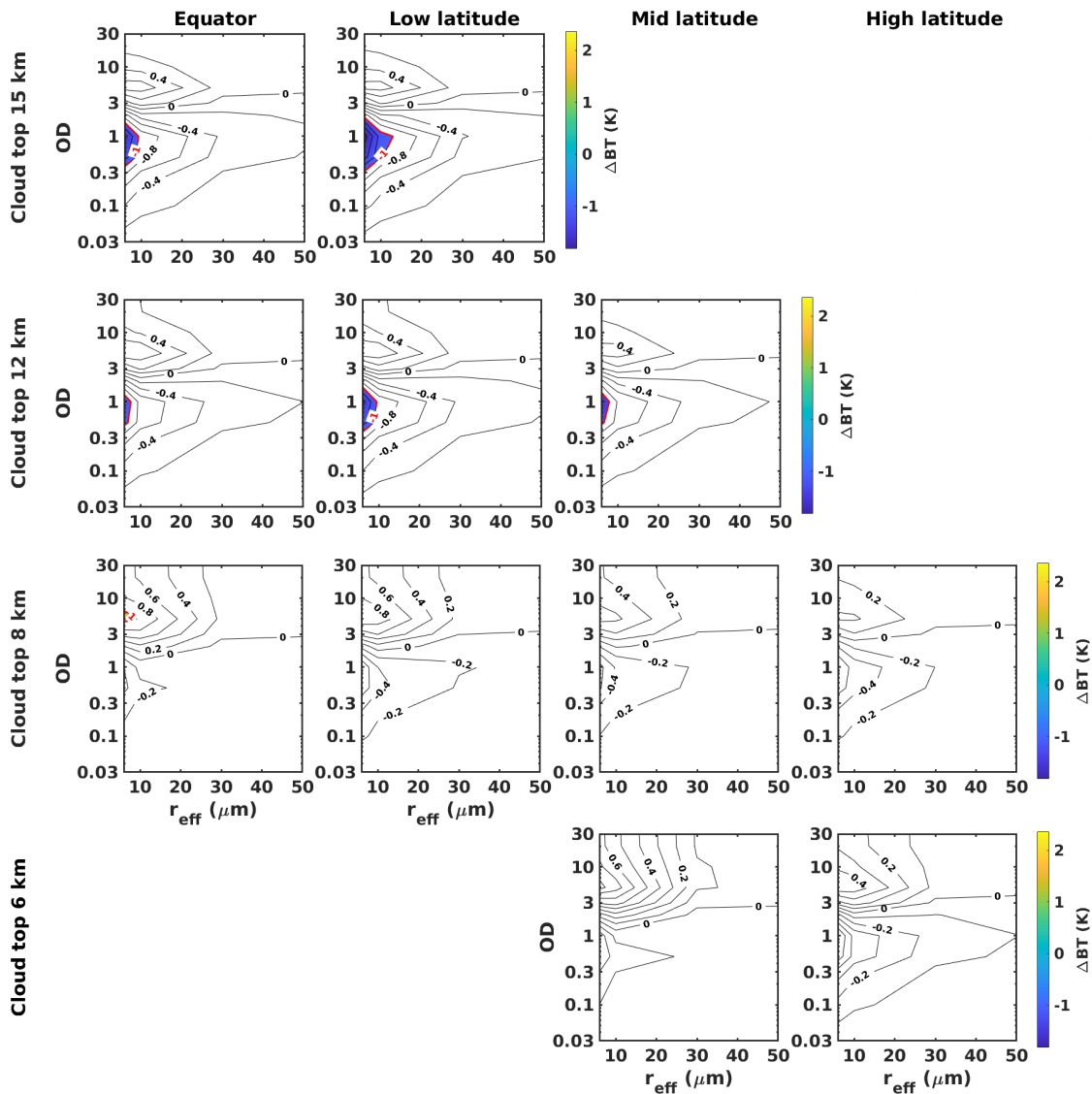


FIGURE 3.10: Radiance (ΔI , contour) and brightness temperature (ΔBT , color) differences between CA and FS approaches at 1203 cm^{-1} (MIR), for ice clouds. The white color indicates differences below the FORUM noise level (red contour line). Y-axes are in log scale.

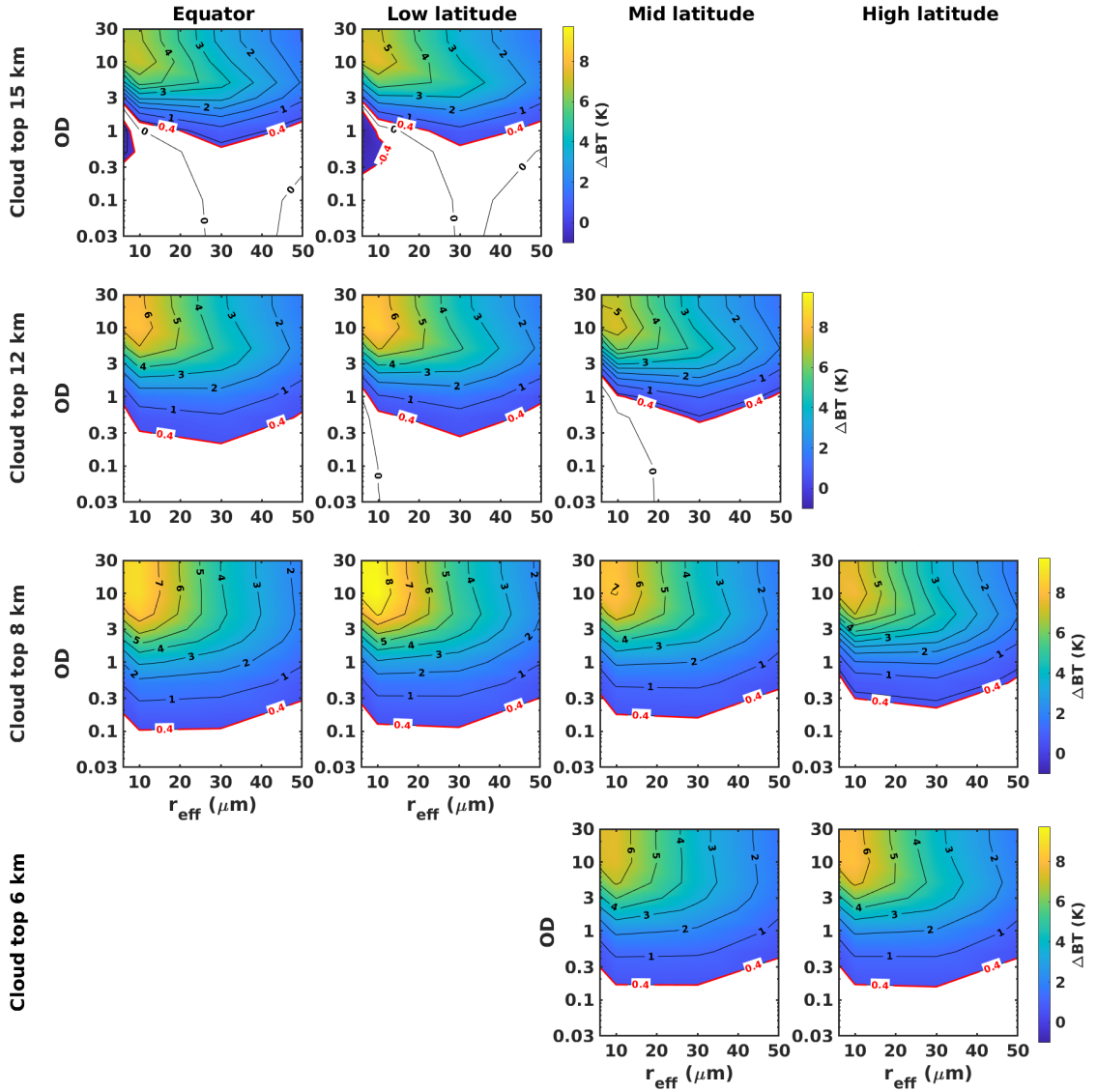


FIGURE 3.11: Radiance (ΔI , contour) and brightness temperature (ΔBT , color) differences between CA and FS approaches at 410 cm^{-1} (FIR), for ice clouds. The white color indicates differences below the FORUM noise level (red contour line). Y-axes are in log scale.

It is shown that, for optically thick ice clouds ($OD \geq 3$), the assumption on the geometric cloud thickness has a negligible effect on the computed radiance differences, both at MIR and at FIR. For optically thin ice clouds, the ΔI is independent of cloud thickness at MIR and shows very small variations at FIR when assuming a 0.5 km or a geometrically thicker cloud. The magnitude of the ΔI variations due to assumptions on cloud thickness is anyway negligible when compared to the variation due to cloud optical thickness or particles' effective dimensions. In conclusion, the results shown in Figures 3.10 and 3.11, obtained for a single

layer cloud of 0.5 km , can be assumed as representatives of clouds of any vertical extent. We noted earlier (Section 3.4.2) that apparent optical depths for extinction, in case of ice clouds, produced by the SP method are smaller than those obtained by using the CA approximation. Thus, it is expected that upwelling radiances in the presence of ice clouds are higher in the SP case than in the CA case. Since the CA solution is shown to overestimate the FS computations, the SP approximation is pejorative for the ice cloud conditions considered in this work. The SP–FS comparisons are reported in Appendix A.

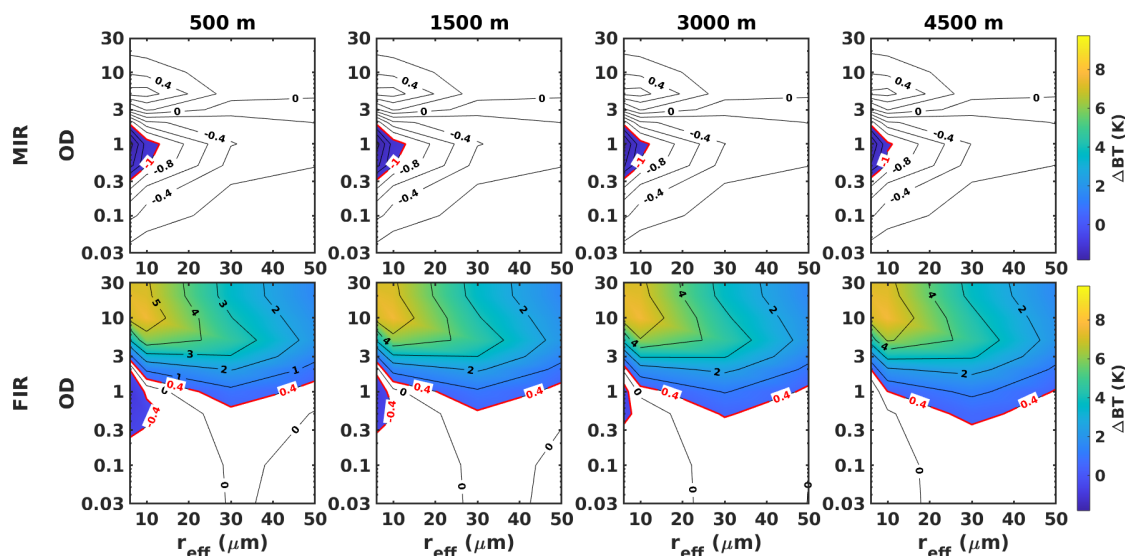


FIGURE 3.12: Radiance (ΔL , contour) and brightness temperature (ΔBT , color) differences between CA and FS approaches, at MIR (top panels, 1203 cm^{-1}) and FIR (bottom panels, 410 cm^{-1}) wavenumbers. All the panels refer to the same low latitude scenario (34°N), and to an ice cloud with top placed at 15 km . The cloud geometrical thickness is indicated on the top of the upper panels and ranges from 500 m to 4500 m . The white color indicates differences below the FORUM noise level, marked by the red contour line. Y-axes are in log scale.

3.4.6 | Aerosols

Two different aerosol scenarios are simulated, consisting of a layer of desert dust (dust-like) at low latitudes and a layer of volcanic dust at mid-latitudes. The two considered scenarios are case studies for typical desert and volcanic dust concentrations, thus not representative of extreme conditions. The aerosol optical properties are described in Section 3.2 and the layers features are summarized in Table 3.2. First, the spectral radiance differences with respect to the clear sky solution are evaluated to define which are the conditions that make the aerosol layers detectable. This also allows to quantify the FIR radiance sensitivity to the aerosol properties. Successively, the differences ΔI between the spectral radiances simulated using CA and FS configurations are computed for the observational conditions that

provide an aerosol signal, with respect to clear sky, larger than the FGN. Figures 3.13 and 3.14 show, in their respective upper panels, the differences between the clear sky solution and the aerosol-loaded scenarios for dust-like and volcanic particles respectively. Multiple ODs are accounted for, spanning over the observed ranges as discussed in Section 3.2.3. In Figures 3.13 and 3.14, the FGN is also plotted and highlighted by the grey-shaded area. With reference to the upper panel of Figure 3.13, it is noted that the dust-like signal is very small in the FIR part of the spectrum, and only aerosol loads with $OD \gtrsim 0.20$ are able to produce a signal larger than the FGN with respect to the clear sky. The impact of the dust-like aerosol on clear sky radiances is larger in the MIR where the FGN is exceeded for $OD \gtrsim 0.10$. The impact of CA re-scaling methodology is thus evaluated only for aerosol scenarios with $OD \geq 0.10$. The bottom panel of Figure 3.13 shows the differences ΔI between the radiances computed using the CA and the FS radiative transfer configurations. ΔI is almost null for wavenumbers below about 350 cm^{-1} and above 1400 cm^{-1} , mostly because of the atmospheric opacity and the low impact of the dust-like aerosol on up-welling radiances. At MIR, between 800 and 1000 cm^{-1} , the computational inaccuracies of the CA method become larger than the FGN only for OD larger than 0.2.

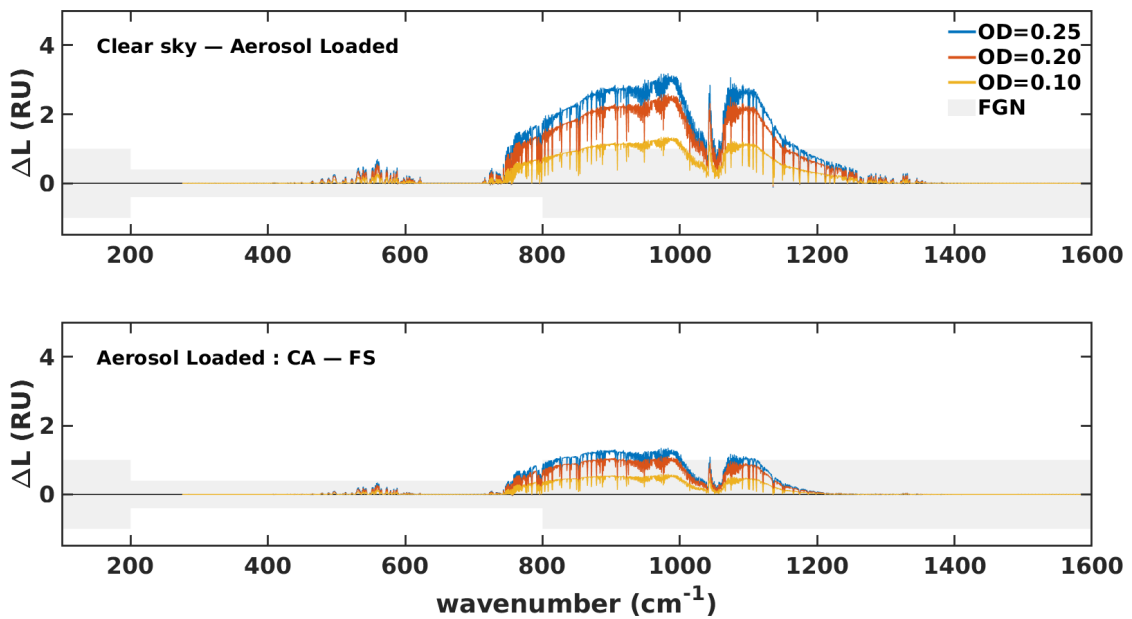


FIGURE 3.13: Top panel: spectral differences between FORUM-like observations in clear sky or in the presence of an aerosol-loaded atmosphere with dust-like particles. Bottom panel: differences between radiances computed using the CA and the FS approaches for the same aerosol cases presented in the upper panel. The simulations are obtained considering a 34°N atmosphere, and $r_{eff} = 2.0 \mu\text{m}$. FGN is highlighted by a grey shaded area.

The volcanic dust scenario (Figure 3.14) shows a larger impact on up-welling radiances with respect to the clear sky spectrum when compared to desert dust (upper panel of the

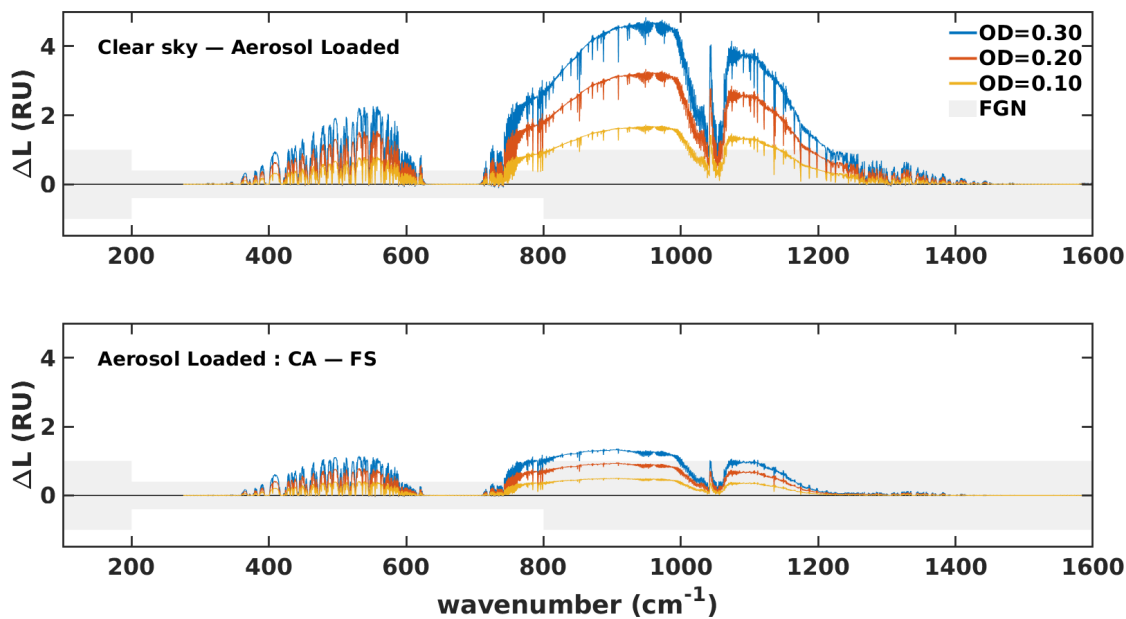


FIGURE 3.14: Top panel: spectral differences between FORUM-like observations in clear sky or in presence of an aerosol-loaded atmosphere with volcanic dust particles. Bottom panel: differences between radiances computed using the CA and the FS approaches for the same aerosol cases presented in the upper panel. The simulations are obtained considering a 50°N atmosphere, and $r_{eff} = 2.0 \mu\text{m}$. FGN is highlighted by a grey shaded area.

Figure). The impact is larger than the FGN for $\text{OD} \geq 0.10$ and is not negligible at FIR wavenumbers. Two main reasons lie behind the higher sensitivity of FIR and MIR radiances in the presence of volcanic dust. The first one is that the imaginary part of the refractive index of volcanic dust is larger than that of dust-like aerosols in the $250\text{--}1400 \text{ cm}^{-1}$ range (see back at Figure 3.2). Since the imaginary part of the refractive index is proportional to the absorption coefficient of the medium, the volcanic aerosol is more absorbing than dust-like aerosol for the same assumptions on aerosol concentration and micro-physics. The second reason is linked to the higher altitude and the higher latitudinal location of the volcanic layers. These last conditions imply a dryer and thus more transparent atmosphere. Note also that as the altitude of the volcanic aerosols increases, the peak of the emission from the layer moves towards the smaller wavenumbers due to a smaller temperature of the layer. For the present case, the layer top height is placed at 4.0 km in accordance with the literature case study taken from [53].

When evaluating the ability of the CA methodology to simulate the up-welling radiances in comparison to the FS method (lower panel of Figure 3.14) it is noted that at FIR wavenumbers the CA methodology is unsuitable for the volcanic layer with OD larger than 0.2 and produces significant simulation errors, of the order of the half of the change in the signal with respect to the clear sky case.

3.5 | Final considerations

The study introduced in this chapter presents two primary outcomes: (i) the comprehensive evaluation of the accuracy of two scaling methodologies, namely the Chou Approximation (CA) and the Similarity Principle (SP), for computing infrared spectral radiance under all-sky conditions; and (ii) an updated collection of back-scattering coefficients employed in the CA method, specifically tailored for low-level stratiform liquid clouds and ice clouds composed of aggregate crystals.

The two approaches (CA and SP) have been compared against Full Scattering (FS) calculations over a wide variety of water and ice clouds, and the results have been analyzed with a focus on the spectral interval 100 to 1600 cm^{-1} , which is the spectral range of the FORUM instrument. The analysis has also been extended to cover two aerosol types, desert dust and volcanic particles, which presented spectral signatures in the atmospheric window at 10 μm and in the FIR as well.

In comparing the two approaches, CA and SP, both have exhibited comparable performances when water clouds are considered. On the contrary, when applied to the simulation of cloudy ice fields, the CA has been found to perform better than SP in all conditions that have been analyzed in this study. The conclusion that we can draw is that SP is not a valid option to be used and implemented in fast-forward models for ice cloud simulations.

When Chou's approximation is taken into consideration, radiance calculations for both ice and water cloud scenarios exhibit a sufficiently good level of accuracy in the MIR. Nevertheless, when simulations of ice clouds in the FIR are considered, this solution yields to acceptable results only in the limit of OD below 0.1–1.0, depending on the atmospheric conditions and cloud altitude. In the case of aerosols, the situation is more varied. CA scaling methods provide reliable results when the optical depth is below 0.2, and the performance is better for desert dust than for volcanic aerosol.

In practice, this does not appear to be a significant limitation for an instrument like FORUM, which spans the spectral range from 100 to 1600 cm^{-1} and its main goal in terms of cloud observation is the characterization of cirrus clouds. At this regard, it is important to recall that the far-infrared region is particularly suitable for the identification of thin cirrus clouds and the derivation of their physical and optical properties [68]. The same clouds are almost transparent in the mid-infrared. In this respect, the results presented in this Chapter appear particularly promising for an instrument such as FORUM, because they imply that effective, fast-forward models can be developed and used to exploit the synergy between FIR and MIR to retrieve microphysical properties of water and thin ice clouds.

Modern satellite sensors stop their lower wavenumber to $\approx 640 cm^{-1}$, and in fact, all-sky fast forward models have been mostly developed for the mid-infrared (e.g., [1, 21, 80]). These results open the way to reliable, fast-forward models in the FIR, with the quality expected to retrieve liquid and thin ice water content profiles along with information about the corresponding effective radius. To conclude, when ice clouds are considered, the CA in the FIR

yields acceptable results only in the limit of OD below 0.1–1.0, whereas in the MIR, the approximation can be validly extended to thick clouds. Therefore, a comprehensive analysis of thin cirrus clouds is possible by resorting to CA-fast radiative transfer schemes, covering both FIR and MIR spectral ranges.

In perspective, the CA-based optical depth can be suitably parameterized through look-up tables as a function of LWC/IWC and effective radius. In effect, as a further output of this study, such a parametrization has been already developed for the fast-forward model σ -IASI ([1]). An all-sky σ -IASI spectrum over the whole FORUM spectral range (100 to 1600 cm^{-1}) takes ≈ 0.5 s to run on a personal computer platform, with Intel(R) Core(TM) i7-1065G7 CPU @ 1.30GHz. The forward model will allow us to check the whole FORUM sensitivity to the optical properties of clouds. Because of its independence of a given forward model, the same parameterization could be embedded in models such as those developed by [21, 80], to name a few, which could open the way to new all-sky fast forward models covering the infrared Earth emitted spectrum in the MIR.



4 | Tang's adjustment scheme and its application

4.1 | Errors in the scaling methods

The analysis performed in Chapter 3 proved that, if we are interested in computing FORUM-like spectrally resolved radiances, the application of scaling methodologies introduces errors that are generally acceptable in the MIR for most of the realistic cloud scenarios. On the other hand, when simulations of ice clouds in the FIR are considered, accurate results are obtained only in the case of optically thin clouds ($OD < 0.1-1$). The overall effect is an overestimation of the top-of-the-atmosphere upwelling radiance. This is particularly visible in the FIR when ice clouds are considered, mainly due to the optical properties of ice crystals and the elevated altitude of this class of clouds. These results are not completely unexpected: various authors observed the presence of overestimates in simulated upwelling fluxes when employing these scaling methodologies (e.g. [57, 106]).

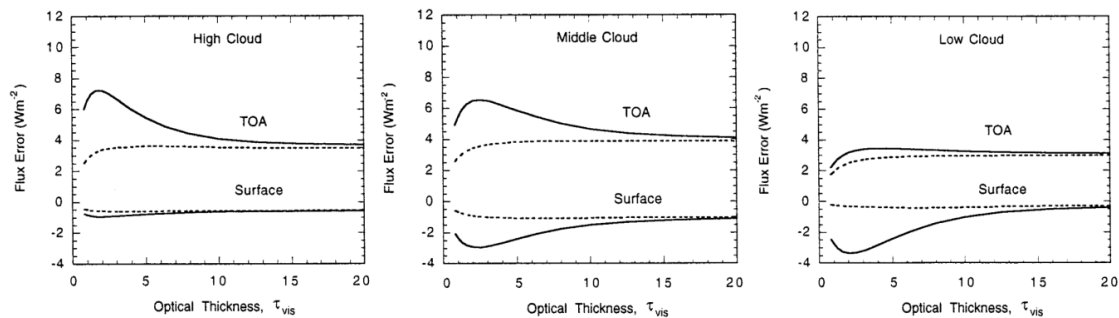


FIGURE 4.1: Errors in the TOA and surface fluxes for high, middle, and low clouds. Solid and dashed lines represent the case where scattering is neglected and the case where the scaling method proposed by Chou is implemented respectively. The calculations are obtained for a mid-latitude summer atmosphere. Figure adapted from Chou et al., (1999) [13] Figure 5.

A similar behavior is also documented by Chou et al., (1999) [13], who demonstrated that upwelling fluxes simulated with his scaled optical depths contain positive errors with respect

to the full-scattering solutions. Figure 4.1 summarizes these results, showing the differences between the approximate approaches (solid line for scattering neglected and dashed line for scaling methodology) and the full-scattering routine applied to irradiance calculations. The discrepancies are considered for different cloud optical thickness (τ_{vis} evaluated in the visible spectral region) and altitudes. In all the cases considered, fluxes are overestimated at the TOA.

It's important to note that fluxes are derived from spectral radiances through integration across both the entire observation hemisphere and the spectral region under consideration. The integration over the spectral region may introduce compensating errors when the sign of the error changes along the spectrum (see Figure 3.9 as an example).

Given the above, the results obtained in Chapter 3 for the computation of spectrally resolved upwelling radiances can be assumed in accordance with the previous study done on the flux simulations.



4.2 | Adjustment scheme for flux computations

A possible way to improve the scaling method proposed by Chou [13] is described in the work done by Tang et al. (2018) [106]. In their study, they present an adjustment routine specifically formulated to the computation of irradiances. In the following section, the derivation of the adjustment method for fluxes computation is described, and the main results obtained by Tang are highlighted.

The primary assumptions made by Chou when deriving his scheme are summarized in Equation 2.59, reposted here for ease of reading. Specifically, the assumption of constant isotropic ambient radiation within the two hemispheres:

$$I(\tau, \mu') = \begin{cases} B(\tau) & \text{if } \mu \cdot \mu' < 0 \\ I(\tau, \mu) & \text{if } \mu \cdot \mu' > 0 \end{cases}$$

where $I(\tau, \mu')$ is the ambient radiation, i.e. the radiance term that appears inside the multiple-scattering integral term in Equation 2.57.

While it may be reasonable to approximate the ambient radiation as approximately equal to incident radiance within the same hemisphere (when $\mu \cdot \mu' > 0$), substantial biases can emerge when assuming that ambient radiation is equivalent to the Planckian term (when $\mu \cdot \mu' < 0$). This is especially true for downward ambient radiation above a high cloud layer. In these scenarios, the real downward radiance is much weaker than the blackbody radiation emitted from the layer, leading to an overestimation of this term. This can be observed from Figure 4.1, where the upwelling flux errors for high and middle clouds present bigger overestimations with respect to lower clouds.

The main idea behind the adjustment scheme proposed by Tang is to reconsider the approximation for the downward ambient radiance when solving for the upward radiance, so that the

assumption for the ambient radiation within the two hemispheres takes the following form (for $\mu > 0$):

$$I(\tau, \mu') = \begin{cases} \langle I_d \rangle & \text{if } \mu \cdot \mu' < 0 \\ I(\tau, \mu) & \text{if } \mu \cdot \mu' > 0 \end{cases} \quad (4.1)$$

where $\langle I_d \rangle$ is a suitable quantity. It can be asserted that, according to the mean value theorem, there exists a precise value for $\langle I_d \rangle$ ensuring the accuracy of the backscattering contribution. However, the direct retrieval of this quantity from the radiation field is not possible, given our lack of knowledge about the radiation field itself.

In a radiative transfer model, when we are solving a Schwarzschild-like equation, it is a common practice to compute first the downward radiation from the top of the atmosphere to the surface. Then, the upward radiation is calculated from the surface, layer by layer until the TOA. This means that, when computing the upwelling radiance, we already have some information about the downward radiance, which can be used to describe the ambient downward radiation. The adjustment scheme proposed by Tang exploits this independence between the downwelling and upwelling solution to assume:

$$I(\tau, \mu') = \begin{cases} \langle I_d \rangle \simeq I(\tau, -\mu) & \text{if } \mu' < 0 \\ I(\tau, \mu) & \text{if } \mu' > 0 \end{cases} \quad (4.2)$$

when we are solving for the upward radiances, i.e. $\mu > 0$. Using the expression 4.2 for the calculation of the upward radiance and the Chou assumptions for the downward radiance, and following what already done in Section 2.3.2, it is possible to write the radiative transfer equation in the form:

$$\begin{cases} \mu \frac{dI(\tau, \mu)}{[1 - \tilde{\omega}(\tau)(1 - b(\tau))]d\tau} = I(\tau, \mu) - B(\tau) & \text{if } \mu < 0 \\ \mu \frac{dI(\tau, \mu)}{[1 - \tilde{\omega}(\tau)(1 - b(\tau))]d\tau} = I(\tau, \mu) - B(\tau) - \frac{\omega(\tau)b(\tau)}{1 - \tilde{\omega}(\tau)(1 - b(\tau))} [I(\tau, -\mu) - B(\tau)] & \text{if } \mu > 0 \end{cases} \quad (4.3)$$

In this formulation, the equation governing upwelling radiation includes an additional non-homogeneous term. This term can be interpreted as a correction factor for the backscattering contribution. From a mathematical perspective, Equation 4.3 remains a first-order linear differential equation, given the known value of downward radiance $I(\tau, -\mu)$ for each level τ . We can exploit the properties of this class of equations to express the solution for the upward radiance at level τ_0 as the sum of two contributions:

$$I(\tau_0, \mu) = I^c(\tau_0, \mu) + I^{ss}(\tau_0, \mu) \quad (4.4)$$

where $I^c(\tau_0, \mu)$ is the solution proposed by Chou [I3] and $I^{ss}(\tau_0, \mu)$ the Tang adjustment term (as in the original paper, the superscript *ss* stands for "specific solution"), obtained from the following form:

$$\mu \frac{dI^{ss}(\tau, \mu)}{[1 - \tilde{\omega}(\tau)(1 - b(\tau))]d\tau} = I^{ss}(\tau, \mu) - \frac{\omega(\tau)b(\tau)}{1 - \tilde{\omega}(\tau)(1 - b(\tau))} [I(\tau, -\mu) - B(\tau)] \quad (4.5)$$

Due to the vertical discretization generally adopted in the radiative transfer models, it is convenient to express the correction for a single homogeneous layer. Let's consider a generic layer between the j -th and the $(j + 1)$ -th level as shown in Figure 4.2.

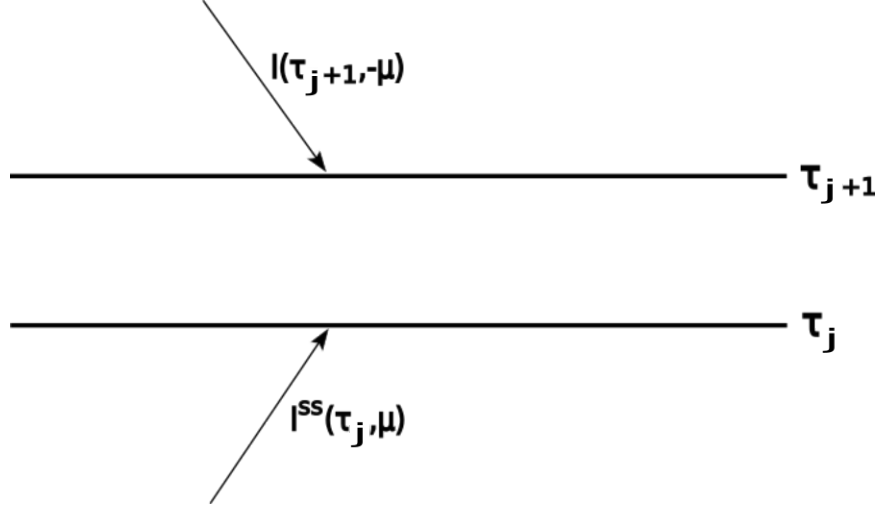


FIGURE 4.2: Single layer representation assuming plane-parallel approximation. The quantity τ_j represents the optical depth from the top of the atmosphere to the level j .

It is possible to solve Equation 4.5 for $\tau \in [\tau_{j+1}, \tau_j]$, noting that boundary conditions for a single layer correction requires that $I^{ss}(\tau_j, \mu) = 0$. An explicit form for the downward radiance term $I(\tau, -\mu)$ can be calculated from Equation 4.3. To simplify the problem, we can assume homogeneous layers with constant temperature, i.e. $B(\tau) = B_{j+1}$ for $\tau_{j+1} \leq \tau < \tau_j$. Given this assumption, we have that the downward radiation within the layer is described by:

$$I(\tau, -\mu) - B_{j+1} = [I(\tau_{j+1}, -\mu) - B_{j+1}] e^{-\frac{[1-\tilde{\omega}(1-b)](\tau-\tau_{j+1})}{\mu}}; \quad \mu > 0 \quad (4.6)$$

Where this solution is obtained from Equation 4.3 for $\mu < 0$. Using this form for the downward radiance in Equation 4.5, the correction term for the single layer becomes:

$$\begin{aligned} \mu \frac{dI^{ss}(\tau, \mu)}{[1-\tilde{\omega}(1-b)]d\tau} = & I^{ss}(\tau, \mu) + \\ & - \frac{\tilde{\omega}b [I(\tau_{j+1}, -\mu) - B_{j+1}]}{1-\tilde{\omega}(1-b)} e^{-\frac{[1-\tilde{\omega}(1-b)](\tau-\tau_{j+1})}{\mu}}; \quad \mu > 0 \end{aligned} \quad (4.7)$$

And its solution can be expressed as:

$$I^{ss}(\tau_{j+1}, \mu) = \frac{1}{2} \frac{\tilde{\omega}b}{1 - \tilde{\omega}(1 - b)} \left[[I(\tau_{j+1}, -\mu) - B_{j+1}] + \right. \\ \left. - [I(\tau_{j+1}, -\mu) - B_{j+1}] e^{-2 \frac{[1 - \tilde{\omega}(1 - b)](\tau - \tau_{j+1})}{\mu}} \right]; \quad \mu > 0 \quad (4.8)$$

Where $\tilde{\omega}$ and b are optical properties of the homogeneous layer. The form expressed in Equation 4.8 represents the correction for the $(j + 1)$ -th layer. To calculate the overall correction for a vertically discretized atmosphere with N layers, we must sum the contributions from each layer, each weighted by the transmissivity from that layer to the observer. Assuming an observer located at the top of the atmosphere, the total correction can be expressed as follows:

$$I_{tot}^{ss}(\mu) = \sum_{n=1}^N I^{ss}(\tau_j, \mu) e^{-\frac{[1 - \tilde{\omega}_j(1 - b_j)]\tau_j}{\mu}} = \sum_{j=1}^N I^{ss}(\tilde{\tau}_j, \mu) e^{\tilde{\tau}_j/\mu} \quad (4.9)$$

Where $\tilde{\tau}_j$ is the scaled optical depth for the j -th layer as defined in Equation 2.64. This correction term $I_{tot}^{ss}(\mu)$ is basically negative, and reduces the overestimation for the fluxes computation in the presence of clouds or aerosols.

Tang, in his treatise [106], suggests to use an iterative process to reach a better accuracy. After determining the adjusted solution for upward radiance, this information can be utilized to calculate an adjustment term for downward radiance. Subsequently, this adjustment can be applied to refine the upwelling radiation once more.

The main drawback associated with employing this iterative approach is the increase in computational time. Since the main reason to use this class of scaling methods (scaling and adjusted scaling methods) is to save computational time, the use of the iterative approach may be inconvenient. An alternative suggested by the authors is to optimize the scale of the adjustment term described by 4.8 based on simulations. Specifically, for irradiance computations with the Chou adjusted scheme, the authors suggest to replace the 0.5 coefficient with a 0.3 coefficient. An example of application algorithm for the Tang adjustment scheme is given in Figure 4.3.

In the following part of this section, some of the results obtained by the authors for the flux calculations are summarized. The presented results are not exhaustive, and the reader is encouraged to refer to the original work by Tang et al. [106] and the assessment on longwave radiative transfer models by Kuo et al. [57] for further information.

The analysis presented by the authors is mainly based on simulations. The longwave radiation model, RRTM [49], is used to implement all the approximate solutions. The model allows for a single or multiple (1–4) angles radiance calculations over 16 spectral bands (from 10 to 3250 cm^{-1}), from which, irradiance can be obtained through integration (e.g. Gaussian quadrature). In this review, only the results concerning the Chou scheme are considered. The simulated scenarios are obtained starting from six climatological atmospheric profiles (U.S. Standard Atmosphere, 1976 [112]) and using multiple ice cloud particle models (spherical ice particle [45], surface-roughened single-hexagonal-column [31], eight-hexagonal-column

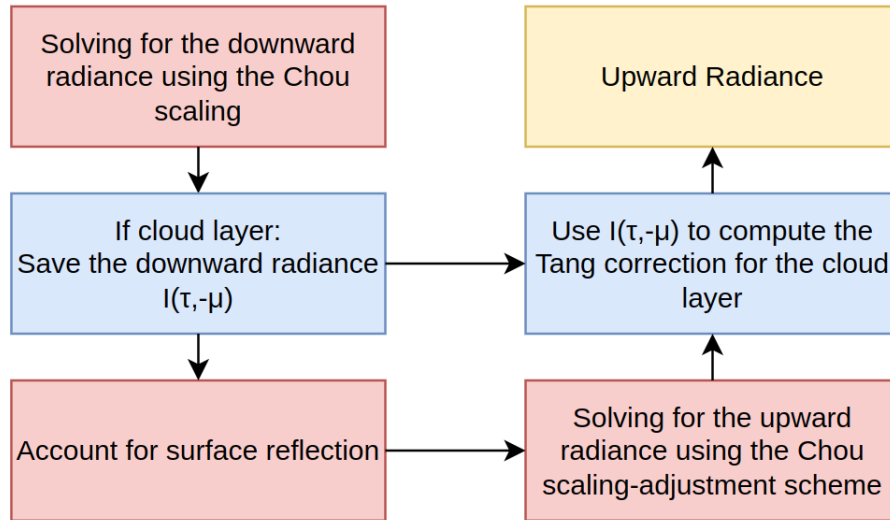


FIGURE 4.3: Example of adjustment scheme algorithm flowcharts

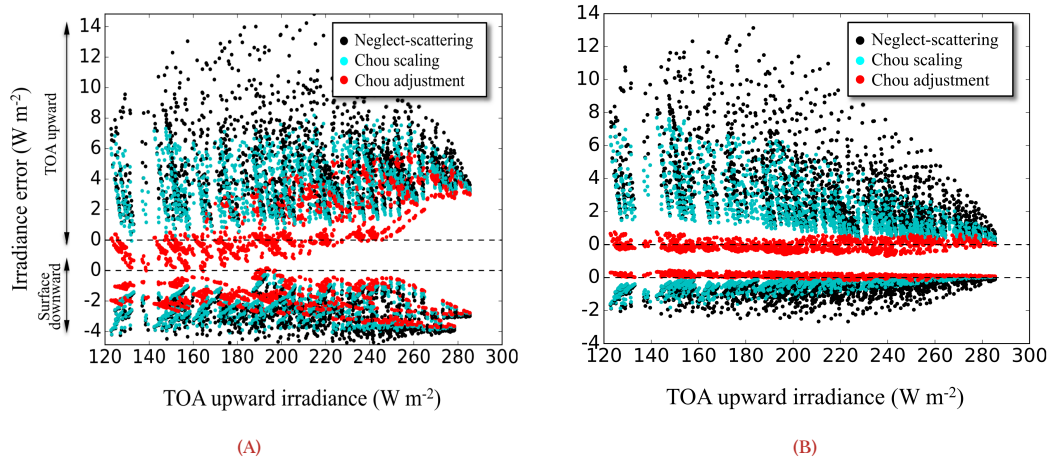


FIGURE 4.4: Error of TOA upward and surface downward irradiances vs reference TOA upward irradiance scatterplot of three schemes: neglect scattering (black), Chou scaling (cyan), and Chou-Tang adjustment (red). The results are presented for 1 integration point (A) and for 3 integration points (B). Adapted from Tang et al., (2018) [106].

aggregate [122], and the two-habit model consisting of a surface-roughened single-hexagonal-column and a 20-column aggregate [91]). The ice clouds are simulated at different altitudes and with different parameters (OD and r_{eff}). Finally, the surface emissivity is assumed to be unity.

RRTM equipped with the DISORT solver (16-streams) is used as the reference model. The results are here summarized in Figure 4.4. The differences between the three schemes (neglect-scattering, Chou scaling and Chou adjustment) and the reference solution are shown for both upwelling and downwelling irradiances. In the Chou adjustment solution, the coefficient 0.5 in 4.8 is replaced with 0.3, as mentioned earlier. The results are derived by considering either a single integration point (A) or three integration points (B), corresponding to one or three radiance calculations, respectively. Although generally superior to the other two methodologies, the Chou adjustment, when applied with a single integration point, still exhibits significant errors. On the other hand, when multiple integration points are considered, the adjustment scheme is capable of effectively correcting both the upwelling and downwelling irradiances. The authors demonstrated that implementing the adjustment scheme is effective also in reducing errors in the vertical average heating rate.

4.3 | Extension of adjustment schemes for upwelling radiances computation

Both Chou and Tang's schemes have been developed for fluxes calculation, and the assumption that they can be directly applied to spectral radiance computations should be considered with caution. A clear sign that these scaling methods are designed for irradiances can be found in the definition of the backscattering parameter b introduced by Chou et al, [13] and described in Equation 2.61 (provided here for clarity).

$$b = \frac{1}{2} \int_0^1 \int_{-1}^0 P(\mu, \mu') d\mu' d\mu = \frac{1}{2} \int_{-1}^0 \int_0^1 P(\mu, \mu') d\mu' d\mu$$

This quantity, which can be interpreted as the backscattered fraction for isotropically incident radiation, is integrated over the entire observation hemisphere. Specifically, the same quantity naturally emerges in the derivation of the two-stream approximation¹, proving its close relation with the flux calculations. J. A. Coakley Jr. and Petr Chylek (1975) [17], along with the study by W. J. Wiscombe and G. W. Grams (1976) [119] offer an in-depth analysis of this parameter and its application in the computation of two-stream fluxes.

The radiances obtained using the Chou scaling are meant to be calculated over a set of observational directions, μ , and then integrated to obtain the irradiance (e.g. using an n -points Gauss quadrature). When our focus is on obtaining radiances along a specific direction, μ , the backscattering parameter, b , must be interpreted as an average quantity, describing the mean fraction of radiation backscattered in the upward/downward direction. Additionally,

¹The backscattering parameter b arises automatically from the derivation of the Schuster-Schwarzschild two-stream approximation, where the ambient radiation is assumed to be hemispherically isotropic [119].

the methodology's applicability and accuracy must be assessed, as done in Chapter 3.

In the same way, the adjustment term proposed by Tang et al., (2018) [106], and described by Equation 4.8, is meant to be integrated over a set of observation directions, μ , in order to obtain a correction for the fluxes. This appears to be clear also from the results presented by the authors of the scheme. With reference to Figure 4.4, the corrections prove to be more reliable when multiple integration points are considered.

For these reasons, the direct application of Tang's adjustment to spectral radiance calculations with specific observation geometry (such as nadir-looking geometry, particularly important for satellite application) may result in significant errors. However, following a similar approach used by the authors for fluxes computation, we can generate a correction coefficient $k(\mu)$ to optimize the application of the scheme to radiance calculations. This coefficient replaces the 0.5 coefficient in Equation 4.8:

$$I^{ss,k}(\tau_{j+1}, \mu) = k(\mu) \frac{\tilde{\omega}b}{1 - \tilde{\omega}(1 - b)} \left[[I(\tau_{j+1}, -\mu) - B_{j+1}] + [I(\tau_{j+1}, -\mu) - B_{j+1}] e^{-2 \frac{[1 - \tilde{\omega}(1 - b)](\tau - \tau_{j+1})}{\mu}} \right]; \quad \mu > 0 \quad (4.10)$$

The coefficient $k(\mu)$ is obtained from simulation. When spectral radiance calculations are considered, its value varies with both the direction, μ , and the wavenumber. For irradiances, the authors set it to $k(\mu) = k = 0.3$.

4.3.1 | Calculation of $k(\mu)$

To extend the applicability of Tang's adjustment to spectrally resolved radiance computations, a correction coefficient $k(\mu)$ is computed through numerical simulations. This coefficient is then employed to replace the existing 0.5 coefficient in 4.8 as shown in Equation 4.10, resulting in improved accuracy of the simulated radiances. Since the application of Chou's scaling methodologies introduces errors that are generally acceptable in the MIR for most of the realistic cloud scenarios [74], in this section, the Tang adjustment is applied only for the FIR part of the spectrum.

The value of $k(\mu)$ depends on the observation direction, μ . Moreover, due to the spectral dependency of the problem, a general description of this coefficient should depend also on the wavenumber. In the present study, we will adopt an averaged representation of $k(\mu)$ for the entire FIR range (100-667 cm^{-1}), and assuming a nadir-looking geometry ($\mu = 1$).

A set of $k(\mu)$ is produced starting from accurate simulations obtained with the DISORT model [103]. We consider three climatological atmospheric profiles taken from the Level 2 Initial Guess (IG2) database (high- mid- and low-latitude) version 5.7 [92]. We perform nadir-looking simulations for each profile considering different cloud altitudes, optical depths, and effective radii. Then, for each case, we compute the residuals between the DISORT solution, I_{FS} , and Chou's solution I_{CA} . For the same scenarios, the Tang correction term is computed as described in Equation 4.9, using a σ -IASI model module [1].

Following a similar approach to the one described in Chapter 3, each of the considered solutions (FS, CA, and Tang's correction term) is obtained using the same simulation chain of

radiative transfer models. Figure 4.5 gives a representation of this models chain. The first part of the model chain in consists of the LBLRTM input/output stream. In this study we utilized the LBLRTM model version v12.13, equipped with the continuum model MT_CKD v3.6 and the spectroscopic database AER v3.8.1, built from HITRAN 2016. The optical depths produced are then used as direct input for both the DISORT routine and the σ -IASI module. For this reason, due to the nature of the σ -IASI model, the vertical grid set in LBLRTM to characterize the atmospheric profiles is the same one used by σ -IASI.

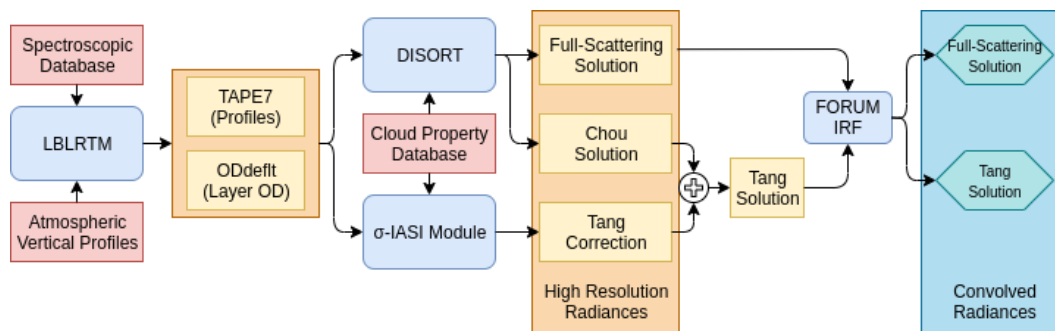


FIGURE 4.5: Flow diagram of the code chain used for the radiative transfer simulations. Databases are in red boxes, codes are in blue and outputs are in yellow. The two final solutions are highlighted in green and are convolved to a FORUM-like resolution. See text for more details.

Table 4.2 presents the ranges for the cloud parameters employed in the simulations. The cloud particle habits and optical properties utilized in this study remain consistent with those detailed in Chapter 3.

TABLE 4.1: Values and ranges of the cloud parameters used in the selected case studies.

Particle type	PSD type	r_{eff} (μm)	Top Height (km)	OD ($900 cm^{-1}$)
Liquid water	lognormal ($\sigma=0.38$)	4–30	0.5–3	1–50
Ice Aggregates	gamma ($\mu=7$)	4–50	6–15	1–50

The discrepancies between the Chou solution and the reference solution are calculated for each scenario considered:

$$\Delta I_V(\mu) = I_{V,CA}(\mu) - I_{V,FS}(\mu) \quad (4.11)$$

Where the dependence on the wavenumber and on the observational direction is made explicit. Along with ΔI , the adjustment term, I_{tol}^{ss} , is computed as shown in Equation 4.9. The value for $k(\mu)$ is then computed as:

$$k(\mu) = \frac{1}{2} \frac{\int_{\nu_1}^{\nu_2} \Delta I_\nu(\mu) d\nu}{\int_{\nu_1}^{\nu_2} I_{\nu,tot}^{ss}(\mu) d\nu} \quad (4.12)$$

where ν_1 and ν_2 define the spectral interval of interest. With the definition given in 4.12, the coefficient can be interpreted as the average value over the spectral region defined by ν_1 and ν_2 . In this study we assumed the following values: $\nu_1 = 100 \text{ cm}^{-1}$ and $\nu_2 = 667 \text{ cm}^{-1}$. As our focus lies in applying these routines to simulate FORUM-like measurements, we assume a nadir-looking geometry in the simulations, where $k(\mu = 1) = k$. Nevertheless, extending the simulation to accommodate various observational angles is a straightforward process. Figure 4.6 shows the values of these coefficients for all the simulations (green dots) performed considering a nadir-looking geometry. The coefficients are parameterized as a function of the effective radius of the particle size distribution. Specifically, they are interpolated with the following function:

$$k(r_{eff}) = P_0 + P_1 \frac{1}{r_{eff}} + P_2 \frac{1}{r_{eff}^2} \quad (4.13)$$

The interpolated function is shown as a solid black line in the same panels. The values of the coefficients P_i for ice (column aggregates) and water clouds are listed in Table 4.2.

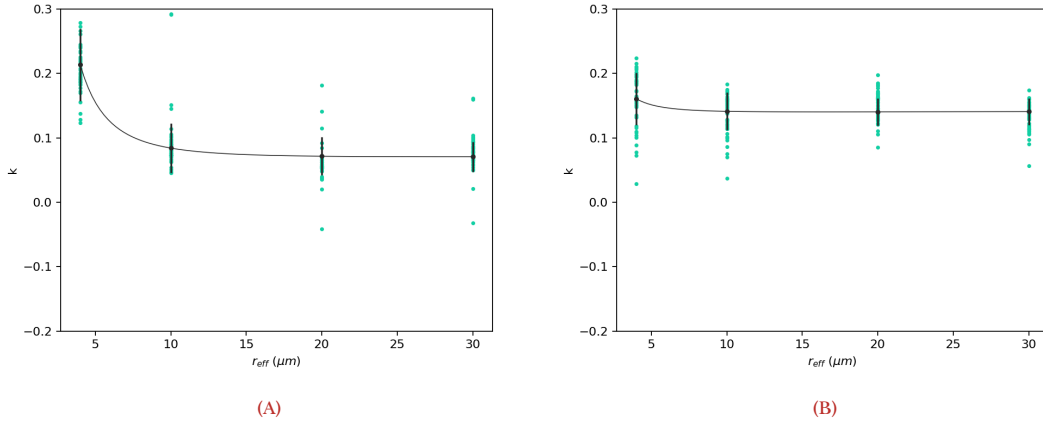
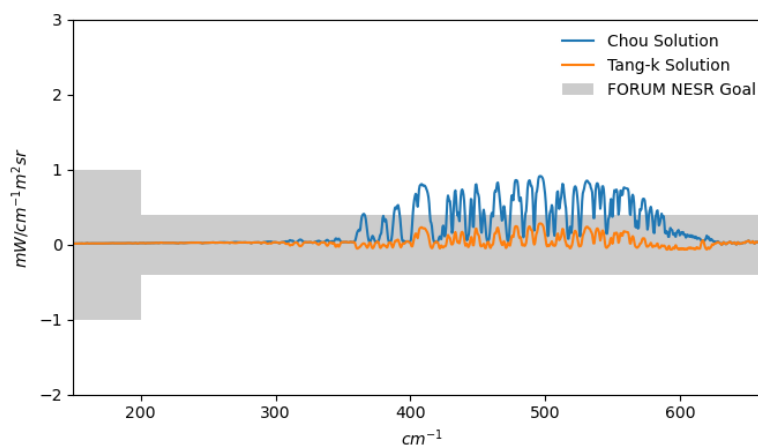


FIGURE 4.6: Coefficients for water spheres (A) and column aggregates (B) as a function of the effective radius (μm). The black solid line represents the parameterization as a function of the effective radius of the PSD.

Similarly to what done in the assessment of the accuracy for the scaling methodologies, presented in Chapter 3, the effectiveness of the newly parameterized coefficient k for Tang's adjustment routine is tested over a wide set of simulations, considering different climatological profiles from those used for the calculations of k .

TABLE 4.2: Values of the coefficients P_i used in the expression 4.13.

Particle type	P_0	P_1	P_2
Liquid water	0.074	-0.206	3.055
Ice Aggregates	0.143	-0.069	0.570


FIGURE 4.7: Radiance differences between Chou's solution (blu line) and Tang adjusted solution (orange line) with respect to the reference solution (DISORT) for a water cloud scenario. Tang correction routine is applied considering a suitable k coefficients as described above. The water cloud is described by an $OD = 5.0$, $r_{eff} = 10 \mu m$ and its top altitude is 3 km.

Figures 4.7 and 4.8 show two examples for the application of the Tang correction routine using the k coefficients previously computed (called Tang-k solution). The radiance differences are computed with respect to the DISORT reference solution, and are obtained considering a water cloud (with $OD = 5.0$ and $r_{eff} = 10 \mu m$) and a cirrus cloud (with $OD = 1.0$ and $r_{eff} = 30 \mu m$) respectively.

From the FIR window bands, the wavenumbers 410 cm^{-1} is selected in order to provide an assessment of the level of accuracy of the Tang-k solution for multiple atmospheric and ice cloud conditions. The atmospheric profile, and the cloud positions considered are presented in Figure 4.9. Figure 4.10 illustrates the differences between the tested method and the complete-scattering solution. Additionally, the errors associated with the Chou solution are depicted in the same figure, providing a basis for comparison. The green dashed-dotted line represents the parameterization of the effective radius of the ice cloud as a function of temperature and total ice water content. This parameterization is based on Sun and Rikus' (1999) work, which was subsequently revised by Sun (2001) [105].

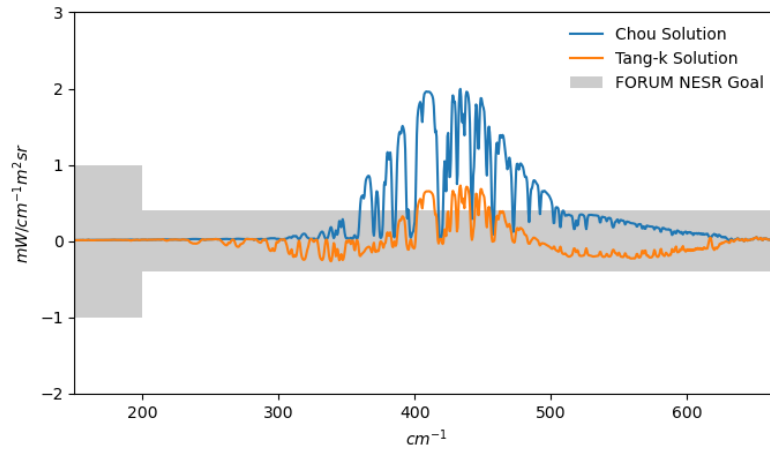


FIGURE 4.8: Radiance differences between Chou's solution (blue line) and Tang adjusted solution (orange line) with respect to the reference solution (DISORT) for an ice cloud scenario. Tang correction routine is applied considering a suitable k coefficients as described above. The ice cloud is described by an $OD = 1.0$, $r_{eff} = 30 \mu m$ and its top altitude is 8 km.

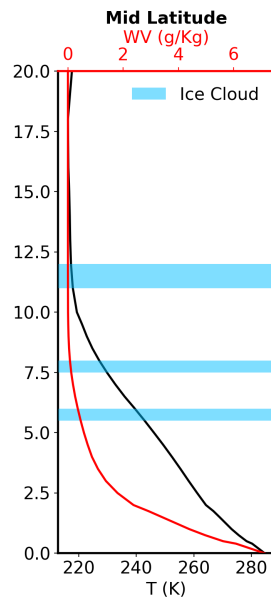


FIGURE 4.9: Vertical profiles of temperature (black solid line) and water vapor mixing ratio (red solid line) for the considered scenarios. Light blue shaded layers show the height position and thickness of the analyzed ice clouds.

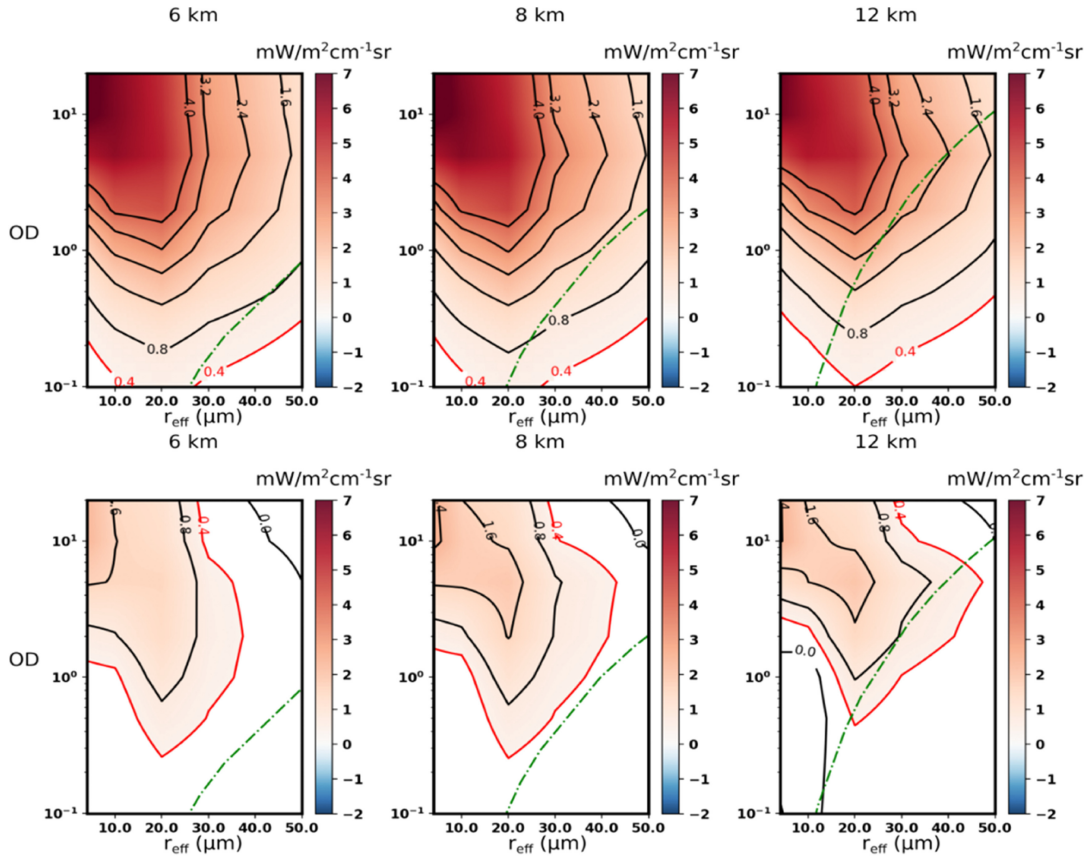


FIGURE 4.10: Radiance differences ΔI , $mW/(m^2sr cm^{-1})$, between Chou solution (upper panels) or Tang solution (lower panels) and the DISORT code as a function of multiple combinations of PSD effective radius and cloud optical depths. The 410 cm^{-1} (FIR) spectral channel is considered. The three panels of each row are for ice clouds at 6 km, 8 km, and 12 km of altitude, respectively. The white color indicates differences below the FORUM noise level, marked by the red contour line. Y-axes are in log scale. The green line indicates the OD- r_{eff} combination obtained from the Sun (2001) [105] parameterization.

Applying the new methodology improved the radiance residuals across a wide range of naturally occurring cloudy cases. Specifically, using the Tang methodology with the updated coefficients proves to be sufficiently accurate in computing radiance fields in the presence of thin cirrus clouds, a key focus of the FORUM mission. Note that the multiplicative coefficients can be computed for the zenith view as well as for additional Gaussian angles (not shown), allowing an angular characterization of the whole radiance field and a fast and accurate computation of fluxes by Gaussian quadrature. Nevertheless, inaccuracies are still encountered for medium-large optical depths ($OD > 1, 2$) and small effective radii, highlighting the need for more accurate approaches to envisage all possible cloudy conditions. It is important to mention that a similar work has been undertaken by the team developing

the RTTOV fast radiative transfer model [59]. In their study, a set of realistic atmospheric profiles, coupled with the Baran model for ice cloud microphysics, are used to retrieve the best k coefficient (in their work it is called Tang Factor) for the Tang adjusted solution. It is interesting to note that, even though a different mathematical approach is used to calculate the effective value of k , and a different RT model is used to simulate the radiances, their final results align with those shown in Figure 4.6. Specifically, it is found that an optimal average Tang Factor is $k \approx 0.1$.



5 | σ -IASI/F2N radiative transfer code

This Chapter describes the main features of the fast radiative transfer code σ -IASI/F2N, and it is adapted from the work done by Masiello et al., (2024) [77] of which I am a co-author. Specifically, my main contributions to this work are the parameterization of the clouds and aerosol's optical properties, the implementation of cloud scaling schemes, and the formal analysis of the cloud scaling schemes.

5.1 | Introduction to σ -IASI

The σ -IASI radiative transfer model [1] is a monochromatic fast code, written in fortran, and tailored for calculating the Earth spectrum and its related Jacobian matrices. The code, originally developed by the University of Basilicata, has been recently updated to effectively extend the spectral range to the Far Infrared (FIR, down to 10 cm^{-1}) and to include new modules for calculations in the cloudy sky, taking advantage of improvements for the application of scaling methods [13] that parametrize the optical depth of ice and liquid water clouds and several aerosols species (e.g. the updated backscattering parameters presented in Section 3.4.1). The extension to the FIR is motivated by the long-standing scientific interests in that spectral region (e.g., [37]), which the initiative of ESA and NASA have recently boosted by funding new missions such as the FORUM and PREFIRE missions. These missions will provide the first full spectral measurements of FIR radiation from orbit, filling a major gap in our knowledge of Earth's energy budget and the role of FIR radiation in Arctic warming, sea ice loss, ice sheet melting, and sea level rise. In this framework, we have developed a new version of σ -IASI radiative transfer model, which will be referred to as σ -IASI/F2N (where F2N stands for Far- to Near-infrared) in the rest of the chapter. The model σ -IASI/F2N covers the spectral range that goes from 10 to 2760 cm^{-1} , with a spectral resolution of 0.01 cm^{-1} . This allows to simulate a wide range of infrared spectrometers/radiometers by convolving the high-resolution spectra with the correct Instrument Spectral Response Function (ISRF). Figure 5.1 provides a schematic representation of the model. The radiance calculations in the cloudy sky rely upon an updated implementation of the simple analytical scaling method developed by Chou et al. (1999) [13], which allows using the same formalism of gas transmittance calculations while still retaining the capability of considering multiple scattering. In addition, the Tang methodology [106] is adapted to simulate the radiance fields over

the FIR spectral range by appropriate multiplicative coefficients. The implementation of this scheme allows to improve the radiance computations in the presence of multiple scattering, as described in Section 4.3.

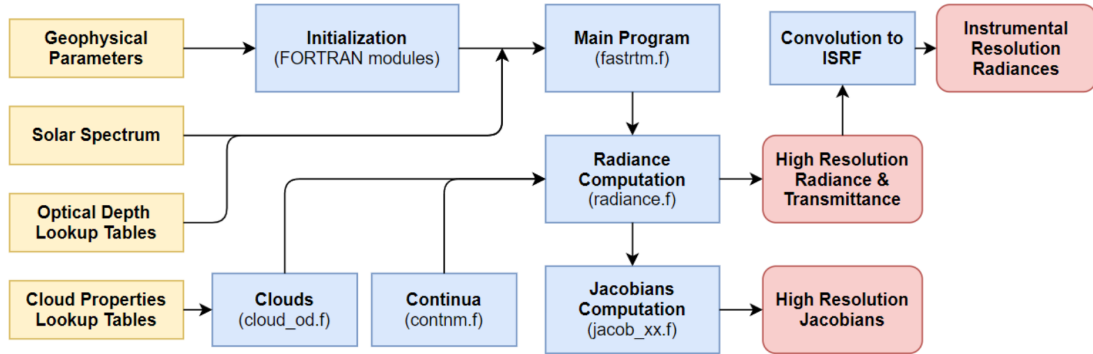


FIGURE 5.1: Schematic representation of σ -IASI.

Currently, the σ -IASI/F2N code can run in two modes: 1) the Chou or C-mode and 2) the Chou-Tang mode or C-T mode. The C-mode uses the Chou scaling approximation for the whole spectral range of 10 to 2760 cm^{-1} . As demonstrated in Chapter 3, the Chou approximation tends to overestimate spectral radiances, particularly in the far-infrared region. Using the C-T mode, the extended Tang methodology is applied to correct the spectral radiance computation in the FIR. In contrast to other methods like the doubling-adding and discrete ordinates schemes (employed by important reference codes such as DISORT [103]), our solver, σ -IASI/F2N, demonstrates superior speed while keeping, at the same time, good accuracy for operational end-users (as it will be shown in this Chapter).

Various works in recent years, such as those by [40, 64, 65, 98], have explored the applications and limitations of approximate models, and comprehensive comparison of radiative transfer codes for cloudy skies has also been presented by Aumann et al. (2018) [3]. The study introduced in this chapter is intended to support both FORUM and PREFIRE missions with a flexible radiative transfer code, which can be used for the scientific and operational analysis of observations. In addition to the application of the Tang correction scheme, we have extensively evaluated the accuracy of the forward model calculations in C-mode, for the spectral range 645 to 2760 cm^{-1} using IASI (Infrared Atmospheric Sounding Interferometer [43]) observations on a global scale. The evaluation could not be extended to the C-T mode, given the lack of satellite observations in the FIR. The IASI observations are collocated with ECMWF analysis fields, including the Temperature, humidity, ozone, and liquid and ice water content profiles. The ECMWF analysis profiles are used as inputs to σ -IASI/F2N to compute radiances, which are then compared to collocated IASI observations. The results show that the new σ -IASI/F2N can simulate cloudy radiances with a bias well below 1 K in brightness temperature along the whole IASI spectral range.

TABLE 5.1: Quantities contained in the σ -IASI/F2N state vector.

Temperature and gases					
Temperature (K)	H_2O (g/kg)	HDO (ppv)	CO_2 (ppv)	O_3 (ppv)	N_2O (ppv)
CO (ppv)	CH_4 (ppv)	SO_2 (ppv)	HNO_3 (ppv)	NH_3 (ppv)	CF_4 (ppv)
Surface and scalars					
Emissivity	T_s (K)	tcc (total cloud coverage)			
Clouds					
q_w (kg/kg)	q_i (kg/kg)	r_{eff} (μm)	D_{eff} (μm)		

5.2 | The basic radiative transfer in σ -IASI/F2N

The σ -IASI/F2N code is a monochromatic, one-dimensional fast radiative transfer model capable of simulating the Earth's emission spectrum in all-sky conditions. The model employs a vertical discretization of atmospheric profiles, utilizing a constant grid of 60 pressure layer, covering the range from 1100 to 0.005 hPa . The 61 atmospheric pressure levels, which divide the atmosphere into 60 layers, are shown in Figure 5.2, while Figure 5.3 shows the numbering convention used. Note the relatively higher density of layers at pressure levels just above the Tropopause. This is the optimal configuration to simulate data recorded by ground, orbit, or instruments on board an aircraft flying at about 20 km altitude [35]. The monochromatic optical depth calculation is based upon suitable lookup tables for atmospheric gases and clouds. For atmospheric gases, the lookup table is generated from LBLRTM v.12.7 [14], and related MT_CKD v. 3.2 for water vapor continuum absorption, whereas for clouds, we use LBLDIS [110].

In the current version of σ -IASI/F2N, the surface state is specified by the surface temperature (T_s) and the emissivity spectrum (ϵ). For the atmosphere, a set of atmospheric profiles must to be specified: the temperature (T) plus the mixing ratio profiles (q) of H_2O , HDO , O_3 , CO_2 , N_2O , CO , CH_4 , SO_2 , HNO_3 , NH_3 , OCS , and CF_4 . The former profiles form the basis of the state vector for clear sky. On the other hand, when cloudy sky simulations are considered, additional profiles are incorporated, specifically the mass mixing ratios (kg/kg) for liquid and ice water content (q_w and q_i), along with the associated parameters of effective radius (r_{eff}) for water clouds and effective dimension (D_{eff}) for ice. The input state vector is summarized in Table 5.1.

Apart from parameters and species listed in Table 5.1 whose concentration can be varied inside the state vector, σ -IASI/F2N also embodies a set of fixed species that impact the simulated radiance in the forward model. This set includes the major species N_2 and O_2 , which are considered through their collision-induced continuum (and very weak quadrupole or magnetic dipole lines). In addition, σ -IASI/F2N considers other trace gases, such as NO , NO_2 , OH , HCl , H_2CO , HCN , CH_3Cl , and C_2H_2 (numbers 8, 10, 13, 15, 20, 23, 24, 26, respectively, in LBLRTM list of species). The vertical reference profiles of these molecules are fixed according to the U.S. Standard Atmosphere model. Fixed gases also include heavy

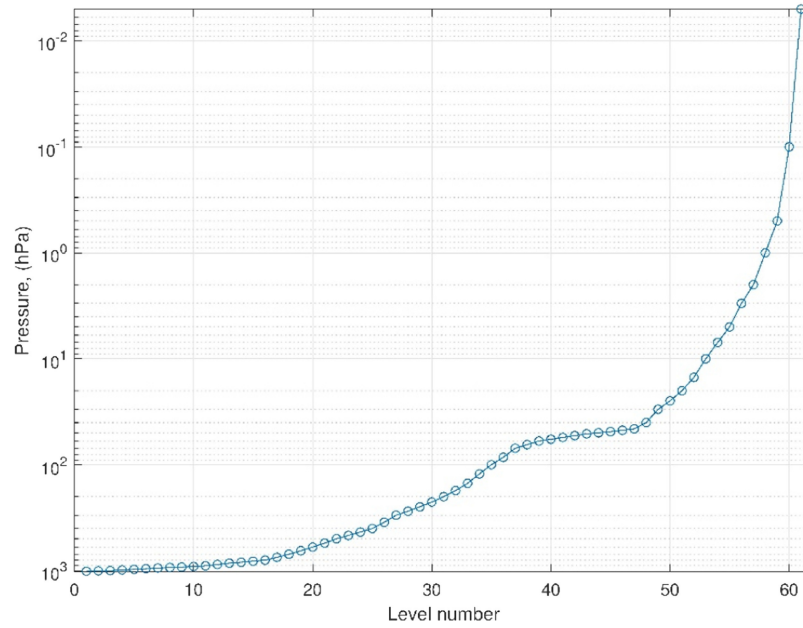


FIGURE 5.2: The definition of the atmospheric pressure levels used in σ -IASI/F2N.

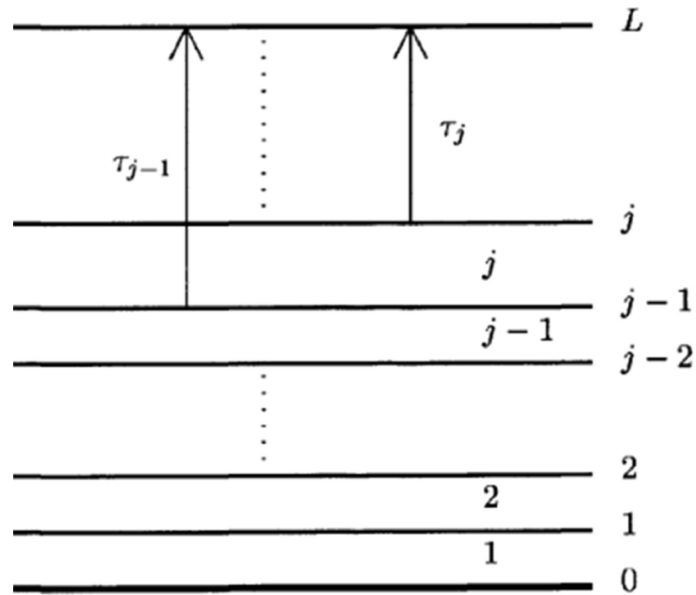


FIGURE 5.3: σ -IASI/F2N layering. The level L represents the last layer of the model ($L = 60$). The optical depth values τ_j are calculated from the level j to the TOA.

molecules whose radiative effect is modeled through cross-sections. In the present work, four

of these molecules are considered: CCl₄, CFC-11, CFC-12, and HCFC-22. Their mixing ratio is assumed to be vertically uniform and scaled according to the 2015 report of WD-CGG (World Data Centre for Greenhouse Gases) [117].

The σ -IASI/F2N forward model solves the radiative transfer equation in the following form:

$$I_\nu = I_\nu^s + I_\nu^a + I_\nu^r + I_\nu^i \quad (5.1)$$

where I_ν is the spectral radiance, decomposed in its surface term at the top of the atmosphere (I_ν^s), the contribution from the atmosphere (I_ν^a), the downward infrared radiation reflected at the surface (I_ν^r), and the solar radiation reflected at the surface I_ν^i . All these quantities depend on the wavenumber ν , and the dependence over the directional angle is made implicit. The first term on the right side of Equation 5.1 can be written in the following form:

$$I_\nu^s = \epsilon_\nu B_\nu(T_s) \mathbb{T}_\nu^0 \quad (5.2)$$

where ϵ_ν the emissivity spectrum, B is the blackbody Planck function, and \mathbb{T}_ν^0 is the total transmittance of the atmosphere. The atmospheric component is expressed as:

$$I_\nu^a = \int_0^{+\infty} B_\nu(T(z)) \frac{d\mathbb{T}_\nu}{dz} dz \quad (5.3)$$

with z the vertical spatial coordinate and \mathbb{T}_ν the transmittance from altitude z to $+\infty$. The term I_ν^r is appropriately dealt with according to the surface type. For the sea surface, a specular model is employed:

$$I_\nu^r = (1 - \epsilon) \mathbb{T}_\nu^0 \int_{+\infty}^0 B_\nu(T(z)) \frac{d\mathbb{T}_\nu^*}{dz} dz = (1 - \epsilon) (\mathbb{T}_\nu^0)^2 \int_0^{+\infty} B_\nu(T(z)) \frac{1}{\mathbb{T}_\nu^2} \frac{d\mathbb{T}_\nu}{dz} dz \quad (5.4)$$

where \mathbb{T}_ν^* is the transmittance from altitude z to $z = 0$, and the last expression is obtained noting that $\mathbb{T}_\nu^0 = \mathbb{T}_\nu \cdot \mathbb{T}_\nu^*$. On the other hand, when a Lambertian surface is considered:

$$I_\nu^r = (1 - \epsilon) \mathbb{T}_\nu^0 \int_{+\infty}^0 B_\nu(T(z)) \frac{d\mathbb{T}_\nu^{*f}}{dz} dz \quad (5.5)$$

where \mathbb{T}_ν^{*f} is the diffuse transmittance, which is defined as:

$$\mathbb{T}_\nu^{*f} = 2 \int_0^1 \mathbb{T}_\nu^* \mu d\mu \quad (5.6)$$

According to Elsasser [25] it is assumed that $\mathbb{T}_\nu^{*f} = \mathbb{T}_\nu^*(\bar{\mu})$ with $\bar{\mu}$ an effective zenith angle of 52.96° . This choice yields accurate results depending on the optical depth; the effective zenith angle is spectrally dependent. For optical depth below 1, exact and approximate calculations nearly coincide (e.g., [60]). However, for analyses that need better accuracy, the spectral-dependent effective angle can be coded up in terms of rapidly evaluating exponential integrals of the third kind [20].

Finally, the last term, I_v^i , represents the reflected sunlight at the surface. If a water surface is considered, it is modeled through:

$$I_v^i = r(\theta_{sun}, \theta_{sat}, v^2, \Phi) \mathbb{T}_v^{0,sun} \mathbb{T}_v^{0,sat} F_{sun} \quad (5.7)$$

where $r(\theta_{sun}, \theta_{sat}, v^2, \Phi)$ is the bidirectional reflectance distribution function according to the Cox-Munk model [51]. In this case, θ_{sun} and θ_{sat} are the Sun and satellite zenith angles respectively, v^2 is a wind speed parameter, and $\Phi = \Phi_{sat} - \Phi_{sun}$ is the difference of sun and satellite azimuth angles. Finally, F_{sun} represents the monochromatic stellar (solar) irradiance. On the other hand, when a lambertian surface is simulated, Equation 5.7 becomes:

$$I_v^i = r \mathbb{T}_v^{0,sun} \mathbb{T}_v^{0,sat} \frac{F_{sun} \mu_{sun}}{\pi} = (1 - \epsilon) \mathbb{T}_v^{0,sun} \mathbb{T}_v^{0,sat} \frac{F_{sun} \mu_{sun}}{\pi} \quad (5.8)$$

In order to obtain a numerical solution for the radiative transfer problem, we need to compute the atmospheric emission integral of Equation 5.3 and its downwelling counterpart appearing in Equations 5.4 and 5.5. To this end, considering the atmospheric layering shown in Figure 5.2 and adopting the approximation of parallel-plane atmosphere, the upwelling thermal radiation of Equation 5.3 can be approximated according to:

$$I^s = \sum_{j=1}^L \left(\int_{z_{j-1}}^{z_j} B(T(z)) \frac{d\mathbb{T}}{dz} dz \right) \quad (5.9)$$

where we dropped the explicit dependence on the wavenumber ν . Using the mean value theorem, we can analytically compute the integral:

$$\int_{z_{j-1}}^{z_j} B(T(z)) \frac{d\mathbb{T}}{dz} dz = B(T(z^*)) (\mathbb{T}_j - \mathbb{T}_{j-1}) \quad (5.10)$$

Where $T(z^*)$ can be interpreted as an (wavenumber-dependent) average temperature of the layer. An explicit derivation of this quantity can be found in [77]. A similar treatment is performed with the downwelling thermal radiation integral.

For a clear sky, the σ -IASI/F2N forward model strictly applies to the case of a non-scattering atmosphere, which is a good approximation for a clear sky in the MID/FAR-infrared, where only the absorption by atmospheric gas is considered. In the presence of clouds and aerosols, a source function is needed to properly deal with multiple scattering. Our approach is to use the scaling approximation introduced by Chou et al. [13], which allows to consider multiple scattering while still using the radiative transfer equations for a clear atmosphere. In this way, the difficulties in applying a multiple-scattering algorithm to a partly cloudy scene are avoided, and the computational efficiency is comparable to that for a clear scene. The details on the approach used in cloudy sky are provided in the next section.

5.2.1 | Transmittance calculations and the optical depth lookup table

Transmittances in clear-sky and cloudy cases are defined according to the considered absorbers. In σ -IASI/F2N, it is assumed that the clear-sky transmittance is affected both by gas and aerosol particles, namely assuming that aerosols are uniformly distributed on the entire Field of View or FOV. The cloudy portion of the FOV will be additionally affected by the extinction due to water and ice clouds. To combine them, we assume the additive model:

$$I = (1 - f)I_{clear} + fI_{cloud} \quad (5.11)$$

where f is the cloud fraction, so that $f = 0$ means a clear FOV and $f = 1$ is a fully overcast FOV. Equation 5.11 implements the maximum overlap model and says that the cloudy spectra are calculated as the linear combination of clear and cloudy columns based on the cloud fraction. I is the spectrum calculated with the maximum overlap assumption and f is defined as the maximum cloud fraction in the cloud coverage profile. I_{clear} is the clear-sky spectrum, and I_{cloud} is the spectrum assuming full overcast (i.e., clouds fill the entire satellite footprint).

The general expression for the transmittance at pressure level j can be expressed as:

$$\mathbb{T}_j = \prod_{i=j+1}^L e^{-(\tau_{gas,i} + \tau_{cloud,i} + \tau_{aerosol,i})} \quad (5.12)$$

where τ is the layer optical depth of the given parameter or species.

Here we remark that the optical depth for the atmospheric gases is computed based on a monochromatic Lookup Table (LUT) generated by the forward model LBLRTM version 12.7 and the line database AER v. 3.2¹. The LUT based on LBLRTM covers the spectral range of 5 to 2760 cm^{-1} , and the sampling is $\Delta\nu = 0.01 cm^{-1}$. This sampling is optimized for nadir-sounding sensors such as IASI and FORUM, primarily sensitive to the lower atmosphere and Troposphere, where pressure broadening widens the absorption line widths of molecular species. We also have a LUT with $\Delta\nu = 0.001 cm^{-1}$, which is used for trade-off analysis between spectral resolution and accuracy when we add new spectral segments. It is important to note that even with the coarser sampling rate, since the LUT database was built starting from the resolution of $2 \times 10^{-4} cm^{-1}$, the code shows a greater sensitivity to the stratosphere with respect to other non-monochromatic fast models [76]. This analysis is ongoing for the far-infrared portion of the spectrum.

The next section focuses on the formulation and parameterization of the optical depth for water and ice clouds. For what concerns the aerosol particles, the same formalism used for clouds is applied. Details are given in the work done by Martinazzo et al. (2021) [74] and summarized in Chapter 3. These situations are not presented here, and the aerosol profile has been set to zero for all calculations considered in the present analysis.

¹See the website <http://rtweb.aer.com/main.html>

5.2.2 | Cloud optical depth parameterization, the C-mode

This section will discuss how the optical depth for clouds is parameterized within the forward module σ -IASI/F2N when the C-mode is used.

The considered cloud layers include liquid water and ice clouds, as also described in Chapter 3. The single scattering optical properties are selected using state-of-the-art databases or produced in-house using referenced codes. In the case of liquid water clouds, water spheres are assumed to be the primary constituent, and the optical quantities are generated through the Scattlay model [89]. The model utilizes complex refractive indexes (Downing and Williams, 1975 [24]) to solve the Mie scattering problem and obtain the desired properties. The code also allows to account for mixed-phase particles, constituted by an ice core with a liquid water coating. The results concerning mixed phase are not presented in this paper, since we are limited by the state vector as provided by ECMWF analyses.

Ice clouds are assumed to be composed of ice crystals, specifically column aggregates of hexagonal columns. The reference database is the Yang database (Yang et al., 2013 [122]) which accounts for 8 different pristine habits.

The considered single-particle single-scattering optical properties are then combined according to realistic particle size distributions, $n(D)$. Multiple lognormal size distributions (Miles et al., 2000) are used for liquid water clouds while a set of modified gamma distributions is assumed in the case of ice clouds.

Below is a description of the bulk (macrophysical) quantities. The effective size, D_{eff} , of the PSD is defined according to Equation 3.6, reported here for ease of reading.

$$D_{eff} = \frac{3 \int_0^{\infty} V(D)n(D)dD}{2 \int_0^{\infty} A(D)n(D)dD}$$

where A and V are the cross-sectional area and the volume of the particle with maximum dimension D . From Equation 3.6 we can obtain a definition for the effective radius as $D_{eff} = 2r_{eff}$.

According to the classical treatment for the description of the cloud optical depth [60], we can define the extinction coefficient k_{ext} which, for a homogeneous path Δz :

$$k_{ext} = \frac{OD}{\Delta z} = \int_{D_{min}}^{D_{max}} Q_{ext}(D)A(D)n(D)dD \quad (5.13)$$

where Q_{ext} is the extinction efficiency defined in Chapter 2. Next, the liquid water (ice) content at a given pressure level is defined according to:

$$xWC = \rho_x \int_{D_{min}}^{D_{max}} V(D)n(D)dD \quad (5.14)$$

where the ρ_x is the density of ice/liquid water, and the subscript x stands indifferently for ice or liquid water (IWC and LWC respectively). Using both Equations 5.13 and 5.14, after a bit of algebra we arrive at this basic formula for the cloud optical depth:

$$\frac{OD/\Delta z}{xWC/\rho_x} = \frac{3}{2} \frac{Q_{ext}}{D_{eff}} \quad (5.15)$$

Where Q_{ext} is the bulk extinction efficiency, defined as:

$$Q_{ext} = \frac{\int_{D_{min}}^{D_{max}} Q_{ext}(D)A(D)n(D)dD}{\int_{D_{min}}^{D_{max}} A(D)n(D)dD} \quad (5.16)$$

Equation 5.16 strictly applies to single scattering. The inclusion of multiple scattering effects is obtained by considering the Chou scaling approximation, which demands that the extinction efficiency, Q_{ext} , is changed to \tilde{Q}_{ext} , according to:

$$\tilde{Q}_{ext} = (1 - \tilde{\omega})Q_{ext} + b\tilde{\omega}Q_{ext} \quad (5.17)$$

where the bulk single-scattering albedo is given by:

$$\tilde{\omega} = \frac{\int_{D_{min}}^{D_{max}} Q_{sca}(D)A(D)n(D)dD}{\int_{D_{min}}^{D_{max}} Q_{ext}(D)A(D)n(D)dD} \quad (5.18)$$

The form expressed in 5.17 is equivalent to the optical depth scaling shown in Equation 3.7.

The study presented in Chapter 3 has shown that the correct calculation and parameterization of the back-scattering coefficient, b plays a crucial role when applying the Chou scaling method to compute spectral radiances. The derivation of this parameter is performed in accordance with what is done in Chapter 3 and published by Martinazzo et al, [74].

Applying this scaling, we can write the cloud optical depth as:

$$OD = \Delta z \frac{3}{2} \frac{xWC}{D_{eff}\rho_x} \tilde{Q}_{ext} \quad (5.19)$$

In Equation 5.19 xWC is the Liquid water content LWC (or IWC in case of ice clouds), expressed in units of kg/m^3 . LWC and IWC are easily derived from the mass mixing ratio (kg/kg), normally available from Numerical Weather Prediction centers (e.g., ECMWF), and ingested by the code. Specifically, the mass mixing ratio is expressed as:

$$q_x = \frac{m_x}{m_{air}} \quad (5.20)$$

where m_x is the mass of ice or liquid water and m_{air} is the mass of air. It is therefore possible to transform the mass mixing ratio into liquid or ice water content using the following form:

$$xWC = q_x \rho_a \quad (5.21)$$

where ρ_a is the air density (kg/m^3), obtained from the ideal gas law. Using the mass mixing ratio and recalling that $D_{eff} = 2r_{eff}$, the cloud optical depth is expressed as:

$$OD = \Delta z \frac{3}{4} \frac{q_x \rho_a}{r_{eff} \rho_x} \tilde{Q}_{ext} \quad (5.22)$$

which represents the fundamental equation employed in σ -IASI/F2N to compute the optical depth of ice/water clouds, utilizing the input mass mixing ratio.

All the cloud optical properties are pre-computed and parameterized with 6-th degree polynomials of the effective radius:

$$Y = \sum_{i=0}^6 P_i x^i; \quad x = \frac{1}{r_{eff} + t} \quad (5.23)$$

with P_i and t depending on the wavenumber, and where Y is representing the quantities Q_{ext} , b and $\tilde{\omega}$. As a result, all the important cloud properties in the layer (Q_{ext} , b , $\tilde{\omega}$) are simple functions of the wavenumber and effective radius. In this way, we can produce a LUT that contains only the coefficients P_i and t from which the essential optical properties are derived.

The polynomial interpolation of optical properties enables the derivation of radiance analytical Jacobians with respect to cloud microphysical properties (q_x and r_{eff}). In particular, we have:

$$\frac{\partial k_{ext}}{\partial q_x} = \frac{3}{4} \frac{\rho_a}{r_{eff} \rho_x} \tilde{Q}_{ext}; \quad \left(m^{-1} \frac{kg}{kg} \right) \quad (5.24)$$

$$\frac{\partial k_{ext}}{\partial r_{eff}} = -\frac{3}{4} \frac{q_x \rho_a}{r_{eff}^2 \rho_x} \tilde{Q}_{ext} + \frac{3}{4} \frac{q_x \rho_a}{r_{eff} \rho_x} \frac{\partial \tilde{Q}_{ext}}{\partial r_{eff}}; \quad \left(\frac{m^{-1}}{\mu m^{-1}} \right) \quad (5.25)$$

$$\frac{\partial \tilde{Q}_{ext}}{\partial r_{eff}} = \frac{\partial Q_{ext}}{\partial r_{eff}} [(1 - \tilde{\omega}) + b\tilde{\omega}] + Q_{ext} \left[\frac{\partial \tilde{\omega}}{\partial r_{eff}} (b - 1) + \tilde{\omega} \frac{\partial b}{\partial r_{eff}} \right]; \quad \left(\frac{1}{m} \right) \quad (5.26)$$

where the derivatives, $\frac{\partial b}{\partial Q_{ext}}$, $\frac{\partial b}{\partial r_{eff}}$, $\frac{\partial \tilde{\omega}}{\partial r_{eff}}$, can be easily obtained based on the polynomial parameterization expressed in Equation 5.23. Finally, because clouds are dealt with the same way as gases, the remaining math to compute radiance derivatives is the same as that for gases as shown in [1].

Figures 5.4 and 5.5 show an example of the radiance derivatives over the full range of 10 to 2760 cm^{-1} with respect to the cloud parameters (using the C-mode). The simulated cloud structure is rather complex. The example deals with a double-layer water cloud, with the upper layer centered at ~ 500 hPa showing a water/ice mixed phase, and an uppermost cirrus cloud at ~ 200 hPa.

The derivatives are normalized to their absolute maximum value. The normalization yields functions ranging between $[-1, 1]$. The choice simplifies the graphic rendering and allows us to understand which spectral range is larger sensitive to the given parameter. For example, in tropical atmospheres, where the water vapor concentration is high, all the cloud parameters

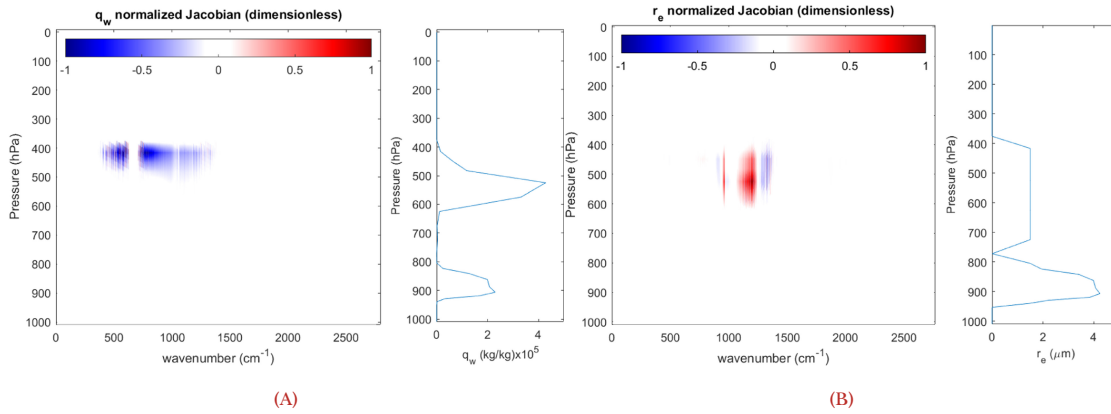


FIGURE 5.4: Radiance derivatives with respect to q_w (A) and r_{eff} (B) for a water cloud on a tropical atmosphere. On the right part of the panels, the vertical profile of the cloud property is presented.

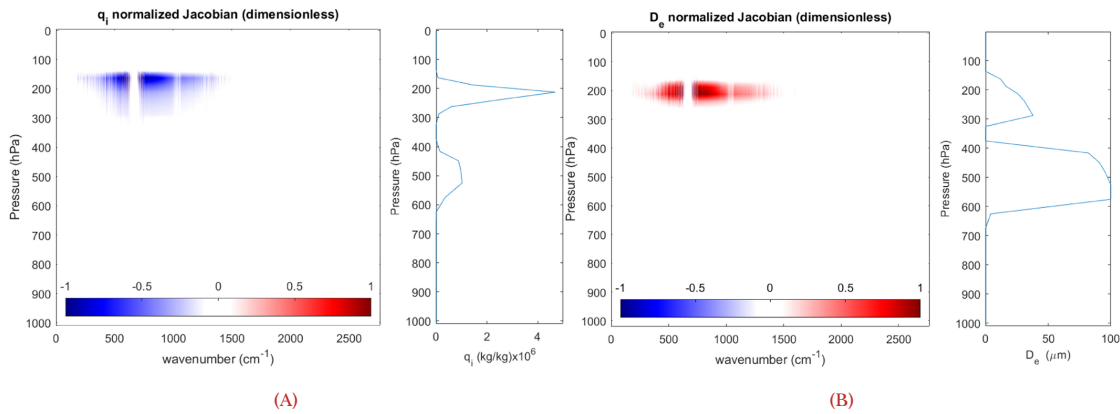


FIGURE 5.5: Radiance derivatives with respect to q_i (A) and D_{eff} (B) for an ice cloud on a tropical atmosphere. On the right part of the panels, the vertical profile of the cloud property is presented.

show the highest sensitivity in the atmospheric window between 8 and 12 μm , and in the water vapor rotation band at around 20 μm . It should be noted that the vibration water vapor band at 6.7 μm is completely saturated and does not show any important sensitivity to cloud properties, demonstrating the importance of the FIR for cloud studies.

5.2.3 | The C-T mode

As mentioned in the previous sections, the radiance calculation in cloudy sky conditions, performed by σ -IASI/F2N, depends on an implementation of a simple analytical scaling method [13]. This methodology, originally developed in the context of broadband fluxes computation, has been proven to be accurate enough to be applied to the simulation of the upwelling radiances over the entire mid-infrared region [74]. Nevertheless, the application of this solution to the FIR results in an overestimation of the upwelling radiances, especially in the presence of ice (thus, also cirrus) clouds. In the perspective of the coming applications to FORUM and PREFIRE, we have also developed a correction scheme to the Chou method, which has been implemented as an additional routine to improve the flexibility of σ -IASI/F2N.

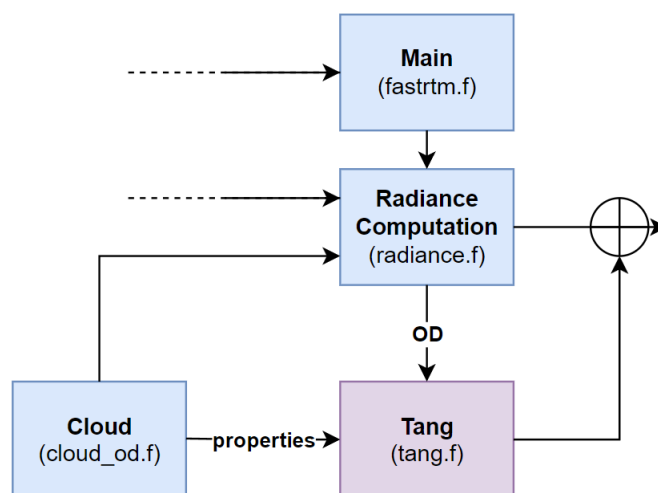


FIGURE 5.6: Flowchart describing the implementation of the C-T mode within σ -IASI/F2N. The incorporation of the new routine exploits the linearity of the correction term, allowing for a complete independent subroutine. If the C-T mode is activated, the correction term is linearly added to the Chou solution.

The correction term is modeled starting from the adjusted scheme proposed by Tang [106]. This paper identifies the root cause of radiance overestimation in the assumptions made by Chou in the form of the ambient radiation (Equation 2.59). The Chou approximation assumes that the back-scattered downward ambient radiation is equivalent to the Planckian emission originated from the layer itself. This assumption can lead to a large bias, as the actual downward ambient radiation is much weaker than the layer blackbody radiance. The adjusted solution proposed by Tang incorporates a more realistic representation of the downward ambient radiation. However, the direct application of the correction routine to

spectrally resolved radiances is not possible. An extension of this adjustment scheme for the computation of spectral radiances in the FIR is implemented as detailed in Section 4.3. The incorporation of this new routine into the σ -IASI/F2N is carried out as illustrated in Figure 5.6.

5.3 | Methods

IASI and ECMWF analysis fields are used to define a global data set of pairs (Observations, Atmospheric State Vector). The ECMWF atmospheric state vector feeds the new σ -IASI/F2N, and the resulting radiances are used to compare with IASI observations. We stress that our exercise could have used many satellite infrared observations. However, we have limited to IASI because the full disk analysis could have become too computationally expensive and also because GSICS (Global Space-based Inter-Calibration System) has selected IASI-A/B/C for assessing infrared channels (Goldberg and Bali, 2021 [36]). To have a validation dataset covering all latitudes and climate regions, we collocated measurements from MetOp-B and MetOp-C with ECMWF analyses. We use MetOp measurements from 23:45 on 8 September 2021 to 00:15 on 10 September 2021, which include MetOp-B orbits 46574-46589 and MetOp-C orbits 14732-14746. The selected measurements are associated with the ECMWF base time analyses. The temporal coincidence interval is set to ± 15 min. With this criterion, we selected 16 MetOp orbits: 8 for MetOp-B (46574, 46575, 46578, 46581, 46582, 46585, 46588, 46589) and 8 for MetOp-C (14732, 14733, 14735, 14736, 14739, 14742, 14743, 14746). The dataset consists of 270200 IASI spectra, of which 167244 are over the sea. These constitute the subset used for the intercomparison exercise to avoid biases arising from wrong assumptions about surface emissivity. It is important to emphasize that, in this study, observations are compared to simulations without retrievals, as we just compared measurements with simulations. The location of the IASI footprints over the sea is shown in Figure 5.7. In addition, information about the acquisition time is provided in the color bar.

The collocated ECMWF analyses provide, for each IASI spectrum, surface temperature and Temperature profile (T), H_2O mixing ratio (Q), O_3 mixing ratio (O), Specific Liquid and Ice Water Content (q_w and q_i expressed in mass mixing ratio, kg/kg) over a pressure grid of 137 levels from the surface to 0.01 hPa . These quantities are used to generate the state vector ingested by σ -IASI/F2N:

$$v_{ECMWF} = (T, T_s, Q, O, D, q_w, q_i, tcc) \quad (5.27)$$

where, tcc is the total cloud cover, and D is the profile of HDO (heavy water), which is derived from Q by multiplying it by the abundance ratio D/Q prescribed by the Standard Vienna Mean Ocean Water (VSMOW) ratio, that is $R_{VSMOW} = 3.1 \times 10^{-4}$. The state vector for σ -IASI/F2N requires additional parameters concerning the effective size of the

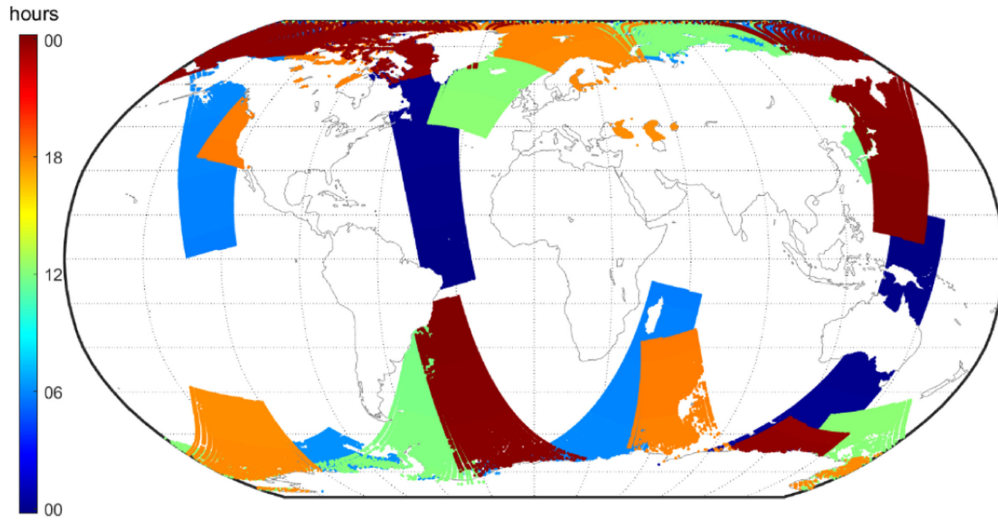


FIGURE 5.7: IASI-B and C footprints in the database. The data are over the sea, and are collected in the period that goes from 8 September 2021 23:45 to 10 September 2021 00:15, coinciding with the ECMWF analysis runs. The color indicates the IASI observation measurement time.

liquid water and ice particles in cloud layers. The effective radius (r_{eff}) and dimension (D_{eff}) are obtained through the Martin formula [73] and the Wyser approach [120]. The definition of the thermodynamic, gas concentration values, and cloud properties in the model layer accounts for a different atmospheric layering between the code and the analyses. In fact, the ECMWF analyses is provided on 137 pressure levels, while σ -IASI/F2N works with a fixed pressure grid of 61 levels and 60 layers.

5.4 | Evaluation of the C-mode with IASI data

The forward model σ -IASI/F2N is used to compute synthetic radiances collocated with the 16 IASI orbits described in the previous section. The radiance calculations are performed on the 100 to 2760 cm^{-1} spectral range. However, to simplify the comparison, we have selected six channels whose spectral location is shown in the σ -IASI/F2N spectrum of Figure 5.8. The σ -IASI/F2N calculations are convolved with the IASI instrument spectral function [2]. In this way, we can adequately compare calculated and observed IASI radiances.

The rationale behind this comparison is to check the capability of σ -IASI/F2N to follow the observed pattern of spatial clouds, a combination of both the cloud modeling accuracy in our forward model and the accuracy of the ECMWF thermodynamic and cloud model fields. For clarity and conciseness, we first limit ourselves to show the comparison between

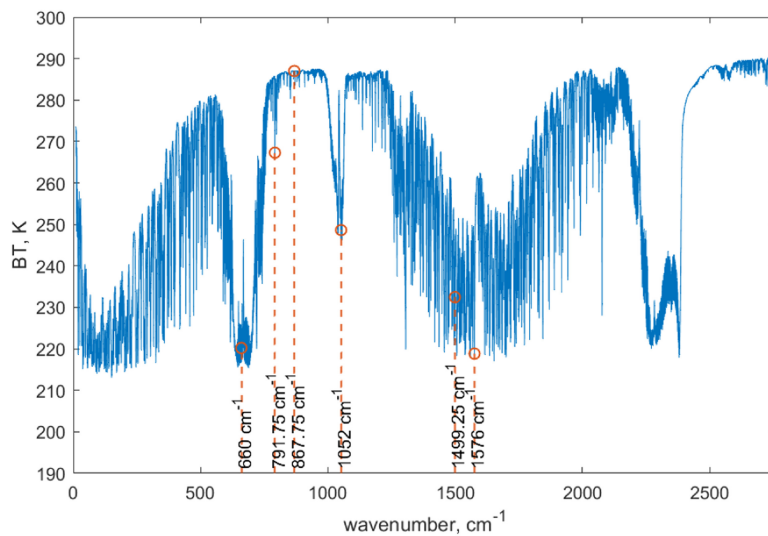


FIGURE 5.8: Example of σ -IASI/F2N spectrum showing the spectral channels selected to check the consistency between observations and simulations.

Observations and Calculations (Obs - Calc) on 9 September 2021 at 0 : 00 UTC. The complete set of maps corresponding to the UTC hours 00 : 00, 06 : 00, 12 : 00, and 18 : 00 of 9 September 2021, encompassing IASI B and C, will be used later in this section to compile statistics for bias and standard deviation. Clearly, the comparison depends on likely discrepancies in the time-space collocation of ECMWF profiles and IASI observations. To minimize as much as possible the collocation error, we consider IASI observations that are distant ± 15 min from the ECMWF canonical hours. Even so, (Obs - Calc) discrepancies are expected due to many circumstances, such as the fact that the ECMWF model spatial grid of 0.05° is larger than the IASI footprint, and because of inherent limitations of the ECMWF analysis, in particular the cloud location errors.

Maps of computed and observed radiances in the selected channels are mapped in Figures 5.9 and 5.10. The leftmost-hand side panel shows the channel at wavenumber 660 cm^{-1} . This channel is in the core of the CO_2 absorption band at 667 cm^{-1} ; therefore, it is sensitive to the upper atmosphere, where clouds are extremely rare. And in fact, the comparison shows a smooth spatial pattern with the expected latitudinal gradients. Both the calculated and observed maps identify the tropical trough in the brightness temperature because of the higher Tropopause at that latitude. Also, calculations and observations determine the colder Stratosphere close to the Antarctic region.

Next, we consider the channel at wavenumber 791.75 cm^{-1} . The channel is in the middle of a weaker Q-branch of CO_2 and is sensitive to the middle Troposphere. The patterns in the related maps show the structure of the middle tropospheric cloudiness. Again, we notice consistency between calculations and observations regarding the spatial structure.

The channel at wavenumber 867.75 cm^{-1} in the atmospheric window is sensitive to the surface and lower clouds. Therefore, in this channel we expect a somewhat more significant

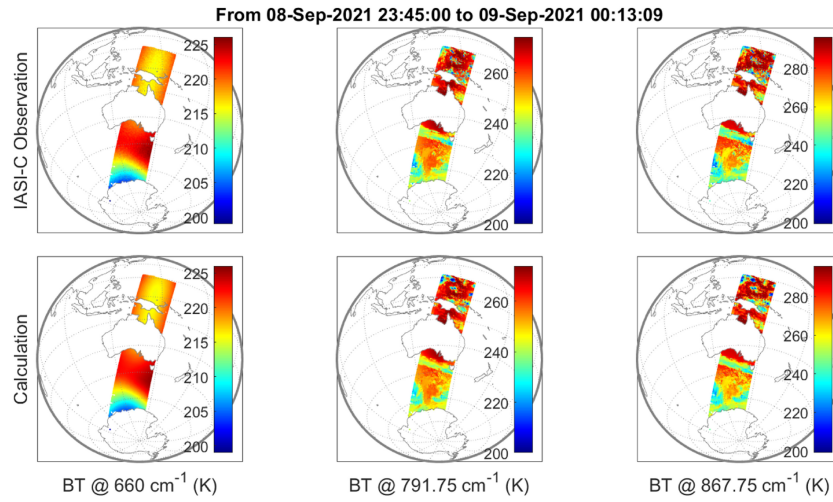


FIGURE 5.9: Comparison of the spatial maps of the observed (IASI) and calculated (σ -IASI/F2N) radiances in the first three of six selected channels (660 cm^{-1} , 791.75 cm^{-1} , and 867.75 cm^{-1}).

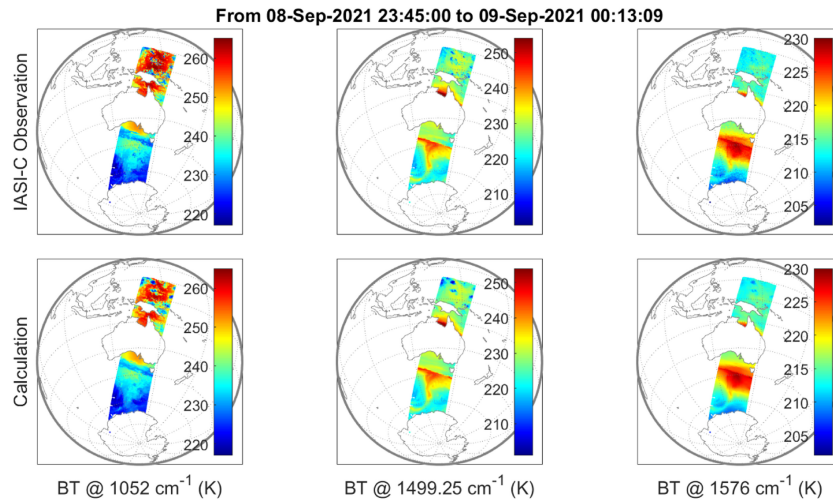


FIGURE 5.10: As in Figure 5.9 but in the last three selected channels (1052 cm^{-1} , 1499.25 cm^{-1} , and 1576 cm^{-1}).

variability; in fact, we see that the range of brightness temperatures goes from 220 to about 300 K. Calculations reproduce well the spatial gradients observed by IASI.

The 1052.00 cm^{-1} channel is in the middle of the ozone band at $9.7 \mu\text{m}$. We expect less absorption in the tropics than at mid-high latitudes because of the diverse Tropopause height. In September, we also expect the Tropopause to be lower in the Southern Hemisphere. Therefore, the brightness temperature in this channel is expected to be lower in the South

than in the North. Observations and calculations both reproduce the expected patterns.

Next, we come to the channel at 1499.25 cm^{-1} , which is within the water vapor band at $6.7\ \mu\text{m}$ and is mostly influenced by the emission of the middle Troposphere. We expect to observe the pattern of the humidity fields and their variability also because of cloud patterns. Once again, calculations reproduce accurately the spatial temperature gradients as seen by IASI.

Finally, the results at 1576 cm^{-1} are shown on the rightmost-hand side of Figure 5.10. The channel is within the water vapor band at $6.7\ \mu\text{m}$, but unlike the previous one, this channel is mostly sensitive to the upper Troposphere. Therefore, we expect to observe the higher altitude patterns of the humidity field. As shown by both observations and calculations, the spatial patterns are smoother than those associated with the channel at 1499.25 cm^{-1} .

Figure 5.10 shows that σ -IASI/F2N can follow the spatial patterns of cloud fields, in addition to features characteristics of T , Q , O fields. We underline that the ECMWF model is unanimously considered a reference Numerical Weather Prediction (NWP) system. Therefore, for channels that are sensitive to T , Q , O , we expect a good consistency between observations and calculations.

A detailed comparison is the objective of the remainder of this section. We consider the six channels described above, but all the observations shown in Figure 5.7 are accounted for (and not only one single IASI orbit). The same criterion accounting for a time difference < 15 min is assumed. Moreover, a criterion concerning the state of the scene is added: if the AVHRR IASI native cloud masque and the ECMWF total cloud content are equal to 100 % (cloudy sky) or 0 % (clear sky), the data is retained and analyzed. By applying this rule 32364 IASI cloudy soundings and 2269 clear sky soundings are left for comparison. However, even with this reduced time slot of half hour, we expect the cloudy sky to have some remaining collocation problems. In contrast, we expect fewer problems for a clear sky because the variation of T , Q , O fields has characteristic time scales longer than cloud properties.

The first result concerns the cloudy sky case and is reported in Figure 5.11. The figure shows the histogram of the difference $\Delta = \text{Obs} - \text{Calc}$, together with the mean and standard deviation of the differences and the Pearson correlation coefficient, r^2 , or simply linear correlation between Obs and Calc. Overall, we observe a good agreement between the calculated radiances with those calculated.

The histograms of the residuals for channels 660 , 1499.25 , and 1576 cm^{-1} , which refer to the higher atmosphere, are nearly Gaussian, which suggests that the IASI measurement error mostly dominates the difference. In fact, if we look at the mean of the differences, we see that it is close to zero at 660 cm^{-1} and ≤ 0.5 K for the other two channels. The linear correlation is above 0.96, and the standard deviation is in the range ~ 0.5 -1.5 K.

The histograms show more variability for the highest transmissive channels, 791.75 , 867.75 , and 1052 cm^{-1} . This is expected because of meteorological processes close to the surface, whose characteristic time and space scales are much shorter, and they cannot be exactly reproduced with the intrinsic limitation of the collocation system. Although for such channels, the mean difference is largely below 1.5 K, the standard deviation reaches values as large as 7.5 K and r^2 drops down to 0.85. This result exemplifies problems with a correct time-space collocation.

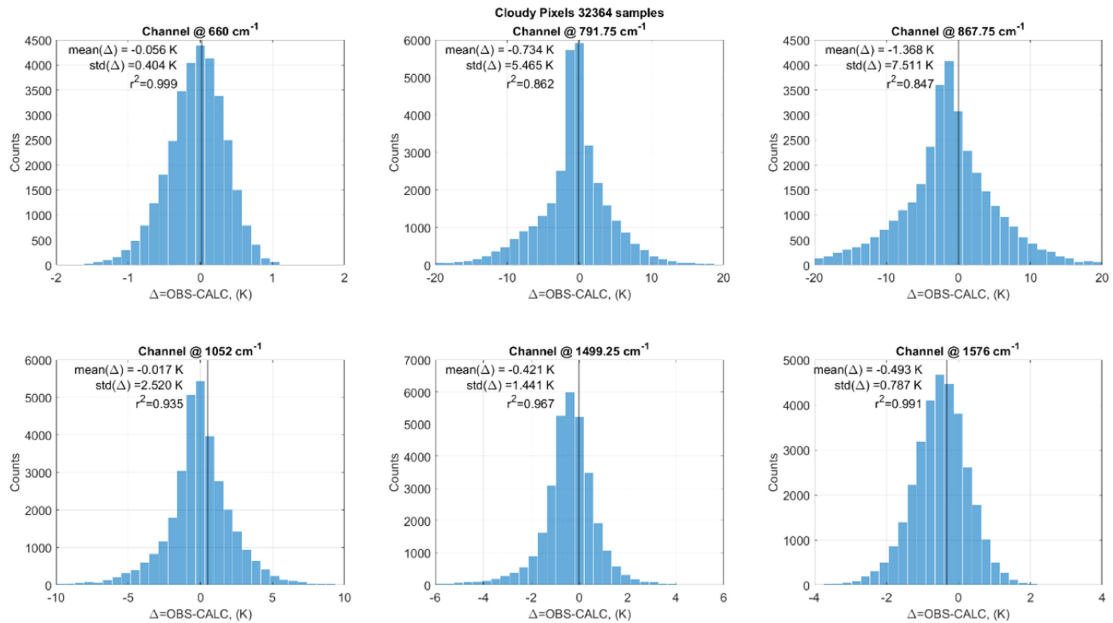


FIGURE 5.11: Histograms of Obs-Calc for the six channels listed in Figure 5.8. The difference in the figure corresponds to cloudy soundings (in the number 32364) in the maps of Figure 5.7.

As for the histograms of $\Delta = \text{Obs} - \text{Calc}$ (Figure 5.12) in clear sky, we see that the mean differences are below 0.3 K, standard deviations are in the range 0.3-0.7 K, and r^2 is above 0.98. In Figure 5.11, the x-axis scale is the same as that used for Figure 5.12, which allows us to compare the variability in cloudy and clear skies properly. The better agreement for the clear sky is partly due to a smaller variability of clear sky atmospheric parameters with respect to q_w , q_i . Therefore, the error of interpolating/extrapolating from the ECMWF grid mesh to that of the IASI soundings is attenuated.

To assess the accuracy over the entire spectral range, we produce plots (presented in Figures from 5.13 to 5.16) comparing the average spectrum obtained from calculations to the average spectrum of the observations. The figures show cloudy/clear and day/night conditions separately. Clear and cloudy calculations (Figures 5.13 and 5.14 respectively) at night agree with IASI observations within 1 K in almost all channels. The mean difference oscillates around the zero line without any systematic discrepancy, except for those expected, corresponding to gas absorption, such as CH_4 , N_2O , and CO for which climatological values are assumed in the simulations.

Conversely, for daytime, a discrepancy in the $4.3 \mu\text{m}$ absorption band of CO_2 is expected due to nonLTE (non Local Thermodynamic Equilibrium) effects, which are not accounted for in the code. The effect of nonLTE is seen in Figure 5.15, which refers to daytime and clear sky. Furthermore, note the excellent agreement at the shortwave window region of the spectrum (mostly above 2400 cm^{-1}), where the reflection of solar radiation in the shortwaves

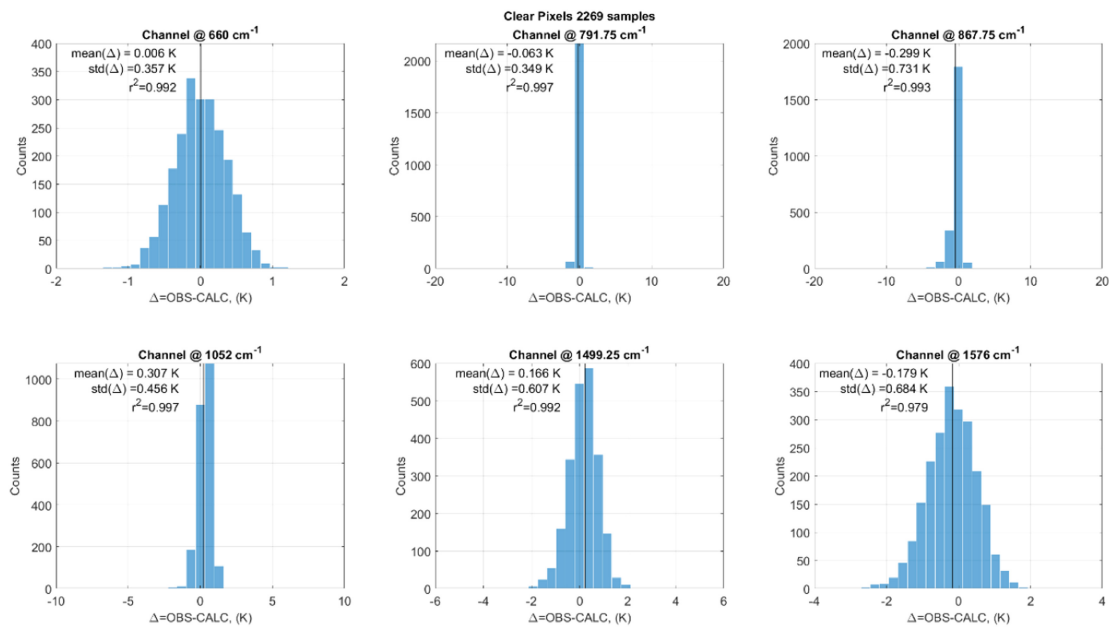


FIGURE 5.12: Histograms of Obs-Calc for the six channels listed in Figure 5.8. The difference in the figure corresponds to clear soundings (in the number 2269) in the maps of Figure 5.7.

needs to be considered. For this band σ -IASI/F2N assumes the Cox-Munk BRDF [52], which is appropriate for clear sky conditions over the sea.

Figure 5.16 shows the comparison for the cloudy condition in the daytime. As expected, significant differences are obtained at around 2100 cm^{-1} because of nonLTE and above 2200 cm^{-1} spectral region because of intense scattering from clouds of solar radiation. These two processes are not yet modeled in the current version of σ -IASI/F2N. In the next version of the code we plan to adopt for the nonLTE approach adopted in SARTA fast models [20].

A systematic difference of about 1 – 2 K in the 8 – 12 μm atmospheric window is observed in the presence of clouds during the day. Note that an excellent agreement was observed for cloudy sky cases during nighttime. Since the methodology used, when compared to the full scattering model at mid-infrared wavelengths, showed to be more accurate than 0.4 K for any realistic cloud conditions [74], the result is unexpected. A possible explanation could be related to photosynthetically active Polar Stratospheric Clouds or PSC [108], which are not represented in the ECMWF analysis. PSC can yield in daylight reactive form of large nitric acid trihydrate (NAT) and ice particles, which add an aerosol load, hence absorption, in the window region. In effect, 2021 has been the year with the largest and longest Antarctic ozone hole, and its formation began in September 2021 (Krummel et al., 2022). Additional information is available in the published paper by Masiello et al. (2024) [77].

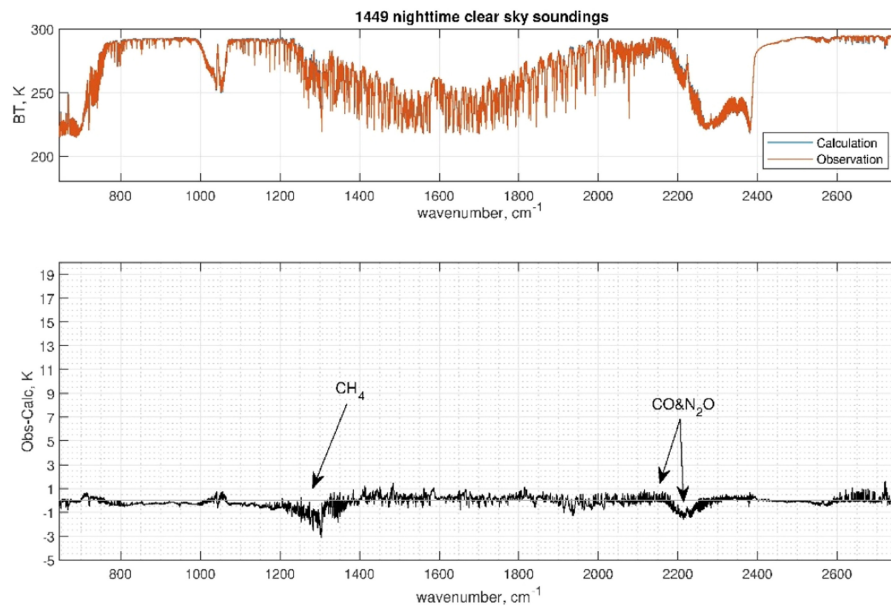


FIGURE 5.13: Observations and Calculations averaged over the whole set of night-time clear sky soundings.

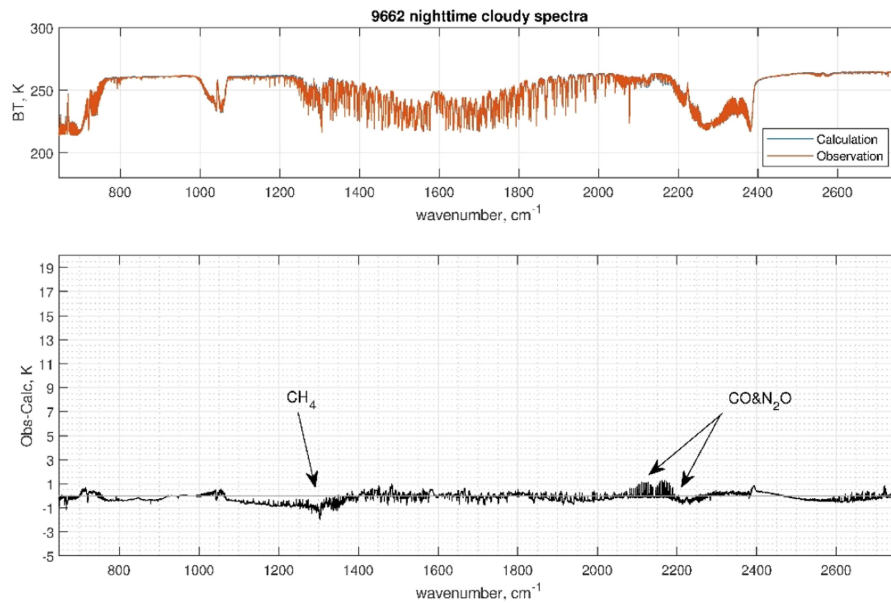


FIGURE 5.14: Observations and Calculations averaged over the whole set of night-time cloudy sky soundings.

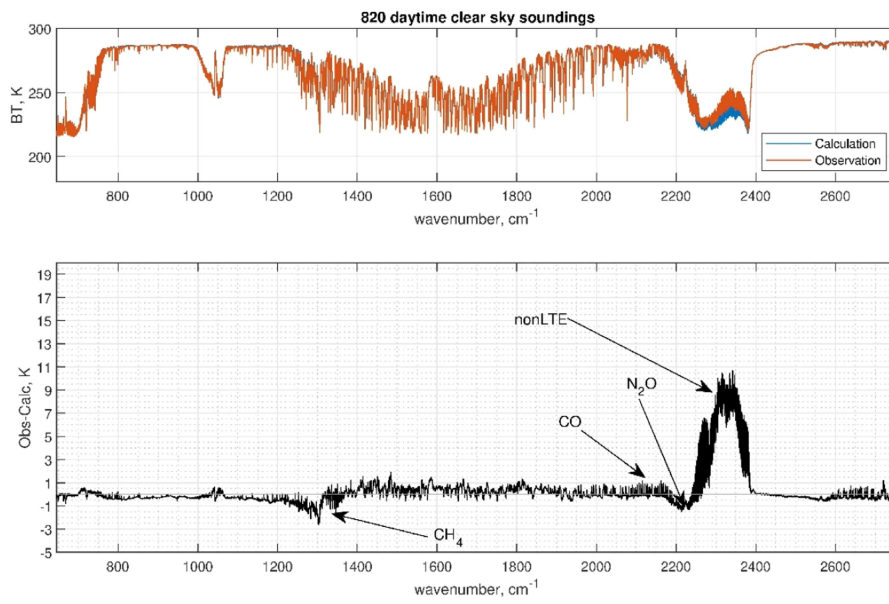


FIGURE 5.15: Observations and Calculations averaged over the whole set of day-time clear sky soundings.

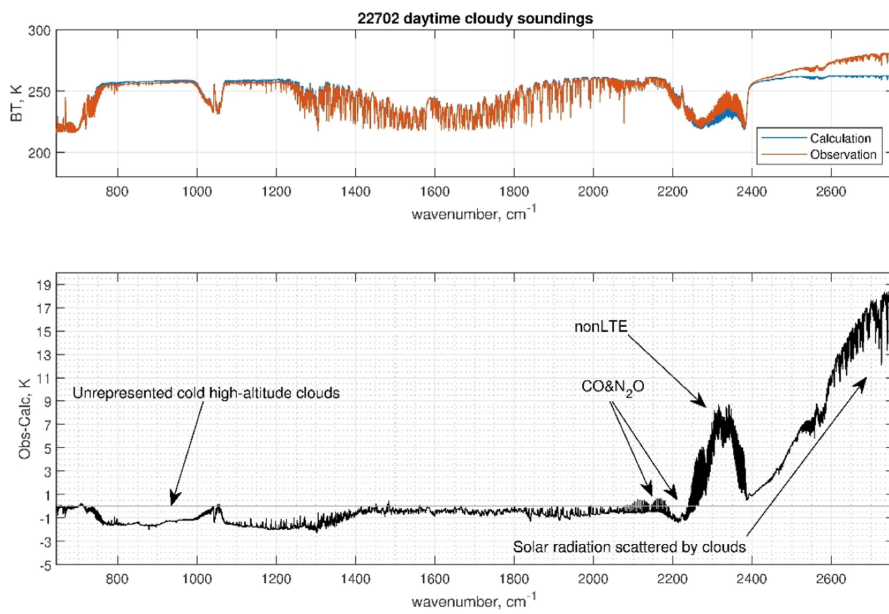


FIGURE 5.16: Observations and Calculations averaged over the whole set of day-time cloudy sky soundings.

5.5 | Final considerations

At the state of art, σ -IASI/F2N can be run in two modes: (i) the C-mode, which implements the Chou scaling approximation as updated according to what is shown in Chapter 3, and (ii) the C-T mode, which embodies the Tang-corrected Chou algorithm, as described in Section 4.3, for the computation of the radiances in the FIR. This choice is also a compromise between the computational efficiency and complexity of the code. A comprehensive comparison of Chou vs. LBLDIS has already been performed in Chapter 3 and published in [74]. The results from that study demonstrated that Chou, once properly updated, performs well over the mid-infrared range. Therefore there is no need for further adjustment of Chou in this range. On the other hand, when the FIR is taken into account, the Tang adjustment becomes important. As detailed in Section 4.3, the application of the Tang correction to the simulation of radiances is not straightforward, and a tuning process of the correction term is needed. We follow what is described in Section 4.3 to determine a correction to the radiances. The C-T mode is computationally more costly than the Chou method alone, for this reason, it is safer to apply it only where it is needed.

The C-mode code performance has been extensively validated in the spectral range 645 to 2760 cm^{-1} using a large dataset of actual IASI observations. The IASI soundings have been collocated with ECMWF analyses, which have provided the basic state vector to perform σ -IASI/F2N calculations. The model shows good agreement with IASI observations, with spectral residuals normally below 1 K, over the whole range of IASI spectra. In the daytime, larger discrepancies are observed, as expected, in the 4.3 μm band of CO_2 because of nonLTE (for both the cloudy and clear sky) and in the shortwave (only for cloudy sky) because of scattering effects from cloud tops. These two processes are not yet included in the code. The spectral range below 1600 cm^{-1} shows good performances for cloudy/clear and day/night conditions, which is suitable for developing a custom version for FORUM and PREFIRE.

In the perspective of applications to FORUM and PREFIRE, which also make observations below 645 cm^{-1} , we have developed a new scaling scheme in the FIR by exploiting a correction term based on the Tang methodology. The proposed approach allows simple correction coefficients that depend on the observational angles. Again, all the radiative properties (including the Tang correction coefficients) are parametrized in terms of the effective radius of the particle size distribution, thus allowing an explicit description of the cloud microphysics and the radiance analytical Jacobians computations.



6 | Asymmetric adjusted scaling for upward radiances computation

The results presented in this Chapter are derived from the work published by Martinazzo and Maestri (2023) [75].

6.1 | Introduction

This Chapter introduces a methodology for the computation of spectrally resolved upwelling radiances in the presence of atmospheric diffusive layers. The algorithm provides fast simulations over the whole longwave spectrum, with high accuracy, particularly for optically thin scattering layers like cirrus clouds. The solution is obtained through a simplification of the multiple scattering term in the general equation of the radiative transfer in plane-parallel assumption. The scattering contribution is interpreted as a linear combination of the mean ambient radiances involved in the forward and backscatter processes which are multiplied by factors derived from the diffusive features of the layer. At this purpose, a fundamental property of the layer is introduced, named angular back-scattering coefficient, which describes the fraction of radiation coming from a hemisphere and back-scattered into a specific direction (the observer in our case). This property, easily derived from the phase function of the particle size distribution, can be calculated from any generic single scattering properties database which allows for simple upgrades of the reference optical properties within the code. The paper discusses the solutions for mean upward and downward ambient radiance and their use in the simplification of the general radiative transfer equation at thermal infrared. To assess the algorithm performances, results obtained with the new algorithm are compared with those derived with a discrete-ordinate based radiative transfer model for a large range of physical and optical properties of ice and liquid water clouds and for multiple atmospheric conditions. It is demonstrated that, for liquid water clouds, its accuracy is mostly within $0.4 \text{ mW}/(\text{m}^2\text{cm}^{-1}\text{sr})$ with respect to the reference code both at far and mid-infrared wavelengths. Ice cloud spectra are also accurately simulated at mid-infrared for all realistic cloud cases which makes the newly introduced solution suitable for the analysis of any spectral measurements of current satellite infrared sounders. At far infrared, its

accuracy is excellent when ice clouds with optical depth less than 2 are considered, which is particularly valuable since cirrus clouds are one of the main targets of the future mission FORUM of the European Space Agency. In summary, the algorithm, from now on called MAMA (Martinazzo-Maestri), allows computations of cloudy sky high-resolution radiances over the full longwave spectrum (4-100 μm) in less than a second (for pre-computed gas optical depths and on a standard personal computer). The algorithm exploits fundamental properties of the scattering layers and the code can be easily updated in relation to new scattering properties.

6.2 | The radiative transfer equation and its approximation

In a plane parallel approximation with azimuthal symmetry, the radiative transfer equation in local thermodynamic equilibrium describing the upward monochromatic radiance I at long-wave wavelengths and in the presence of multiple scattering events is:

$$\mu \frac{dI(\tau, \mu)}{d\tau} = I(\tau, \mu) - [1 - \tilde{\omega}(\tau)] B(\tau) - \frac{\tilde{\omega}(\tau)}{2} \int_{-1}^1 I(\tau, \mu') P(\mu, \mu') d\mu' \quad (6.1)$$

where $\mu = \cos(\theta)$ indicates the direction of observation of the monochromatic radiance I , τ is the integrated optical depth from the top of the atmosphere (TOA) to the level of interest, $\tilde{\omega}$ is the single scattering albedo of the layer at level τ , B is the Planck function at level τ , and $P(\mu, \mu')$ is the azimuthally averaged scattering phase function describing the scattering events for radiation entering the layer at zenith angle μ' and exiting in the μ direction.

An accurate description of the multiple scattering processes (last term of equation 6.1) requires an explicit description of the angular dependence of the radiance field. This leads to an increase in the dimensionality of the problem, which becomes computationally demanding, especially when conducting simulations with high spectral resolution. For computations of cloudy sky spectra in the MIR part of the spectrum (about from 667 to 2500 cm^{-1}) scaling methods, such as the one proposed by Chou [13], provide sufficiently accurate results as shown in Chapter 3, even if initially conceived for computations of spectral irradiance fluxes. The main reason lies in the fact that the spectral signatures of the radiance at atmospheric windows in the mid-infrared are mostly dependent on the clouds absorption features than on scattering ones [69] which can thus be easily approximated by a correction term. Nevertheless, in the FIR part of the spectrum, and mainly around 410 cm^{-1} , the imaginary part of the index of refraction of ice reaches a local minimum making the ice crystal absorption very low and thus enhancing the role of scattering [122]. It is, in fact, demonstrated that in the far-infrared portion of the spectrum, the sensitivity of radiance to the assumed ice habit is notably greater compared to mid-infrared wavelengths [70]; [88]. In this region, simple scaling methods, conceived for fast radiative fluxes computations, fail at reproducing the heterogeneous angular variation of the radiance field when multiple scattering events are occurring [74].

To overcome this problem, a new methodology is presented, which aims at approximating

the radiative transfer equation for the upwelling radiance, with the goal of allowing fast but accurate computations in the presence of clouds and aerosol layers in the infrared part of the spectrum (100-2500 cm^{-1}). The description of the methodology accounts for a simplification of the radiative transfer equation. Following the scheme proposed by Tang et al. (2018) [I06], the multiple scattering integral term is separated into two distinct components, specifically the forward scattering and backward scattering contributions. These components correspond to the last two terms in the following equation 6.2:

$$\mu \frac{dI(\tau, \mu)}{d\tau} = I(\tau, \mu) - [1 - \tilde{\omega}(\tau)] B(\tau) + \frac{\tilde{\omega}(\tau)}{2} \left[\int_{-1}^0 I(\tau, \mu') P(\mu, \mu') d\mu' + \int_0^1 I(\tau, \mu') P(\mu, \mu') d\mu' \right] \quad (6.2)$$

From the above, two average quantities, representative of the upward and downward ambient radiances (respectively $\langle I_u(\tau) \rangle$ and $\langle I_d(\tau) \rangle$) are defined so that equation 6.2 is written as:

$$\mu \frac{dI(\tau, \mu)}{d\tau} = I(\tau, \mu) - [1 - \tilde{\omega}(\tau)] B(\tau) + \frac{\tilde{\omega}(\tau)}{2} \left[\langle I_d(\tau) \rangle \int_{-1}^0 P(\mu, \mu') d\mu' + \langle I_u(\tau) \rangle \int_0^1 P(\mu, \mu') d\mu' \right] \quad (6.3)$$

Note that the integral terms in equation 6.3 depend only on the layer scattering properties. The values of these terms are completely determined once the single scattering properties and the particle size distribution are assumed. It is thus possible to define a new optical parameter, here called the *angular back-scattering coefficient*¹, $c(\mu)$, which describes the fraction of radiation coming from a hemisphere and back-scattered in the μ direction. Formally:

$$c(\mu) = \frac{1}{2} \int_{-1}^0 P(\mu, \mu') d\mu' \quad (6.4)$$

And, since the azimuthally averaged scattering phase function $P(\mu, \mu')$ is normalized, it turns out that:

$$1 - c(\mu) = \frac{1}{2} \int_0^1 P(\mu, \mu') d\mu' \quad (6.5)$$

which defines an *angular forward-scattering coefficient*.

A schematic representation of the angular back-scattering, $c(\mu)$, and forward scattering coefficient, $1 - c(\mu)$, in the zenith direction is provided in Figure 6.1. Note the conceptual

¹The angular back-scattering coefficient is similar to the backscattered fraction for monodirectional radiation defined in Wiscombe and Grams (1976) [I19], Equation 5. However, it has to be noted that, even if the numerical value of these two coefficients are the same for randomly oriented particles, the physical meaning of these quantities are different. Specifically, $c(\mu)$ describes the radiation entering from one hemisphere and backscattered toward the direction μ .

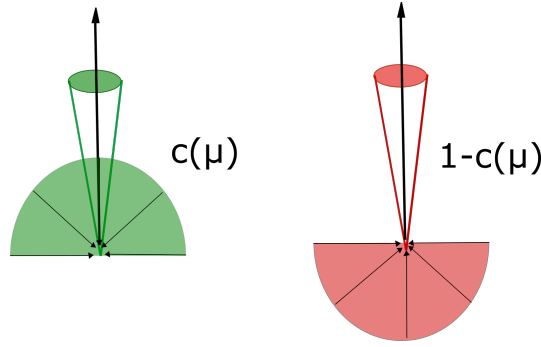


FIGURE 6.1: The angular coefficients $1-c(\mu)$ (red) and $c(\mu)$ (green). The semicircle indicates the hemispheric radiation scattered in the μ direction by the layer. In the figure $\mu = 1$

similarity with the back-scatter parameter b , introduced by Chou, which was used to represent the fraction of radiation back-scattered over a full hemisphere and adopted in flux computations.

To preserve the same structure as Equation 6.2, the averaged terms of equation 6.3 must satisfy the following requirements:

$$\langle I_u(\tau, \mu) \rangle = \frac{\int_0^1 d\mu' I(\tau, \mu') P(\mu', \mu)}{\int_0^1 d\mu' P(\mu', \mu)} \quad (6.6)$$

and

$$\langle I_d(\tau, \mu) \rangle = \frac{\int_{-1}^0 d\mu' I(\tau, \mu') P(\mu', \mu)}{\int_{-1}^0 d\mu' P(\mu', \mu)} \quad (6.7)$$

These two quantities can be interpreted as effective radiances representative of the mean radiation involved in the forward- and back-scattering processes. The exact solutions of equations 6.6 and 6.7 can only be derived when the angular dependence of the radiance field is known. Nevertheless, we can employ certain assumptions to approximate these two terms. In the solution proposed by Chou [13], these two terms are assumed to be isotropic in both the upward and downward hemisphere, and equal to $\langle I_u(\tau) \rangle \approx I(\mu, \tau)$ and $\langle I_d(\tau) \rangle \approx B(\tau)$ respectively. With these assumptions equation 6.1 can be simplified, resulting a Schwarzschild-like equation.

It has been proven that the application of the Chou scheme results in a systematic overestimation of simulated nadir radiances at the TOA [74]. These discrepancies can be primarily attributed to the average quantities employed to approximate equations 6.6 and 6.7, which are larger than their true values. To establish a more accurate computational scheme for upward radiances, it is essential to incorporate a more realistic representation of these two terms.

In this work, we will focus on producing an improved solution for the radiance computation

in the upwelling nadir-looking geometry, i.e. the solution of equation 6.3 for $\mu = 1$. A more general solution encompassing other viewing angles is briefly discussed in Appendix D. By making use of the nadir value of the angular back-scatter and forward-scatter coefficients ($c(\mu = 1)$ and $1 - c(\mu = 1)$) equation 6.3 becomes:

$$\begin{aligned} \frac{dI(\tau, 1)}{d\tau} = I(\tau, 1) - [1 - \tilde{\omega}(\tau)]B(\tau) \\ - \tilde{\omega}(\tau) [\langle I_d(\tau, 1) \rangle c(1) + \langle I_u(\tau, 1) \rangle (1 - c(1))] \end{aligned} \quad (6.8)$$

where the observation zenith angle is set to $\mu = 1$ so that $c(\mu = 1) = c(1)$

6.2.1 | The mean upward ambient radiation $\langle I_u(\tau, \mu) \rangle$

The objective of this paragraph is to provide a solution for the mean upward radiance, shown in equation 6.6, assuming a nadir-looking geometry ($\mu = 1$). An accurate representation of the upward ambient radiation $I(\tau, \mu')$ is required to obtain a satisfactory description of the multiple scattering contribution. In the scaling method proposed by Chou et al. (1999) [13], this quantity is assumed constant over the entire hemisphere, which is not realistic for generic conditions. In fact, $I(\tau, \mu')$ usually decreases as the viewing zenith angle increases. In the present work, it is proposed to assume a simple relation between the ambient radiation $I(\tau, \mu')$ and the cosine of the observational angle μ' . A linear relation (the dependency on the vertical coordinate is implicit) is considered:

$$I(\tau, \mu') = I^\uparrow(\tau) \cdot \mu' + \vec{I}(\tau) \cdot (1 - \mu'), \quad \mu' > 0 \quad (6.9)$$

Where the $I^\uparrow(\tau)$ and $\vec{I}(\tau)$ represent two limit cases: the ambient radiation directed toward $\mu' = 1$ and toward $\mu' = 0$ respectively. The value for the first limit case ($\mu' = 1$) is simply the upward radiance $I(\tau, \mu = 1) = I(\tau, 1)$. On the other hand, when $\mu' = 0$, a proper description for $\vec{I}(\tau)$ needs to be found. For this purpose, the radiative transfer equation in the presence of multiple scattering, using the same assumption made by Chou et al., (1999) is exploited. With the assumption of horizontal symmetry of the problem, the solution is:

$$\vec{I}(\tau) = (1 - \frac{\tilde{\omega}}{2})B(\tau) + \frac{\tilde{\omega}}{2}I(\tau, 1) \quad (6.10)$$

Where $\tilde{\omega}$ is the single scattering albedo of the layer. The detailed derivation of equation 6.10 is described in Appendix B. Given these descriptions of the first and second limit cases ($\mu' = 1$ and $\mu' = 0$ respectively), the ambient radiance (equation 6.9) is written as:

$$I(\tau, \mu') = I(\tau, 1) \cdot \mu' + \left[(1 - \frac{\tilde{\omega}}{2})B(\tau) + \frac{\tilde{\omega}}{2}I(\tau, 1) \right] \cdot (1 - \mu') \quad (6.11)$$

$I(\tau, \mu')$ in equation 6.11 is thus used to explicitly solve the equation 6.6 describing the average upward radiation $\langle I_u(\tau, 1) \rangle$. By making use of the angular back-scattering coefficient, the equation 6.6 is written as follows:

$$\langle I_u(\tau, 1) \rangle = \frac{\frac{1}{2} \int_0^1 d\mu' [I(\tau, 1) \cdot \mu' + [(1 - \frac{\tilde{\omega}}{2})B + \frac{\tilde{\omega}}{2}I(\tau, 1)] \cdot (1 - \mu')] P(1, \mu')}{1 - c(1)} \quad (6.12)$$

Where $c(1) = c(\mu = 1)$ and $P(1, \mu') = P(\mu = 1, \mu')$ as we are considering a nadir-looking case. After few operations, the integral in the numerator of equation 6.12 is easily derived:

$$\begin{aligned} \langle I_u(\tau, 1) \rangle \cdot [1 - c(1)] = & \left[\frac{\tilde{\omega}}{2} I(\tau, 1) + \left(1 - \frac{\tilde{\omega}}{2}\right) B(\tau) \right] \cdot \frac{1}{2} \int_0^1 P(1, \mu') d\mu' + \\ & \left[\left(1 - \frac{\tilde{\omega}}{2}\right) I(\tau, 1) - \left(1 - \frac{\tilde{\omega}}{2}\right) B(\tau) \right] \cdot \frac{1}{2} \int_0^1 P(1, \mu') \mu' d\mu' \end{aligned} \quad (6.13)$$

Note that the first integral term in the numerator (Equation 6.13) is $1 - c(\mu)$. The second integral term, on the other hand, is a new quantity, here called gamma, $\gamma(\mu)$.

$$\gamma(\mu) = \frac{1}{2} \int_0^1 P(\mu, \mu') \mu' d\mu' \quad (6.14)$$

This quantity $\gamma(\mu)$ resembles the asymmetry parameter, from which it differs only for the limits of integration. As the $c(\mu)$ parameter, it is a physical property of the layer that can be easily computed once the single scattering properties and particle size distribution are assumed. If the exit direction is set to $\mu = 1$, the definition of the $\gamma(\mu)$ coefficient is equal to the definition of the asymmetry parameter g over the forward hemisphere. For this reason, the value of $\gamma(\mu)$ gets closer to the value of g as the effective dimension of the particle increases.

Using the definition 6.14, the average upward radiation becomes:

$$\begin{aligned} \langle I_u(\tau, 1) \rangle = & \frac{1}{1 - c(1)} \left(\left[\frac{\tilde{\omega}}{2} I(\tau, 1) + \left(1 - \frac{\tilde{\omega}}{2}\right) B(\tau) \right] (1 - c(1)) + \right. \\ & \left. + \left[\left(1 - \frac{\tilde{\omega}}{2}\right) I(\tau, 1) - \left(1 - \frac{\tilde{\omega}}{2}\right) B(\tau) \right] \gamma(1) \right) \end{aligned} \quad (6.15)$$

Equation 6.15 will be used as the expression of the mean upward radiance to solve the radiative transfer equation 6.3.

6.2.2 | The mean downward ambient radiation $\langle I_d(\tau, \mu) \rangle$

In this paragraph, a solution for the mean downward radiance term present in equation 6.7 is provided for a nadir-looking geometry.

For a non-scattering atmosphere, the radiative transfer equation has a Schwarzschild-like

form and the computation of the downward and upward radiances is independent. This allows to approximate the average downward ambient radiation $\langle I_d(\tau, \mu) \rangle$ with a downward radiance computed at an optimal viewing angle $\tilde{\mu}$. In the proposed scheme, the scaling method derived by Chou et al. (1999) [13] is used for the calculation of the downward radiation, which will be described by an equation (6.16) of the following form:

$$\mu \frac{dI(\tau, \mu)}{[1 - \tilde{\omega}(1 - b)]d\tau} = I(\tau, \mu) - B(\tau), \quad \mu < 0 \quad (6.16)$$

Where b is the back-scattering coefficient as defined by Chou [13]. In the present context, a suitable description for the downward ambient radiation $I(\tau, \mu')$ is obtained by solving equation 6.16 at an optimal observation angle $\tilde{\mu}$:

$$\tilde{\mu} \frac{dI(\tau, \tilde{\mu})}{[1 - \tilde{\omega}(1 - b)]d\tau} = I(\tau, \tilde{\mu}) - B(\tau) \quad (6.17)$$

It is assumed that $\tilde{\mu}$ is the cosine of an effective zenith angle $\theta = -60.0$ degrees ($\tilde{\mu} = 0.5$). The ambient downward radiation at level τ ($I(\tau, \mu')$) is therefore taken equal to the solution of equation 6.17:

$$I(\tau, \mu') = I(\tau, \tilde{\mu}), \quad \mu' < 0 \quad (6.18)$$

And equation 6.7 becomes:

$$\langle I_d(\tau, 1) \rangle = \frac{\int_{-1}^0 d\mu' I(\tau, \tilde{\mu}) P(\mu', 1)}{\int_{-1}^0 d\mu' P(\mu', 1)} = I(\tau, \tilde{\mu}) \quad (6.19)$$

Note that, for a single homogeneous layer, an analytical solution of equation 6.17 can be obtained for $I(\tau, \tilde{\mu})$. Setting $\tau = 0$ at the top of the layer, it is derived that:

$$\langle I_d(\tau, 1) \rangle = I(\tau, \tilde{\mu}) = I(0, \tilde{\mu}) e^{-\alpha_c \tau / \tilde{\mu}} + \left[1 - e^{-\alpha_c \tau / \tilde{\mu}} \right] B(\tau) \quad (6.20)$$

where $\alpha_c = 1 - \tilde{\omega}(1 - b)$ is the scaling term proposed by [13], $I(0, \tilde{\mu})$ is the boundary condition at the top of the layer, and $B(\tau)$ is the Planck function, at level τ , which is considered constant within the layer thickness.

Note that, in any radiative transfer model, the diffuse downward radiance needs to be computed to account for the surface reflection. For this reason, the computation of the mean downward ambient radiation comes at almost no cost.

6.2.3 | Solution of the radiative transfer equation

In the previous sections, the descriptions of the average upward and downward ambient radiation are obtained (respectively equation 6.15 and 6.19). These results are used to solve the equation for the upwelling radiance (equation 6.8), whose expression becomes:

$$\begin{aligned}
\frac{dI(\tau)}{d\tau} &= I(\tau) - [1 - \tilde{\omega}(\tau)] B(\tau) + \\
&\quad - \tilde{\omega} \left[\left[\frac{\tilde{\omega}}{2} I(\tau) + \left(1 - \frac{\tilde{\omega}}{2} \right) B(\tau) \right] (1 - c) + \right. \\
&\quad \left. + \left[\left(1 - \frac{\tilde{\omega}}{2} \right) I(\tau) - \left(1 - \frac{\tilde{\omega}}{2} \right) B(\tau) \right] \gamma \right] + \\
&\quad - \tilde{\omega} c I(\tau, \tilde{\mu})
\end{aligned} \tag{6.21}$$

where the dependency on $\mu = 1$ (nadir view) is made implicit. After some algebra, equation 6.21 is re-arranged:

$$\begin{aligned}
\frac{dI(\tau)}{d\tau} &= \left[1 - \tilde{\omega}\gamma - \frac{\tilde{\omega}^2}{2} (1 - c - \gamma) \right] I(\tau) + \\
&\quad - \left[1 - \tilde{\omega}(c + \gamma) - \frac{\tilde{\omega}^2}{2} (1 - c - \gamma) \right] B(\tau) + \\
&\quad - \tilde{\omega} c I(\tau, \tilde{\mu})
\end{aligned} \tag{6.22}$$

To improve its readability, the first coefficient on the right-hand-side of equation 6.22 is indicated as α :

$$\alpha = 1 - \tilde{\omega}\gamma - \frac{\tilde{\omega}^2}{2} (1 - c - \gamma) \tag{6.23}$$

This allows to rewrite the equation 6.22 in a very simple form:

$$\frac{dI(\tau)}{d\tau} = \alpha I(\tau) - [\alpha - \tilde{\omega}c] B(\tau) - \tilde{\omega} c I(\tau, \tilde{\mu}) \tag{6.24}$$

This is the final form of the equation used by the MAMA algorithm to compute the upwelling radiance in a nadir-looking geometry. This solution can be viewed as an adjusted asymmetrical scaling, as $I(\tau)$ and $B(\tau)$ are scaled with two different parameters, and the last term adjusts for the backscattered radiation.

This equation requires the computation of fundamental optical properties of the scattering layers such as the c , $\tilde{\omega}$ and γ and the Chou backscatter parameter b which is hidden in the last term of equation 6.24. The latter is solved by using equation 6.17. For an in-depth analysis of the newly defined scattering parameters see Appendix C

Equation 6.24 allows for simple analytical solutions. Since the computation of the upward radiance can be made layer by layer, the focus is posed on single homogeneous layers. To simplify the problem, the temperature inside the layer can be assumed constant. This assumption is generally accurate only for sufficiently thin layers. However, the solution for layers where the temperature vary linearly with the vertical coordinate is also easy to compute. Using 6.20 into 6.24, and solving for $I(\tau)$, the nadir-looking radiance at the top of the layer is derived as:

$$I(\tau) = [1 - e^{-\alpha\tau}] B(\tau) + \left[1 - e^{-\left(\frac{\alpha_c}{\tilde{\mu}} + \alpha\right)\tau}\right] \frac{\tilde{\omega}c[I(0, \tilde{\mu}) - B(\tau)]}{\frac{\alpha_c}{\tilde{\mu}} + \alpha} \quad (6.25)$$

In conclusion, it is interesting to note that if we assume that the downward radiation is well described by the black body emission from the layer $I(\tau, \tilde{\mu}) = B(\tau)$ (as done in the Chou theory) the equation 6.24 simplifies into the:

$$\frac{dI(\tau)}{\alpha d\tau} = I(\tau) - B(\tau) \quad (6.26)$$

which can be interpreted as a new scaling method where an apparent absorption optical depth is defined as $\tau_a = \alpha\tau$. The simplification has the advantage of being very easy to implement. Nevertheless, it produces a general overestimation in the upward radiance field at far and mid-infrared wavelengths, such as Chou's solution (not shown). For this reason, the solution obtained from equation 6.25 is the one considered in the MAMA algorithm.

6.3 | Methods and Results

As done for the study presented in Chapter 3 and Section 4.3, the results obtained from the comparison between the new solution and the reference methodology are here presented. The reference results are obtained from the DISORT routine [103] in the LBLDIS (LBLRTM + DISORT) [109] code chain. LBLDIS uses the optical depths computed by LBLRTM [15] and the DISORT v2.0 routine to solve the radiative transfer problem in the presence of multiple scattering layers.

The vertical profiles of the concentration of the main gas species active at FIR and MIR wavelengths are obtained from the climatological database IG2 v5.7 [92], and are calculated in order to be representative of low-, mid-, and high-latitude atmosphere. The database is used for the specification of the pressure, temperature and gas volume mixing ratio for the following molecules (including isotopes): H_2O , CO_2 , O_3 , N_2O , CO , CH_4 , O_2 , NO , SO_2 , NO_2 , NH_3 , and HNO_3 . Figure 6.2 shows the vertical profiles of temperature and water vapor mixing ratio, from the ground up to 20 km height, for the three scenarios considered which are representative of low, medium, and high latitudes.

For each one of the three scenarios reported in figure 6.2, the presence of a single ice or liquid water cloud is assumed. Multiple conditions are considered which account for different cloud heights, optical depths, and microphysical parameters (i.e. the effective radius of the particle size distribution). A focus is posed on cirrus clouds and low level water clouds. In case of medium-high clouds the geometrical parameters (altitude of the height and thickness) are defined in accordance with the statistics found by [113] which is obtained by a global analysis of CALIOP data. The goal is to have an accurate characterization of the cirri which are one of the goals of the FIR observations which will be performed by the FORUM mission. In the case of low liquid water clouds generic features are assumed for layers below 3 km of altitude. The main parameters used for the characterization of the clouds in the radiative transfer computations are briefly described in the following sub-section.

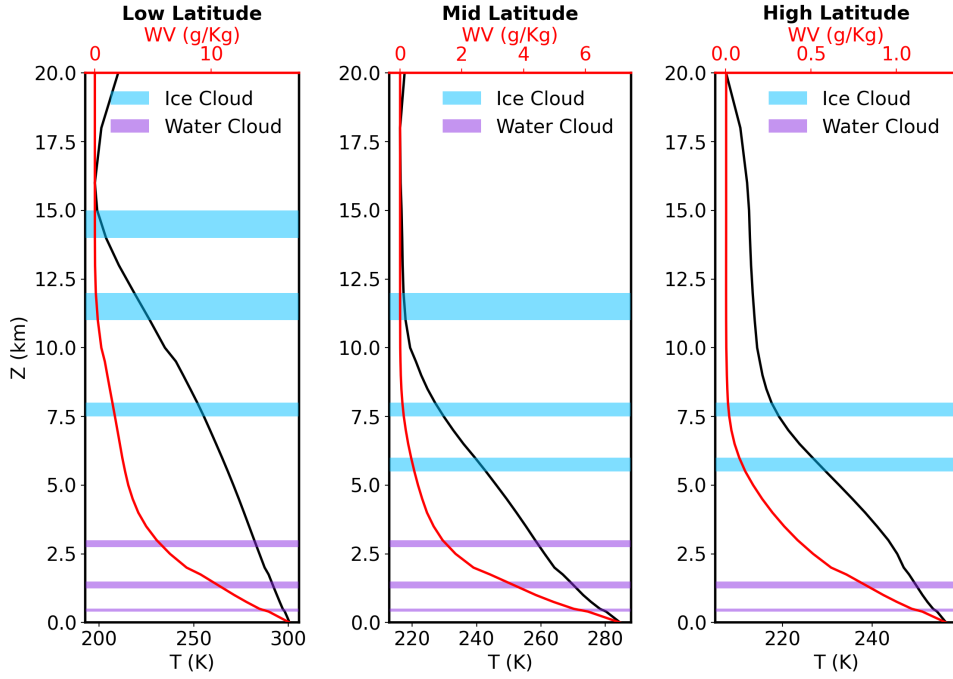


FIGURE 6.2: Temperature (black solid line) and water vapor mixing ratio (red dashed line) vertical profiles for three different scenarios. Light blue and purple shaded bands indicate the height position and thickness of the ice and liquid water clouds, respectively, used in the computations.

6.3.1 | Assumptions on Liquid Water and Ice Clouds

We consider liquid water clouds composed of water spheres, whose optical properties are generated by using a Mie solution-based algorithm. The Mie code is the Scattlay model [89] which allows for the computation of scattering coefficients, efficiency factors, and scattering phase functions for single, isolated, spherical particles from complex refractive indices [24, 116]. The optical properties are then combined to obtain the bulk radiative properties for the particle size distributions (PSDs) representative of the cloud layer, across the desired spectral range.

The analytical PSDs assumed to model the low-level water clouds are lognormal distributions [82], whose number of particles per unit volume is given by:

$$n(r) = \frac{n_0}{r\sqrt{2\pi}\sigma} \exp\left\{-\frac{(\ln(r) - \ln(r_m))^2}{2\sigma^2}\right\} \quad (6.27)$$

where r is the particle radius, r_m is the mode radius of the distribution, σ is the scale parameter, and n_0 is a normalization factor depending on the total number of particles per volume used in the radiative transfer computations. According to [82], assuming low-level

stratiform clouds, the average value for the scale parameter is set to $\sigma = 0.38$ and considered constant. This allows us to refer to different PSDs only by using their effective radius r_{eff} , which is defined as the fraction of the third to the second moment of the particle size distribution:

$$r_{\text{eff}} = \frac{\int_0^{\infty} r^3 n(r) dr}{\int_0^{\infty} r^2 n(r) dr} \quad (6.28)$$

It is easy to prove that for a lognormal PSD, the relation between effective and mode radius is governed by the following:

$$r_{\text{eff}} = r_m \cdot \exp\left\{\frac{5}{2}\sigma^2\right\} \quad (6.29)$$

The simulations are performed considering different effective radii, optical depths (OD, at 900 cm^{-1}), and cloud heights. The equation defining the total OD for a vertically homogeneous cloud with a geometrical thickness Δz is given by:

$$OD = N_{\text{tot}} \cdot \beta(r_{\text{eff}}, 900) \cdot \Delta z \quad (6.30)$$

where $\beta(r_{\text{eff}}, 900)$ is the extinction coefficient at 900 cm^{-1} of the PSD corresponding to a specific effective radius, normalized to a single particle per unit of volume. Finally, N_{tot} represents the total number of particles in the considered volume.

Ice clouds observed in nature show multiple crystal shapes, depending on the cloud thermodynamic conditions, formation processes, and evolution. In this work, we refer to ice clouds as PSDs of aggregates of eight hexagonal ice columns, whose single particle radiative properties are described by [122].

A commonly assumed PSD for ice clouds is the three parameters gamma type distribution, here below written as a function of D , which is the maximum dimension of the ice particle:

$$n(D) = n_0 D^\mu \exp\{-\lambda D\} \quad (6.31)$$

where n_0 is the normalization factor, μ is the shape parameter, and λ is the slope parameter. An average value of $\mu = 7$ is assumed in this work. For positive values of μ the shape of the gamma distribution is of under-exponential type and the maximum of the distribution lies in between the minimum and maximum dimension of the crystals. As for the case of water clouds, assuming a constant value for μ allows us to describe the different PSDs using the effective dimension only. For non-spherical particles, an effective dimension of the distribution can be defined as:

$$D_{\text{eff}} = \frac{3 \int_0^{\infty} dDV(D)n(D)}{2 \int_0^{\infty} dDA(D)n(D)} = 2r_{\text{eff}} \quad (6.32)$$

where $A(D)$ and $V(D)$ are the cross-sectional area and the volume of the particle with maximum dimension D .

The atmospheric profiles and cloud properties described above are used as inputs for a wide

range of simulations. Table 6.1 summarizes the main cloud parameters used in the simulations and their range of variation.

TABLE 6.1: The main cloud parameters (and their range) used for the simulation comparisons.

Particle type	PSD type (fixed parameter)	r_{eff} (μm)	Top Height (km)	OD (at 900 cm^{-1})
Liquid water droplets	lognormal ($\sigma=0.38$)	1–20	0.5–3	1–50
Ice Aggregates crystals	gamma ($\mu=7$)	4–50	6–15	0.1–20

6.3.2 | Comparison with the reference Model

The radiative transfer code LBLRTM is exploited for the generation of gaseous optical depths. The gas ODs are then, respectively, ingested by the DISORT routine and a Python script implementing the MAMA algorithm. For comparison, a set of simulations based on the scaling method proposed by Chou et al. (1999) [13] is also performed for each simulated condition. Radiance simulations are run at 0.01 cm^{-1} for both the new method and the full-scattering solution. The number of streams used in the DISORT simulations is 18 which is considered a reasonable trade-off between accuracy and computational time. Successively, high spectral resolution radiances are convolved to the nominal FORUM Sounding Instrument resolution of 0.5 cm^{-1} by using a sinc function. To evaluate the accuracy of the approximate methodology, we compare the FORUM-like radiance values obtained from the MAMA solution to those obtained using the discrete ordinate method. Specifically, the differences are computed as shown in equation 6.33:

$$\Delta I = I_M - I_{FS} \quad (6.33)$$

where I_M is the radiance obtained from the MAMA methodology (or the Chou scaling method) and I_{FS} from the reference (Full-Scattering) radiative transfer model. The differences between the computed values (ΔI) are compared to the goal noise equivalent spectral radiance (NESR) of the FORUM mission. This approach provides a metric to determine whether the differences ΔI are within acceptable limits. Specifically, the FORUM goal NESR is $0.4\text{ mW}/(\text{m}^2\text{cm}^{-1}\text{sr})$ within the $200\text{--}800\text{ cm}^{-1}$ spectral region and $1.0\text{ mW}/(\text{m}^2\text{cm}^{-1}\text{sr})$ outside (https://esamultimedia.esa.int/docs/EarthObservation/FORUM_MRD_v2.0_091220_issued.pdf)

Liquid Water Cloud

Low-level liquid water cloud spectra for the three climatological profiles using multiple values of cloud top height, effective radii, and optical depth are computed. A first example of comparison comprising the full spectrum is reported in Figure 6.3 for a mid-latitude cloud

layer with optical depth of 10 and altitude placed at 3.0 km . The difference with respect to the reference code (ΔI) are calculated as shown in equation 6.33 for both the MAMA solution and the Chou scaling method. The shaded grey area indicates the range of the goal FORUM NESR.

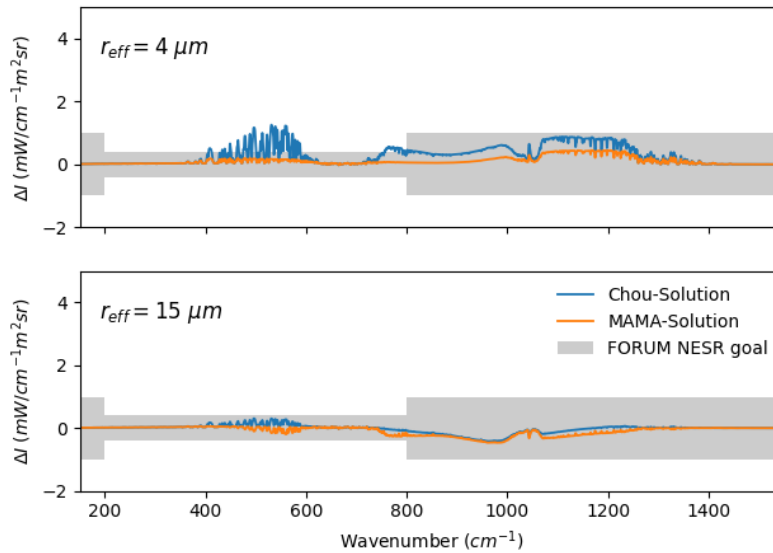


FIGURE 6.3: Top panel: radiance differences between approximate solutions (Chou’s scaling method in blue and MAMA solution in orange) and the reference approach for a mid-latitude water cloud with $OD = 10$, $r_{eff} = 4\ \mu\text{m}$ and cloud top at 3 km . Bottom panel: the same as upper panel, but for an effective radius of $15\ \mu\text{m}$. The range of values of the FORUM NESR are highlighted by a grey shaded area.

Both solutions show a ΔI nearly zero at small and large wavenumbers, i.e., below 350 cm^{-1} and above 1400 cm^{-1} which are spectral intervals affected by high atmospheric absorption caused by water vapor. Similarly, the strong absorption due to the CO_2 band around 667 cm^{-1} masks completely the cloud effects on the top-of-atmosphere radiance. Figure 6.3 highlights that the MAMA methodology accurately simulates the considered water clouds at any wavenumber in the longwave part of the spectrum. Notably, the newly introduced method achieves accurate results also for small effective radii of the PSD, which is typically challenging for scaling methods [74] due to the enhanced multiple scattering effects.

To provide a comprehensive assessment of the accuracy of this algorithm compared to the reference solution, a set of results is reported in Figures 6.4 and 6.5. The multiple panels of the figures show the radiance differences evaluated at two specific wavenumbers representative of the MIR (1203 cm^{-1}) and the FIR (531 cm^{-1}) for various atmospheric and liquid water cloud conditions. The selected wavenumbers constitute the worst cases in terms of radiance differences in the mid- and far-infrared regions. The values are displayed as a function

of cloud OD and effective radius to assess the dependence of the results on these parameters. Note that, for both Figure 6.4 and 6.5, the panel accounting for liquid water clouds at high latitudes and with cloud top at 3 km is not plotted due to the rare occurrence of these conditions.

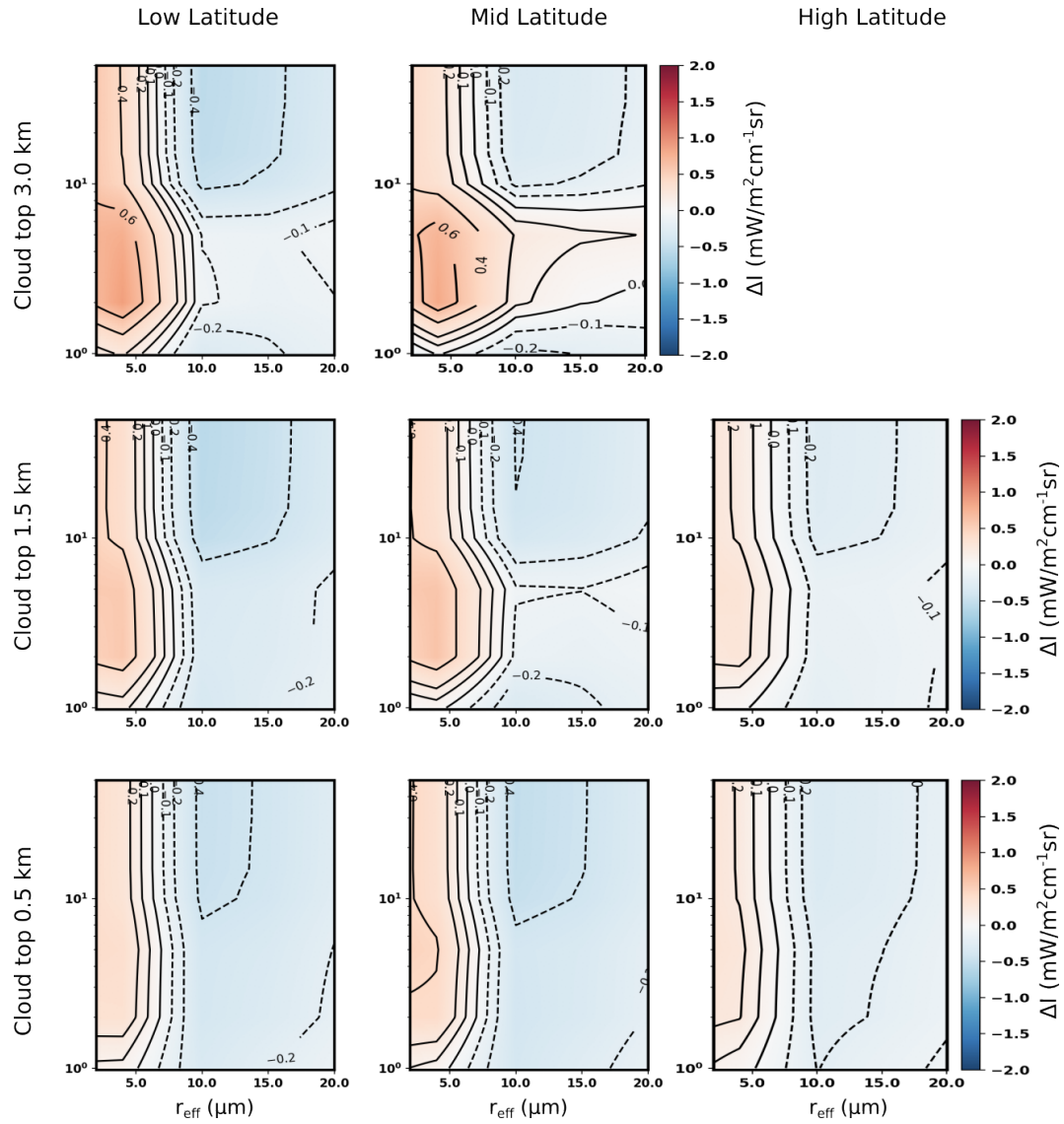


FIGURE 6.4: Radiance differences (ΔI) between the MAMA and the reference solution at 1203 cm^{-1} (MIR), for multiple liquid water clouds (varying ODs and r_{eff}) and atmospheric conditions (Low, Mid and High latitude). If present, the red and blue contour lines highlight the regions where the differences values are above the goal FORUM NESR.

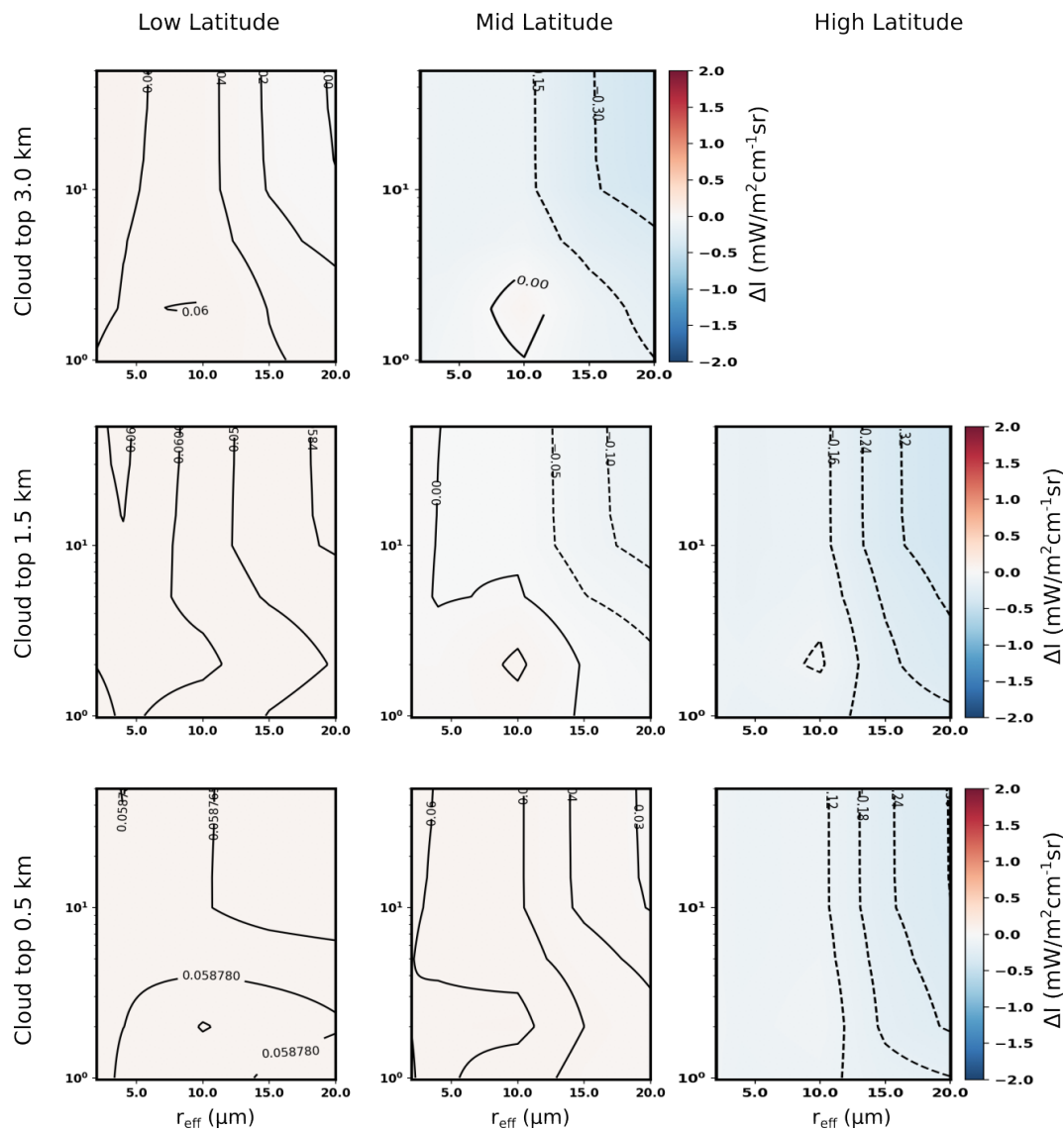


FIGURE 6.5: Same as Figure 6.4 but for radiance differences (ΔI) at 531 cm^{-1} (FIR).

The contour lines in the figures show the ΔI values in units of $\text{mW}/(\text{m}^2\text{cm}^{-1}\text{sr})$. As a term of comparison, the FORUM NESR goal is $1.0\text{ mW}/(\text{m}^2\text{cm}^{-1}\text{sr})$ at 1203 cm^{-1} and $0.4\text{ mW}/(\text{m}^2\text{cm}^{-1}\text{sr})$ at 531 cm^{-1} . The plots are meant to provide a detailed overview of the accuracy of the MAMA computational method for various atmospheric and liquid water cloud conditions.

Figure 6.4 and 6.5 highlight the effectiveness of the new methodology in computing top of the atmosphere radiances in the presence of water clouds. The new solution is capable to obtain accurate simulations (with respect to the FORUM NESR goal) for all the atmospheric and cloud conditions considered which includes very extreme cases such as high op-

tical depths and small effective radii (and vice versa). This holds over the entire spectral region considered (FIR and MIR) and also when small effective radii of the PSD are assumed. For r_{eff} larger than $10 \mu m$, the new solution produces a slight underestimation of the upwelling radiance which is anyway less than $0.4 \text{ mW}/(\text{m}^2\text{cm}^{-1}\text{sr})$ and thus smaller than the FORUM NESR.

At FIR wavenumbers and in a tropical scenario (first column of Figure 6.5) the radiance differences are close to zero for all the studied cases also because of the attenuating effect of precipitable water vapor (PWV) above the cloud layers, which is related to the upper atmospheric layer transmissivity. The higher the PWV above the cloud top level, the smaller the radiance difference. This masking effect becomes particularly effective for PWV values larger than about 4 mm [74] and it is the reason of why radiance differences (slightly) increase with the increasing cloud top for a fixed latitude, as well as with increasing latitude for fixed cloud top height.

Ice Cloud

The spectral radiance differences between simulations obtained using the MAMA code and the reference algorithm (DISORT) are evaluated also in the presence of ice clouds. Figure 6.6 illustrates a result for a full spectrum where the top of the atmosphere radiance differences are plotted for a mid-latitude cirrus cloud (top altitude placed at 8 km) and for two different effective radii ($r_{eff} = 20$ and $r_{eff} = 30 \mu m$). The cloud OD is set to unity so that the multiple scattering effects are maximized [70] and the quality of the scaling method can be tested in challenging configurations. The results show the excellent level of agreement of the new approach with the reference solution over the entire spectral range considered. Specifically, the MAMA code performs significantly better than the Chou scaling method in reproducing the spectral radiance at FIR wavenumbers where scattering effects are amplified by the minimum in ice absorption (with maximum effect at around 410 cm^{-1}).

The overall accuracy of the new methodology for different atmospheric and ice cloud conditions is evaluated at two wavenumbers. The chosen wavenumbers are representatives of the highest spectral discrepancies along the spectrum between the MAMA and the reference code solution in the MIR and FIR spectral regions considered. The multiple panels in Figures 6.7 and 6.8, show the ΔI values at 1203 cm^{-1} and 410 cm^{-1} for three typical atmospheric conditions (Low, Mid and high latitudes), and for varying cloud altitude, OD, and effective radius. A logarithmic scale is used on the OD axis to highlight the method accuracy at small values of cloud optical depths (i.e. $OD \leq 2$) since the study of cirrus clouds is one of the targets of the FORUM mission. Note that ice clouds with top altitudes higher than 12 and 8 km are not considered for Mid Latitude and High Latitude conditions respectively due to their rare occurrence. Similarly, low level ice clouds at Low Latitudes are ignored; in this case, the high concentration of water vapor in the upper layers of the tropical atmosphere makes the FIR channels almost opaque to low-medium level clouds.

Figure 6.7 displays the radiance differences at MIR (1203 cm^{-1}). The computed ΔI values are small all over the entire set of scenarios considered, with the exception of cloud cases characterized by high altitudes, small effective radii ($r_{eff} < 15 \mu m$) and OD around 5. The

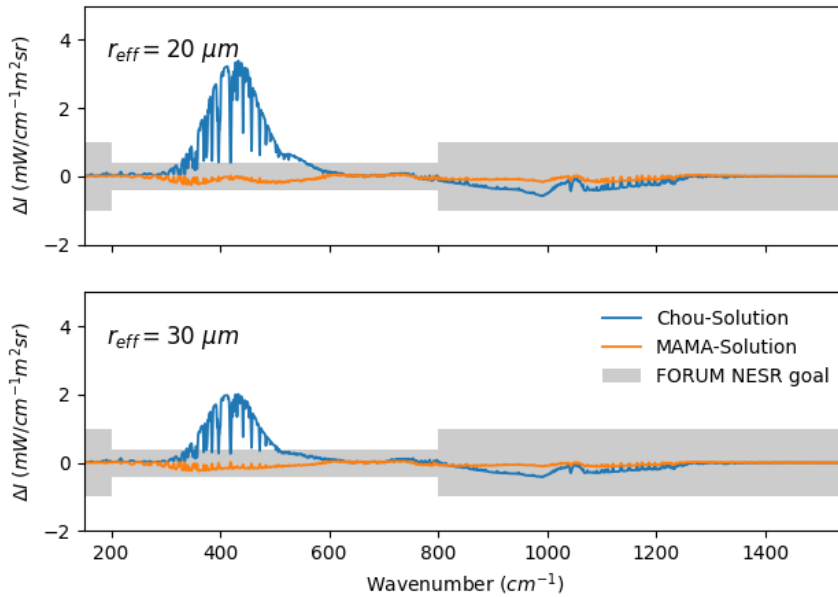


FIGURE 6.6: Top panel: radiance differences between the approximate solutions (Chou’s scaling method in blue and MAMA in orange) and the reference algorithm in the presence of a mid latitude ice cloud with $OD = 1$, $r_{eff} = 20 \mu m$ and top altitude at $8 km$. Bottom panel: the same as above, but for an effective radius of $30 \mu m$. The range of values of the FORUM NESR are highlighted by a grey shaded area

predominantly pale color in most of the panels of the figure indicates that the difference between the two solutions is lower than the FORUM NESR goal at that particular wavenumber. The results confirm the reliability of the MAMA methodology at mid-infrared (MIR) wavelengths for the simulation of both thick ice clouds and cirrus clouds. It’s worth noting that the monthly mean effective radius derived from MODIS AQUA L3 products for analogous scenarios is approximately 30 micrometers in the presence of ice clouds (including cirrus) [90].

Simulations at $410 cm^{-1}$ are reported in Figure 6.8 which shows that the MAMA solution deviates from the reference code only for OD greater than 5 and small effective radii ($r_{eff} < 15 \mu m$). For optically thin cirrus clouds ($OD < 2$), areas with ΔI values lower than FORUM NESR are observed almost independently of the assumed effective dimension of the PSD. As the cloud OD increases, the accuracy of the solution gets worse, and the synthetic radiances are slightly overestimated in the case of small effective radii and underestimated for large ones. Nevertheless, the overestimation never exceeds $2 mW/m^2 cm^{-1} sr$. The values reported in Figure 6.8 represent the largest discrepancies in terms of radiance across the entire FORUM spectrum.

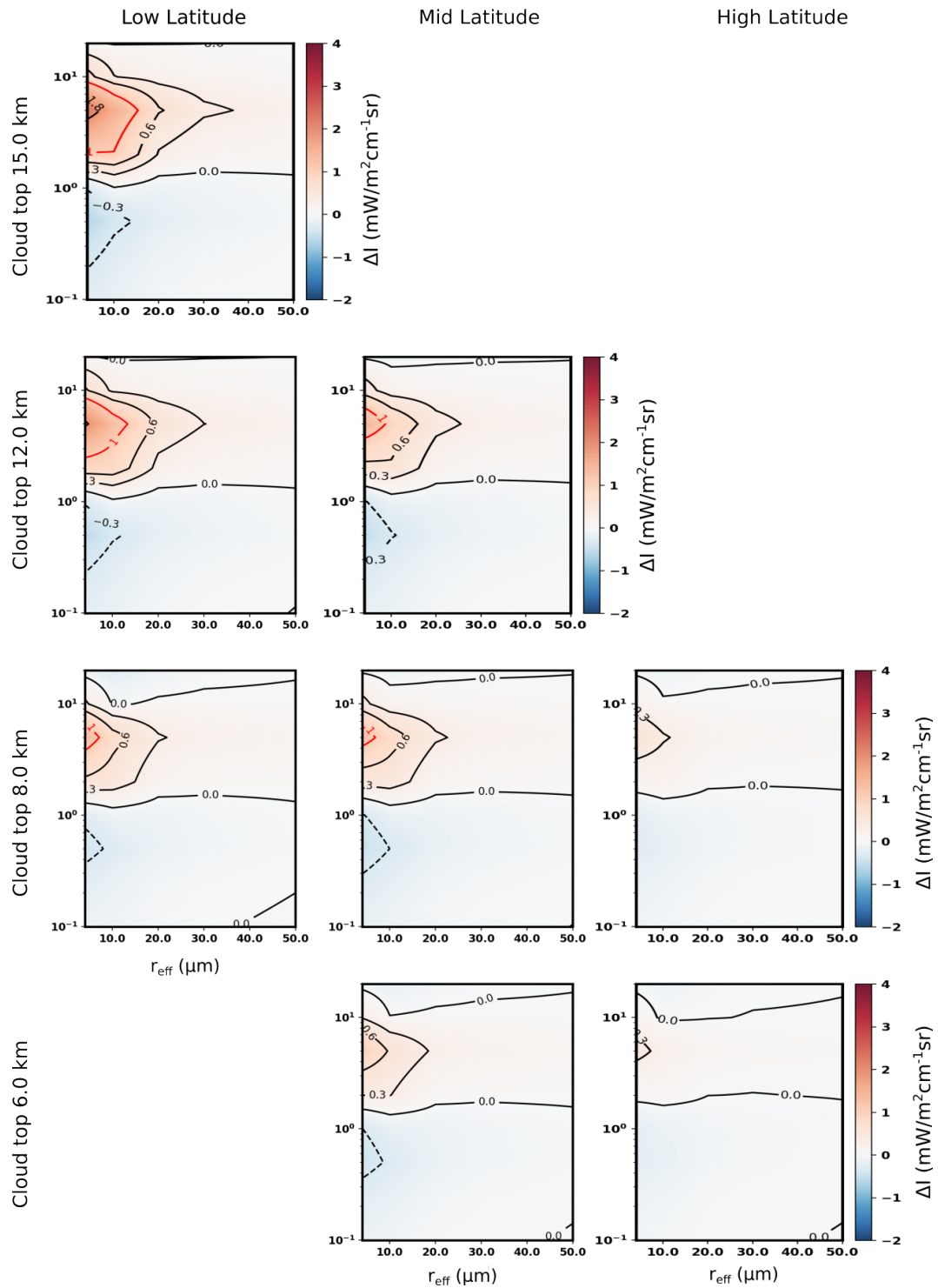


FIGURE 6.7: Radiance differences (ΔI , contour) between the MAMA and the full-physics solution at 1203 cm^{-1} (MIR), for multiple ice clouds (varying ODs and r_{eff}) and atmospheric conditions (Low, Mid and High latitude). If present, the red and blue contour lines highlight the regions where the differences values are above the goal FORUM NESR.

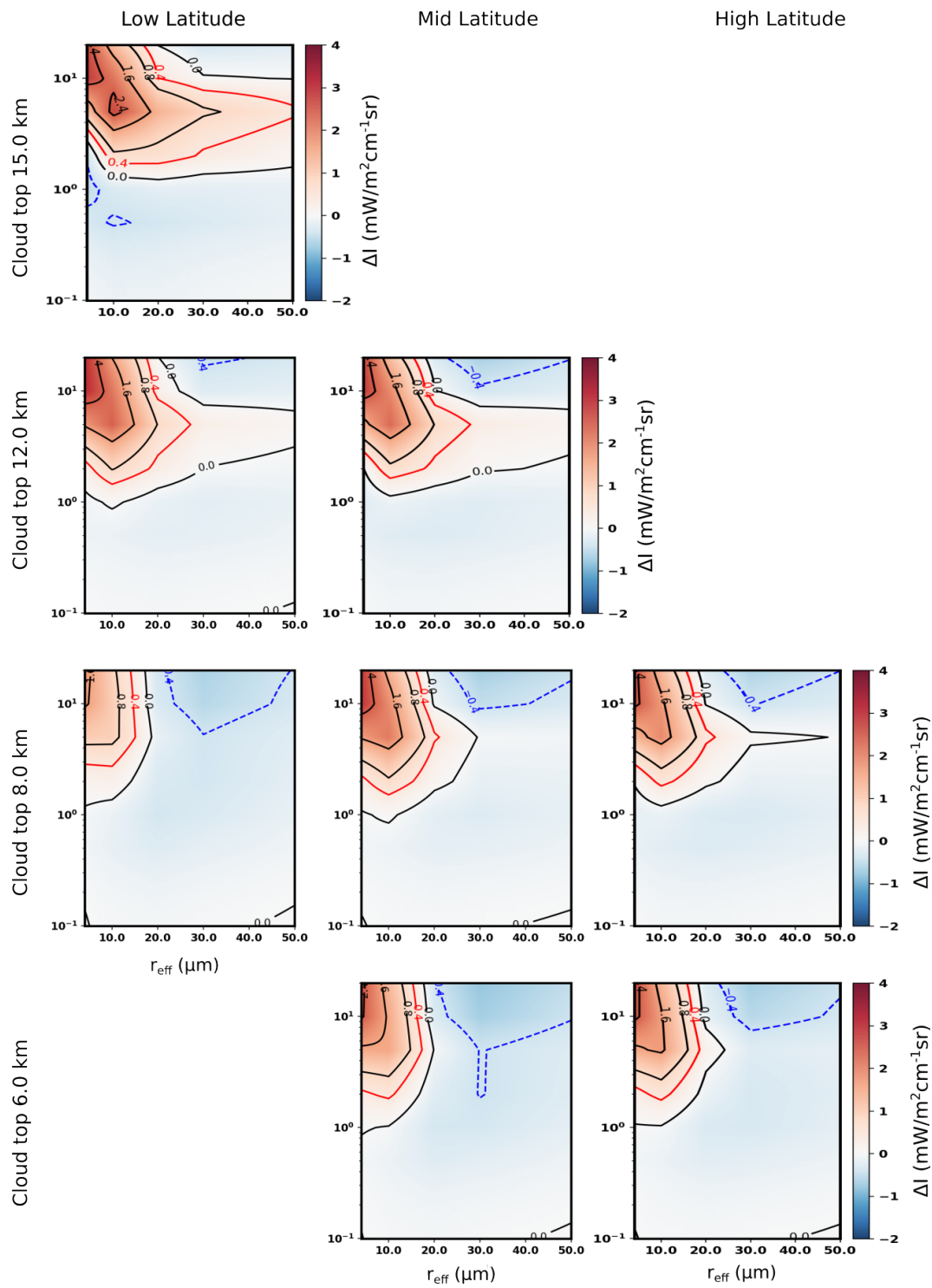


FIGURE 6.8: Radiance differences (ΔI , contour) as in Figure 6.7 but for values at 410 cm^{-1} (FIR).

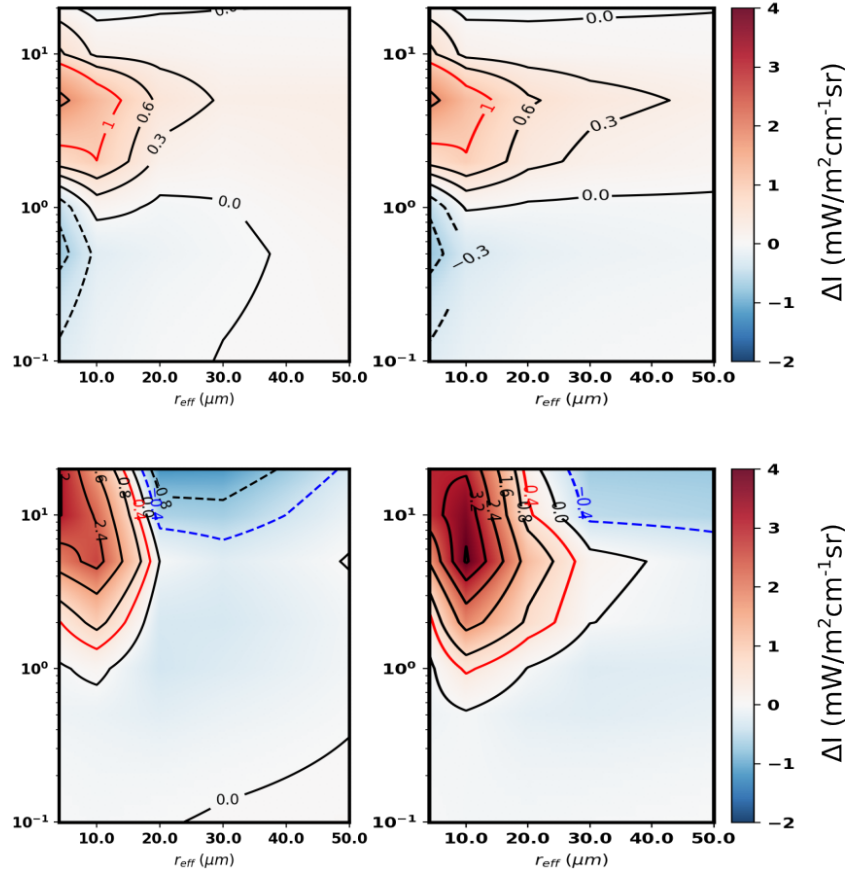


FIGURE 6.9: Top panels: Radiance differences (ΔI , contour) between the MAMA and the full-physics solution at 1203 cm^{-1} (MIR), for ice clouds characterized by plates crystals (left panel) and solid columns (right panel) and varying ODs and r_{eff} . The cloud is placed at 12 km of altitude and in tropical conditions (Low latitude). Red and blue contour lines indicate the regions where the differences values are above the goal FORUM NESR. Bottom panels: same as above but at 410 cm^{-1} (FIR).

The MAMA method is implemented for different particle habits available in the reference single scattering single particle dataset [122]. For comparison, an example of the results obtained for other habits is reported in Figure 6.9. The upper panels refer to ΔI obtained for tropical atmospheric scenario and ice clouds with top height of 12 km when the 1203 cm^{-1} wavenumber is considered. The simulations are performed considering plate (left panel) and solid column (right panel) ice crystals. The lower panels show results for the wavenumber at 410 cm^{-1} . The results are in accordance with the simulations obtained when in the presence of column aggregate particles and show the capability of the MAMA methodology to accurately simulate spectral radiances for optically thin clouds ($OD < 2$) also at FIR spectral

bands.

6.4 | Final considerations

In this Chapter a new radiative transfer methodology for spectral infrared simulations in the presence of cloud is presented. The computational algorithm takes inspiration from scaling methods, however, it is tailored to compute the up-welling radiance in the presence of any type of scattering layers. Scaling methods have become very popular in the radiative transfer modeling community due to their theoretical simplicity and ease of implementation. In general, these methods (e.g. [13]) allow clear sky radiative transfer models to simulate cloudy conditions maintaining the same computational structure by approximating the scattering processes with scaled absorption properties. Since the scaling approach is usually based on simplistic assumptions concerning the down-welling radiation, correction terms are often introduced (as in [106]), which slightly complicate the computational algorithm's structure. While scaling methodologies were developed for broadband longwave irradiance computations, they are also effectively applied for calculating spectral infrared radiance [77, 98]. The advantage in this sense relies in the speed of computations which, being of the order of 10^{-1} seconds on a standard personal computer for a full infrared spectrum, results smaller of about 1 order of magnitude with respect to a two-stream model (i.e. [22]). The MAMA methodology is built to be as fast as scaling methods in terms of computational time, easy to implement and upgrade in terms of radiative properties, and accurate to work all over the longwave spectral range from far to mid-infrared. The MAMA algorithm has also the advantage of being based on fundamental optical properties of the layers and thus it allows to retain an explicit treatment of the cloud micro-physics which is usually lost in hyper-fast methodologies such as in [63].

The solution is based on the separation of the multiple-scattering term in two parts (a back- and a forward-scattering contribution), which are described as the product of an effective average ambient radiation ($\langle I_u \rangle$ and $\langle I_d \rangle$) and a new parameter called the angular back-scattering coefficient, $c(\mu)$. The physical meaning of $c(\mu)$ is related to the radiation coming from a hemisphere and back-scattered into a specific direction, as the one defined by the observer (μ). The back-scattering coefficient is easily computed from the phase function of the particle size distribution of the layer; it is a fundamental property of the layer itself, meaning that it defines how the layer interacts with radiation in terms of scattering processes. The variability of $c(\mu)$ with the observational angle is smooth, as shown in Appendix C which makes the computed values representative of a set of angles and allows its application to radiative transfer computations.

The upward effective ambient radiation $\langle I_u \rangle$ is calculated assuming a linear in μ dependency of the radiance $I(\mu)$ within the considered hemisphere. The limit value of $I(\mu)$ for $\mu = 0$ is estimated, within a scattering layer, using a Chou-like scaling methodology. On the other hand, the value of the down-ward effective ambient radiance $\langle I_d \rangle$ is approximated as the downward radiance computed using the Chou solution for an effective angle $\tilde{\mu}$. The resulting equation (6.22) is a Schwarzschild-like equation based on fundamental parameters easily

derivable from the optical properties databases of the scattering layers.

The MAMA accuracy is assessed by comparing the computed up-welling radiance with those derived using a reference solution (DISORT) which is taken as the truth within the goal Noise Equivalent Spectral Radiance of the future FORUM (Far-infrared Outgoing Radiation Understanding and Monitoring) sensor. FORUM is the 9th ESA Earth Explorer and will observe both the far and mid-infrared part of the spectrum at about 0.5 cm^{-1} un-apodized resolution. As for water clouds the MAMA code accurately simulates far and mid-infrared spectral radiances for all the combinations of optical depths, effective dimensions and cloud altitudes accounted for in the simulations. Radiance spectra in the presence of ice clouds are mostly accurately simulated with the exception of very uncommon cases which account for small crystal dimensions and large optical depth and only at far infrared wavelengths. In conclusion, the proposed methodology is suitable for the computation of radiance spectra at high resolution at all mid-infrared wavenumbers and in case of any cloud conditions. This makes it an appropriate tool for the analysis of observations from current infrared sounders such as the Infrared Atmospheric Sounding Interferometer - IASI² or the Cross-track Infrared Sounder - CrIS³ among others. In the far infrared part of the spectrum, the MAMA algorithm shows the largest improvements with respect to previous scaling methods [71, 74]. Despite the challenging conditions due to enhanced scattering processes, the MAMA code accurately simulates far infrared radiances in the presence of ice clouds with an optical depth less than 2 and for any atmospheric condition. The MAMA computational performances in terms of speed, its accuracy at far-infrared and its readiness for implementation and easiness in updating, make it suitable to be applied to the future measurements of the FORUM mission.



²<https://www.eumetsat.int/iasi>

³<https://www.nesdis.noaa.gov/current-satellite-missions/currently-flying/joint-polar-satellite-system/cross-track-infrared>

7 | Summary and final discussions

Recognizing the value of Far Infrared Region observations, in September 2019, the European Space Agency selected FORUM (Far-infrared Outgoing Radiation Understanding and Monitoring) as the 9th Earth Explorer (EE9) [88] whose launch is foreseen in 2027. In the same period, NASA has scheduled the launch of the PREFIRE (Polar Radiant Energy in the Far-InfraRed Experiment) satellites for 2024, with the aim of studying Arctic heat emissions.

Both FORUM, dedicated to globally mapping Earth's far-infrared emission, and PREFIRE, focused on characterizing the Earth's polar longwave radiation, are anticipated to generate significant amounts of new data, requiring the implementation of fast radiative transfer models, applicable to the entire IR spectral region, for an effective data exploitation and analysis. Different solvers for the radiative transfer problem exist. These algorithms differ in physical assumptions, geometry, resolution, accuracy, speed and computational resources. Choosing the appropriate algorithm involves finding a balance, as the specific application demands trade-offs among these factors. Specifically, in the framework of operational assimilation of satellite radiance data or remote sensing retrievals, the application of slow, accurate solvers can be prohibitive. In this sense, when observing the Earth infrared emission, the physical characterization of multiple scattering processes, induced mainly by the presence of clouds and aerosols, requires important resources, both in terms of computational time and memory.

This thesis investigates the implementation of fast scaling methodologies to the computation of mid and far-infrared spectrally resolved radiances in the presence of scattering. This class of methods, introduced in Section 2.3.2, is used to avoid the direct computation of the multiple scattering effects, reducing in this way the computational cost of the solver. The application of such methodologies becomes important in the context of operational satellite radiance data assimilation or remote sensing retrievals.

Two important scaling methodologies are considered, namely Chou's scaling method [13] and the similarity principle [23]. These solutions were originally derived for fluxes calculation, for this reason, their ability to accurately reproduce spectrally resolved radiances in the MIR and FIR needs to be assessed. A reference code, implementing an accurate solution (DISORT [103]), is used to perform the analysis, assuming a nadir-looking geometry and a spectral range representative of the FORUM instrument (100-1600 cm^{-1}). The analysis is presented in Chapter 3. The results highlight the good performance of the Chou method (with respect to the FORUM expected noise) in reproducing the radiances in the MIR for

both water and ice clouds. Nevertheless, when ice clouds in the FIR are considered, this solution yields acceptable results only in the limit of OD below 0.1–1.0. The application of this solution, overall, leads to a general overestimation of the upwelling radiances. This effect is particularly visible for ice in the FIR due to the behavior of the cloud’s optical properties.

To reduce the computational errors of this basic scaling method, a correction term is modeled and computed starting from the solution proposed by Tang et al. (2018) [106], which assumes a downward ambient radiation term not necessarily equal to the blackbody radiance, as it is done in Chou’s approximation. The implementation of this adjustment scheme is presented in Chapter 4. Similarly to scaling methods, the adjustment term proposed by Tang is derived for fluxes computation, and its application to spectrally resolved radiances is not straightforward. The extension of this correction term to radiances is obtained through a coefficient optimization, whose value is generated starting from reference simulations. The application of this methodology shows a reduction of the radiance residuals over most of the cloudy cases encountered in nature. In particular, the use of the Tang correction routine with the new coefficients is accurate for the computation of radiance fields in the presence of thin cirrus clouds which are one of the targets of the FORUM mission. Nevertheless, inaccuracies are still encountered for medium-large optical depths and small effective radii, highlighting the need for more accurate approaches to envisage all possible cloudy conditions.

The whole set of radiative parameters needed to solve the radiative transfer equation using the previously described approximations (Chou and Tang schemes) is parametrized by means of polynomial functions of the effective dimension of the cloud particle size distribution. These parameters are then implemented in the σ -IASI/F2N code, a forward model designed for the fast calculation of radiance and its derivatives with respect to atmospheric and spectroscopic parameters. σ -IASI/F2N, described in Chapter 5, is an updated version of the σ -IASI code (Amato et al., 2002 [1]), a fast monochromatic radiative transfer model tailored to compute all-sky Earth’s emission spectra (covering both FIR and MIR). The strategy enables fast, accurate radiance and analytical derivatives calculations in clear sky or in the presence of cloud and aerosol layers.

Finally, an improved approach to solve the radiative transfer equation, called MAMA, is presented in Chapter 6. The provided methodology, which can be interpreted as an asymmetric adjusted scaling, is designed for efficiently calculating spectrally resolved upwelling radiances in the presence of atmospheric diffusive layers. It excels in simulating the entire longwave spectrum with high accuracy, particularly for optically thin scattering layers such as cirrus clouds. The algorithm simplifies the radiative transfer equation in the plane parallel assumption, interpreting the scattering contribution as a linear combination of mean ambient radiances involved in forward and backscatter processes. The algorithm introduces the angular back-scattering coefficient, a property derived from the particle size distribution’s phase function. This coefficient describes the fraction of radiation back-scattered into a specific direction (observer). The algorithm flexibility allows for straightforward updates of reference optical properties based on any generic single scattering properties database.

A direct comparison between Chou, Tang and MAMA is presented in Appendix E.

Overall, in the mid-infrared, the application of scaling methodologies for computing

FORUM-like radiances yields satisfactory results. The Chou approximation effectively reproduces scattering contributions induced by clouds or aerosols in nadir-looking geometry, as demonstrated by Martinazzo et al. [74]. This is noteworthy, considering that these methodologies were originally developed for irradiance calculations. On the other hand, when FIR is taken into account, these methodologies fail to effectively describe the scattering effects, especially when ice clouds are considered.

The use of these methodologies is discouraged for simulating FIR radiances, and the application of other methods is recommended.

In this thesis, two alternative solutions are presented and examined, preserving the inherent simplicity of implementation and computational efficiency found in the original scaling methods. Furthermore, the explicit treatment of cloud microphysics enables quicker incorporation of new optical properties and updates.

Future developments will aim to further improve these two solutions. Specifically:

- The coefficient utilized in section 4.3 to extend the Tang adjustment routine to spectrally resolved radiances calculation will be parameterized as a function of the size parameter, in order to naturally incorporate the spectral dependency of the problem.
- The MAMA algorithm will be extended to simulate other observational angles.



A | Similarity principle analysis

Radiance (ΔL , contour plot) and brightness temperature (ΔBT , color scale) differences between the similarity principle and full-scattering solutions are shown for liquid water clouds at MIR and FIR wavenumbers in Figure A.1 and A.2, respectively. Results for ice clouds are shown in Figure A.3 and A.4.

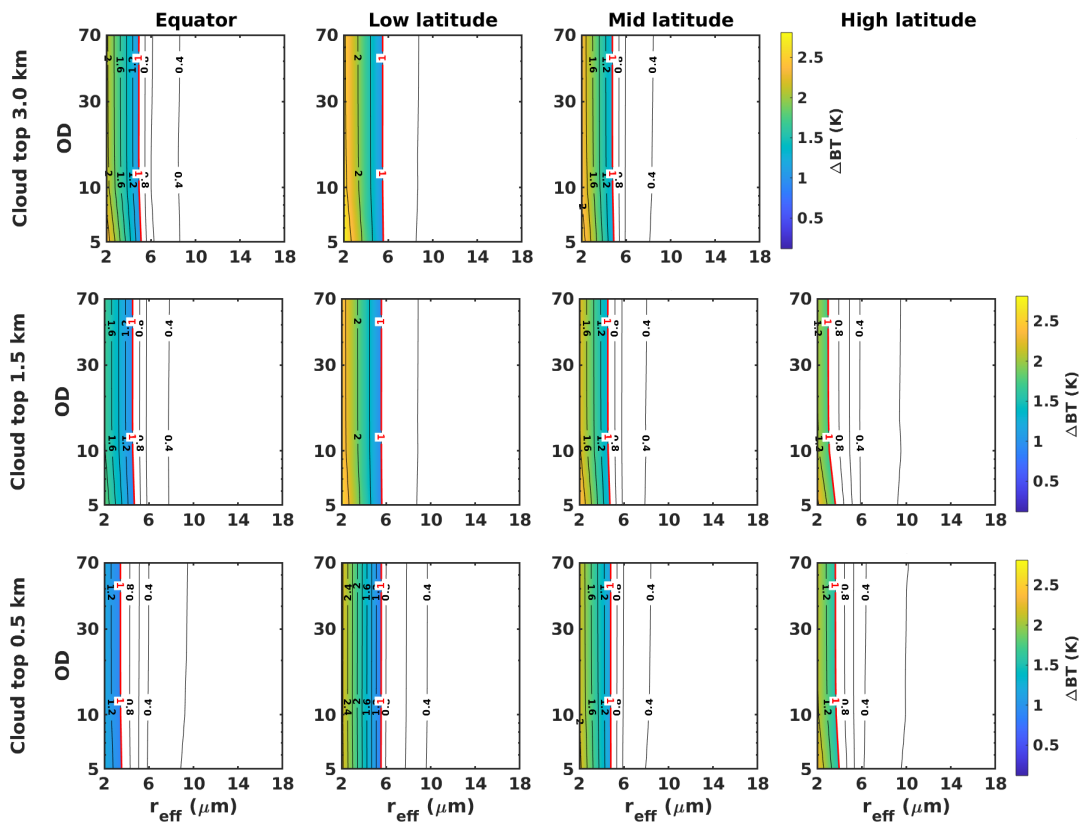


FIGURE A.1: Radiance (ΔL , contour plot) and brightness temperature (ΔBT , color scale) differences between SP and FS for liquid water clouds at 1203 cm^{-1} (MIR). The white color indicates differences below the FORUM noise level, marked by the red contour line. Y-axes are in log scale.

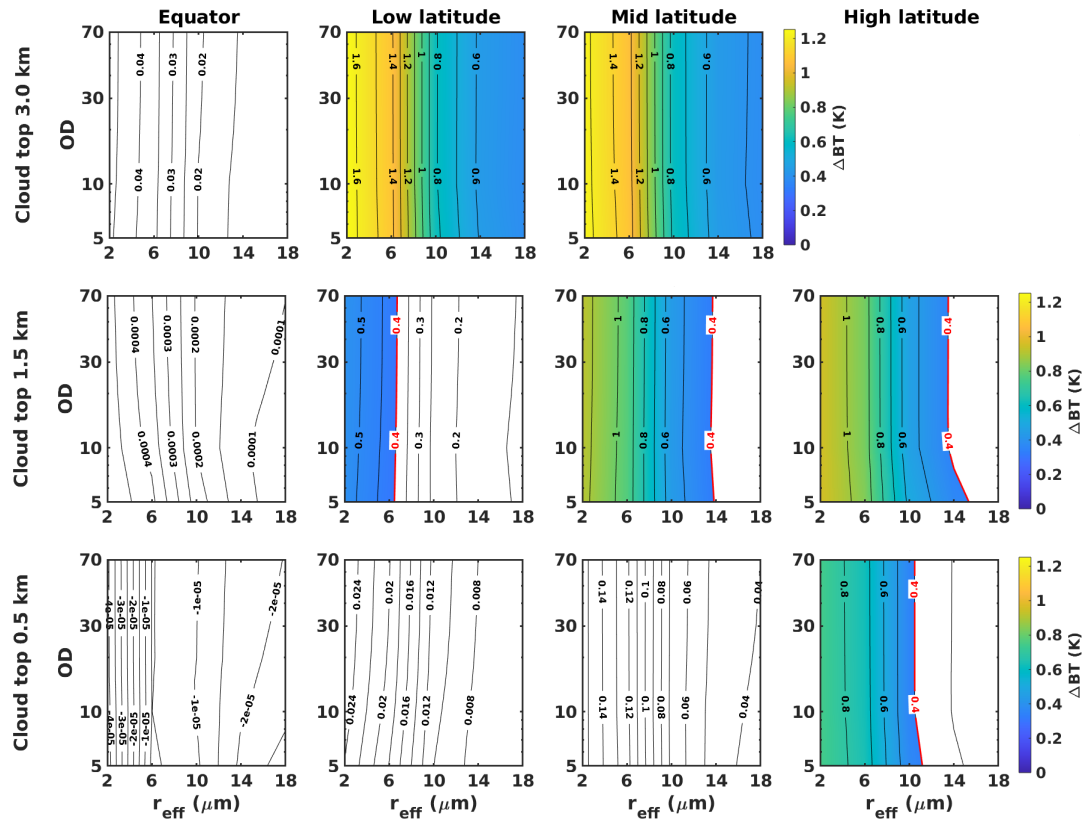


FIGURE A.2: Radiance (ΔL , contour plot) and brightness temperature (ΔBT , color scale) differences between SP and FS for liquid water clouds at 531 cm^{-1} (FIR). The white color indicates differences below the FORUM noise level, marked by the red contour line. Y-axes are in log scale.

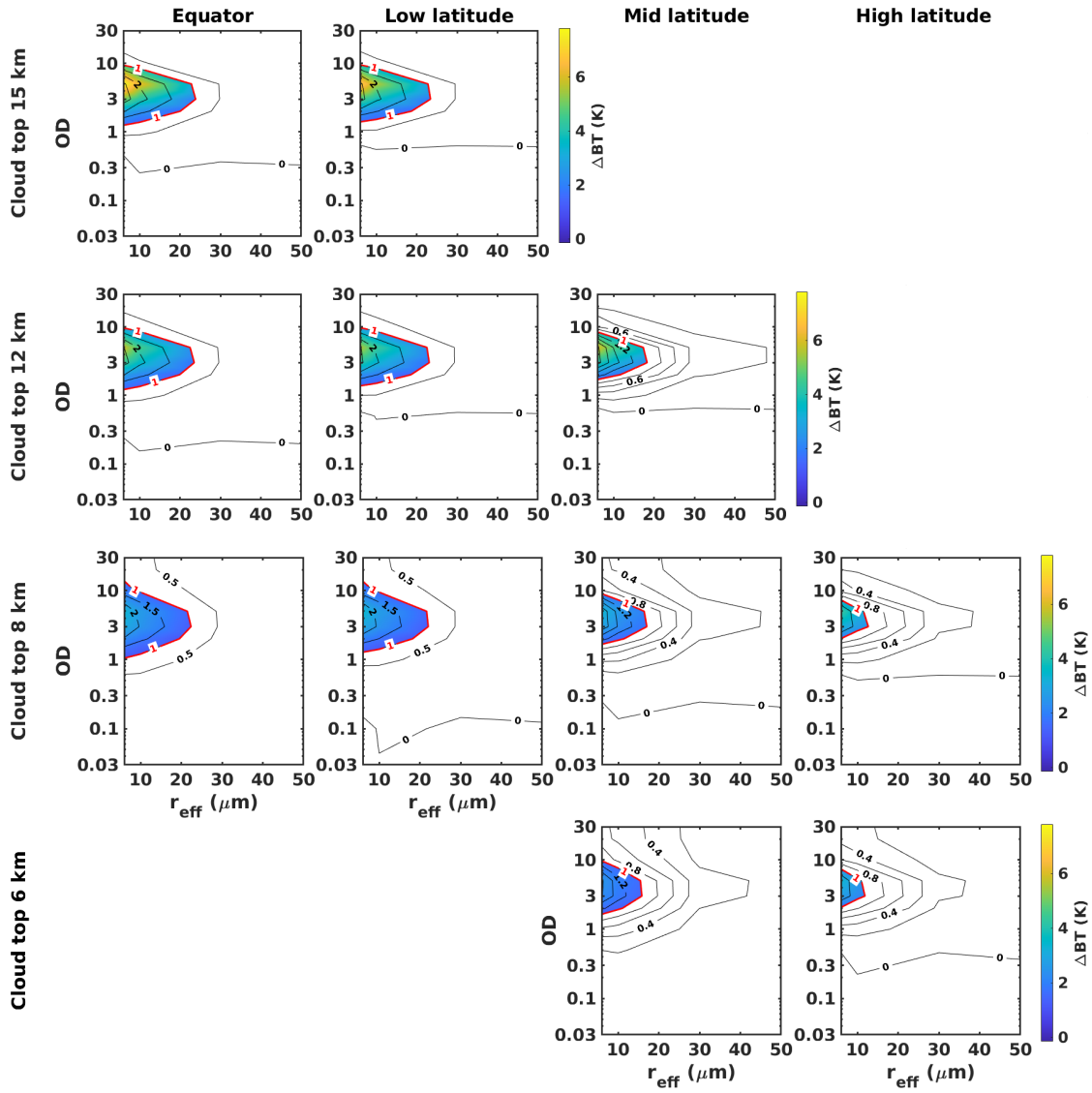


FIGURE A.3: ΔL , contour plot) and brightness temperature (ΔBT , color scale) differences between SP and FS for column aggregate ice clouds at 1203 cm^{-1} (FIR). The white color indicates differences below the FORUM noise level, marked by the red contour line. Y-axes are in log scale.

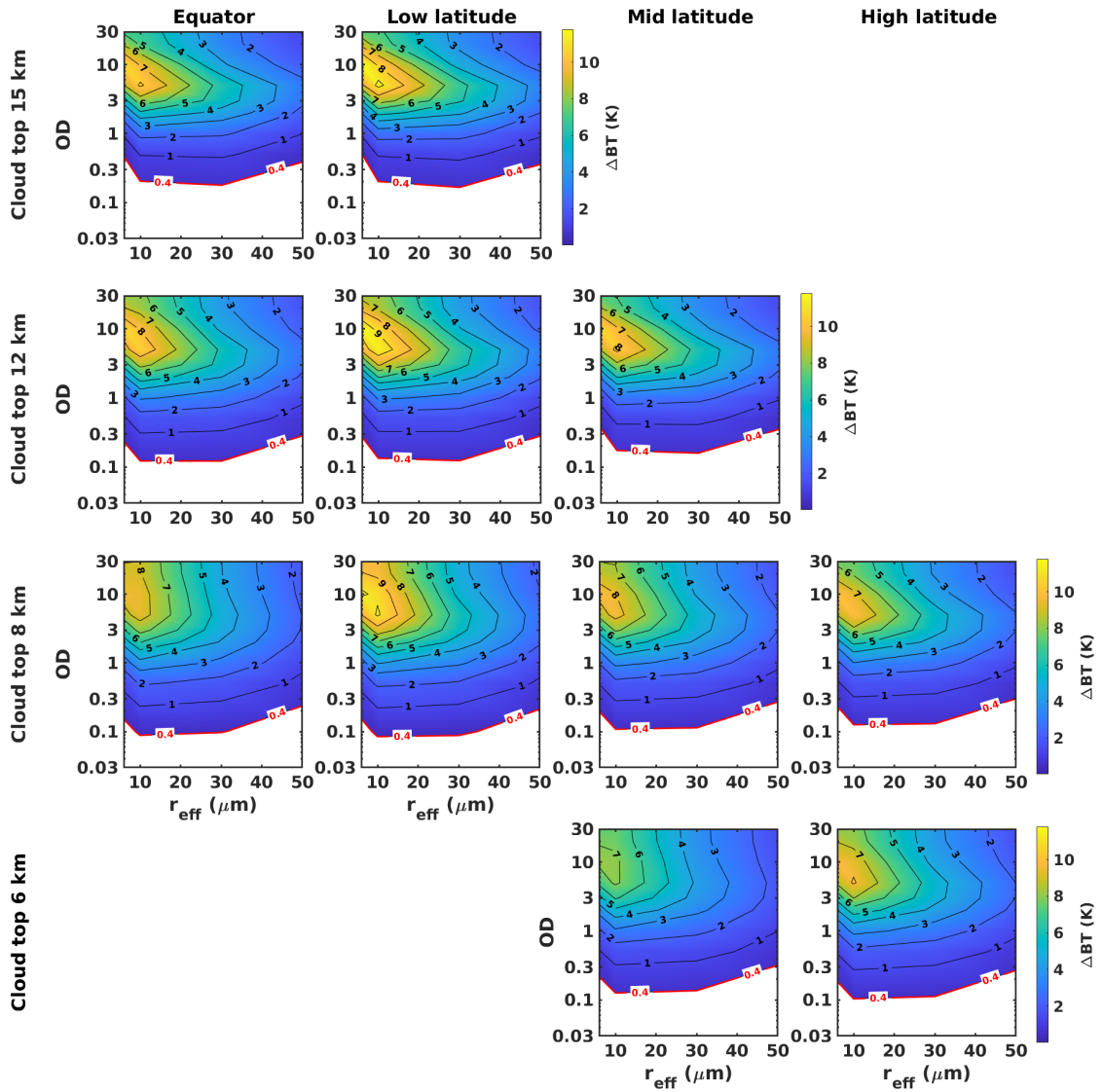


FIGURE A.4: ΔL , contour plot) and brightness temperature (ΔBT , color scale) differences between SP and FS for column aggregate ice clouds at 410 cm^{-1} (FIR). The white color indicates differences below the FORUM noise level, marked by the red contour line. Y-axes are in log scale.

B | Derivation of \vec{I}

To obtain a suitable form for \vec{I} , we can start considering the following scenario. Let's place in a plane parallel atmosphere a thin cloud layer, which is capable of absorbing, emitting and scattering the radiation. Assuming plane parallel conditions, the equation governing the radiative transfer for the radiance parallel to the surface inside the cloud is written as:

$$\begin{aligned} \frac{d\vec{I}(\tau, \tau', \mu = 0)}{d\tau'} = & \vec{I}(\tau, \tau', \mu = 0) - [1 - \tilde{\omega}(\tau)] B(\tau) + \\ & - \frac{\tilde{\omega}(\tau)}{2} \int_{-1}^1 d\mu' I(\tau, \mu') P(\mu = 0, \mu') d\mu' \end{aligned} \quad (\text{B.1})$$

Where τ indicates the optical depth along the vertical coordinate and τ' along the horizontal coordinate, i.e. the optical depth along the horizontal direction. The term $I(\tau, \mu')$ inside the integral is the ambient radiation at the level τ . This last term does not depend on τ' as we are considering a horizontal symmetry for this problem. Figure B.1 shows a schematic representation of the horizontal radiance \vec{I} .

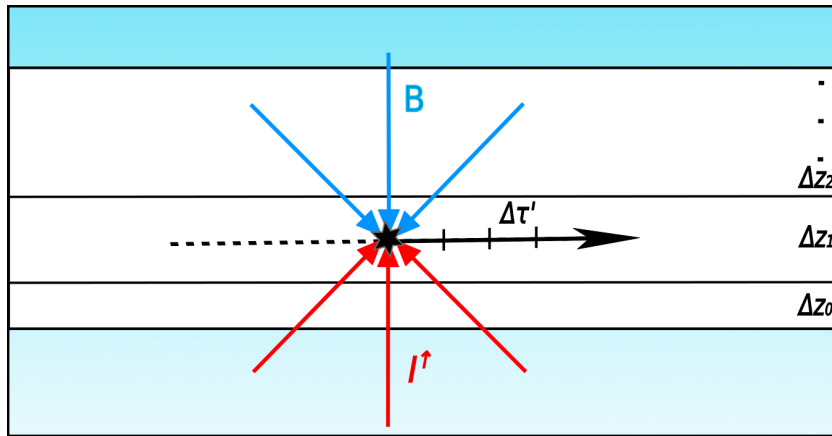


FIGURE B.1: Schematic representation of the processes assumed to model the horizontal radiance \vec{I} within a cloud layer.

To estimate the solution of the equation B.1, simple assumptions are considered regarding the ambient radiation $I(\tau, \mu')$. Similarly to what done by Chou et al. (1999) [13], it is assumed that the radiation coming from the upper hemisphere ($\mu' < 0$) is equal to the Planckian emission from the layer $B(\tau)$. On the other hand, the upward ambient radiation ($\mu' > 0$) is taken equal to the incident upward radiance $I(\mu = 1)$. Thus in summary the ambient radiation within the cloud is here assumed:

$$I(\tau, \mu') = \begin{cases} B(\tau) & \text{if } \mu' < 0 \\ I(\mu = 1) & \text{if } \mu' > 0 \end{cases} \quad (\text{B.2})$$

Using the B.2 in equation B.1 it is obtained:

$$\begin{aligned} \frac{d\vec{I}(\tau, \tau', \mu = 0)}{d\tau'} &= \vec{I}(\tau, \tau', \mu = 0) - [1 - \tilde{\omega}(\tau)] B(\tau) + \\ &\quad - B(\tau) \frac{\tilde{\omega}(\tau)}{2} \int_{-1}^0 P(\mu = 0, \mu') d\mu' + \\ &\quad - I(\mu = 1) \frac{\tilde{\omega}(\tau)}{2} \int_0^1 P(\mu = 0, \mu') d\mu' \end{aligned} \quad (\text{B.3})$$

where the multiple scattering term is split in two contributions, one for the downward and one for the upward ambient radiance respectively. Using the definition for the directional back-scattering coefficient given in 6.4, and noting that $c(\mu = 0) = 0.5$, we can write the equation B.3 as:

$$\begin{aligned} \frac{d\vec{I}(\tau, \tau', \mu = 0)}{d\tau'} &= \vec{I}(\tau, \tau', \mu = 0) - [1 - \tilde{\omega}(\tau)] B(\tau) + \\ &\quad - B(\tau) \frac{\tilde{\omega}(\tau)}{2} - I(\mu = 1) \frac{\tilde{\omega}(\tau)}{2} \end{aligned} \quad (\text{B.4})$$

which is solved by:

$$\vec{I}(\tau, \tau', \mu = 0) = \vec{I}_0(\tau) e^{-\tau'} + \left[\left(1 - \frac{\tilde{\omega}(\tau)}{2} \right) B(\tau) + \frac{\tilde{\omega}(\tau)}{2} I(\mu = 1) \right] (1 - e^{-\tau'}) \quad (\text{B.5})$$

Where $\vec{I}_0(\tau)$ is the boundary condition for the parallel radiance. Taking the limit for a large optical path τ' (the cloud extends along the horizontal direction), the solution simplifies to:

$$\vec{I}(\tau, \mu = 0) = \left(1 - \frac{\tilde{\omega}(\tau)}{2} \right) B(\tau) + \frac{\tilde{\omega}(\tau)}{2} I(\mu = 1) \quad (\text{B.6})$$

In this solution, the parallel radiance is composed of only two contributions consisting of one from the emission from the cloud layer itself and the other from the scattered radiation.

C | Optical Properties of Water and Ice Clouds

An overview of the optical properties required by the MAMA code is provided. In particular, the two newly defined parameters, namely the angular back-scattering coefficient $c(\mu)$ and the gamma coefficient $\gamma(\mu)$ are discussed.

The angular back-scattering coefficient is defined in a similar way to what done for the back-scattering coefficient, b , proposed by Chou [13], but for application to radiance instead of irradiance. The angular backscattering coefficient physical meaning is related to the fraction of radiation back-scattered toward a specific direction indicated by μ with respect the hemispheric incident radiation. Its mathematical definition 6.4 is repeated here for convenience:

$$c(\mu) = \frac{1}{2} \int_{-1}^0 d\mu' P(\mu', \mu) \quad (\text{C.1})$$

The spectral variation of two angular back-scattering coefficients for a couple of cases of water and ice clouds are reported in Figure C.1 in the upper and lower panel respectively. For comparison the spectral variation of the b coefficient is also plotted. Each panel of Figure C.1 accounts for small and large effective radii. Results are computed for a nadir-looking geometry ($\mu = 1$). The angular back-scattering coefficient shows smooth variation with the wavenumber and value approaching to 0.5 for small wavenumbers and particle dimensions. For large effective radii and large wavenumbers, the phase function presents a strong forward peak, and $c(\mu)$ reduces to values smaller than 0.1.

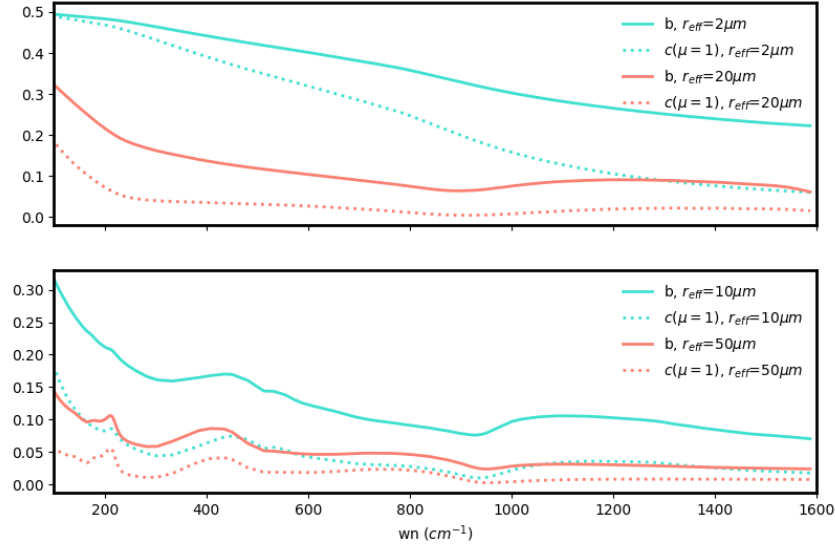


FIGURE C.1: Upper panel: angular back-scattering $c(\mu = 1)$ and back-scattering b coefficients for water clouds as a function of the wavenumber. Two effective radii are considered as reported in the legend. Lower panel: the same as upper panel but for ice clouds.

The gamma coefficient definition is similar to that for the asymmetry parameter g except for the lower limit of integration over the zenith angle. In fact, in the case of γ the integration is performed over the forward hemisphere only:

$$\gamma(\mu) = \frac{1}{2} \int_0^1 d\mu' P(\mu', \mu) \mu' \quad (\text{C.2})$$

For nadir-looking observations ($\mu = 1$), the cosine of the angle between the entering and exiting direction θ in the scattering problem results equal to μ' as easily derived from the equation C.3 relating the scattering angle to the zenith and azimuth of exiting and entering angles:

$$\cos(\theta) = \mu\mu' + (1 - \mu^2)^{\frac{1}{2}}(1 - \mu'^2)^{\frac{1}{2}}\cos(\phi' - \phi) \quad (\text{C.3})$$

In the case of highly forward peaked phase function (usually associated to limited back-scattering), the resulting gamma parameter's values are very close to those obtained for the asymmetry parameter g .

Figure C.2 shows the spectral variation of γ for both water and ice clouds. Each panel considers cloud PSDs representatives of small and large effective radii. Results are computed for a nadir-looking geometry ($\mu = 1$). For comparison, the g coefficients computed in the same cloud conditions are also reported in the Figure. As expected the γ values are larger than

g values and the spectral variation are smooth. The gamma parameter increases for large particle dimensions and large wavenumbers.

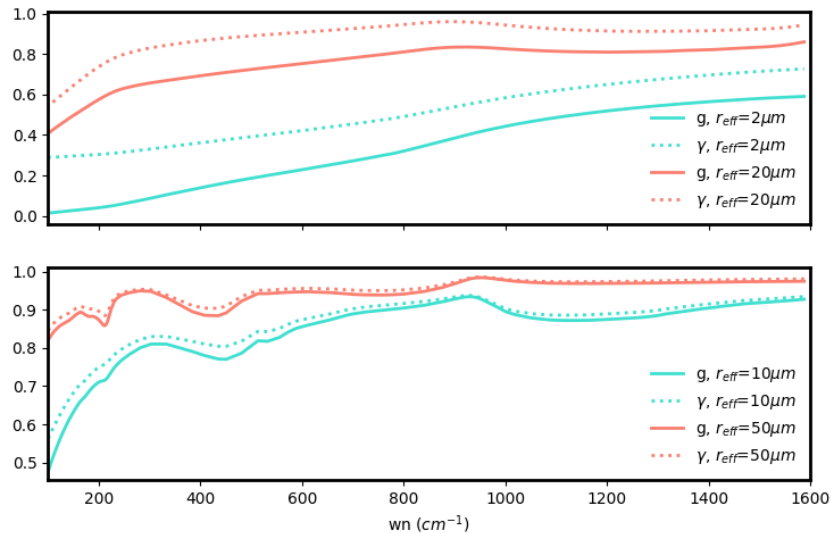


FIGURE C.2: Upper panel: Values of the asymmetry parameter g (solid line) and the gamma coefficient $\gamma(\mu = 1)$ (dotted line) of a water cloud as a function of the wavenumber. The values are reported for two different effective radii of the distribution. Lower panel: the same of above but for an ice cloud.

The main focus of this study is on the RT solution at nadir-looking geometry, thus, the cloud optical parameters (the angular back-scattering coefficient and the gamma parameter), are computed under the assumption of a fixed viewing angle $\mu = 1$. Nevertheless, it is noteworthy that these quantities exhibit a smooth variation with the viewing angle. This feature makes the computed properties representative not only of nadir-looking angles, but also of small off-nadir angles. Figure C.3 and C.4 show the value of the angular back-scattering parameter c as a function of the viewing angle for a liquid water cloud and an ice cloud respectively. At FIR and MIR wavenumbers, the variation of the c parameters is less than 2% for off-nadir angles smaller than 10° . The gamma parameter has a similar behavior (not shown).

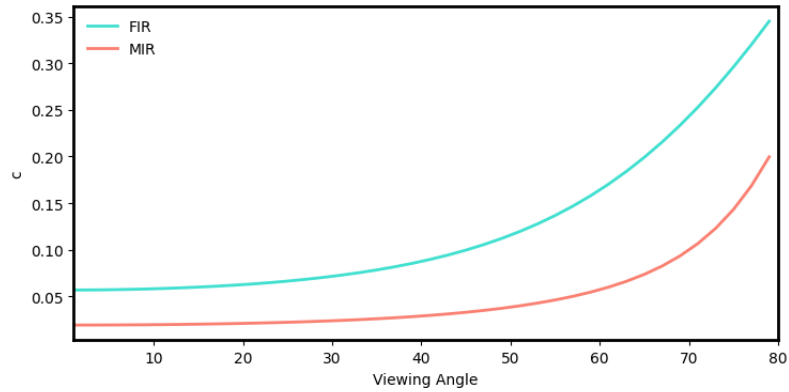


FIGURE C.3: Angular back-scattering coefficient, $c(\mu)$, as a function of the viewing angle (in degrees). A water cloud with an effective radius of $10 \mu m$ is considered. The blue and pink lines refer to wavenumbers at 531 (FIR) and 1203 (MIR) cm^{-1} , respectively.

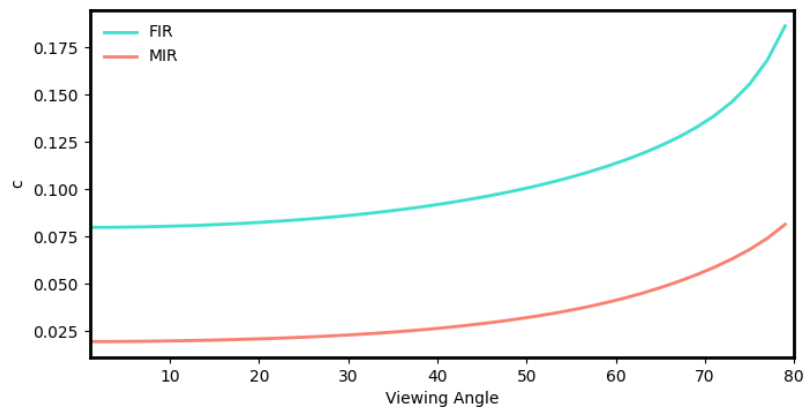


FIGURE C.4: Angular back-scattering coefficient, $c(\mu)$, as a function of the viewing angle (in degrees). An ice cloud with an effective radius of $20 \mu m$ is considered. The blue and pink lines refer to wavenumbers at 410 (FIR) and 1203 (MIR) cm^{-1} , respectively.

D | Solution for off-nadir observation angles

The MAMA solution can be generalized for any observational angle. The extension of equation 6.22 requires to account for an explicit dependence on the cosine of the viewing angle, μ . At this regard, equation 6.8 becomes:

$$\frac{1}{\mu} \frac{dI(\tau, \mu)}{d\tau} = I(\tau, \mu) - [1 - \tilde{\omega}(\tau)] B(\tau) + \tilde{\omega}(\tau) [\langle I_d(\tau, \mu) \rangle c(\mu) + \langle I_u(\tau, \mu) \rangle (1 - c(\mu))] \quad (\text{D.1})$$

where the mean downward and upward ambient radiations explicitly depend on μ .

The derivation of these two quantities mirrors the one already proposed for the nadir-looking geometry. Specifically, the mean downward ambient radiation remains unchanged since its expression (equation 6.20) does not contain any directional term and it can thus be considered as general. On the other hand, the mean upward ambient radiation exploited in the MAMA solution (equations 6.12 and 6.15) was written accounting for the specific upward radiation along the vertical direction. For a generalization of the mean upward radiation, it is thus necessary to modify the linear relation assumed in Equation 6.9. A possible solution for the ambient radiation is provided by the following relation:

$$I(\tau, \mu', \mu) = \frac{I(\tau, \mu) - \vec{I}(\tau)}{\mu} \cdot \mu' + \vec{I}(\tau), \quad \mu' > 0 \quad (\text{D.2})$$

where the limit case for $\mu' = 1$ is linearly extrapolated.

Equation D.2 can be used to derive a new expression for the mean ambient radiation and from this a general solution of the MAMA algorithm for any observational angle is obtained. The detailed derivation of the general solution and the assessment of the accuracy of the code at any observational angle are not provided in this work and require further extended investigations and computations.

E | Tang's adjustment and MAMA solution

In this section, a direct comparison between the optimal Tang adjustment solution described in Chapter 4 and the asymmetric adjusted scaling solution presented in Chapter 6 is performed. It is important to highlight that these two methodologies are intrinsically different. The adjustment scheme proposed by Tang was originally derived for fluxes computation. The extension of this methodology to the computation of spectrally resolved radiances is performed by using a tuning coefficient (k described in equation 4.12), and the effectiveness of the final results deeply rely on the quality of these coefficients and on the method used to generate them. On the other hand, the solutions presented in Chapter 6 is an approximate analytical approach directly developed for radiances computation in the FIR and MIR. It does not require any tuning coefficient.

The application of these solutions on the same set of scenarios considered in Chapter 4. From the FIR window bands, the wavenumbers 410 cm^{-1} is selected in order to provide an assessment of the level of accuracy of the Tang- k and MAMA solutions for multiple atmospheric and ice cloud conditions. The atmospheric profile, and the cloud positions considered are presented in Figure 4.9.

A comparison for the same scenarios of these different methodologies are presented in Figure E.1, considering the FIR spectral region and an ice cloud model. The results are in line with those already discussed in Chapters 4 and 6, and will not be commented on further in this section.

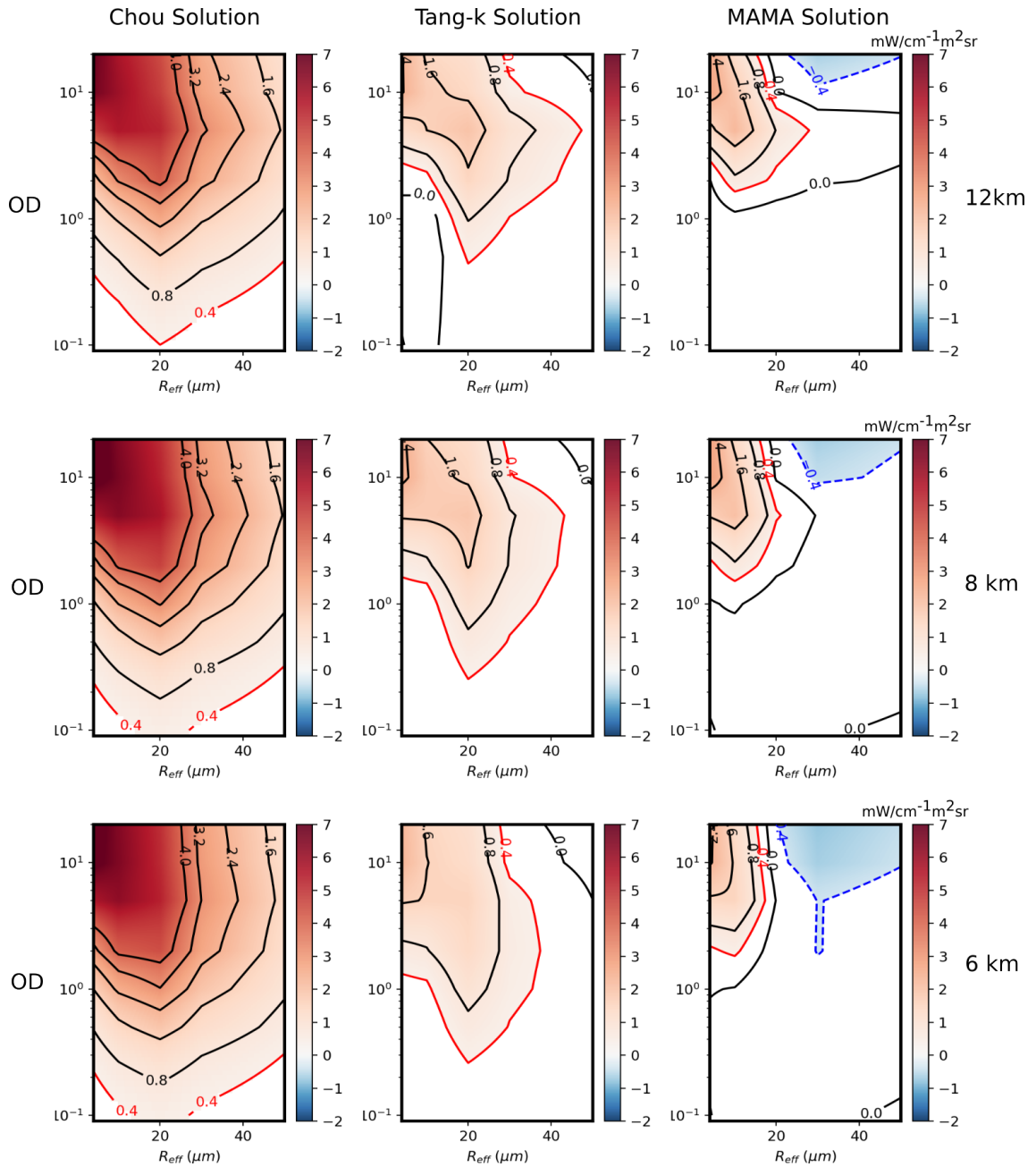


FIGURE E.1: Radiance differences ΔI , $\text{mW}/(\text{m}^2\text{sr cm}^{-1})$, between Chou solution (first column), Tang solution (second column) or MAMA solution (third column) and the DISORT. The results are presented as a function of multiple combinations of PSD effective radius and cloud optical depths. The 410 cm^{-1} (FIR) spectral channel is considered. The three panels of each row are for ice clouds at 6 km, 8 km, and 12 km of altitude, respectively. The white color indicates differences below the FORUM noise level, marked by the red contour line. Y-axes are in log scale.

Bibliography

- [1] U. AMATO, G. MASIELLO, C. SERIO, and M. VIGGIANO. “The σ -IASI code for the calculation of infrared atmospheric radiance and its derivatives”. *Environmental Modelling & Software* 17(7) (2002), pp. 651–667. ISSN: 1364-8152. DOI: [https://doi.org/10.1016/S1364-8152\(02\)00027-0](https://doi.org/10.1016/S1364-8152(02)00027-0).
- [2] U. AMATO, D. D. CANDIUS, and C. SERIO. “Effect of apodization on the retrieval of geophysical parameters from Fourier-transform spectrometers”. *Appl. Opt.* 37(27) (Sept. 1998), pp. 6537–6543. DOI: 10.1364/AO.37.006537.
- [3] H. H. AUMANN *et al.* “Evaluation of Radiative Transfer Models With Clouds”. *Journal of Geophysical Research (Atmospheres)* 123(11) (June 2018), pp. 6142–6157. DOI: 10.1029/2017JD028063.
- [4] R. J. BANTGES *et al.* “A test of the ability of current bulk optical models to represent the radiative properties of cirrus cloud across the mid- and far-infrared”. *Atmospheric Chemistry and Physics* 20(21) (2020), pp. 12889–12903. DOI: 10.5194/acp-20-12889-2020.
- [5] M. BEN-YAMI *et al.* “Emissivity retrievals with FORUM’s end-to-end simulator: challenges and recommendations”. *Atmospheric Measurement Techniques* 15(6) (2022), pp. 1755–1777. DOI: 10.5194/amt-15-1755-2022.
- [6] A. BENEDETTI *et al.* “Aerosol analysis and forecast in the European Centre for Medium-Range Weather Forecasts Integrated Forecast System: 2. Data assimilation”. *Journal of Geophysical Research: Atmospheres* 114(D13) (2009). DOI: <https://doi.org/10.1029/2008JD011115>.
- [7] F. BERNARD *et al.* “Overview of IASI-NG the new generation of infrared atmospheric sounder”. *International Conference on Space Optics - ICSO 2014*. Ed. by Z. SODNIK, B. CUGNY, and N. KARAFOLAS. Vol. 10563. International Society for Optics and Photonics. SPIE, 2017, 105633H. DOI: 10.1117/12.2304101.

- [8] R. BHAWAR *et al.* “Spectrally resolved observations of atmospheric emitted radiance in the H₂O rotation band”. *Geophysical Research Letters* 35(4), L048I2 (Feb. 2008), p. L048I2. DOI: 10.1029/2007GL032207.
- [9] A. BOZZO, T. MAESTRI, and R. RIZZI. “Combining visible and infrared radiometry and lidar data to test simulations in clear and ice cloud conditions”. *Atmospheric Chemistry and Physics* 10(15) (2010), pp. 7369–7387. DOI: 10.5194/acp-10-7369-2010.
- [10] H. BRINDLEY and J. HARRIES. “The impact of far i.r. absorption on clear sky greenhouse forcing: sensitivity studies at high spectral resolution”. *Journal of Quantitative Spectroscopy and Radiative Transfer* 60(2) (Aug. 1998), pp. 151–180. DOI: 10.1016/S0022-4073(97)00152-0.
- [11] P. M. CAMPBELL. “Monte carlo method for radiative transfer”. *International Journal of Heat and Mass Transfer* 10(4) (Apr. 1967), pp. 519–527. DOI: [https://doi.org/10.1016/0017-9310\(67\)90171-8](https://doi.org/10.1016/0017-9310(67)90171-8).
- [12] S. CHANDRASEKHAR. *Radiative transfer*. 1960.
- [13] M.-D. CHOU, K.-T. LEE, S.-C. TSAY, and Q. FU. “Parameterization for Cloud Longwave Scattering for Use in Atmospheric Models”. *Journal of Climate* 12(1) (1999), pp. 159–169. DOI: [https://doi.org/10.1175/1520-0442\(1999\)012<0159:PFCLSF>2.0.CO;2](https://doi.org/10.1175/1520-0442(1999)012<0159:PFCLSF>2.0.CO;2).
- [14] S. A. CLOUGH, F. X. KNEIZYS, L. S. ROTHMAN, and W. O. GALLERY. “Atmospheric Spectral Transmittance And Radiance: FASCOD_I B”. *Atmospheric transmission*. Vol. 277. Society of Photo-Optical Instrumentation Engineers (SPIE) Conference Series. July 1981, p. 152. DOI: 10.1117/12.931914.
- [15] S. A. CLOUGH *et al.* “Atmospheric radiative transfer modeling: a summary of the AER codes”. *Journal of Quantitative Spectroscopy and Radiative Transfer* 91(2) (Mar. 2005), pp. 233–244. DOI: 10.1016/j.jqsrt.2004.05.058.
- [16] S. A. CLOUGH, M. J. IACONO, and J.-L. MONCET. “Line-by-Line Calculations of Atmospheric Fluxes and Cooling Rates: Application to Water Vapor”. *Journal of Geophysical Research (Atmospheres)* 97(D14) (Oct. 1992), pp. 15, 761–15, 785. DOI: 10.1029/92JD01419.
- [17] J. A. COAKLEY and P. CHYLEK. “The Two-Stream Approximation in Radiative Transfer: Including the Angle of the Incident Radiation”. *Journal of Atmospheric Sciences* 32(2) (1975), pp. 409–418. DOI: [https://doi.org/10.1175/1520-0469\(1975\)032<0409:TTSAIR>2.0.CO;2](https://doi.org/10.1175/1520-0469(1975)032<0409:TTSAIR>2.0.CO;2).
- [18] W. COSSICH *et al.* “Ice and mixed-phase cloud statistics on the Antarctic Plateau”. *Atmospheric Chemistry and Physics* 21(18) (2021), pp. 13811–13833. DOI: 10.5194/acp-21-13811-2021.

- [19] C. V. COX *et al.* “Measurement and simulation of mid- and far-infrared spectra in the presence of cirrus”. *Quarterly Journal of the Royal Meteorological Society* 136(648) (2010), pp. 718–739. DOI: 10.1002/qj.596.
- [20] S. DESOUZA-MACHADO, L. L. STROW, H. MOTTELER, and S. HANNON. “kCARTA: a fast pseudo line-by-line radiative transfer algorithm with analytic Jacobians, fluxes, nonlocal thermodynamic equilibrium, and scattering for the infrared”. *Atmospheric Measurement Techniques* 13(1) (2020), pp. 323–339. DOI: 10.5194/amt-13-323-2020.
- [21] S. DESOUZA-MACHADO *et al.* “Single-footprint retrievals for AIRS using a fast Two Slab cloud-representation model and the SARTA all-sky infrared radiative transfer algorithm”. *Atmospheric Measurement Techniques* 11(1) (2018), pp. 529–550. DOI: 10.5194/amt-11-529-2018.
- [22] G. DI NATALE, L. PALCHETTI, G. BIANCHINI, and M. RIDOLFI. “The two-stream delta-Eddington approximation to simulate the far infrared Earth spectrum for the simultaneous atmospheric and cloud retrieval”. *Journal of Quantitative Spectroscopy and Radiative Transfer* (2020). DOI: 10.1016/j.jqsrt.2020.106927.
- [23] J. DING *et al.* “Validation of quasi-invariant ice cloud radiative quantities with MODIS satellite-based cloud property retrievals”. *Journal of Quantitative Spectroscopy and Radiative Transfer* 194 (June 2017), pp. 47–57. DOI: 10.1016/j.jqsrt.2017.03.025.
- [24] H. D. DOWNING and D. WILLIAMS. “Optical constants of water in the infrared”. *Journal of Geophysical Research* 80(12) (Apr. 1975), pp. 1656–1661. DOI: 10.1029/JC080i012p01656.
- [25] W. M. ELSASSER. “Heat transfer by infrared radiation in the atmosphere”. *Harvard Meteorological Studies* 6 (1947), p. 107.
- [26] ESA. *Report for Mission Selection: FORUM*. Tech. rep. ESA-EOPSM-FORM-RP-3549, 263pp. <https://esamultimedia.esa.int/docs/EarthObservation/EE9-FORUM-RfMS-ESA-v1.0-FINAL.pdf> (accessed on 29 October 2020). Noordwijk, The Netherlands: European Space Agency, 2019.
- [27] K. EVANS and G. STEPHENS. “A new polarized atmospheric radiative transfer model”. *Journal of Quantitative Spectroscopy and Radiative Transfer* 46(5) (Nov. 1991), pp. 413–423. DOI: 10.1016/0022-4073(91)90043-p.
- [28] J. EYRE. *A fast radiative transfer model for satellite sounding systems*. Technical memorandum 176. Shinfield Park, Reading: ECMWF, Mar. 1991. DOI: 10.21957/xsg8d92y3.

- [29] D. FELDMAN *et al.* “Far-infrared surface emissivity and climate”. *Proceedings of the National Academy of Sciences* 111 (Nov. 2014). DOI: 10.1073/pnas.1413640111.
- [30] J. S. FOOT. “Some observations of the optical properties of clouds. I: Stratocumulus”. *Quarterly Journal of the Royal Meteorological Society* 114(479) (Jan. 1988), pp. 129–144. DOI: 10.1002/qj.49711447907.
- [31] Q. FU, P. YANG, and W. B. SUN. “An Accurate Parameterization of the Infrared Radiative Properties of Cirrus Clouds for Climate Models.” *Journal of Climate* 11(9) (Sept. 1998), pp. 2223–2237. DOI: 10.1175/1520-0442(1998)011<2223:AAPOTI>2.0.CO;2.
- [32] D. T. GILLESPIE. *The Monte Carlo Method of Evaluating Integrals*. <https://apps.dtic.mil/dtic/tr/fulltext/u2/a005891.pdf>. China Lake, CA, USA: Naval Weapons Center, 1975.
- [33] R. M. GOODY and Y. L. YUNG. *Atmospheric radiation : theoretical basis*. 1989.
- [34] I. E. GORDON *et al.* “The HITRAN2016 molecular spectroscopic database”. *Journal of Quantitative Spectroscopy and Radiative Transfer* 203 (Dec. 2017), pp. 3–69. DOI: 10.1016/j.jqsrt.2017.06.038.
- [35] G. GRIECO *et al.* “Demonstration and validation of the ϕ -IASI inversion scheme with NAST-I data”. *Quarterly Journal of the Royal Meteorological Society* 133(S3) (2007), pp. 217–232. DOI: <https://doi.org/10.1002/qj.162>.
- [36] “GSICS Quarterly Vol. 14 No. 4” (2021). DOI: <https://doi.org/10.25923/jmbt-d994>.
- [37] J. HARRIES *et al.* “The Far-infrared Earth”. *Reviews of Geophysics* 46(4), RG4004 (Dec. 2008), RG4004. DOI: 10.1029/2007RG000233.
- [38] A. HEIDINGER *et al.* “Retrieval of Cirrus Cloud Optical Depth under Day and Night Conditions from MODIS Collection 6 Cloud Property Data”. *Remote Sensing* 7(6) (June 2015), pp. 7257–7271. ISSN: 2072-4292. DOI: 10.3390/rs70607257.
- [39] S. HEILLIETTE and L. GARAND. “A practical approach for the assimilation of cloudy infrared radiances and its evaluation using airs simulated observations”. *Atmosphere-Ocean* 45(4) (2007), pp. 211–225. DOI: 10.3137/ao.450403.
- [40] S. HEILLIETTE and L. GARAND. “A practical approach for the assimilation of cloudy infrared radiances and its evaluation using airs simulated observations”. *Atmosphere-Ocean* 45(4) (2007), pp. 211–225. DOI: 10.3137/ao.450403.

- [41] H. HERSBACH *et al.* *Complete ERA5: Fifth generation of ECMWF atmospheric reanalyses of the global climate*. Copernicus Climate Change Service (C3S) Data Store (CDS). (Accessed on 13-07-2020). 2017.
- [42] M. HESS, P. KOEPKE, and I. SCHULT. “Optical Properties of Aerosols and Clouds: The Software Package OPAC.” *Bulletin of the American Meteorological Society* 79(5) (May 1998), pp. 831–844. DOI: 10.1175/1520-0477(1998)079<0831:OPOAAC>2.0.CO;2.
- [43] F. HILTON *et al.* “Hyperspectral Earth Observation from IASI: Five Years of Accomplishments”. *Bulletin of the American Meteorological Society* 93(3) (2012), pp. 347–370. DOI: <https://doi.org/10.1175/BAMS-D-11-00027.1>.
- [44] Y. HONG and G. LIU. “The Characteristics of Ice Cloud Properties Derived from CloudSat and CALIPSO Measurements”. *Journal of Climate* 28(9) (2015), pp. 3880–3901. DOI: <https://doi.org/10.1175/JCLI-D-14-00666.1>.
- [45] Y. X. HU and K. STAMNES. “An Accurate Parameterization of the Radiative Properties of Water Clouds Suitable for Use in Climate Models”. *Journal of Climate* 6(4) (1993), pp. 728–742. DOI: [https://doi.org/10.1175/1520-0442\(1993\)006<0728:AAPOTR>2.0.CO;2](https://doi.org/10.1175/1520-0442(1993)006<0728:AAPOTR>2.0.CO;2).
- [46] X. HUANG, X. CHEN, D. K. ZHOU, and X. LIU. “An Observationally Based Global Band-by-Band Surface Emissivity Dataset for Climate and Weather Simulations”. *Journal of Atmospheric Sciences* 73(9) (Sept. 2016), pp. 3541–3555. DOI: 10.1175/JAS-D-15-0355.1.
- [47] Y. HUANG *et al.* “Separation of longwave climate feedbacks from spectral observations”. *Journal of Geophysical Research (Atmospheres)* 115(D7), D07104 (Apr. 2010), p. D07104. DOI: 10.1029/2009JD012766.
- [48] P. HUBANKS, S. PLATNICK, M. KING, and B. RIDGWAY. *MODIS Atmosphere L3 Gridded Product Algorithm Theoretical Basis Document (ATBD) and Users Guide*. English. Version Version 4.4. 2019. February 20, 2019.
- [49] M. J. IACONO, E. J. MLAWER, S. A. CLOUGH, and J.-J. MORCRETTE. “Impact of an improved longwave radiation model, RRTM, on the energy budget and thermodynamic properties of the NCAR community climate model, CCM3”. *Journal of Geophysical Research: Atmospheres* 105(D11) (2000), pp. 14873–14890. DOI: <https://doi.org/10.1029/2000JD900091>.
- [50] IPCC. *Climate Change 2013: The Physical Science Basis. Contribution of Working Group I to the Fifth Assessment Report of the Intergovernmental Panel on Climate Change*. Cambridge: Cambridge University Press, 2013. ISBN: 978-92-9169-138-8.

- [51] C. R. JACKSON and W. ALPERS. “The role of the critical angle in brightness reversals on sunglint images of the sea surface”. *Journal of Geophysical Research: Oceans* 115(C9) (2010). DOI: <https://doi.org/10.1029/2009JC006037>.
- [52] C. R. JACKSON and W. ALPERS. “The role of the critical angle in brightness reversals on sunglint images of the sea surface”. *Journal of Geophysical Research: Oceans* 115(C9) (2010). DOI: <https://doi.org/10.1029/2009JC006037>.
- [53] B. JOHNSON *et al.* “In situ observations of volcanic ash clouds from the FAAM aircraft during the eruption of Eyjafjallajökull in 2010”. *Journal of Geophysical Research (Atmospheres)* 117(D20), D00U24 (Oct. 2012), D00U24. DOI: 10.1029/2011JD016760.
- [54] J. H. JOSEPH *et al.* “Determination of most probable height of desert dust aerosol layer from space”. *Journal of Geophysical Research (Atmospheres)* 113(D20), D20S93 (Oct. 2008), D20S93. DOI: 10.1029/2007JD009646.
- [55] M. D. KING *et al.* “Spatial and Temporal Distribution of Clouds Observed by MODIS Onboard the Terra and Aqua Satellites”. *IEEE Transactions on Geoscience and Remote Sensing* 51(7) (2013), pp. 3826–3852. DOI: 10.1109/TGRS.2012.2227333.
- [56] S. KORKIN, A. SAYER, A. IBRAHIM, and A. LYAPUSTIN. “A practical guide to writing a radiative transfer code”. *Computer Physics Communications* 271 (2022), p. 108198. ISSN: 0010-4655. DOI: <https://doi.org/10.1016/j.cpc.2021.108198>.
- [57] C. KUO *et al.* “Assessing the accuracy and efficiency of longwave radiative transfer models involving scattering effect with cloud optical property parameterizations”. *Journal of Quantitative Spectroscopy and Radiative Transfer* 240 (Jan. 2020). DOI: <https://doi.org/10.1016/j.jqsrt.2019.106683>.
- [58] T. L'ECUYER *et al.* “The Polar Radiant Energy in the Far Infrared Experiment”. *BAMS*. 2021. DOI: <https://doi.org/10.1175/BAMS-D-20-0155.1>.
- [59] L. C. LABONNOTE, J. HOCKING, and J. VIDOT. “Improvement of the scattering parameterization in RTTOV”. *Document NWPSAF-MO_VS-059* (Sept. 2022).
- [60] K. N. LIOU. *An introduction to atmospheric radiation*. Amsterdam Boston: Academic Press, 2002. ISBN: 0-12-451451-0.
- [61] K.-N. LIOU. “A Numerical Experiment on Chandrasekhar’s Discrete-Ordinate Method for Radiative Transfer: Applications to Cloudy and Hazy Atmospheres”. *Journal of the Atmospheric Sciences* 30(7) (1973), pp. 1303–1326. DOI: [https://doi.org/10.1175/1520-0469\(1973\)030<1303:ANE OCD>2.0.CO;2](https://doi.org/10.1175/1520-0469(1973)030<1303:ANE OCD>2.0.CO;2).

- [62] K.-N. LIU. “Analytic Two-Stream and Four-Stream Solutions for Radiative Transfer”. *Journal of the Atmospheric Sciences* 31 (July 1974). doi: [https://doi.org/10.1175/1520-0469\(1974\)031<1473:ATSAFS>2.0.CO;2](https://doi.org/10.1175/1520-0469(1974)031<1473:ATSAFS>2.0.CO;2).
- [63] X. LIU *et al.* “Development of a fast and accurate PCRTM radiative transfer model in the solar spectral region.” *Applied Optics* 55(29) (Oct. 2016), pp. 8236–8247. doi: <https://doi.org/10.1364/AO.55.008236>.
- [64] G. LIUZZI *et al.* “All-sky radiative transfer calculations for IASI and IASING: The σ -IASI-as code”. *Radiation Processes in the Atmosphere and Ocean*. Vol. 1810. American Institute of Physics Conference Series. Feb. 2017, 040004, p. 040004. doi: 10.1063/1.4975506.
- [65] G. LIUZZI *et al.* “Consistency of dimensional distributions and refractive indices of desert dust measured over Lampedusa with IASI radiances”. *Atmospheric Measurement Techniques* 10(2) (Feb. 2017), pp. 599–615. doi: 10.5194/amt-10-599-2017.
- [66] T. MAESTRI and R. RIZZI. “A study on infrared diabatic forcing of ice clouds in the tropical atmosphere”. *Journal of Geophysical Research* 108 (2003), p. 4139. doi: <https://doi.org/10.1029/2002JD002146>.
- [67] T. MAESTRI *et al.* “Analysis of cirrus cloud spectral signatures in the far infrared”. *Journal of Quantitative Spectroscopy and Radiative Transfer* 141 (July 2014), pp. 49–64. doi: 10.1016/j.jqsrt.2014.02.030.
- [68] T. MAESTRI, W. COSSICH, and I. SBROLLI. “Cloud identification and classification from high spectral resolution data in the far infrared and mid-infrared”. *Atmospheric Measurement Techniques* 12(7) (July 2019), pp. 3521–3540. doi: 10.5194/amt-12-3521-2019.
- [69] T. MAESTRI and R. E. HOLZ. “Retrieval of Cloud Optical Properties From Multiple Infrared Hyperspectral Measurements: A Methodology Based on a Line-by-Line Multiple-Scattering Code”. *IEEE Transactions on Geoscience and Remote Sensing* 47(8) (2009), pp. 2413–2426. doi: 10.1109/TGRS.2009.2016105.
- [70] T. MAESTRI *et al.* “Antarctic Ice Cloud Identification and Properties Using Downwelling Spectral Radiance From 100 to 1400 cm^{-1} ”. *Journal of Geophysical Research (Atmospheres)* 124(8) (Apr. 2019), pp. 4761–4781. doi: 10.1029/2018JD029205.
- [71] T. MAESTRI *et al.* “Innovative solution for fast radiative transfer in multiple scattering atmospheres at far and mid infrared wavelengths”. *Proceedings of the IRS 2022* (2023).

- [72] T. MARKE, K. EBELL, U. LOHNERT, and D. D. TURNER. “Statistical retrieval of thin liquid cloud microphysical properties using ground-based infrared and microwave observations”. *Journal of Geophysical Research: Atmospheres* 121(24) (2016), pp. 14558–14573. DOI: <https://doi.org/10.1002/2016JD025667>.
- [73] G. M. MARTIN, D. W. JOHNSON, and A. SPICE. “The Measurement and Parameterization of Effective Radius of Droplets in Warm Stratocumulus Clouds”. *Journal of the Atmospheric Sciences* 51 (1994), pp. 1823–1842. DOI: 10.1175/1520-0469(1994)051<1823:TMAPOE>2.0.CO;2.
- [74] M. MARTINAZZO *et al.* “Assessment of the accuracy of scaling methods for radiance simulations at far and mid infrared wavelengths”. *Journal of Quantitative Spectroscopy and Radiative Transfer* 271 (2021). DOI: <https://doi.org/10.1016/j.jqsrt.2021.107739>.
- [75] M. MARTINAZZO and T. MAESTRI. “The MAMA Algorithm for Fast Computations of Upwelling Far- and Mid-Infrared Radiances in the Presence of Clouds”. *Remote Sensing* 15(18) (2023). ISSN: 2072-4292. DOI: 10.3390/rs15184454.
- [76] G. MASIELLO, M. MATRICARDI, and C. SERIO. “The use of IASI data to identify systematic errors in the ECMWF forecasts of temperature in the upper stratosphere”. *Atmospheric Chemistry and Physics* 11(3) (2011), pp. 1009–1021. DOI: 10.5194/acp-11-1009-2011.
- [77] G. MASIELLO *et al.* “The new σ -IASI code for all sky radiative transfer calculations in the spectral range 10 to 2760 cm⁻¹: σ -IASI/F2N”. *Journal of Quantitative Spectroscopy and Radiative Transfer* 312 (2024), p. 108814. ISSN: 0022-4073. DOI: <https://doi.org/10.1016/j.jqsrt.2023.108814>.
- [78] M. MATRICARDI. *The inclusion of aerosols and clouds in RTIASI, the ECMWF fast radiative transfer model for the infrared atmospheric sounding interferometer*. Technical memorandum 474. Corrected version posted on December 2012. Shinfield Park, Reading: ECMWF, July 2005. DOI: 10.21957/1krvb28qL.
- [79] M. MATRICARDI, F. CHEVALLIER, G. KELLY, and J.-N. THEPAUT. “An improved general fast radiative transfer model for the assimilation of radiance observations”. *Quarterly Journal of the Royal Meteorological Society* 130(596) (2004), pp. 153–173. DOI: <https://doi.org/10.1256/qj.02.181>.
- [80] M. MATRICARDI and R. SAUNDERS. “Fast radiative transfer model for simulation of infrared atmospheric sounding interferometer radiances”. *Appl. Opt.* 38(27) (Sept. 1999), pp. 5679–5691. DOI: 10.1364/AO.38.005679.

- [81] A. MERELLI and D. D. TURNER. “Comparing information content of upwelling far-infrared and midinfrared radiance spectra for clear atmosphere profiling.” *J. Atmos. Oceanic Technol.* 29 (2012), pp. 510–526. DOI: <https://doi.org/10.1175/JTECH-D-11-00113.1>.
- [82] N. L. MILES, J. VERLINDE, and E. E. CLOTHIAUX. “Cloud Droplet Size Distributions in Low-Level Stratiform Clouds.” *Journal of Atmospheric Sciences* 57(2) (Jan. 2000), pp. 295–311. DOI: 10.1175/1520-0469(2000)057<0295:CDSIDL>2.0.CO;2.
- [83] Q. MIN and M. DUAN. “A successive order of scattering model for solving vector radiative transfer in the atmosphere”. *Journal of Quantitative Spectroscopy and Radiative Transfer* 87(3) (2004), pp. 243–259. ISSN: 0022-4073. DOI: <https://doi.org/10.1016/j.jqsrt.2003.12.019>.
- [84] E. J. MLAWER *et al.* “Development and recent evaluation of the MT_CKD model of continuum absorption”. *Philosophical Transactions of the Royal Society of London Series A* 370(1968) (June 2012), pp. 2520–2556. DOI: 10.1098/rsta.2011.0295.
- [85] M. G. MLYNCZAK *et al.* “First light from the Far-Infrared Spectroscopy of the Troposphere (FIRST) instrument”. *Geophysical Research Letters* 33(7), L07704 (Apr. 2006), p. L07704. DOI: 10.1029/2005GL025114.
- [86] J.-J. MORCRETTE *et al.* “Aerosol analysis and forecast in the European Centre for Medium-Range Weather Forecasts Integrated Forecast System: Forward modeling”. *Journal of Geophysical Research: Atmospheres* 114(D6) (2009). DOI: <https://doi.org/10.1029/2008JD011235>.
- [87] A. MORTIER *et al.* “Detection and characterization of volcanic ash plumes over Lille during the Eyjafjallajökull eruption”. *Atmospheric Chemistry & Physics* 13(7) (Apr. 2013), pp. 3705–3720. DOI: 10.5194/acp-13-3705-2013.
- [88] L. PALCHETTI *et al.* “FORUM: unique far-infrared satellite observations to better understand how Earth radiates energy to space”. *Bulletin of the American Meteorological Society* (Aug. 2020), pp. 1–52. ISSN: 0003-0007. DOI: 10.1175/BAMS-D-19-0322.1.
- [89] O. PEÑA and U. PAL. “Scattering of electromagnetic radiation by a multilayered sphere”. *Computer Physics Communications* 180(11) (Nov. 2009), pp. 2348–2354. DOI: 10.1016/j.cpc.2009.07.010.
- [90] S. PLATNICK, P. HUBANKS, K. MEYER, and M. D. KING. *MODIS Atmosphere L3 Monthly Product*. Tech. rep. MODIS Collection 6.1 - Level 1, Atmosphere, Land (ArchiveSet 61). http://dx.doi.org/10.5067/MODIS/MYD08_M3.061 (accessed on 23 December 2020). Goddard Space Flight Center, USA: NASA MODIS Adaptive Processing System, 2015.

- [91] S. PLATNICK *et al.* “The MODIS Cloud Optical and Microphysical Products: Collection 6 Updates and Examples From Terra and Aqua”. *IEEE Transactions on Geoscience and Remote Sensing* 55(1) (2017), pp. 502–525. DOI: 10.1109/TGRS.2016.2610522.
- [92] J. J. REMEDIOS *et al.* “MIPAS reference atmospheres and comparisons to V4.6I/V4.62 MIPAS level 2 geophysical data sets”. *Atmospheric Chemistry & Physics Discussions* 7(4) (2007), pp. 9973–10017.
- [93] M. RIDOLFI *et al.* “FORUM Earth Explorer 9: Characteristics of Level 2 Products and Synergies with IASI-NG”. *Remote Sensing* 12(9) (2020). ISSN: 2072-4292. DOI: 10.3390/rs12091496.
- [94] R. RIZZI *et al.* “Feasibility of the spaceborne radiation explorer in the far infrared (REFIR)”. *Proc.SPIE* 4485 (2002). DOI: 10.1117/12.454252.
- [95] L. S. ROTHMAN *et al.* “The HITRAN2012 molecular spectroscopic database”. *Journal of Quantitative Spectroscopy and Radiative Transfer* 130 (2013), pp. 4–50. DOI: 10.1016/j.jqsrt.2013.07.002.
- [96] M. SAITO *et al.* “Spaceborn middle- and far-infrared observations improving nighttime ice cloud properties retrievals.” *Geophysics Research Letter* 47 (2020). DOI: <https://doi.org/10.1029/2020GL087491>.
- [97] K. SASSEN and G. C. DODD. “Haze Particle Nucleation Simulations in Cirrus Clouds, and Applications for Numerical and Lidar Studies.” *Journal of Atmospheric Sciences* 46(19) (1989), pp. 3005–3014. DOI: 10.1175/1520-0469(1989)046<3005:HPNSIC>2.0.CO;2.
- [98] R. SAUNDERS *et al.* “An update on the RTTOV fast radiative transfer model (currently at version 12)”. *Geoscientific Model Development* 11(7) (2018), pp. 2717–2737. DOI: 10.5194/gmd-11-2717-2018.
- [99] C. SERIO *et al.* “Retrieval of foreign-broadened water vapor continuum coefficients from emitted spectral radiance in the H₂O rotational band from 240 to 590 cm⁻¹”. *Optics Express* 16(20) (2008), p. 15816. DOI: 10.1364/OE.16.015816.
- [100] L. SGHERI *et al.* “The FORUM end-to-end simulator project: architecture and results”. *Atmospheric Measurement Techniques* 15(3) (2022), pp. 573–604. DOI: 10.5194/amt-15-573-2022.
- [101] A. SINHA and J. E. HARRIES. “Water vapour and greenhouse trapping: The role of far infrared absorption”. *Geophysical Research Letters* 22(16) (1995), pp. 2147–2150. DOI: 10.1029/95GL01891.

- [I02] S. SOLOMON *et al.* “Contributions of Stratospheric Water Vapor to Decadal Changes in the Rate of Global Warming”. *Science* 327(5970) (2010), pp. 1219–1223. DOI: 10.1126/science.1182488.
- [I03] K. STAMNES, S. C. TSAY, K. JAYAWEEERA, and W. WISCOMBE. “Numerically stable algorithm for discrete-ordinate-method radiative transfer in multiple scattering and emitting layered media”. *Applied Optics* 27 (1988), pp. 2502–2509. DOI: 10.1364/AO.27.002502.
- [I04] G. G. STOKES. *On the intensity of the light reflected from or transmitted through a pile of plates.* 1862.
- [I05] Z. SUN. “Reply to comments by Greg M. McFarquhar on ‘Parametrization of effective sizes of cirrus-cloud particles and its verification against observations’. (October B, 1999, 125, 3037–3055)”. *Quarterly Journal of the Royal Meteorological Society* 127(571) (2001), pp. 267–271. DOI: <https://doi.org/10.1002/qj.49712757116>.
- [I06] G. TANG *et al.* “Improvement of the Simulation of Cloud Longwave Scattering in Broadband Radiative Transfer Models”. *Journal of Atmospheric Sciences* 75(7) (2018), pp. 2217–2233. DOI: 10.1175/JAS-D-18-0014.1.
- [I07] O. TOON, C. MCKAY, T. ACKERMAN, and K. SANTHAMAN. “Rapid calculation of radiative heating rates and photodissociation rates in inhomogeneous multiple scattering atmospheres”. *Journal of Geophysical Research* (1989). DOI: 10.1029/JD094ID13P16287.
- [I08] I. TRITSCHER *et al.* “Polar Stratospheric Clouds: Satellite Observations, Processes, and Role in Ozone Depletion”. *Reviews of Geophysics* 59(2) (2021). e2020RG000702 2020RG000702, e2020RG000702. DOI: <https://doi.org/10.1029/2020RG000702>.
- [I09] D. D. TURNER *et al.* “Cloud Phase Determination Using Ground-Based AERI Observations at SHEBA”. *Journal of Applied Meteorology* 42(6) (2003), pp. 701–715. DOI: [https://doi.org/10.1175/1520-0450\(2003\)042<0701:CPDUGA>2.0.CO;2](https://doi.org/10.1175/1520-0450(2003)042<0701:CPDUGA>2.0.CO;2).
- [I10] D. D. TURNER *et al.* “Cloud Phase Determination Using Ground-Based AERI Observations at SHEBA.” *Journal of Applied Meteorology* 42(6) (2003), pp. 701–715. DOI: 10.1175/1520-0450(2003)042<0701:CPDUGA>2.0.CO;2.
- [I11] D. D. TURNER *et al.* “Ground-based high spectral resolution observations of the entire terrestrial spectrum under extremely dry conditions”. *Geophysical Research Letters* 39(10), L10801 (2012), p. L10801. DOI: 10.1029/2012GL051542.
- [I12] *U.S. Standard Atmosphere.* NOAA, 1976.

- [I13] P. VEGLIO and T. MAESTRI. “Statistics of vertical backscatter profiles of cirrus clouds”. *Atmospheric Chemistry & Physics* 11(24) (2011), pp. 12925–12943. DOI: 10.5194/acp-11-12925-2011.
- [I14] F. E. VOLZ. “Infrared optical constants of ammonium sulfate, Sahara dust, volcanic pumice, and fly ash”. *Applied Optics* 12(3) (1973), p. 564. DOI: 10.1364/AO.12.000564.
- [I15] F. E. VOLZ. “Infrared refractive index of atmospheric aerosol substances”. *Applied Optics* 11(4) (1972), p. 755. DOI: 10.1364/AO.11.000755.
- [I16] S. G. WARREN and R. E. BRANDT. “Optical constants of ice from the ultraviolet to the microwave: A revised compilation”. *Journal of Geophysical Research (Atmospheres)* 113(D14), D14220 (July 2008), p. D14220. DOI: 10.1029/2007JD009744.
- [I17] WDCGG (*World Data Centre for Greenhouse Gases*). <https://gaw.kishou.go.jp/publications/summary>. Accessed: 2023-02-23.
- [I18] B. A. WIELICKI *et al.* “Achieving Climate Change Absolute Accuracy in Orbit”. *Bulletin of the American Meteorological Society* 94(10) (2013), pp. 1519–1539. DOI: 10.1175/BAMS-D-12-00149.1.
- [I19] W. J. WISCOMBE and G. W. GRAMS. “The Backscattered Fraction in two-stream Approximations”. *Journal of Atmospheric Sciences* 33(12) (1976), pp. 2440–2451. DOI: [https://doi.org/10.1175/1520-0469\(1976\)033<2440:TBFITS>2.0.CO;2](https://doi.org/10.1175/1520-0469(1976)033<2440:TBFITS>2.0.CO;2).
- [I20] K. WYSER. “The Effective Radius in Ice Clouds”. *Journal of Climate* 11(7) (1998), pp. 1793–1802. DOI: [https://doi.org/10.1175/1520-0442\(1998\)011<1793:TERIIC>2.0.CO;2](https://doi.org/10.1175/1520-0442(1998)011<1793:TERIIC>2.0.CO;2).
- [I21] P. YANG *et al.* “A Review of Ice Cloud Optical Property Models for Passive Satellite Remote Sensing”. *Atmosphere* 9(12) (2018), p. 499. DOI: 10.3390/atmos9120499.
- [I22] P. YANG *et al.* “Spectrally Consistent Scattering, Absorption, and Polarization Properties of Atmospheric Ice Crystals at Wavelengths from 0.2 to 100 μm ”. *Journal of the Atmospheric Sciences* 70(1) (2013), pp. 330–347. DOI: 10.1175/JAS-D-12-039.1.
- [I23] W. ZDUNKOWSKI, T. TRAUTMANN, and A. BOTT. *Radiation in the Atmosphere: A Course in Theoretical Meteorology*. Cambridge: Cambridge University Press, 2007. ISBN: 0-521-87107-7.